



NorthWest Research Associates, Inc.

P.O. Box 3027 • Bellevue, WA 98009-3027

NWRA-CR-97-R170

July 21, 1997

Sea Ice Mechanics Research

Final Report

For Contract N00014-92-C-0027

*Prepared by
Max D. Coon, Ph.D.*

DTIC QUALITY INSPECTED &

DISTRIBUTION STATEMENT 2

**Approved for public release
Distribution Unlimited**

Prepared for

*Dr. Randy Jacobson
High Latitude Program
Office of Naval Research/Code 321TS
Ballston Tower One
800 Quincy Street
Arlington, VA 22217-5660*

19970724 104

NWRA-CR-97-R170

July 21, 1997

Sea Ice Mechanics Research

Final Report

For Contract N00014-92-C-0027

*Prepared by
Max D. Coon, Ph.D.*

*Prepared for

Dr. Randy Jacobson
High Latitude Program
Office of Naval Research/Code 321TS
Ballston Tower One
800 Quincy Street
Arlington, VA 22217-5660*

TABLE OF CONTENTS

1.0 Sea Ice Mechanics Research	1
2.0 Published papers (full text in Appendix).....	1
3.0 The Sea Ice Mechanics and Arctic Modeling Workshop.....	2
3.1 Proceedings of the Sea Ice Mechanics and Arctic Modeling Workshop Volume 1: TABLE OF CONTENTS.....	4
3.1 Proceedings of the Sea Ice Mechanics and Arctic Modeling Workshop Volume 2: TABLE OF CONTENTS.....	6
3.2 Summary of Workshop Results.....	10
Recent Accomplishments and Research Needed	10
3.3 Results of Panel discussions.....	10
Appendix	
Pack Ice Anisotropic Constitutive Model	A
Microwave Response to Stress in Sea Ice A Report on Initial Field Tests	B
Phenomenological Constitutive Model for Columnar Ice.....	C
Contemporaneous Field Measurements of Pack Ice Stress and Ice Strain Measurements from SAR Imagery	D
The Sea Ice Mechanics Initiative (SIMI)	E
Sea Ice Mechanics Research	F
Panel Report on 100 km Scale (Pack Ice)	G
Sea Ice Deformation and Stress A Comparison across Space Scales	H
Acoustic Signatures of Falling Ice Blocks	I
Force-Displacement Measurements of a First-Year Pressure Ridge Keel	J
An Oriented Thickness Distribution for Sea Ice	K

1.0 Sea Ice Mechanics Research

The work conducted under this Contract has covered Arctic field measurements, sea ice model development, and the organization of a workshop on Sea Ice Mechanics and Arctic Modeling. The research is best summarized by the published papers. They are presented in the Appendix, and the titles are listed here. A discussion of the workshop follows this section.

2.0 Published papers (full text with Appendix)

- "Pack Ice Anisotropic Constitutive Model," M.D. Coon, D.C. Echert, and G.S. Knoke (1992), IAHR Ice Symposium, Banff, Alberta, pp 1188-1205.
- "Microwave Response to Stress in Sea Ice – A Report on Initial Field Tests," M.D. Coon, R.G. Onstott, D.C. Echert (1993), *Cold Regions Science and Technology*, pp 79-83.
- "Phenomenological Constitutive Model for Columnar Ice," M.D. Coon and G.S. Knoke (1993), ISOPE-93 Singapore: 3rd International Offshore and Polar Engineering Conference, Singapore.
- "Contemporaneous Field Measurements of Pack Ice Stress and Ice Strain Measurements from SAR Imagery," M.D. Coon, G.S. Knoke, D.C. Echert, and H.L. Stern (1993), OCEANS'93, Oct. 18-21, Victoria, British Columbia.
- "The Sea Ice Mechanics Initiative," M.D. Coon, G.S. Knoke, and D.C. Echert (1994), 26th Annual Offshore Technology Conference (OTC), Houston, TX, pp 499-506.
- "Sea Ice Mechanics Research," D.M. Coon, D.C. Echert, and G.S. Knoke (1995), Sea Ice Mechanics and Arctic Modeling Workshop, Anchorage, AK, pp 150-159.
- "Panel Report on 100 km Scale (Pack Ice)," M.D. Coon, R. Preller, A. Proshutinsky (1995), Sea Ice Mechanics and Arctic Modeling Workshop, Anchorage, AK, pp 10-15.
- "Sea Ice Deformation and Stress, A Comparison across Space Scales," M.D. Coon, D.C. Echert, G.S. Knoke, J.E. Overland, S. Salo, R.S. Pritchard, D.A. Rothrock, and H.L. Stern (1995), Sea Ice Mechanics and Modeling Workshop, Anchorage, AK, pp 216-229.
- "Acoustic Signatures of Falling Ice Blocks," R.S. Pritchard, Y.Xie, M.D. Farmer, M.D. Coon, G.S. Knoke, and D.C. Echert (1995), *AMD-Ice Mechanics*, pp 219-230.
- "Force-Displacement Measurements of a First-Year Pressure Ridge Keel," D.M. Coon, D.C. Echert, and G.S. Knoke (1995), *AMD-Ice Mechanics*, pp 239-254.
- "An Oriented Thickness Distribution for Sea Ice," D.M. Coon, D.C. Echert, and G.S. Knoke and R.S. Pritchard (undated), submitted to *JGR*, 1997.

3.0 The Sea Ice Mechanics and Arctic Modeling Workshop

NorthWest Research Associates, Inc. (NWRA) organized the Sea Ice Mechanics and Arctic Modeling Workshop and published the 2-volume proceedings.

The Sea Ice Mechanics and Arctic Workshop was held in Anchorage, Alaska, April 25-28, 1995. The workshop focused on current state of the practice and future research needs relative to offshore oil and gas facilities, and also reviewed the results of the U.S. Navy's Office of Naval Research (ONR) Sea Ice Mechanics Initiative (SIMI). SIMI was an Office of Naval Research Accelerated Research Initiative (ARI), spanning the years 1991 to 1996. Its goals were to:

- understand sea ice constitutive laws and fracture mechanics over the full range of geophysical scales; and
- determine the scaled response to applied external forces and develop physically based constitutive and fracture models.

The goals of SIMI were established at a planning meeting held at Airlie, Virginia, in November 1990. Oil industry representatives participated in this planning process. The report from that meeting is included as Appendix A in volume 1 of these Proceedings. The main field experiments were defined at a second SIMI planning meeting held at Sidney, British Columbia, in August 1993 and are described in the Summary Plan included as Appendix B in Volume 1. The main field experiments were conducted in the Beaufort Sea during 1993 and 1994. The Proceedings of the workshop are presented in Volume 2. The Table of Contents of Vol. 1&2 are presented below.

The workshop received financial support from a number of government agencies and oil companies, including:

U.S. Navy Office of Naval Research
U.S. Minerals Management Service
Canadian National Energy Board
Amoco, Arco, Chevron, Exxon, and Mobil

The workshop sponsored travel and expenses for five Russian scientists and provided partial support for a sixth Russian scientist to attend the workshop. Funding for these individuals was provided by Minerals Management Service, Arco and Mobil. These scientists were:

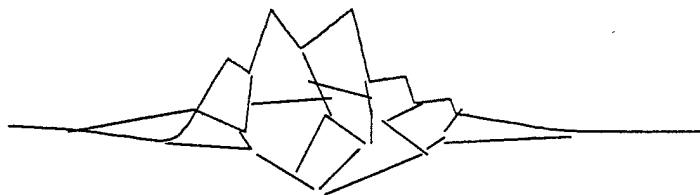
- Prof. Robert V. Goldstein of the Institute for Problems in Mechanics, Moscow, Russia;
- Dr. Anatoly M. Polomoshnov of the Sakhalin Oil and Gas Institute, Sakhalin Island, Russia;
- Dr. Vladimir E. Ryabinin of the Hydropmetcentre of Russia, Moscow, Russia;
- Dr. Victor N. Smirnov of the Arctic and Antarctic Research Institute, St. Petersburg, Russia;

- Dr. Pavel A. Truskov of the Sakhalin Oil and Gas Institute, Sakhalin Island, Russia; and
- Dr. Alexander Bekker of the Far-Eastern State Technical University, Vladivostok, Russia.

The workshop began with a day of providing information to, and among, the attendees. On Tuesday morning, a series of speakers provided background information to all participants. That afternoon was a poster session in which 43 posters were presented and discussed. The remainder of the week was spent in working panel sessions and in presenting results to, and discussing them with, the other attendees. On Wednesday morning (April 26), five panel sessions were held, each focusing on processes at different physical scales. On Thursday morning, four panels were held on topics of current importance. The afternoons of Wednesday and Thursday were spent in presenting and discussing the results of the morning sessions to the other attendees. Friday morning was a plenary wrap-up and summary session of the workshop results.

A summary of workshop results, "Recent Accomplishments and Research Needed," is presented after the Table of Contents of Vol. 1 and 2.

3.1 Proceedings of the Sea Ice Mechanics and Arctic Modeling Workshop



Sea Ice Mechanics and Arctic Modeling Workshop Volume 1

Table of Contents

1. Introduction
2. Acoustics
 - Farmer, D., and Y. Xie, "Acoustic and Seismic Studies of Ice Mechanics"
 - Mikhalevsky, P., A. B. Baggeroer, H. Schmidt, K. von der Heydt, E. K. Sheer, and A. Gavrilov, "Transarctic Acoustic Propagation"
 - Pritchard, R. S., "Sea Ice Failure Mechanisms"
 - Rajan, S. D., "Sea Ice Mechanics Research: Tomographic Imaging of Wave Speeds and Acoustic Emission Event Localization"
 - Schmidt, H., A. B. Baggeroer, I. Dyer, K. von der Heydt, and E. K. Scheer, "Seismo-Acoustic Remote Sensing of Ice-Mechanical Processes in the Arctic"
 - Stein, P. J., D. W. Andersen, A. Bahlavouni, S. E. Euerle, G. M. Santos, and R. K. Menoche, "SIMI Winter-Over Geophone/Hydrophone System"
3. Fracture Mechanics
 - Bažant, Z. P., Y.-N. Li, M. Jirásek, Z. Li, and J.-J. Kim, "Effect of Size on Distributed Damage and Fracture of Sea Ice"
 - Dempsey, J., and R. Adamson, "Scale Effects on the Fracture and Constitutive Behavior of Sea Ice"
4. Ice Properties
 - Cole, D. M., "Field and Laboratory Experiments and Modeling of the Constitutive Behavior of Sea Ice"
 - Gupta, V., R. C. Picu, J. Bergström, and H. J. Frost, "Crack Nucleation Mechanisms in Columnar Ice -- Recent Developments"
 - Schulson, E. M., "Compressive Failure of Columnar Saline Ice under Multiaxial Loading"
 - Shapiro, L. H., W. F. Weeks, and W. D. Harrison, "Studies of the Influence of Fabric and Structure on the Flexural Strength of Sea Ice and, of the Consolidation of First-Year Pressure Ridges"

5. Ice Stress, Ice Strain, and Ice Conditions
 - Coon, M. D., D. C. Echert, and G. S. Knoke, "Sea Ice Mechanics Research"
 - O'Hara, S. and J. Ardai, Jr., "SIMI GPS Position and CTD Cast Data"
 - Overland, J., S. Salo, S. Li, and L. McNutt, "Regional and Floe-Floe Deformation"
 - Richter-Menge, J. A., B. C. Elder, W. B. Tucker III, and D. K. Perovich "Pack Ice Stresses and their Relationship to Regional Deformation"
6. Modeling
 - Connor, J. J., S. Shyam-Sunder, A. Elvin, D. Choi, and J. Kim, "Physically Based Constitutive Modeling of Ice"
 - Hopkins, M. A., "Numerical Simulation of Arctic Pressure Ridging"
 - Lewis, J. K., and P. J. Stein, "Sea Ice Mechanics Related to Thermally-Induced Stresses and Fracturing of Pack Ice"
 - Petrenko, V., and O. Gluschenkov, "Measurements of Crack Velocity in Sea Ice Using Electromagnetic Techniques"
 - Rodin, G., R. Shapery, K. Abdel-Tawab, and L. Wang, "Constitutive Equations and Fracture Models for Sea Ice"
 - Wu, M. S., J. Niu, Y. Zhang, and H. Zhou, "Physically-Based Constitutive Modeling of Ice: Damage and Failure"

Appendix A -- Air-Ice-Ocean Interaction: Lead Dynamics, Ice Mechanics, Ice Acoustics
(Sea Ice Mechanics Workshop at Airlie, VA, 1990)

Appendix B -- Sea Ice Mechanics Initiative (SIMI) Summary Plan, FY94-95 (Workshop
at Sidney, BC, 1993)

3.1 Proceedings of the Sea Ice Mechanics and Arctic Modeling Workshop

Volume 2

TABLE OF CONTENTS

Preface	i
Introduction	1
1. PART 1-RESULTS OF WORKSHOP SESSIONS	5
1.1 Summary of Workshop Results - Recent Accomplishments and Research Needed	5
1.2 Results of Panel Discussions	5
1.2.1 100 km Scale (pack ice)	10
1.2.2 10 km Scale (floe cluster)	16
1.2.3 1 km Scale (floe ridge crack)	22
1.2.4 10 m Scale (macro-crack)	28
1.2.5 1 cm to 1 m Scale (materials)	45
1.2.6 Ice Loads on Fixed and Floating Structures, Including Vessels	60
1.2.7 Ice Forecasting for Ship Routing and Operations	79
1.2.8 Ice Gouging of the Sea Floor	84
1.2.9 Oil Spills and Oil Transport by the Ice	97
2. PART II - INVITED SPEAKERS AND POSTERS	102
2.1 Speakers on Tuesday, April 25, Opening Session	102
2.1.1 "Industry-Government Cooperation in Ice Mechanics and Modeling," Albert Wang (Exxon)	103
2.1.2 "Program for Energy Research and Development (PERD), Ice-Structure Interaction Program," Ibrahim Konuk, (National Energy Board of Canada)	118
2.1.3 "MMS Programs," Jeff Walker (MMS) (no text available)	
2.1.4 "Application of Ice Cover Mechanics in Design and Operations of Marine Structures", Jukka Tuhkuri, (Arctic Offshore Research Centre, Helsinki Univ. of Tech.)	123
2.1.5 "Ice-Structure Interaction Research and Arctic Development," Ben Danielewicz (Canadian Marine Drilling)	135
2.1.6 "BP Program," Graham A. N. Thomas (BP International Ltd.)	141
2.2 Invited Speaker at Banquet, Thursday, April 27	
"A Review of Select Exploration and Development Activities in State Nearshore Areas," James Hansen, Manager of Oil and Gas Leasing Program, Alaska Department of Natural Resources.	145

2.3 SIMI Papers not included in Volume 1 175

"Ice Surface Oscillation Measurements on SIMI using Strain, Heave and Tilt Sensors,"
Peter Wadhams and Stephen C. S. Wells, Scott Polar Research Institute, Cambridge, UK. 176

"AUV Operations in the Arctic," J. G. Bellingham, J. J. Leonard, J. Vaganay, C. A.
Goudey, D. K. Atwood, T. R. Consi, J. W. Bales, H. Schmidt and C. Chrysostomidis,
Mass. Inst. of Tech. 190

"Multipath Navigation in the Arctic: A Feasibility Test," Max Deffenbaugh, Henrik
Schmidt and James G. Bellingham, Mass. Inst. of Tech. 199

"Performance Assessment of the High Resolution GPS Ranging System," Max
Deffenbaugh, Henrik Schmidt and James G. Bellingham, Mass. Inst. of Tech. 204

2.4 Poster Session 207

Author(s) and Title

Anderson, Robert M., and Burton L. Markham, "Submarine Force Support of Arctic
Science: The SCICEX Program." 212

Bažant, Z. P., Y.-N. Li, M. Jirásek, Z. Li, and J.-J. Kim, "Effect of Size on
Distributed Damage and Fracture of Sea Ice." V1, 73

Bekker, A. T., "Ice Structure Dynamic Interaction: Destruction Ice Model." 213

Bekker, A. T., and S. G. Gomolsky "Determination of the Ice Strength for Calculation
of the Ice Load." 214

Cole, D. M., "Field and Laboratory Experiments and Modeling of the Constitutive
Behavior of Sea Ice." V1, 101

Cole, David M., Lewis H. Shapiro, Wilford F. Weeks, Carl Byers, John P. Dempsey,
Robert M. Adamson, Victor F. Petrenko, and Oleg V. Gluschenkov, "The
Barrow Experiments." 215

Connor, J. J., S. Shyam-Sunder, A. Elvin, D. Choi, and J. Kim, "Physically Based
Constitutive Modeling of Ice." V1, 189

Coon, M. D., D. C. Echert, and G. S. Knoke, "Sea Ice Mechanics from 20 cm to 80
km." V1, 151

Coon, M. D., D. C. Echert, G. S. Knoke, J. E. Overland, S. Salo, R. S. Pritchard, D.
A. Rothrock, and H. L. Stern "Sea Ice Deformation and Stress, a Comparison
across Space Scales." 216

Dempsey, J., and R. Adamson, "Scale Effects on the Fracture and Constitutive
Behavior of Sea Ice." V1, 84

Farmer, D., and Y. Xie, "Acoustic and Seismic Studies of Ice Mechanics." V1, 7

Gupta, V., R. C. Picu, J. Bergström, and H. J. Frost, "Crack Nucleation Mechanisms in Columnar Ice -- Recent Developments."	V1, 110
Hedstrom, Katherine, "A Coupled Ice-Ocean-Atmosphere Model of the Bering Sea."	230
Hopkins, M. A., "Numerical Simulation of Arctic Pressure Ridging."	V1, 199
Kerman, Bryan, "Information States in Sea Ice Imagery."	239
Kristensen, Dirk, Vera Alexander, Thomas Royer, and Robert Elsner, "The Planned NSF/UNOLS Arctic Research Vessel for the United States Arctic Science".	249
Lai, Ronald J., and Walter R. Johnson, "Minerals Management Service Environmental Studies Program and Oil Spill Risk Analysis for the Beaufort Sea".	262
Lewis, J. K., and P. J. Stein, "Sea Ice Mechanics Related to Thermally-Induced Stresses and Fracturing of Pack Ice."	V1, 209
Mikhalevsky, P., A. B. Baggeroer, H. Schmidt, K. von der Heydt, E. K. Sheer, and A. Gavrilov, "Transarctic Acoustic Propagation."	V1, 24
O'Hara, S., and J. Ardai, Jr., "SIMI GPS Position and CTD Cast Data."	V1, 160
Ostoja-Starzewski, Martin, "Micromechanically Based Constitutive Laws for Ice Fields."	263
Overland, J., S. Salo, S. Li, and L. McNutt, "Regional and Floe-Floe Deformation."	V1, 168
Petrenko, V., and O. Gluschenkov, "Measurements of Crack Velocity in Sea Ice Using Electromagnetic Techniques."	V1, 216
Pham, Thomas Thang, "The Polar Ice Prediction System at Fleet Numerical Meteorology and Oceanography Center (FLENUMMETOCCEN)."	264
Pritchard, R. S., "Sea Ice Failure Mechanisms."	V1, 34
Proshutinsky, Andrey, and Mark Johnson, "The Arctic Ocean Ice and Water Transport During 1946-1988."	265
Rajan, S. D., "Sea Ice Mechanics Research, "Tomographic Imaging of Wave Speeds and Acoustic Emission Event Localization."	V1, 41
Richter-Menge, J. A., B. C. Elder, W. B. Tucker III, and D. K. Perovich, "Pack Ice Stresses and their Relationship to Regional Deformation."	V1, 178
Rodin, G., R. Schapery, "Constitutive Equations and Fracture Models for Sea Ice. "	V1, 226
Ryabinin, Vladimir E., Alexander I. Danilov, Vladimir V. Elisov, Alexander V. Klepikov, Vladimir A. Kurdumov, Valery N. Malek, Victor N. Smirnov, Igor N. Stepanov, Oleg Ya. Timofeev, "Marine Ice Bottom Scouring: Some Mechanisms and an Approach to Depth Evaluation."	276
Schmidt, H., A. B. Baggeroer, I. Dyer, K. von der Heydt, and E. K. Scheer, "Seismo-Acoustic Remote Sensing of Ice-Mechanical Processes in the Arctic."	V1, 51
Schulson, E. M., "Compressive Failure of Columnar Saline Ice under Multiaxial Loading."	V1, 122

Shapiro, L. H., W. F. Weeks, and W. D. Harrison, "Studies of the Influence of Fabric and Structure on the Flexural Strength of Sea Ice and, of the Consolidation of First-Year Pressure Ridges."	V1, 141
Simpson, J. J., and R. H. Keller "An Improved Fuzzy Logic Segmentation of Sea Ice Clouds and Ocean in Remotely Sensed Arctic Imagery."	286
Simpson, James J., and Robert H. Keller, "Accurate Segmentation of Complex Satellite Scenes."	287
Smirnov, Victor, and V. Korostelev, "Small and Mesoscale Physical Processes in Ice Cover."	288
Stein, P. J., D. W. Andersen, A. Bahlavouni, S. E. Euerle, G. M. Santos, and R. K. Menoche, "SIMI Winter-Over Geophone/Hydrophone System."	V1, 62
Truskov, P.A., and A.M. Polomoshnov, "Ice Studies on the Northern Sakhalin Offshore."	297
Woodworth-Lynas, C. M. T., R. Phillips, J. I. Clark, R. Meaney, F. Hynes and X. Xiao, "PRISE - the Pressure Ridge Ice Scour Experiment: Preliminary Verification of Ice Keel Scour Centrifuge Model Results against Field Data."	310
Wu, M. S., J. Niu, Y. Zhang, and H. Zhou, "Physically-Based Constitutive Modeling of Ice: Damage and Failure."	V1, 236
Zagorodnov, V., and J. J. Kelley, "Instruments for Coring, Structure and Composition Analysis and Monitoring Sea Ice."	311
 Appendix A - Errata to Volume 1	 319
Appendix B - Author, Speaker, and Panel Member Index	319
Appendix C - List of Workshop Participants	323

3.2 Summary of Workshop Results

Recent Accomplishments and Research Needed

This section is a summary of the Friday (April 28) morning session. The objective of this session was to describe the research needed in each workshop topic area:

- 100 km scale (pack ice)
- 10 km Scale (floe cluster)
- 1 km Scale (floe, ridge, crack)
- 10 meter Scale (macro-crack)
- 1 cm to 1 m Scale (micro-crack, crystal)
- Ice Loads on Fixed and Floating Structures, including Vessels
- Ice Forecasting for Ship Routing and Operations
- Ice Gouging of the Sea Floor
- Oil Spills and Oil Transport by the Ice

For most of the topic areas, the most important accomplishment by SIMI and most important area for future research, as judged by the panels, are contained on the table below. The topics on ice forecasting, ice gouging of the seafloor, and oil spills were not specifically addressed by SIMI. The main text for the ice forecasting topic includes a description of the current state of the practice. For the ice gouging topics, we include a summary of what currently is known. The needs and findings on any topic are best determined by reading the panel report on that topic.

3.3 Results of Panel discussions

The results of the discussions are summarized in Table 1.

Table 1 - Summary of Recent Accomplishments and Research Needed

Panel Name	Most Important Accomplishment	Most Important Future Research
100 km Scale (pack ice)	From GPS buoys, stress buoys, and SAR, the importance of lead formation and direction on the large scale behavior of pack ice has been verified. New leads have been shown to be created from states of compression and shear stress as measured on the scale of a floe but representing stress on tens of km. Also, when leads are open, the measured stress state is compression parallel to the lead and zero perpendicular to the lead.	Need formulation and verification of model against deformation (strain rates), leads (direction and deformation), and ice concentration using buoy and satellite data.
10 km Scale (floe cluster)	SIMI acquired the first major data set of stress and strain rate of a pack ice cover on scales of 1-100 km. Results confirm the hypothesis that ice behaves as a hardening plastic, with the basic unit for continuum behavior being a cluster of floes on the scale of 10 km.	Understand what mechanical properties control the spacing of discontinuities (slip lines, leads, etc.). By mechanical properties we imply what determines the minimum strength of sea ice as a composite material on a 1 km scale, i.e. existence of cracks and floe distribution, orientation, and thickness.
1 km Scale (floe, ridge, crack)	The ratio of work to potential energy in pressure ridging is 10:1 to 17:1, depending on ice thickness.	Determine the effects of consolidation (formation of a frozen layer growing down from the water level and contact freezing between ice blocks) on the strength of first-year ridges and rubble fields.
10 meter Scale (macro-crack)	The significant scale effect on the failure strength of first year sea ice is given by the relationship: $\sigma_n = \frac{0.68}{(1+L/0.26)^{1/2}}$ where L is the characteristic dimension of the structure.	Complete the ongoing development of a nonlinear fracture model and sea ice constitutive model to make full use of the large scale fracture and constitutive measurements made to date; this, in turn, must then be used to assess and refine the scale effect predictions for the 100 - 1000m scale.

**1 cm to 1 m scale
(micro-crack, crystal)**

Established failure mechanisms: both dislocation relaxation and grain boundary relaxation account for the anelasticity of first-year sea on both the small and the large scale; grain boundary sliding accounts for high-rate crack nucleation in pore-free ice under compression; frictional crack sliding and crack interaction account for brittle compressive failure; competition between crack propagation and crack-tip creep accounts for the brittle-to-ductile transition under compression; and brine-filled pores inhibit crack propagation.	Using meter-sized blocks of pre-cracked columnar sea ice loaded under controlled conditions, test predictions that the ductile-to-brittle transition strain rate scales inversely with crack size, as (crack size) ^{-1.5} , and that the brittle compressive strength scales inversely with crack size, as (crack size) ^{-0.5} .
Developed compressive failure envelopes and surfaces and found that Hill's criterion and a truncated Coulomb criterion describe the ductile and brittle failure stress, respectively.	Determine compressive failure envelopes/surfaces and failure criteria for first-year columnar sea ice where the loading axes are inclined to the growth direction.
Found that large-scale anelasticity can be predicted from laboratory experiments, that c-axis alignment affects ice sheet compliance, and predicted that the ductile-to-brittle transition strain rate scales inversely with lead size, as (lead size) ^{-1.5} , and that the brittle compressive failure stress also scales inversely with lead size, as (lead size) ^{-0.5} .	Establish and model the relationship between sea ice growth and loading history with the in-situ anelastic and viscous creep behavior.

Ice Loads on Fixed and Floating Structures, Including Vessels

<p>Applications of SIMI Results:</p> <p><i>Ice Crushing</i> - Use the newly measured failure envelopes for columnar saline ice obtained from multi-axial testing by Schulson's group to predict ice crushing pressures. The envelopes plot the failure stress versus degree of confinement, the strain rate and the temperature. They are significant because when combined with stress analysis of the contact zone, the envelopes allow failure pressures to be calculated. However, the results may be applicable only to local ice pressure design criteria because lab scale tests cannot account for size effects on ice crushing.</p> <p>Better understanding of scale on the ductile to brittle transition has been obtained. Specifically, laboratory experiments suggest that the transition strain rate decreases with increasing flaw size (l), scaling as $l^{-3/2}$. Again, however, there is a potential problem in extrapolating lab scale results to larger scales.</p> <p><i>Sloping Structures</i> - The discrete element modelling by Hopkins to simulate ridge formation could be applied to the problem of ridge disintegration when interacting with a structure.</p> <p><i>Pack Ice Driving Forces</i> - A pack ice stress envelope was developed by Coon and others. This envelope is the largest 2-D stress state that the pack ice can withstand. Such a stress envelope can be used to: a) Define the effect of confining stress on the driving forces on a blocking floe. b) Help define the effect of ice conditions on these forces and enable probabilistic load calculations to be performed (by combining the stress envelope as a yield surface with wind and current distributions).</p>	<p>Use the learnings from the recent SIMI lab tests and theoretical analyses to improve the interpretations of full scale load measurements, and enable their extrapolation to other situations.</p> <p>Test the ductile to brittle transition size effect theory on larger samples, but before doing this, it is recommended that a scheme for incorporating the results into an ice crushing pressure size effect be demonstrated.</p> <p>Field measurements to better define the physical and mechanical properties of ridge keels (strength - cohesion - friction angle - constitutive properties; porosity; density etc.).</p> <p>Complete the interpretation of the in-situ pack ice stress measurements from an ice loading perspective: (i.e. to assess whether there is spatial averaging of ridge building forces across the width of influence and use existing data to establish pack ice stresses as a function of floe width).</p>
--	--

<p>Ice Forecasting for Ship Routing and Operations</p> <p>Ice Gouging of the Sea Floor</p>	<p><i>Floe Splitting</i> - The fracture research in the SIMI program will determine the scale dependence on the tensile failure strength as well as provide a fracture model that is applicable to sea ice in the range of 0.1 to 1 km.</p>	<p>Complete the interpretation of the SIMI experimental work to develop a size effect law for fracture and splitting. Develop a new theory for flow splitting from the above (with and without surrounding pack ice).</p>
<p>The SIMI anisotropic plasticity ice dynamics model can describe and forecast ice behavior on smaller scales (~ 3 km) than previous models.</p> <p>What we now know:</p> <p>The form of the gouge depth distribution at a given instant of time is a negative exponential.</p> <p>The coefficients of the gouge depth distribution function vary systematically with water depth.</p> <p>To obtain meaningful statistics concerning the number of gouges per km or per km² per year, a sampling period of several years duration is required.</p> <p>Gouges generally run parallel to the isobaths.</p> <p>The deepest, as well as the most frequent, gouges occur at water depths of between 25 and 40 m.</p>	<p>The SIMI anisotropic plasticity ice dynamics model can describe and forecast ice behavior on smaller scales (~ 3 km) than previous models.</p> <p>What we now know:</p> <p>The form of the gouge depth distribution at a given instant of time is a negative exponential.</p> <p>The coefficients of the gouge depth distribution function vary systematically with water depth.</p> <p>To obtain meaningful statistics concerning the number of gouges per km or per km² per year, a sampling period of several years duration is required.</p> <p>Gouges generally run parallel to the isobaths.</p> <p>The deepest, as well as the most frequent, gouges occur at water depths of between 25 and 40 m.</p>	<p>Develop failure laws for a complete suite of full-scale processes (e.g., opening, rafting, and ridging), develop a numerical scheme, and test model performance.</p> <p>There is a critical need to develop procedures for determining gouge depth distributions for regions where sediment transport is so large that gouges are so quickly destroyed as to leave no record on the sea floor.</p>
<p>Oil Spills and Oil Transport by the Ice</p>	<p>What we now know:</p> <p>Improved coupled ice-ocean models for central Arctic have been constructed.</p> <p>Nested ocean and ice model techniques have been applied to Arctic problems.</p> <p>Improvements in the convection parameterization in ocean models has been shown to accelerate the melting rate of ice.</p> <p>Improved wind fields from atmospheric models has been applied for input to ice-ocean models.</p>	<p>Small-scale (2 to 10 km) ice-ocean model development and validation, including the anisotropic parameterizations of ice mechanics, to properly characterize the nearshore ice motion since oil transport is primarily by ice motion.</p>

Pack Ice Anisotropic Constitutive Model

M.D. Coon,
D.C. Echert,
and
G.S. Knoke

IAHR Ice Symposium, 1992
Banff, Alberta



PACK ICE ANISOTROPIC CONSTITUTIVE MODEL

Max C. Coon Principal Scientist	Williamson & Associates, Inc. Seattle	USA
Douglas C. Echert Senior Scientist	Williamson & Associates, Inc. Seattle	USA
Gerald S. Knoke Senior Scientist	Williamson & Associates, Inc. Seattle	USA

ABSTRACT

Arctic sea ice may prove to be an important indicator of global climate change. However, the inter-annual variability of ice extent and thickness clouds the issue. The focus of this work is to improve the accuracy of ice models so that effects due to climate change can be distinguished from inter-annual variability. This paper describes the development of a 2-D plastic anisotropic constitutive model of the ice cover which includes the creation of new leads in thick ice and the effects of leads and their orientation on the strength of the ice cover. The model requires an oriented thickness distribution to account for the growth and ridging of ice in refrozen leads. The shear and compressive strength of each lead are functions of the lead ice thickness distribution. Plans to verify the new model with ice stress field measurements, Arctic buoy ice motion data, ice vectors, and lead orientation data provided by synthetic aperture radar satellite imagery, are discussed.

INTRODUCTION

An understanding of the heat, mass, and momentum balance of the Arctic has been known to be important to global climate change for over 30 years (e.g., National Academy of Sciences, 1967 and Barry, 1985 and 1986). According to Parkinson (1990), sea ice thickness and distribution is a good indicator of climate change. It is highly sensitive to changes in climate, and it can be routinely measured on a global scale through satellite remote sensing. Parkinson identified a shortcoming of its use as its poorly-understood inter-annual variability; the climate signal may be lost in the year-to-year variation. If the causes of the variability were understood, the utility of sea ice as an indicator would be greatly enhanced. This understanding can be obtained through improved ice dynamics and thermodynamics models.



In polar regions, the sea ice cover acts as a barrier between the atmosphere and ocean, curtailing the transfer of thermal and mechanical energy as well as mass transport. The energy exchange over open leads and young sea ice in the Central Arctic has pronounced effects on the atmosphere and ocean. For example, Badgley (1966) reports that the turbulent energy input to the atmosphere over a freezing lead is more than 2 orders of magnitude larger than that over typical 3 m ice. Maykut (1978) has shown that heat input to the atmosphere over 0-40 cm thick ice during the cold months is between 1 and 2 orders of magnitude larger than that over perennial ice. Thus, even though leads account for a small percentage of the ice pack, their effects dominate the large scale turbulent heat exchange and alter boundary layer stability. For these reasons, proper characterization of lead formation and fate in Arctic climate models is required.

The first comprehensive ice dynamics and thermodynamics model was developed by the Arctic Ice Dynamics Joint Experiment (AIDJEX) in the 1970's. This model is summarized in Coon, et al. (1974) and Coon (1980). The model contains a constitutive law consisting of a yield surface which is a prescribed function of the yield strength and internal ice stress. This model, and subsequent modifications and improvements to this model (e.g. Hibler, 1986), assumed that sea ice is isotropic, i.e., that leads are randomly distributed and oriented. These investigators recognized the shortcomings of this assumption but, since they lacked a suitable alternative, the approximation was reasonable. This paper offers a mathematical description of the anisotropic nature of sea ice which is suitable for incorporation into ice dynamics and thermodynamics models.

In the section below we describe the development of the model. Plans for validating the model and a summary of how the model can be used in an ice dynamics/thermodynamics model are described in following sections.

MODEL DEVELOPMENT

Our motivation for describing the ice behavior more accurately is so that climate, ice dynamics, and ice-generated noise can be better understood and forecasted. Existing models of these features are of the continuum type. Therefore, we elected to use a continuum approach for our constitutive model so that it will readily adapt to existing models.



Model Overview

The behavior of the pack ice element shown in Figure 1 is controlled by the behavior of the thick ice and the lead ice. The plastic failure of the thick ice and the active leads is characterized by ice strength parameters written as stress resultants (the integral of the stresses through the ice thickness) to be independent of the local variations in ice thickness.

The thick ice is assumed to be plastic with a Coulomb yield criterion and a normal flow rule. Coon (1974) used the Coulomb yield criterion for pack ice and, in addition, the normal flow rule has been used in many sea ice models (e.g., Coon, 1980; Hibler, 1979; and Pritchard, 1981). More recently, Hopkins and Hibler (1991) found a normal flow rule through numerical simulations of compact ice floes. The thick ice is assumed to be homogeneous and isotropic. The cohesive strength and angle of friction of the thick ice are assumed to be controlled by the flawed (cracked) ice floes. Another view of the Coulomb criterion is that in two dimensions the ice behavior is controlled by a compressive strength which is much greater than its tensile strength. Here again, the cracked floes produce this smaller tensile strength. Lastly, new leads are formed in this thick ice along characteristic directions which admit velocity discontinuities (Pritchard, 1988).

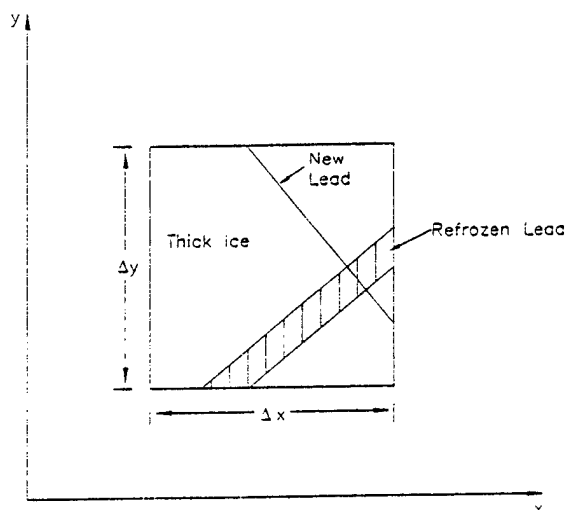


Figure 1. Element of pack ice with a new lead forming in the thick ice and a refrozen lead.

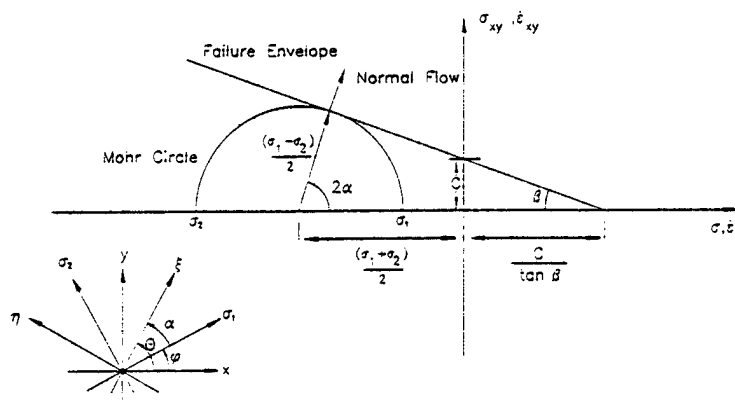


Figure 2. Failure Envelope of a Mohr-Coulomb Solid using a Mohr Circle

The following angles are used in physical space:

α - from principal stress resultant direction to the new lead direction

β - from new lead direction to the oblique angle of the motion-of one side of the new lead relative to the other (the friction angle)

ϕ - from x-axis direction (Figure 1) to principal stress resultant direction

θ - from x-axis direction (Figure 1) to new lead direction

From the geometry in Figure 2, we can find the angle α from the angle β .

$$\alpha = \pm \left(\frac{\pi}{4} + \frac{\beta}{2} \right) \quad (1)$$

Thus, the angle α is also a material property. Now, the angle of the new lead can be found from angle of the principal direction and the angle β :

$$\theta = \phi \pm \left(\frac{\pi}{4} + \frac{\beta}{2} \right) \quad (2)$$

The sign depends upon the sign of the shear stress resultant. Also from the geometry in Figure 2, the equation for the line representing the Mohr-Coulomb yield surface is

$$\sin \beta = \frac{\frac{\sigma_1 - \sigma_2}{2}}{-\frac{\sigma_1 + \sigma_2}{2} + \frac{C}{\tan \beta}} \quad (3)$$



The axis goes from the tip through the origin and the square root in Equation (8) is the radius of the cone. A new stress resultant coordinate system is useful for viewing the yield surface. We define the following variables:

$$P = \frac{\sigma_x + \sigma_y}{2} ; D = \frac{\sigma_x - \sigma_y}{2} ; S = \sigma_{xy} \quad (10)$$

where P is the pressure resultant, D is the difference between the normal stress resultants, and S is the shear stress resultant. As illustrated in Figure 3, the cone now lies along the P axis with D and S in the plane of the circle normal to the axis of the cone. The yield function in P - D - S stress resultant space now follows:

$$F = \sqrt{D^2 + S^2} + P \sin \beta - C \cos \beta \quad (11)$$

From Equation (6) it can be seen that 2ϕ is the angle of the stress resultant in the D - S plane from the D -axis towards the S -axis.

The normal flow rule states that the plastic strain rate must be normal to the yield surface at a smooth point or, at a corner, must lie between the outward normals to the adjacent yield surfaces. Therefore, the mechanical properties of a lead which

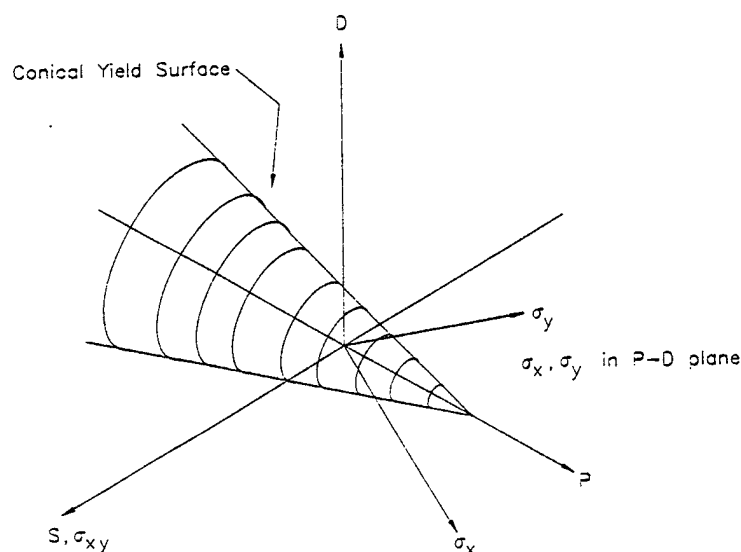


Figure 3. Conical Yield Surface of Thick Ice

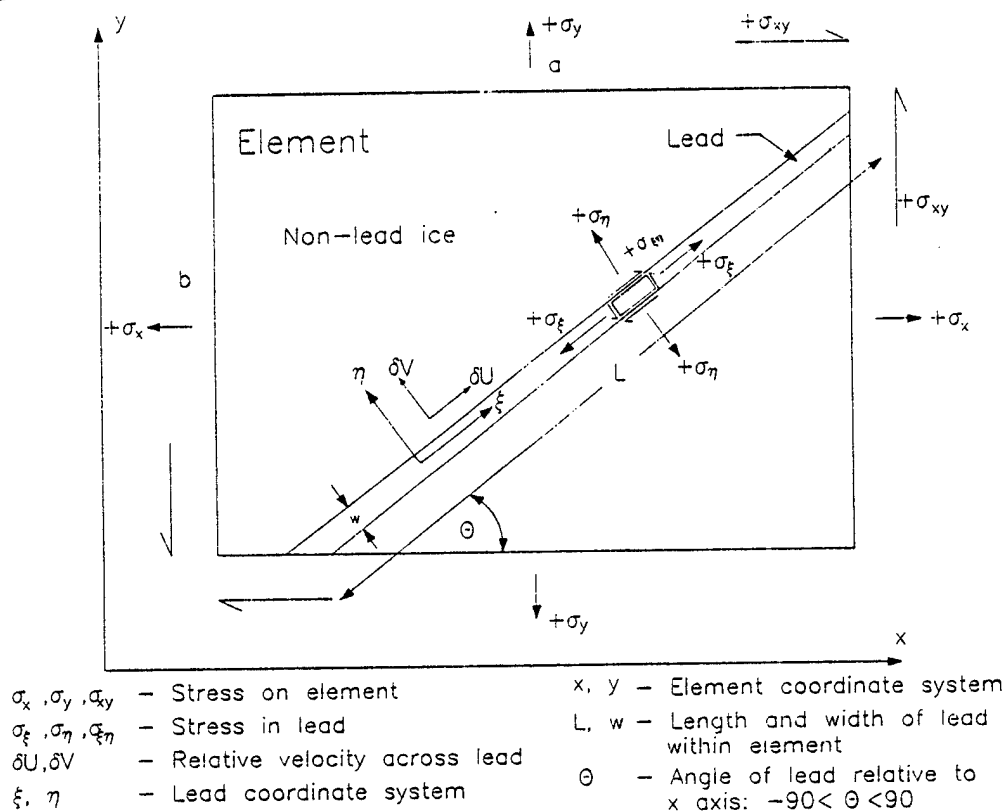


Figure 4. Single Lead in the Element

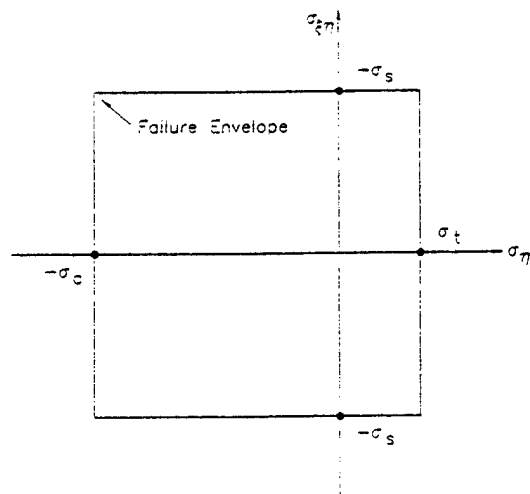


Figure 5. Yield Surface for a Lead



Table 1. Lead Strain Rates

Strain Rate	Tension	Compression	Shear
$\dot{\epsilon}_x$	$\frac{\lambda}{2} (1 - \cos 2\theta)$	$-\frac{\lambda}{2} (1 - \cos 2\theta)$	$-\frac{\lambda}{2} \sin 2\theta$
$\dot{\epsilon}_y$	$\frac{\lambda}{2} (1 + \cos 2\theta)$	$-\frac{\lambda}{2} (1 + \cos 2\theta)$	$\frac{\lambda}{2} \sin 2\theta$
$\dot{\epsilon}_{xy}$	$-\frac{\lambda}{2} \sin 2\theta$	$\frac{\lambda}{2} \sin 2\theta$	$\frac{\lambda}{2} \cos 2\theta$

Table 2. Example Material Properties

Thick Ice	Lead Ice
$h = 3 \text{ m}$	$h = 0.30 \text{ m}$
$\beta = 25^\circ$	$\sigma_c = 45,000 \text{ N/m}$
$C = 90,000 \text{ N/m}$	$\sigma_t = 9,000 \text{ N/m}$
	$\sigma_s = 6,000 \text{ N/m}$

Figure 6a shows the lead aligned with the x-axis. For this case, $\theta = 0$, so the equations for the yield surface are as follows.

For the thick ice:

$$\sqrt{D^2 + S^2} + P \sin 25^\circ = 9000 \cos 25^\circ \quad (18)$$



For shearing the lead (positive shear has the far side of the lead moving to the right):

$$S = \pm 6000 \quad (21)$$

The equation for thick ice failure forms a right circular cone with its axis along the P-axis. The lead failure is a long rectangular prism with two opposite sides representing shear failure and the other two sides representing opening and closing of the lead. When the two yield surfaces are combined, the rectangular prism intersects with the cone to form a rectangular prism with rounded ends. Since the rounded ends came from the cone, these rounded ends represent the only portion of the yield surface which can form new leads.

Figure 6 also shows three views of the combined yield surface: Figure 6b is the plane for P equal to zero, Figure 6c is for D equal to zero, and Figure 6d is for S equal to zero. In the $P=0$ and $D=0$ views, the thick ice, represented by the dashed lines, is not involved in the ice failure. As seen in Figure 6d, the rectangular prism associated with the lead makes an angle of 45° with the P axis. The effect of the lead orientation angle θ is to rotate the lead's prism around the P-axis while maintaining a constant angle of 45° between the prism axis and the P-axis. The physical deformations associated with different faces of the yield surface have been noted on the figure. The plastic strain rate vectors associated with each surface is the outward normal, except at the intersections. For example, the intersection of 'lead closing' and 'new lead forming' in Figure 6d shows a fan for the outward normal, which implies that both motions can act simultaneously and their proportion is determined by the given problem.

It is interesting to note that a yield surface formed by two leads excludes the contribution from the thick ice, i.e., the origin is completely enclosed by the intersection of the two prisms. Consequently, a third lead cannot be created. Therefore, it appears that there are only three types of yield surfaces: thick ice with no leads, thick ice with one lead, and thick ice with two leads. Summer ice conditions with open water surrounding all the floes is represented by the yield surface collapsed to the origin, i.e., the ice has no strength.



Very High Resolution Radiometer (AVHRR) satellite imagery, will provide a view of ice conditions in the study area.

APPLICATION TO ICE DYNAMICS MODELS

To incorporate this anisotropic pack ice constitutive model into other models, such as ice dynamics models, a procedure was developed to update the yield surface as a result of ice deformations and thermodynamics. Based on the strain rates found by the ice dynamics model at each time step, the change in lead area is calculated. The change in lead area causes changes in the distribution of ice thickness within the lead. The lead ice thickness also changes due to thermodynamics. The thinnest ice in the updated lead provides the basis for estimating an updated set of strength parameters.

The distribution of ice thickness must be calculated for each lead system to determine its ice strength parameters. It is anticipated that satellite data will be used to establish and correct these oriented lead ice thickness distributions when available. There is also an ice thickness associated with the thick ice to establish its strength parameters.

The rate of area change for each lead system is calculated from the element strain rates. Since all the ice in the element is assumed rigid except for the active lead, all energy dissipation due to plastic yielding of the ice occurs in the active lead, and the strain rate parallel to the active lead is zero. The shearing and normal velocity components of one side of the lead relative to the other, as shown in Figure 4, are derived to dissipate energy at the same rate as in the whole element, with the result that

$$\begin{aligned} \frac{L \delta U}{ab} &= -\dot{\epsilon}_x \cot \theta + \dot{\epsilon}_y \tan \theta \\ \frac{L \delta V}{ab} &= \dot{\epsilon}_x + \dot{\epsilon}_y \end{aligned} \quad (22)$$

where ab is the element area, δU is the shearing velocity jump across the lead, and δV is the normal velocity jump across the lead (opening velocity).

DISCUSSION

It has been shown that a plastic model of the behavior of pack ice can be developed which accounts the creation of new leads and the strength and orientation



- Coon, M. D. (1980) "A Review of AIDJEX Modeling" in Sea Ice Processes and Models, edited by R. S. Pritchard, University of Washington Press, Seattle, pp. 12-27.
- Coon, M. D., D. C. Echert, P. A. Lau, and C. M. Browne (1991) "Ice Mechanics in the LEADDEX Program," in Proceedings of OCEANS'91, Honolulu, HI, September.
- Coon, M. D., R. J. Evans, and D. H. Gibson (1984) "Failure Criteria for Sea Ice and Loads Resulting from Crushing," Proceedings of International Association for Hydraulic Research Ice Symposium 1984, Vol. III, Hamburg.
- Coon, M. D., G. A. Maykut, R. S. Pritchard, D. A. Rothrock, and A. S. Thorndike (1974) "Modeling the Pack Ice as an Elastic-Plastic Material," AIDJEX Bulletin No. 24, University of Washington, Seattle, pp. 1-106.
- Hibler, W. D. III (1979) "A Dynamic/Thermodynamic Sea Ice Model," Journal of Physical Oceanography, Vol. 9, No. 4, pp. 815-846.
- Hibler, W. D. III (1986) "Ice Dynamics," In The Geophysics of Sea Ice, H. Untersteiner, editor, Plenum Press, New York, pp. 577-640.
- Maykut, G.A. (1978) "Energy Exchange Over Young Sea Ice in the Central Arctic" Journal of Geophysical Research, 83(C7), pp. 3646-3658.
- National Academy of Sciences (1967) "Glaciology in the Arctic" prepared by the Committee on Polar Research, in Transactions, American Geophysical Union, 48, pp. 759-767.
- Parkinson, C. L. (1990) "Strengths and Weakness of Sea Ice as a Potential Early Indicator of Climate Change", presented at the Intl. Conf. on the Role of the Polar Regions in Global Change, University of Alaska, Fairbanks, June 11-15.
- Prager, W. (1959) An Introduction to Plasticity, Addison-Wesley Publishing Co., Reading, MA.
- Prager, W. and P. G. Hodge, Jr. (1951) Theory of Perfectly Plastic Solids, John Wiley and Sons, New York, NY.
- Pritchard, R. S. (1981) "Mechanical Behavior of Pack Ice," in Mechanics of Structured Media, Part A, edited by A. P. S. Selvadurai, Elsevier, New York, pp. 371-405.
- Pritchard, R. S. (1988) "Mathematical Characteristics of Sea Ice Dynamics Models," J. Geophys. Res., Vol. 93, No. C12, pp. 15609-618.
- Pritchard, R. S. and M. D. Coon (1981) "Canadian Beaufort Sea Ice Characterization," in Proceedings of POAC'81, Université Laval, Quebec, Canada, pp. 609-618.

**Microwave Response to Stress in Sea Ice
A Report on Initial Field Tests**

M.D. Coon,
R.G. Onstott,
and
D.C. Echert

Cold Regions Science and Technology, 1993

Microwave response to stress in sea ice — a report on initial field tests

M.D. Coon^a, R.G. Onstott^b, D.C. Echert^a

^a NorthWest Research Associates Inc., P.O. Box 3027, Bellevue, WA 98009, USA

^b Environmental Research Institute of Michigan, Ann Arbor, MI 48113, USA

Received 22 January 1993; accepted 15 September 1995

Abstract

An initial field test was conducted to determine if the stress state of sea ice has an effect on its microwave signature. The tests were conducted during March and April of 1992 in the Beaufort Sea. An inflatable jack was placed into a vertical slot in the ice to induce stress in the ice while a microwave transmitter/receiver monitored the backscatter from the ice. Measurements were made at X-Band and C-Band frequencies, with various polarization combinations, on 1.3 m thick first-year ice and on a freshwater melt pond within a multiyear floe. Changes in backscatter were seen in both the first-year ice and the melt pond ice at both X-Band and C-Band frequencies, but not at all polarizations and orientations. In general, the largest change in microwave response took place when the ice was pressurized for the first time. The measured changes in microwave response were less than 2 dB. However, after accounting for the mismatch between the radar footprint and the size of the area stressed, the effect on the backscatter signal was 13 dB. Response was seen at jack pressures as low as about 70 kPa, which resulted in an average stress over the radar footprint of about 13 kPa. In comparison, natural pack ice stresses range up to 400 kPa.

Keywords: Microwave response; Stress in sea ice; Sea ice; Initial field tests

1. Introduction

The effect of sea ice properties on active microwave imaging of sea ice has been the subject of numerous studies, covering a period of more than twenty years. It is generally accepted that the parameters that have been investigated to date do not explain all of the variation in sea ice microwave signature. A parameter that has not previously been investigated is the stress state of the ice. From previous studies (e.g., Coon et al., 1989, and Lau and Knoke, 1991), it is known that the stress state of pack ice can vary markedly over periods of an hour

or less. Increased stress will cause microcracking within the ice which should have an effect on the microwave signature. Additionally, in thin, warm ice, stress is expected to expel brine onto the ice surface which may also have a significant effect on the microwave signature.

Considerable work has been done to document stress-induced microcracking in the laboratory (e.g., Sinha, 1982; Hallam et al., 1986; and Cole, 1986). However, we are aware of no previous work investigating the effect of ice stress state and/or microcracking on microwave signature.

This is a report of an initial series of field tests to

investigate the effect of ice stress on the microwave signature of sea ice. Demonstrating and quantifying such an effect may lead to a better understanding and interpretation of radar imagery of sea ice, and may allow changes in ice stress to be sensed remotely.

2. Equipment and methodology

The microwave system used in this work was developed at The Environmental Research Institute of Michigan (ERIM) and has been used on numerous sea ice investigations. It consists of a frequency-modulated, continuous-wave (FM–CW) radar and operates at wavelengths of 3 cm (X-Band) and 6 cm (C-Band). There are four transmit–receive polarizations possible. These include VV, HH, HV and VH (where the V represents vertical and H represents horizontal). Ground illumination area was about $1\text{ m} \times 1.1\text{ m}$ at the 6 cm wavelength and $0.5\text{ m} \times 0.6\text{ m}$ at the 3 cm wavelength. Additional details of the system may be found in Onstott and Shuchman (1988).

An inflatable jack (a stiffened rubber air bladder) made by OTC Power Team, Owatonna, MN, was used to pressurize the ice. This device measured $38 \times 38 \times 2.5\text{ cm}$ and could be pressurized to 800 kPa. The jack was pressurized with a small air pump

powered by a 12 VDC battery. A photograph of the test configuration is shown in Fig. 1.

The testing was done during the LEADDEX field program in March and April of 1992 in the Southern Beaufort Sea. Measurements were made in two ice types: 1.3 m thick, first-year sea ice, and in a re-frozen melt pond ice on a multiyear floe. A core was taken of the upper 70 cm of the first-year ice. The eight samples analyzed ranged from 3.3 ppt to 6.6 ppt with an average of 5.2 ppt. There was no significant trend with depth. An ice core collected from the melt pond ice had salinities ranging from 0.0 to 1.0 ppt to a depth of 57 cm with an average of 0.55 ppt for the seven samples. Here also there was no significant trend with depth. From the surface to a depth of 57 cm the ice was clear. The ice below this depth had a milky appearance, marking the bottom of the pond. At 62 and 72 cm depths the salinity measured 0.65 and 0.60 respectively.

The general sequence of the tests was as follows:

1. Snow cover was removed from the test area.
2. A chainsaw was used to cut a slot in the sea ice. The slot measured approximately 40 cm long, 36 cm deep, and 3 cm wide. After the initial test, slots were cut in the ice at the ends of, and normal to, the 3 cm slot. These extended approximately 60 cm from the main slot. These were cut

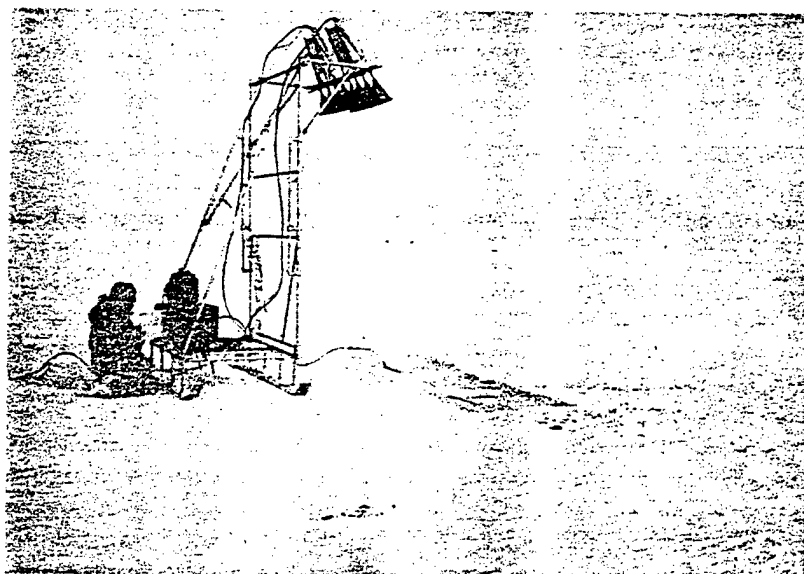


Fig. 1. The microwave system and inflatable jack installed in the ice during test 2 in first-year ice.

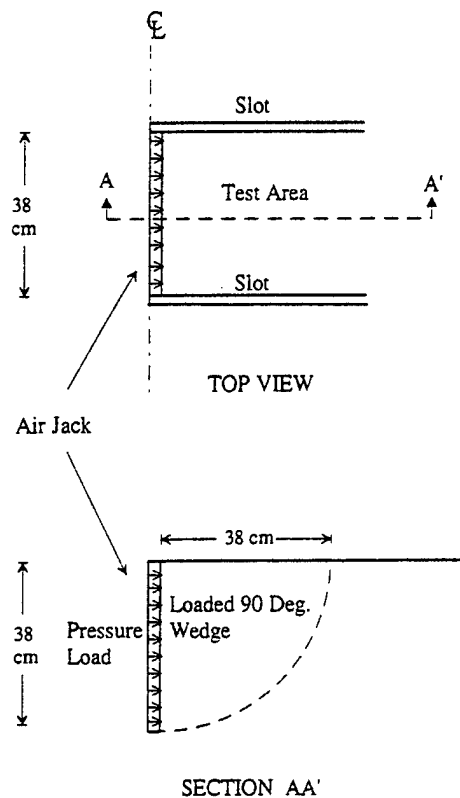


Fig. 2. The test configuration from the top and side showing the air jack and the side slots.

to simplify the calculation of stress in the region around the jack. The ice loading configuration, with the side slots cut, is shown in Fig. 2.

3. An inflatable jack was inserted into the slot and was connected to a manifold with a dial gauge, which in turn was connected to an air pump. The top of the jack extended above the ice surface less than 2 cm.
4. The microwave transmitter/receiver was aimed at the area around the inflatable jack and was set to the desired polarity.
5. The microwave system was turned on.
6. The inflatable jack was pressurized to the desired level, and the pressure and the microwave response were manually recorded.
7. The jack pressure was changed, and new readings were taken. This process was repeated until tests were done at all the desired pressures.

8. Tests were done with the jack both parallel and perpendicular to the axis of the radar.

3. Results

The testing was done both at X-Band and C-Band microwave frequencies. The greatest response was seen at C-Band frequencies, and, for this reason, only data from this frequency are shown in the figures. All of the tests were done at a 30° incidence angle. The results of two of these tests are summarized below.

Test 2 was done in first-year ice. The axis of the radar was parallel with the inflatable jack slot, and stress relief slots were present. This was the second time this ice had been pressurized. As can be seen in Fig. 3, the VV polarization response generally followed the air pressure in the jack. The HH response was not as large.

Test 5 was done in melt pond ice. The melt pond ice had many large cracks, however the ice within the radar footprint had no large cracks. The radar axis was perpendicular to the inflatable jack slot. Ice at this test location had not previously been pressur-

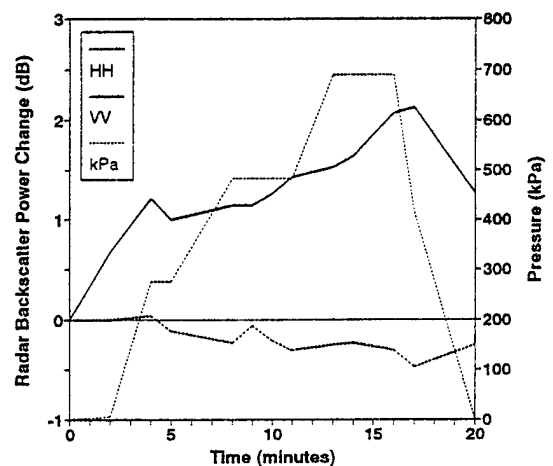


Fig. 3. The backscatter response shown is for test 2, on first-year ice. The radar is oriented with its axis parallel to the pressure slot. The backscatter power scale is shown on the left vertical axis while jack pressure is shown on the right. Jack pressure was increased from 0 to 690 kPa and then returned to 0 kPa. Backscatter for both VV and HH polarizations are shown.

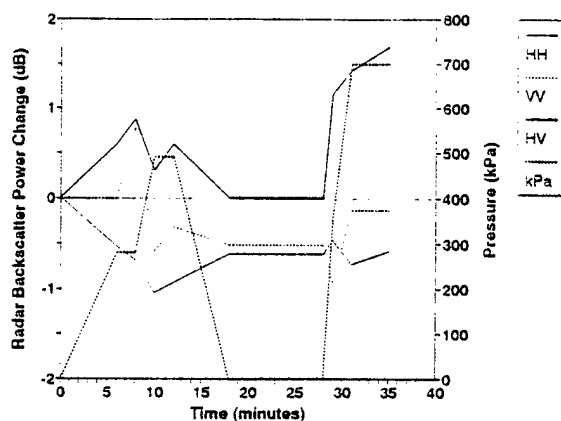


Fig. 4. The backscatter response shown is for test 5, on melt pond ice. The radar is oriented with its axis perpendicular to the pressure slot. Relief slots were present and ran perpendicular to the pressure slot. Jack pressure was increased from 0 to 480 kPa, the pressure was relieved and then was increased to 690 kPa. Responses at VV, HH, and HV polarizations are shown.

ized. Fig. 4 shows the results for HH, VV, and HV polarizations. Here changes were seen in all three polarizations with the largest response in HV.

In general, it appeared that the largest change in microwave response took place when the ice was pressurized for the first time. Subsequent tests on the same ice generally did not have as large a change in backscatter. It appears the response is influenced by loading path and loading history.

It is clear from the data that something within the radar footprint changed during pressurization. We considered two possible causes not directly related to the ice stress state. The first was the size change of the exposed upper part of the inflatable jack during pressurization. The exposed part was less than two cm tall. This size change was small, and after the jack contained a nominal pressure, on the order of a few kPa, virtually no additional size change occurred. For this reason we believe this size change had little or no effect. The second alternative cause considered was that the slope of the ice near the inflatable jack may have changed an imperceptible amount during pressurization. However, if this did occur, we believe the microwave system would not be sensitive to such a small change.

The microwave response changes were small to moderate. For tests 2 and 5, the maximum changes are 1.6 dB, and 1.7 dB, respectively. However, the

radar footprint and the size of the area that was stressed were not well matched. The radar footprint is approximately 2.6 times larger, and the effect on the backscatter signal should be about 7.6 times greater due to the overall difference in area and volume observed for the assumption of total beam filling. This calculates out to effective changes of 12 dB and 13 dB for tests 2 and 5 at air jack pressures of 690 kPa.

A calculation of the stress in the ice was made based on the solution of an elastically loaded 90° wedge as described by Timoshenko and Goodier (1951). This configuration is that shown in Fig. 2. The results show that there is essentially no stress in the ice at a distance greater than 38 cm from the air jack. (For the configuration without side slots the stress zero point would be less than 38 cm from the jack.) Therefore, the average stress in the 38 cm square region would be approximately half of the pressure in the air jack. For example, the maximum test pressure in the jack, 690 kPa, produced an average pressure of 350 kPa over the 38 cm square area. Dividing this pressure by the ratio of the area of the radar footprint to the area stressed, 2.6, results in an average stress in the radar footprint of 135 kPa. A response was seen at jack pressures as low as 70 kPa which results in an average stress in the radar footprint of 13 kPa.

How do the above stress values compare with those in natural sea ice? Pack ice stresses were measured up to 275 kPa by Coon et al. (1989) and to 400 kPa by Perovich et al. (1992) and Richter-Menge et al. (1995). Therefore, the response seen was at stresses well within the range of natural stresses in sea ice.

4. Discussion

Something within the radar footprint changed when the ice was stressed, which markedly altered the radar signature of the ice. This took place for both the first-year ice and the relatively fresh melt-pond ice. We suspect that the change took place due to microcracking or deformation of existing microcracks within the ice or perhaps through deformation of air bubbles within the ice. For the first-year ice, other possible mechanisms include distortion of the

brine channels or brine pockets and expulsion of brine onto the surface of the ice.

More detailed studies should be conducted to better quantify and characterize the effect found in this preliminary work. We believe the most accurate and reliable results will be obtained through testing of natural sea ice under arctic conditions. An improved stress fixture should be used to provide a more uniform stress field and to better match the radar footprint with the stressed area. Variables should include radar frequency, polarizations, orientation, look angle, number of pressure cycles, and ice thickness and ice type. Once the relationship between ice stress and microwave response is better defined, it would be appropriate to conduct analyses of the physical changes in the ice that cause the change in microwave properties. This may best be done as a combination of laboratory and polar field studies.

Acknowledgements

The authors thank Dr. Stuart Knoke of NorthWest Research Associates, Inc. and Ms. Paula Lau for their assistance with the field measurements. This work was supported by the Office of Naval Research under the direction of Dr. Thomas Curtin.

References

- Cole, D.M., 1986. Effect of grain size on the internal fracturing of polycrystalline ice. CRREL Report No. 86-5, U.S. Army Cold Regions Research and Engineering Laboratory, Hanover, NH.
- Coon, M.D., Lau, P.A., Bailey, S.H. and Taylor, B.J., 1989. Observations of ice floe stress in the Eastern Arctic. In: Proc. POAC 89, The 10th International Conference on Port and Ocean Engineering under Arctic Conditions, Lulea, Vol. 1.
- Hallam, D.D., Duval, P. and Ashby, M.F., 1986. A study of cracks in polycrystalline ice under uniaxial compression. In: Proc. of the 7th Symposium on the Physics and Chemistry of Ice, Grenoble.
- Lau, P.A. and Knoke, G.S., 1991. Arctic ice stress measurements. In: Proc. of OCEANS'91, Honolulu, HI.
- Onstott, R.G. and Shuchman, R.A., 1988. Active microwave sensors for arctic applications. In: Proc. of the IEEE Oceanic Engineering Society, Instrumentation and Measurement in Polar Regions, Monterey, CA.
- Perovich, D.K., Jones, K.F. and Tucker, W.B., 1992. Observations of stress in Arctic Pack Ice. In: Proc. of IAHR Ice Symposium 1992, Banff, Alta.
- Richter-Menge, J.A., Elder, B.C., Tucker, W.B. III and Perovich, D.K., 1995. Pack ice stresses and their relationship to regional deformation. In: Proc. Sea Ice Mechanics and Arctic Modeling Workshop, Anchorage, AK, Vol. 1.
- Sinha, N.K., 1982. Delayed elastic strain criteria for first cracks in sea ice. In: Proc. Symposium on Deformation and Failure of Granular Materials, Delft.
- Timoshenko, S. and Goodier, J.N., 1951. *Theory of Elasticity*. McGraw-Hill, New York, Section 41, p. 123.

**Phenomenological Constitutive Model
for Columnar Ice**

M.D. Coon
and
G.S. Knoke

ISOPE-93 Singapore
The 3rd International Offshore and Polar Engineering Conference

PHENOMENOLOGICAL CONSTITUTIVE MODEL FOR COLUMNAR ICE

M. D. Coon and G. S. Knoke
Northwest Research Associates, Inc.
Bellevue, WA, USA

ABSTRACT

This paper presents an ice behavior model based on the study of columnar ice deformation phenomena from many experimental configurations. The important and significant feature of this plastic constitutive law is its reliance on slip planes, analogous to those in soils and within crystals. Thus, deformations which are solutions to the boundary value problems may result from continuous or discontinuous deformations on these planes. The analysis of any ice mechanics problem involves the stresses and strains in a coordinate frame tied to the ice fabric, e.g., the dominant grain direction and, if the c-axes are aligned, the c-axis direction. In this paper, we will present the 3-D formulation and consider how the plastic constitutive model might be applied to such apparently simple cases as uniaxial and biaxial compression test samples.

KEY WORDS: ice, columnar, grain, constitutive, basal, stress, strain

INTRODUCTION

The objective of this paper is to develop a constitutive law for columnar sea ice suitable for solving boundary value problems such as sea ice loads on structures. Such a constitutive law must include recoverable and non-recoverable deformations. To carefully model the behavior of the sea ice, the law must also be anisotropic under multi-axial loading conditions. Assuming that the ice sheet is a horizontal sheet with vertical columnar grains, we have modeled the anisotropic non-recoverable deformations as four shear mechanisms on three types of slip planes: a vertical plane with horizontal slip along grain boundaries, an angled plane which shears across grains, the basal plane, and a vertical plane with vertical slip along grain boundaries. The constitutive model is, however, applicable only to continuous ice pieces with no cracks and for strain rates in the ductile range (10^{-6} to 10^{-3} 1/s).

Columnar sea ice consists of parallel ice grains; mechanically these grains behave as though they were a stack of rods. The rods slide against each other easier than they can be sheared; therefore the ice fails at a lower stress in situations where the rods can slide against each other than when the rods are forced to be sheared off. Furthermore, since the ice has basal planes that are aligned within the grains, the ice can fail at an even lower stress in situations that the basal planes can slip, i.e., when an ice block has all its basal planes aligned.

Columnar ice exhibits four distinct shear mechanisms, as illustrated in Figure 1. In this figure, we consider the x-axis to be normal to the grain

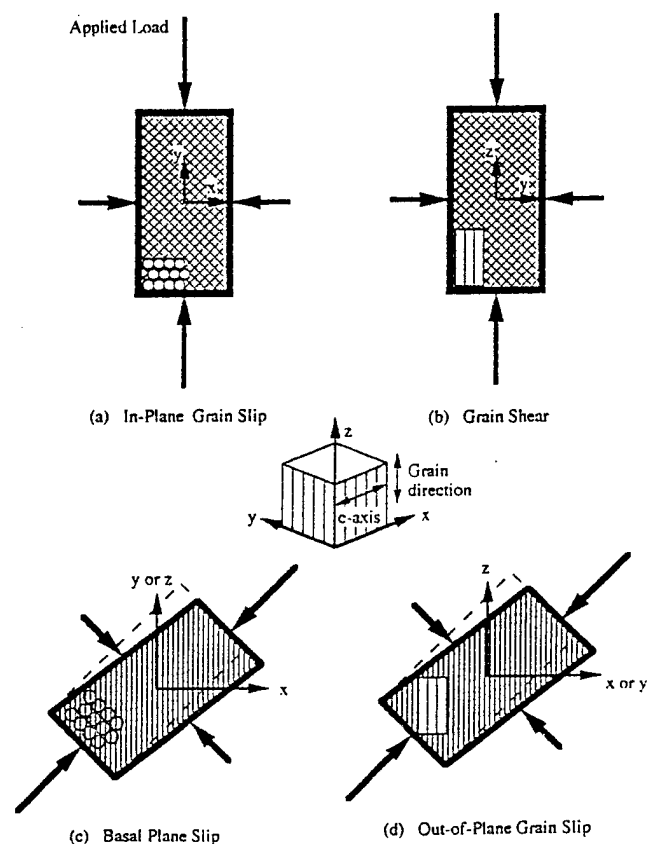


Figure 1. Shear Deformation Mechanisms

direction and normal to the basal planes (parallel to the c-axis within the grain), the y-axis also be normal to the grain direction but in the basal plane, and the z-axis be parallel to the grain direction and vertical. Basal plane slip and out-of-plane grain slip do not occur if the principal stress directions are aligned with these x-y-z axes. The grain direction in Figure 1 is indicated in the lower left corner of each figure; the hatching approximates the directions of the slip planes for each mechanism. Basal plane slip and out-of-plane grain slip result in shear strains in the principal stress directions as indicated by the dashed rectangles; in-plane grain slip and grain shear do not.

1. **In-Plane Grain Slip** Shear stress in the plane of the ice sheet causes the grains to slide past each other in a direction perpendicular to the grain direction. A uniaxial compression test in the plane of the ice sheet would be effective in activating this mechanism.

2. **Grain Shear** The slip plane for grain shear cuts across grain boundaries and basal planes, at an angle to the columnar grain direction. As such, grain shear is the mechanism with the highest strength. This type of out-of-plane deformation occurs when one of the principal stress directions is perpendicular to the ice sheet. A uniaxial compression test normal to the plane of the ice sheet would be effective in generating this mechanism.

3. **Basal Plane Slip** If the basal planes in adjacent grains are parallel, the c-axes are aligned, then shear stress on the basal plane will cause the basal planes to slip past each other. A uniaxial compression test at 45° to the basal plane would be effective in activating this mechanism. Shear stress σ_{xy} causes shearing motion in the plane of the ice sheet and shear stress σ_{xz} causes shearing motion out of the plane. We have assumed that the response is the same in either direction.

4. **Out-of-Plane Grain Slip** Shear stress parallel to the grain direction causes the ice to slide along the grain boundaries parallel to the grains. Since the ice grains run vertical to the plane of the ice sheet, this type of out-of-plane deformation requires shear stress out of the plane, i.e., σ_{xz} or σ_{yz} . A uniaxial compression test at 60° to the plane of the ice sheet would be effective in generating this mechanism. Since we expect the behavior of this mechanism to be significantly different from in-plane slip, we have modeled this as a distinct mechanism, although they both involve slip between grains.

The analysis of an ice load problem can be done with one coordinate frame aligned with the ice fabric and another coordinate frame aligned with the problem. Having defined the two coordinate frames, the six stress components in the coordinate frame of the ice fabric can be determined from the stress state in the problem coordinate frame following Mellor, 1983. The same transformation can be applied to strains and strain rates.

The next section defines the structure of the plastic constitutive law for columnar sea ice in terms of the four shear mechanisms. In the third section, we provide detail, material properties, and examples for the in-plane grain slip and grain shear mechanisms; in the fourth section, the basal plane slip and out-of-plane grain slip mechanisms are considered and an example provided.

PLASTIC CONSTITUTIVE LAW

The phenomenological plastic constitutive law developed in this paper combines many observations of columnar ice behavior and provides for multiaxial stress and deformation. The concept is that all nonrecoverable deformation of columnar ice occurs on discrete planes. The first assumption made here is that the total strain rate $\dot{\epsilon}'_{ij}$ can be separated into a recoverable strain rate $\dot{\epsilon}^r_{ij}$ and a nonrecoverable strain rate $\dot{\epsilon}_{ij}$ expressed by:

$$\dot{\epsilon}'_{ij} = \dot{\epsilon}^r_{ij} + \dot{\epsilon}_{ij} = A_{ijkl} \dot{\sigma}_{kl} + \dot{\epsilon}_{ij} \quad (1)$$

where the recoverable strain rate can be related to the stress rate through the elastic properties A_{ijkl} . The object of this paper is to relate the nonrecoverable part of the strain rate to the stress and determine the yield surface which encloses the origin in stress space. Yield implies ductile failure in plasticity theory, although most laboratory tests measure the failure stress of ice as a peak stress or a sample fracture.

It is assumed that deformations on any of the yield surfaces are controlled by the stress state. Therefore, there is a yield function in stress space which serves as a plastic flow potential. At this point it is valuable to define the plastic constitutive law and boundary value problem solution procedures. For ice it is assumed that there exists a function F:

$$F[\sigma_{ij}, C_1(\dot{\epsilon}_{ij}, a_g), C_2(\dot{\epsilon}_{ij}, a_g), C_3, \dots] = 0 \quad (2)$$

The function F depends on the stress σ_{ij} and the material properties C_1, C_2, C_3, \dots which in turn depend upon the nonrecoverable strain rate and properties of the ice a_g such as temperature, brine volume, and grain size.

The function F in equation (2) has been treated as a yield surface by Coon et al. (1984). In that view, the yield surface depends on the strain rate, the form of F accounts for the anisotropy of the ice, and the yield surface is also the plastic flow potential. We assume that the ice is a stable material, such that work cannot be extracted from plastic deformations in any situation. It follows from this assumption that the yield surface of the material is convex in stress space and that any plastic strain increment vector superposed on the stress space with corresponding axes matching would lie in the direction of the outward normal to the yield surface or between outward normals at a corner. Thus, the nonrecoverable strain rates are directly related to the plastic flow potential as follows.

$$\dot{\epsilon}_{ij} = \frac{1}{2} \left(\frac{\partial v_i}{\partial x_j} + \frac{\partial v_j}{\partial x_i} \right) - \lambda \frac{\partial F}{\partial \sigma_{ij}} \quad (3)$$

where λ is a positive constant to be determined as part of the boundary value problem solution. The six strain rates are related to the three velocities v_i by linear equations in equation (3). The equations to be solved are the three equilibrium equations, the six velocity flow rule equations, and the yield surface; the variables being solved for are the six stresses, three velocities, and λ . In a solution procedure, the yield surface remains constant for a time step and the plastic increment of the deformation is found. The yield surface is then changed, because it depends on the strain rates. The solution then proceeds step by step. The biggest advantage of such a formulation is that all of the procedures of plastic limit analysis can be applied to problems to obtain the limit load, which, for many problems, is of great importance. Large computer codes are being developed to determine ice-structure interactions (e.g., Karna, 1992); the constitutive law presented here could be used in such codes. Ice anisotropy and strain rate dependencies are very important to the failure loads of ice on a vertical structure, as shown by Coon et al. (1984).

The ductile behavior of ice is dependent on the normal stress on the slip plane because the uniaxial tensile strength is less than the uniaxial compressive strength. From test data, it is clear that, when the normal stress is somewhat larger than the compressive strength, this "pressure" sensitivity disappears (Coon et al., 1984). It may return for very large pressures or for very slow (recrystallization) flow; we, however, are not concerned with such problems here.

We now consider the yield surfaces for the first two mechanisms, in-plane grain slip and grain shear, to be those of the Coulomb and Tresca yield criteria, after Coon et al. (1984). The Coulomb yield criterion

$$|S| \leq C - N \tan \beta \quad (4)$$

states that the shear stress S on any surface must not exceed the shear strength of the surface. The shear strength, in turn, depends linearly upon the normal stress N. The material constants, C and β , are called the cohesion and the angle of internal friction. Shield (1955) extended Coulomb's criterion to isotropic materials subjected to a three dimensional state of stress, by a literal three dimensional interpretation of equation (4). If the material is isotropic, the orientation of the stress state has no relevance, and the stress state is completely defined for our purposes by its principal values σ_1, σ_2 , and σ_3 . For definitiveness, take $\sigma_1 \geq \sigma_2 \geq \sigma_3$. Then the possible values of S and N lie inside the σ_1 - σ_3 Mohr's circle and outside the σ_1 - σ_2 circle and the σ_2 - σ_3 circle (see Figure 2). On the other hand, equation (4) plots as a pair of straight lines in N-S space, so the three dimensional extension of Coulomb simply states that the σ_1 - σ_3 Mohr's circle must lie inside the wedge shaped region defined by equation (4).

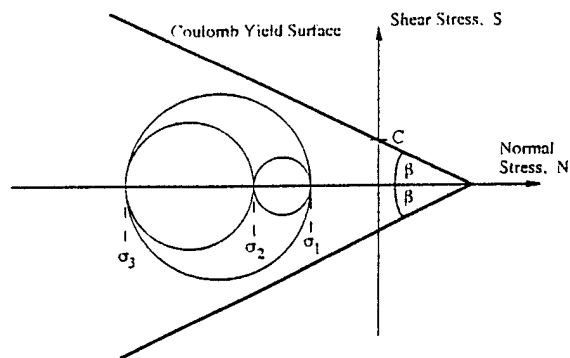


Figure 2. Mohr's Representation of Stress and the Coulomb Yield Surface

Yield occurs when the wedge is tangent to the largest Mohr's circle, i.e., when

$$\sigma_1 - \sigma_3 = 2 C \cos \beta + (\sigma_1 + \sigma_3) \sin \beta \quad (5)$$

The material constants C and β may be calculated from the uniaxial tensile and compressive strengths σ_T and σ_C . In this paper, we shall treat σ_T and σ_C as positive numbers but retain the usual compression negative convention for calculated stresses. Then, application of equation (5) to uniaxial tension and compression tests leads to

$$\begin{aligned} C &= \frac{1}{2} \sqrt{\sigma_C \sigma_T} \\ \sin \beta &= \frac{\sigma_C - \sigma_T}{\sigma_C + \sigma_T} \end{aligned} \quad (6)$$

GRAIN SHEAR AND IN-PLANE GRAIN SLIP MECHANISMS

To extend this model to anisotropic materials, the material properties C and β in equation (4) must become functions of the orientation. There are many ways to do this, but the columnar grain model suggests a particularly simple one. We assume that there are two sets of values for C and β , for grain shear and in-plane grain slip mechanisms. First, we consider grain shear, illustrated in Figure 1b. Yield for grain shear is governed by C_s and β_s . Consider a test specimen whose axis is oriented in the z direction, subjected to a uniaxial state of stress (Figure 1b illustrates this configuration but with a small lateral load). If σ_{Cs} and σ_{Ts} denote the corresponding compressive and tensile strengths, then from equation (6) we have

$$\begin{aligned} C_s &= \frac{1}{2} \sqrt{\sigma_{Cs} \sigma_{Ts}} \\ \sin \beta_s &= \frac{\sigma_{Cs} - \sigma_{Ts}}{\sigma_{Cs} + \sigma_{Ts}} \end{aligned} \quad (7)$$

Next, consider an in-plane specimen, as illustrated in Figure 1a. The values C_i and β_i are the cohesion and angle of internal friction in in-plane grain slip. For definitiveness, let y be along the axis of the specimen. Let σ_y be non-zero, and all the other stress components be zero (Figure 1a illustrates this configuration but with a small lateral load). Thus the load is applied in a plane having less strength than a vertical plane, and, denoting the in-plane strengths as σ_{Ci} and σ_{Ti} , equation (6) yields

$$\begin{aligned} C_i &= \frac{1}{2} \sqrt{\sigma_{Ci} \sigma_{Ti}} \\ \sin \beta_i &= \frac{\sigma_{Ci} - \sigma_{Ti}}{\sigma_{Ci} + \sigma_{Ti}} \end{aligned} \quad (8)$$

For the special case where one of the principal axes of stress is perpendicular to the ice sheet, the equations of the yield surface can be derived from equations (5), (7), and (8). Thus, for the special case of aligned axes of stress and material, the yield surface is defined by the following six equations:

$$\begin{aligned} \sigma_z \frac{\sigma_{Cs}}{\sigma_{Ts}} - \sigma_x - \sigma_{Cs} \\ \sigma_x \frac{\sigma_{Cs}}{\sigma_{Ts}} - \sigma_z - \sigma_{Cs} \\ \sigma_z \frac{\sigma_{Ci}}{\sigma_{Ti}} - \sigma_y - \sigma_{Ci} \\ \sigma_y \frac{\sigma_{Ci}}{\sigma_{Ti}} - \sigma_z - \sigma_{Ci} \\ \sigma_x \frac{\sigma_{Ci}}{\sigma_{Ti}} - \sigma_y - \sigma_{Ci} \\ \sigma_y \frac{\sigma_{Ci}}{\sigma_{Ti}} - \sigma_x - \sigma_{Ci} \end{aligned} \quad (9)$$

where the x - y coordinates are the principal axes of stress in the plane of the ice sheet.

At some point along the negative N axis, the experimental evidence supports a transition to a yield surface which is independent of N , i.e., a cylinder with generators parallel to the N axis (see Figure 3, after Coon et al., 1984). An anisotropic Tresca criterion is consistent with the Coulomb generalization which has been used and is indeed the limit of equation (4) as $\tan \beta \rightarrow 0$. Two parameters are required to define the yield surface: the critical value of shear stress for yield in the weaker x - y plane and the critical value of shear stress for yield in the other planes. These critical values of shear stress must be measured in a test conducted at high enough normal stress on the slip plane so that yield occurs on the Tresca portion of the yield surface. Data from in-plane or out-of-plane triaxial tests provide the critical shear strengths σ_{Si} and σ_{Ss} . When one of the principal stress directions is perpendicular to the ice sheet, the Tresca portion of the yield surface is given by the following six equations:

$$\begin{aligned} \sigma_z - \sigma_x &= \pm 2 \sigma_{Si} \\ \sigma_z - \sigma_y &= \pm 2 \sigma_{Si} \\ \sigma_y - \sigma_x &= \pm 2 \sigma_{Si} \end{aligned} \quad (10)$$

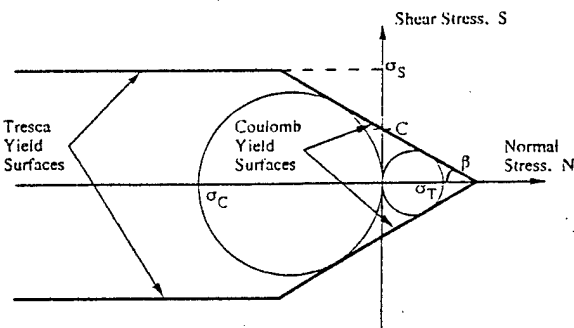


Figure 3. Typical Set of Yield Surfaces

Yield Strength for In-Plane Slip and Grain Shear Mechanisms

The compressive and tensile yield strengths of sea ice are functions of temperature, grain size, brine volume, and strain rate. In Coon and Associates (1984), least squares regression analyses were used to investigate these various functional dependencies to obtain empirical expressions for first year columnar sea ice based on laboratory and field data. The form chosen was

$$\sigma = \left[\beta_0 + \beta_1 T + \beta_2 \sqrt{g} + \beta_3 \sqrt{v_b} \right] \dot{\epsilon}^{\beta_4} \quad (11)$$

where

σ is the strength in MPa,
 T is the ice temperature in $^{\circ}\text{C}$,
 g is the average grain size of an ice sample in mm,
 $\dot{\epsilon}$ is the strain rate (from the platen speed) in $1/s$,
 v_b is the brine volume expressed as a decimal fraction, and
 $\beta_0, \beta_1, \beta_2, \beta_3$, and β_4 are coefficients found from regression analysis.

It was assumed that equation (11) could be written as

$$\sigma = \bar{\beta} \dot{\epsilon}^{\beta_4} \quad \text{or} \quad \log \sigma = \log \bar{\beta} + \beta_4 \log \dot{\epsilon} \quad (12)$$

This allowed the determination of β_4 by a least squares fit. By then rewriting equation (11) as

$$\frac{\sigma}{\dot{\epsilon}^{\beta_4}} = \beta_0 + \beta_1 T + \beta_2 \sqrt{g} + \beta_3 \sqrt{v_b} \quad (13)$$

A linear regression analysis was used to determine the other four coefficients. The following expressions were derived based on the data sources listed in Table 1.

In-Plane Slip:

$$\begin{aligned} \sigma_{CI} &= (65.0 - 0.32T - 12.4\sqrt{g} - 56.5\sqrt{v_b}) \dot{\epsilon}^{0.27} \\ \sigma_{PI} &= 0.71 - 1.74\sqrt{v_b} \\ \sigma_{SI} &= 0.82 \sigma_{CI} \end{aligned} \quad (14)$$

Grain Shear:

$$\begin{aligned} \sigma_{CS} &= (40.5 - 1.02T - 56.5\sqrt{v_b}) \dot{\epsilon}^{0.24} \\ \sigma_{TS} &= 1.48 - 2.18\sqrt{v_b} \\ \sigma_{SS} &= 0.565 \sigma_{CS} \end{aligned} \quad (15)$$

Table 1. Sources of Material Properties Data

	σ_{PI}	σ_{CI}	σ_{SI}	σ_{TS}	σ_{CS}	σ_{SS}
Frederking and Timco (1981)					X	
Frederking and Timco (1983)		X				
Häusler (1981)			X			X
Sinha (1983)					X	
Vaudrey (1977)	X	X		X	X	
Wang (1979)		X				

The only data for tensile strength were Vaudrey's; it was not possible to determine any variation in tensile strength with grain size or strain rate from the data. Also, there was no grain size dependence found on σ_{CS} . The Tresca shear strengths σ_{SI} and σ_{SS} were found only in the data of Häusler (1981). There was insufficient data to determine all dependencies; however, the Häusler data has in-plane and out-of-plane compression strengths as well as test specimens subjected to multi-axial stress states. Therefore, it was decided to determine the ratio of the Tresca strength σ_S to the unconfined compressive strength σ_C from the data sets and assume that the dependence on temperature, grain size, brine volume, and strain rate was the same for the high normal stress in Tresca as for Coulomb. This comparison was done by plotting

$$\begin{aligned} |\sigma_z - \sigma_x| \text{ vs. } |\sigma_z + \sigma_x| \\ \text{and} \\ |\sigma_y - \sigma_x| \text{ vs. } |\sigma_y + \sigma_x| \end{aligned} \quad (16)$$

to find the Tresca shear strengths and, therefore, the ratios specified in equations (14) and (15).

The fundamental way of viewing the dependence of the yield properties in equations (7) and (8) is to find the C's and B's as functions of the shear strain rate on the active slip planes. This is not accomplished by combining equations (7), (8), (14), and (15) because then the C's and B's will depend on the x-y-z strain rates. The transformation to the active slip planes requires the use of the plastic flow potential function, the flow rule, and tensor equations for stress and strain coordinate transformations. This has not been done in this paper.

Example with Principal Stresses Aligned with Ice Fabric

Timco and Frederking (1986) report test data on columnar ice in which the specimens are loaded in five types of test configurations:

$$\begin{aligned} A. \quad & \sigma_x = -\sigma; \quad \dot{\epsilon}_y = 0; \quad \sigma_z = 0 \\ B. \quad & \sigma_x = -\sigma; \quad \sigma_y = 0; \quad \dot{\epsilon}_z = 0 \\ C. \quad & \sigma_x = -\sigma; \quad \sigma_y = 0; \quad \sigma_z = 0 \\ D. \quad & \sigma_x = 0; \quad \dot{\epsilon}_y = 0; \quad \sigma_z = -\sigma \\ E. \quad & \sigma_x = 0; \quad \sigma_y = 0; \quad \sigma_z = -\sigma \end{aligned} \quad (17)$$

To compare this test data with the present model, the material properties must be found from equations (14) and (15). The test conditions were as follows:

$$\begin{aligned} \dot{\epsilon} &= 2 \times 10^{-4} \text{ s}^{-1} \\ T &= -2^{\circ}\text{C} \\ \text{Salinity} &= 1.65 \text{ ppt} \\ \sqrt{v_b} &= 0.2 \end{aligned} \quad (18)$$

No grain size is reported and therefore a grain size of 10 mm has been assumed. Timco and Frederking (1986) account for porosity and brine volume, which has not been done here. Therefore, the yield strengths in MPa are

$$\begin{aligned} \sigma_{CI} \quad \sigma_{PI} \quad \sigma_{SI} \quad \sigma_{CS} \quad \sigma_{TS} \quad \sigma_{SS} \\ 1.52 \quad 0.37 \quad 1.245 \quad 4.05 \quad 1.04 \quad 2.29 \end{aligned} \quad (19)$$

Table 2 lists the faces of the yield surface based on equations (9) and (10), the flow rules based on equation (3), and the type of test configuration intersecting the faces of the yield surface.

The Timco and Frederking test data are compared to the yield surfaces from Table 2 in Figures 4 and 5. The yield surfaces from Table 2 represent the theory presented in this paper using material properties corresponding with the test conditions shown in equation (18), but none of the Timco and Frederking test results were used in determining the yield surfaces in Table 2. In Figure 4, Type A tests are on the Coulomb part of the grain shear yield surface (Face 1) but are very near the Tresca part of the yield surface (Face 7). In Type A tests, it is possible to develop a small amount of σ_z due to friction from the side constraints when the deformation is out of the plane of the ice. Figure 4b shows that a small amount of compression in the σ_z -direction could increase the σ_x yield stress and that again the test is near the Coulomb and Tresca transition of Faces 1 and 7.

Type B and C tests are shown in Figures 4a and 5. In Type B tests, it is possible to predict a small amount of σ_z which has little effect on the yield because it moves the stress state parallel to Face 6 of the yield surface. It was noted by Timco and Frederking that the confining platens had to be hand-tightened after yield for Type B tests. This accounts for the rectangular area of data for Type B tests in Figure 5. The amount of σ_z predicted is small because the deformation is in the plane and therefore does not develop much friction.

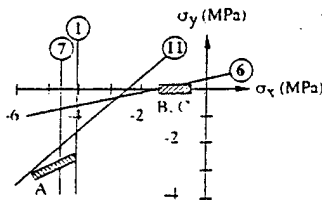
Figure 5 also shows the Type D and E tests. There may be scatter in Type D and E tests because the loading path is again nearly parallel to the yield surfaces and because the Coulomb Face 2 and Tresca Face 8 surfaces are nearly the same. In Type D tests, a small amount of σ_x may have been introduced by friction with the confining platens (which had to be tightened). This is shown in Timco and Frederking's data and will produce large apparent fluctuations in the σ_z yield strength.

The representation of this data by the present model leads to insights about the behavior of columnar sea ice by accounting for anisotropic behavior and "pressure" saturation. However, the model also provides a helpful and succinct way of perceiving the shear failure mechanisms. It is encouraging to see such good agreement between the behavior observed in these tests with predictions based on prior data.

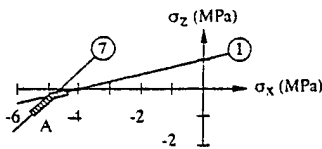
To test the yield surface in Figures 4 and 5, it is important to control the loading paths. This has been done by Häusler (1981) and by Schulson and Smith (1992); however, the strain rates in the second case were greater than those considered in this paper. In most investigations, the strain rates at yield have not been compared with the flow rule. These comparisons would provide a much better insight into the behavior of columnar sea ice. Another way of controlling the load path is to use a confining platen restrained by an elastic spring in a uniaxial test machine, as reported by Coon et al. (1991). The spring stiffness provides the different load paths; the test can be performed in a very simple machine.

Table 1. Yield Surfaces for Timco and Frederking (1986)

Face	Yield Surface	$\frac{\epsilon_x}{\lambda}$	$\frac{\epsilon_y}{\lambda}$	$\frac{\epsilon_z}{\lambda}$	Test Type
1	$3.89\sigma_z - \sigma_x - 4.05$	-1	0	3.89	A
2	$3.89\sigma_x - \sigma_z - 4.05$	3.89	0	-1	D,E
3	$3.89\sigma_z - \sigma_y - 4.05$	0	-1	3.89	
4	$3.89\sigma_y - \sigma_z - 4.05$	0	3.89	-1	E
5	$4.11\sigma_x - \sigma_y - 1.52$	4.11	-1	0	
6	$4.11\sigma_y - \sigma_x - 1.52$	-1	4.11	0	B,C,E
7+, 8-	$\sigma_z - \sigma_x - \pm 4.58$	± 1	0	± 1	A,C on 7, D,E on 8
9+, 10-	$\sigma_z - \sigma_y - \pm 4.58$	0	± 1	± 1	E on 10
11+, 12-	$\sigma_y - \sigma_x - \pm 2.49$	± 1	± 1	0	B,C



(a) $\sigma_z = 0$ Plane



(b) $\sigma_y = -3$ Plane

Figure 4. Timco and Frederking (1986) Data for Types A, B, and C Tests in Shaded Rectangles with Pertinent Yield Surfaces

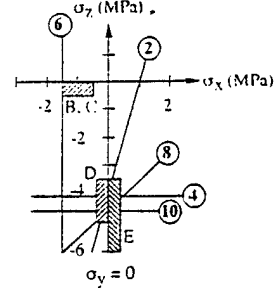


Figure 5. Timco and Frederking (1986) Data for Types B, C, D, and E Tests in Shaded Rectangles with Pertinent Yield Surfaces

BASAL PLANE SLIP AND OUT-OF-PLANE GRAIN SLIP MECHANISMS

We now consider the other two shear mechanisms: basal plane slip and out-of-plane grain slip. It is assumed that the yield surfaces of these mechanisms also exhibit Coulomb/Tresca behavior.

The basal plane slip mechanism occurs in ice with the c-axes aligned in the plane of the ice sheet. The x-axis is defined as normal to the basal plane (parallel to the c-axis), and the normal stress on the basal plane to be used in equation (4) is simply σ_x .

$$N_b = \sigma_x \quad (20)$$

The slip plane is the y-z plane. The ice will slip in the direction of maximum shear stress in the slip plane, defined by the two shear stresses σ_{xy} and σ_{xz} . Let θ_b be the angle of the slip direction from the y-axis towards the z-axis in the slip plane.

$$\theta_b = \tan^{-1} \left(\frac{\sigma_{xz}}{\sigma_{xy}} \right) \quad (21)$$

The largest shear stresses on the basal plane are given by

$$S_b = \sqrt{\sigma_{xy}^2 + \sigma_{xz}^2} \quad (22)$$

Following equation (4), the Coulomb plastic flow potential function for basal plane slip is expressed as a linear function of the normal stress N_b and the shear stress S_b on the slip plane.

$$F_b = S_b + N_b \tan \beta_b - C_b \quad (23)$$

where β_b is the friction angle and C_b is the cohesion for the basal plane shear mechanism. The friction angle and cohesion vary with temperature, grain size, brine volume, and the shear strain rate on the basal slip plane. On the Tresca yield surface, the plastic flow potential is independent of the normal stress, β_b is zero, and the constant C_b is replaced by σ_{sb} , the Tresca shear strength, which also varies with temperature, grain size, brine volume, and shear strain rate on the basal slip plane.

In terms of the x-y-z stresses, the Coulomb and Tresca yield criteria and plastic flow potential functions are

$$\text{Coulomb: } F_b = \sqrt{\sigma_{xy}^2 + \sigma_{xz}^2} + \sigma_x \tan \beta_b - C_b \quad (24)$$

$$\text{Tresca: } F_b = \sqrt{\sigma_{xy}^2 + \sigma_{xz}^2} - \sigma_{sb}$$

Using equations (3) and (21), the corresponding shear and normal strain rates for the basal slip mechanism are therefore

$$\begin{aligned}\dot{\epsilon}_x &= \lambda \tan \beta, \\ \dot{\epsilon}_{xy} &= \pm \frac{\lambda}{2} \left[\frac{\sigma_{xy}}{\sqrt{\sigma_{xy}^2 + \sigma_{xz}^2}} \right] = \pm \frac{\lambda}{2} \cos \theta, \\ \dot{\epsilon}_{xz} &= \pm \frac{\lambda}{2} \sin \theta,\end{aligned}\quad (25)$$

where λ is a proportionality constant equal to the maximum shear strain rate on the basal plane. The factor $1/2$ is needed in the derivative of the plastic flow potential with respect to shear stresses since σ_{ij} and σ_{ji} must be treated as distinct in the differentiation (Hill, 1950). The other strain rates are zero for this mechanism.

The slip plane for out-of-plane grain slip contains the z-axis, and the grains slide vertically. The shear stress on the slip plane causing plastic flow is the vector sum of the components of σ_{xz} and σ_{yz} normal to the slip plane.

$$S_o = \sigma_{xz} \cos \theta_o + \sigma_{yz} \sin \theta_o \quad (26)$$

where θ_o is the angle of the normal to the slip plane from the x-axis towards the y-axis. The normal stress on the slip plane is found using a textbook stress transformation of σ_x , σ_y , and σ_{xy} .

$$N_o = \sigma_x \cos^2 \theta_o + \sigma_y \sin^2 \theta_o + \sigma_{xy} \sin 2\theta_o \quad (27)$$

The out-of-plane plastic flow potential function in terms of the stresses and θ_o is therefore

$$F = |\sigma_{xz} \cos \theta_o + \sigma_{yz} \sin \theta_o| + [\sigma_x \cos^2 \theta_o + \sigma_y \sin^2 \theta_o + \sigma_{xy} \sin 2\theta_o] \tan \beta_o = C \quad (28)$$

The angle of rotation of the slip plane about the z-axis is determined from the maximum value of the plastic flow potential function, which is equivalent to solving the following fourth-order equation for $\sin \theta_o$.

$$\tan \beta \left[(\sigma_x - \sigma_y) \sin 2\theta_o - 2 \sigma_{xy} \cos 2\theta_o \right] \pm [\sigma_{xz} \cos \theta_o - \sigma_{yz} \sin \theta_o] = 0 \quad (29)$$

The strain rates have a shear component parallel to the shear stress and a normal component perpendicular to the slip plane. In the x-y-z coordinate frame, the strain rates are

$$\begin{aligned}\dot{\epsilon}_x &= \lambda \cos^2 \theta_o \tan \beta, \\ \dot{\epsilon}_y &= \lambda \sin^2 \theta_o \tan \beta, \\ \dot{\epsilon}_{xy} &= \frac{\lambda}{2} \sin 2\theta_o \tan \beta, \\ \dot{\epsilon}_{xz} &= \pm \frac{\lambda}{2} \cos \theta_o, \\ \dot{\epsilon}_{yz} &= \pm \frac{\lambda}{2} \sin \theta_o, \\ \dot{\epsilon}_z &= 0\end{aligned}\quad (30)$$

Example of Basal Plane Slip

Richter-Menge (1991) has measured the effects of confinement on the compressive strength of aligned, columnar first-year sea ice using a conventional triaxial test configuration. All of the ice samples were taken from the horizontal plane of the ice sheet, perpendicular to the long direction of the columnar grains. The angle between the applied load and the mean c-axis direction were estimated before the tests and measured after the tests, resulting in some scatter from the desired angles of 0° , 45° , and 90° .

For our analysis of the Richter-Menge data, we have assumed that the stresses normal to the applied load are homogeneous and equal to the confining pressure. This is the conventional approach although Haythornthwaite (1960) points out that such solutions are not necessarily unique. In our coordinates, a compressive load σ is applied at an angle α to the x direction in the x-y plane with a confining pressure P . The stresses on the basal plane are

$$\begin{aligned}\sigma_x &= -\sigma \cos^2 \alpha - P \sin^2 \alpha \\ \sigma_{xy} &= -(\sigma - P) \sin \alpha \cos \alpha \\ \sigma_{xz} &= 0\end{aligned}\quad (31)$$

Combining equations (24) and (31) and solving for the maximum load as a function of angle and confining pressure yields

$$\text{Coulomb: } \sigma = \frac{C_b + P (\sin \alpha \cos \alpha + \sin^2 \alpha \tan \beta)}{\sin \alpha \cos \alpha - \cos^2 \alpha \tan \beta} \quad (32)$$

$$\text{Tresca: } \sigma = \frac{\sigma_{sb} + P \sin \alpha \cos \alpha}{\sin \alpha \cos \alpha}$$

The material constants in equation (32) have been written as functions of the shear strain rate on the basal plane; however, the normal strain rate at the angle α was a controlled test parameter, not the shear strain rate. Therefore, the shear strain rate varies with the load angle throughout this test series. Given that the x-z stresses and shear strain rates are zero, we can write the controlled strain rate in terms of the x-y shear strain rate.

$$\dot{\epsilon} = 2 \dot{\epsilon}_{xy} (\sin \alpha \cos \alpha - \cos^2 \alpha \tan \beta) \quad (33)$$

Richter-Menge reported an unconfined compressive strength of 4.27 MPa at a platen strain rate of 10^{-3} 1/s with the load applied at an angle of 43.3° to the c-axis, and an unconfined compressive strength of 0.59 MPa at a platen strain rate of 10^{-3} 1/s with the load applied at an angle of 39.3° . These findings were summarized with

$$\sigma = 83.7 \dot{\epsilon}^{0.429} \quad (34)$$

Assuming that C_b and σ_{sb} vary with shear strain rate as in equation (34), then equations (32), (33), and (34) can be combined to yield

$$\begin{aligned}C_b &= 18.9 \left[\frac{\dot{\epsilon}}{\sin 2\alpha - 2 \cos^2 \alpha \tan \beta} \right]^{0.526} \\ \sigma_{sb} &= 43 \left[\frac{\dot{\epsilon}}{\sin 2\alpha} \right]^{0.435}\end{aligned}\quad (35)$$

for no confining pressure. For the Coulomb yield surface, a value for β_o of 30° was used, and, for Tresca, the friction angle is zero. Strain rates normal to the load angle need to be measured to determine the variation of β_o with shear strain rate.

Equations (32) are plotted in Figure 6 using the Coulomb and Tresca coefficients from equation (35), along with Richter-Menge's data for unconfined compressive strength as a function of the angle between the load and the c-axis at a strain rate of 10^{-3} 1/s. The in-plane grain slip unconfined compressive strength from her 0° data is also plotted as a straight line. It appears that, in an unconfined compressive strength test, any of three yield surfaces may be intercepted. It also appears that basal slip may have some effect on lower compressive strength value measured at 90° as compared to 0° , considered the scatter of about 5° in the measured angle. A test at an angle of 60° or 70° would be very interesting.

Figure 7 shows additional data from Richter-Menge with significant confining pressures. Here the difference between the compressive stress and the confining pressure is plotted versus the angle between the applied load and the c-axis. Two lines are used to describe the in-plane slip yield surface: one for an unconfined Coulomb mechanism and one for a Tresca mechanism. The confining pressure moves the basal plane coulomb yield surface seen in Figure 6 up and off the graph. It appears that basal slip mechanism may again contribute to the lower values measured at 90° as compared to 0° .

ACKNOWLEDGMENTS

The authors thank Dr. Tom Curtin for his support. This work was funded by the Office of Naval Research under Contract Number N00014-92-C-0027.

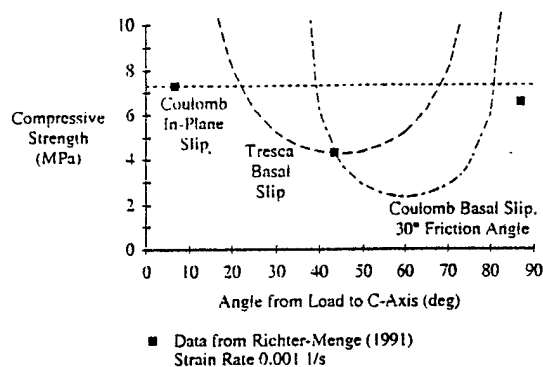


Figure 6. Unconfined Compressive Strength due to Basal Slip and In-Plane Slip

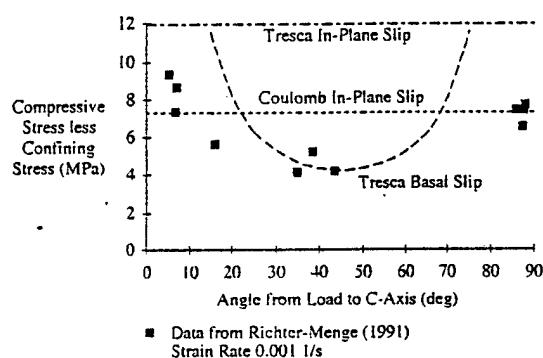


Figure 7. Confined Compressive Strength due to Basal Slip and In-Plane Slip

REFERENCES

- Coon & Associates (1985). "Failure Criteria for Sea Ice and Loads Resulting From Crushing," Final Project Report.
- Coon, MD, Echert, DC, Lau, PA, and Browne, CM (1991). "Ice Mechanics in the LEAD-EX Program," *Proc. of OCEANS'91*, Honolulu, HI, September, Vol. 1, pp. 651-656.
- Coon, MD, Evans, RJ, and Gibson, DH (1984). "Failure Criteria for Sea Ice and Loads Resulting from Crushing," *Proc. of LAHR Ice Symp.*, Hamburg, Vol III, pp 1-16.
- Frederking, RMW, and Timco, GW (1981). "Mid-Winter Mechanical Properties of Ice in the Southern Beaufort Sea," *Proc. of 6th Int'l. Conf. on POAC*, Quebec, pp 25-34.
- Frederking, RMW, and Timco, GW (1983). "Uniaxial Compressive Strength and Deformation of Beaufort Sea Ice," *Proc. of 7th Int'l. Conf. on POAC*, Helsinki, Vol 1, pp 89-98.
- Häusler, FU (1981). "Multiaxial Compressive Strength Tests on Saline Ice with Brush-Type Loading Platens," *Proc. of LAHR Int'l. Symp. on Ice*, Quebec, Vol 2, pp 526-539.
- Haythornthwaite, RM (1960). "Mechanics of the Triaxial Test for Soils," *Proc. of ASCE, J. of Soil Mechanics and Foundations*, Vol 86, No SM 5, pp 35-62, October.
- Hill, R (1950). *The Mathematical Theory of Plasticity*, University Press, Oxford, p. 331.
- Karna, T (1992). "A Procedure for Dynamic Soil-Structure-Ice Interaction," *Proc. of Second (1992) International Offshore and Polar Engineering Conference*, Vol. II, pp. 764-771.
- Mellor, M (1983). "Mechanical Behavior of Sea Ice," CRREL Monograph 83-1, U.S. Army Cold Regions Research and Engineering Laboratory.
- Richter-Menge, JA (1991) "Confined Compressive Strength of Horizontal First-Year Sea Ice Samples," *Trans. of ASME, J. of Offshore and Arctic Engineering*, Vol 113, pp 344-351, November.
- Sinha, NK (1983). "Field Tests on Rate Sensitivity of Vertical Strength and Deformations of First Year Columnar-Grained Sea Ice," *Proc. of 7th Int'l. Conf. on POAC*, Helsinki, Vol 1, pp 231-242.
- Schulson, EM, and Smith, TR (1992). "The Brittle Compressive Failure of Columnar Ice Under Biaxial Loading," *Proc. of LAHR 11th Int'l. Symp. on Ice*, Banff, Vol 2, pp 1047-1064.
- Shield, RT (1955). "On Coulomb's Law of Failure in Soils," *J. Mech. Phys. Solids*, Vol 4, pp 10-16.
- Timco, GW and Frederking, RMW (1986). "Confined Compression Tests: Outlining the Failure Envelope of Columnar Sea Ice," *Cold Regions Science and Technology*, Vol 12, pp 13-28.
- Vaudrey, KD (1977). "Ice Engineering: Study of Related Properties of Floating Sea-ice Sheets and Summary of Elastic and Viscoelastic Analysis," Technical Report R860, 81 pages, Civil Engineering Laboratory, Naval Construction Battalion Center, Port Hueneme, CA.
- Wang, YS (1979). "Sea Ice Properties," in Technical Seminar on Alaska Beaufort Sea Gravel Island Design, presented by Exxon Company, U.S.A., Houston, TX, Oct 18.

**Contemporaneous Field Measurements of Pack Ice Stress
and Ice Strain Measurements from SAR Imagery**

M.D. Coon,
G.S. Knoke,
D.C. Echert,
and
H.L. Stern

OCEANS'93
Victoria, British Columbia, 1993

Contemporaneous Field Measurements of Pack Ice Stress and Ice Strain Measurements from SAR Imagery

Max D. Coon, G. Stuart Knoke, Douglas C. Echert
Northwest Research Associates, Inc., Bellevue, Washington 98005

Harry L. Stern
Polar Science Center, University of Washington, Seattle, Washington 98105

Abstract - Material constitutive laws are commonly developed from stress/strain data which are obtained from laboratory measurements; e.g., a sample of the material is stressed in a load machine, and the resulting deformation is measured. Similarly, developing or verifying a constitutive law for polar pack ice is best done by obtaining contemporaneous ice stress and strain measurements. A pilot program to measure these parameters was performed during April 1992 in the southern Beaufort Sea. Directional stress was measured at two locations by gauges imbedded in the sea ice. Strain was obtained from sequential ERS-1 satellite Synthetic Aperture Radar (SAR) images (typically three days apart). Unfortunately, no significant ice stress or ice motion events occurred during the brief measurement period. However, a failure (yield) envelope for thick ice, based on ice stress measurements taken in the eastern Arctic Ocean, was developed. These pilot studies verified the techniques to be used during an eight-month measurement program which will take place in the Beaufort Sea during the 1993-1994 ice season.

measurements for this modeling approach can now be made, thanks to routine imaging provided by the European Remote Sensing Satellite-1 (ERS-1) SAR, low-powered Global Positioning System (GPS) navigation modules, and the development of ice stress buoys. The model will be verified with contemporaneous field measurements of sea ice stress and ice motion obtained from sequential SAR imagery and buoy motions. The first long-term field program to obtain these data will be the Sea Ice Mechanics Initiative (SIMI) from Fall 1993 to Summer 1994, sponsored by the Office of Naval Research (ONR).

This paper gives a brief description of the new pack ice model and the data gathering and analyses for validation. Stress data from the ONR-sponsored Coordinated Eastern Arctic Experiment (CEAREX) are used to provide a first measure of the strength of the thick ice element of the new model. An example of SAR data for a ridging event is presented. In addition, the data collection plan for the 1993-1994 ice season is outlined.

I. INTRODUCTION

Arctic sea ice may prove to be an important early indicator of global climate change. This will require an understanding (in the form of a model) of Arctic pack ice dynamics and thermodynamics to understand the causes of inter-annual variability. At the heart of current ice dynamics/thermodynamics models is a pack ice constitutive law that assumes pack ice is isotropic. This has simplified model calculations but is a gross simplification of pack ice behavior, since the ice thickness distribution, which controls the heat and mass transfer from the ocean to the atmosphere, is highly anisotropic and irregular. Northwest Research Associates (NWRA), with support from NASA, is developing an anisotropic constitutive law with an oriented ice thickness distribution for pack ice [1]. It is the first model of pack ice to account for leads and ridges explicitly. Therefore, the model can be validated by measuring what happens during individual events, not their ensemble as in the case of an isotropic model. Stress and deformation

Northwest Research Associates, Inc., was sponsored by NASA under contract No. NASW-4701 and by the Office of Naval Research under contract No. N00014-92-C-0027. The Polar Science Center was sponsored by NASA under grant No. NAGW-2513

II. BACKGROUND

The goal of [1] was to develop a constitutive law for pack ice which represents the discontinuous behavior of lead opening, shearing, and closing. The continuum model must account for the discontinuities associated with leads and have the same rate of energy dissipation as occurs in the discontinuous sea ice deformations. Therefore, the model will have an anisotropic behavior.

The behavior of the pack ice element shown in Fig. 1 is controlled by the behavior of the thick ice and the refrozen lead ice. The plastic failures of the thick ice and the active leads are characterized by ice strength parameters written as stress resultants (the integral of the stresses through the ice thickness) which are independent of the local variations in ice thickness. The orientation of the refrozen leads and the thickness of the ice therein dramatically affect the failure strength of the pack ice.

The thick ice is assumed to be a perfectly-plastic material with a Coulomb yield criterion and a normal flow rule. The

Coulomb yield criterion for pack ice was previously used in [2]. The normal flow rule has been used in many sea ice models (e.g., [2], [3], [4], and [5]).

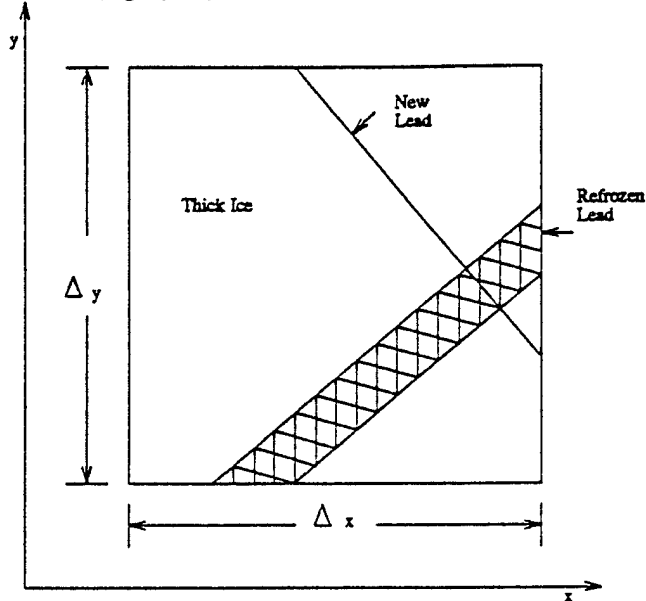
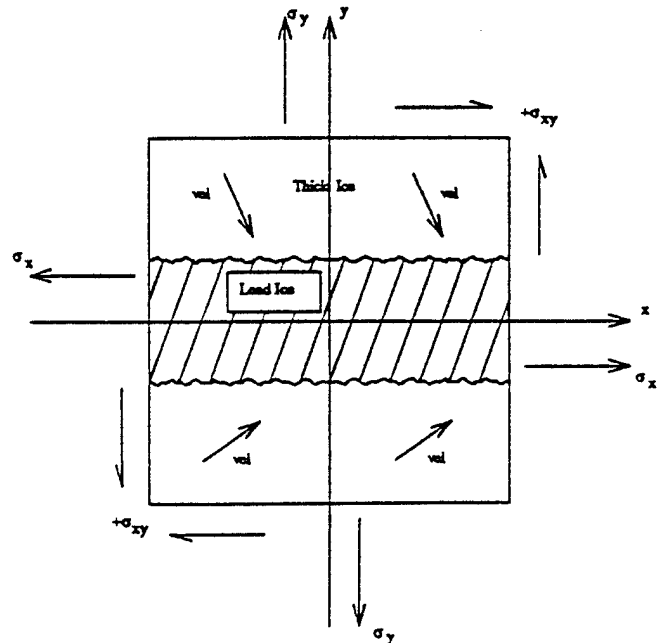


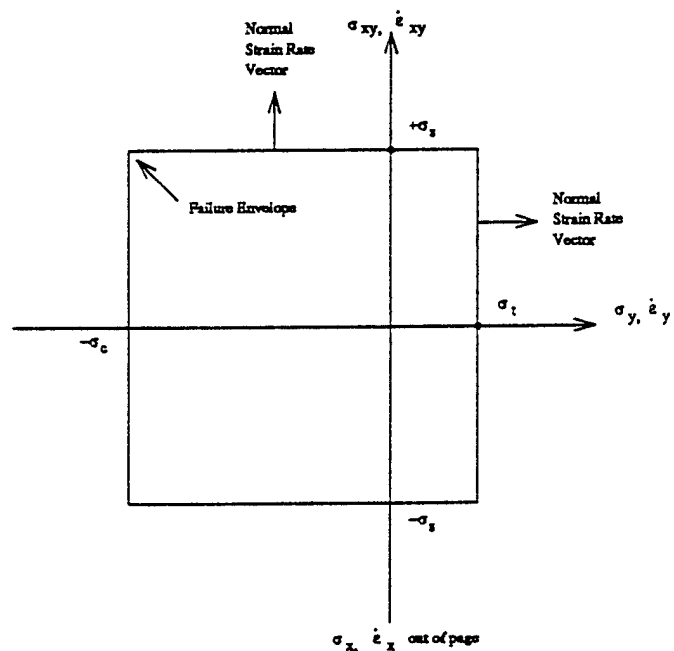
Fig. 1. Element of pack ice with a refrozen lead and a new lead forming in the thick ice.

If it were possible, the material properties of the pack ice would be determined by laboratory tests in which the loads and deformations imposed on the test sample are controlled. For pack ice, however, the test data can only be obtained by interpreting field data. Fig. 2a provides a view of physical space with a refrozen lead lying along the x -axis which may close (rafting or ridging), shear, open (forming open water), or appropriate combinations thereof. Fig. 2b shows a rectangular plastic failure surface for this refrozen lead (expressed in terms of stress resultants, the product of the stress and the thickness of the ice) which increases in size as the lead ice grows in thickness. The normal stress resultant parallel to the lead direction, σ_x , comes out of the page in Fig. 2b, forming a rectangular prism. The yield surface shown in Fig. 2b is thus a surface in 3-D stress space with the three stress coordinates being σ_x , σ_y , and σ_{xy} ; the failure of the lead is, however, independent of σ_x because that stress is taken by the thick ice. The normal flow rule from plasticity theory then defines the strain rate direction as being an outward normal to the surface of the rectangular prism, as illustrated.

The data required to determine a point on the failure surface are the three stresses (σ_x , σ_y , and σ_{xy}) and the three corresponding strain rates. To find the strain rates, the ice velocity on both sides of the lead are needed. The velocity data could come from sequential satellite SAR images or from buoys equipped with GPS receivers.



(a) Physical space.



(b) Yield surface for a lead.

Fig. 2. The stress and deformation data for an ice failure event will provide a stress data point on the failure surface and the strain rate vector for the lead (x -axis is along the lead)

An anisotropic failure envelope has been introduced [1], wherein a conical failure envelope (in 3-D stress space) is used to represent the thick ice; the rectangular prism failure envelopes for the lead ice are at 45° to the axis of the cone. With the 3-D stress space axes defined by

$$P = \frac{s_x + s_y}{2} ; D = \frac{s_x - s_y}{2} ; S = s_{xy} \quad (1)$$

the cone lies along the P axis and the cone corresponds exactly to a straight line in stress invariant coordinates, since the pressure invariant is P and shear invariant is the radial distance out from the pressure axis in 3-D stress space, i.e.,

$$\text{Shear Invariant} = \sqrt{D^2 + S^2} \quad (2)$$

Fig. 3a shows a view in physical space of a lead about to be created in the x-direction. Here again the three stresses and the corresponding ice velocities are needed to get a point on the yield surface and a strain rate vector. The thick ice failure surface, a cone in stress three-space, is shown in Fig. 3b, along with a 2-D cut. The normal flow rule, as illustrated, anticipates a combined opening and shearing motion when the thick ice fails, thereby creating a new lead.

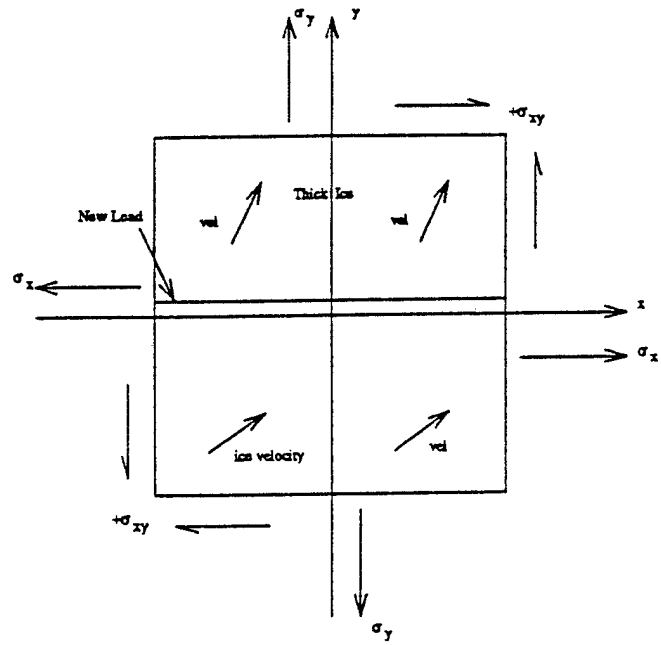
III. DATA GATHERING AND ANALYSIS

To calculate the failure surfaces for various ice thicknesses, one needs to have measurements of directional stress, concurrent ice strain, and the thickness of the deformed ice during periods of deformation. A pilot program was conducted in the Beaufort Sea during April 1992 to gather such data as part of the ONR-sponsored LEADDEX Program. Stress was measured by NWRA investigators at two locations. Ice motion was available from sequential SAR imagery and from ARGOS satellite positioning system buoys. Unfortunately, during the measurement period no geophysical stress events were seen in the data and no significant ice failure events were observed. The gathering of concurrent ice stress and strain during deformation events would have to wait until the field experiments planned for the 1993-1994 ice season.

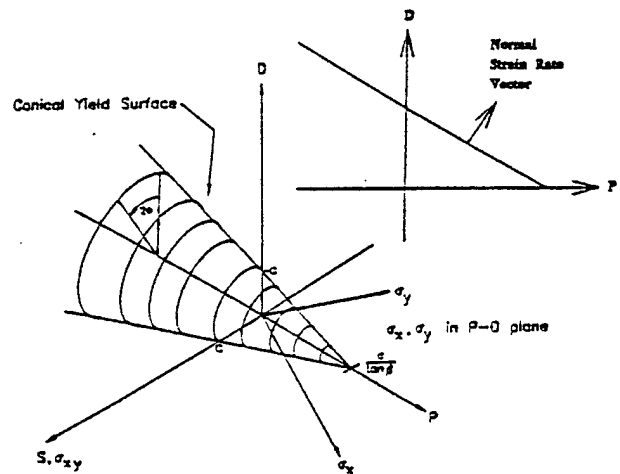
To prepare for the future field experiments, techniques have been developed to analyze stress data and SAR imagery individually. The procedures and results of these analyses are described below.

A. Stress Data Analysis

The measurement of the large scale failure stress of thick pack ice is difficult, but a method to infer it is presented here. Pack ice in the Arctic Ocean is generally composed of thick ice and refrozen lead ice. The thick ice consists of multi-year (MY) floes, thick first year (FY) ice, ridges, and rubbled areas. This ice has an average thickness of about 3 meters, varying from 1 to 50 meters or so. The refrozen lead ice is generally thin (less than 2 meters thick) and saline.



(a) Physical space.



(b) Conical yield surface for thick ice.

Fig. 3. A lead created along the x-axis results from the stress state being on the conical failure surface.

The stress required to fail the refrozen lead ice is smaller than the stress required to fail the thick ice, although the thick ice has cracks and other flaws so that it is not as strong as a homogeneous, continuous block of ice. For certain ice stress states, however, the thick ice fails. Thus, there are three possible ice states, listed in order of increasing stress:

1. No ice is failing;
2. Refrozen lead ice is failing;
3. Thick ice is failing.

Since pack ice cannot exist with a larger stress than that required to fail the thick ice, the plastic failure envelope of the thick ice should provide an upper bound for the ice stress data. The Coordinated Eastern Arctic Experiment (CEAREX) stress data ([6] and [7]) offers an opportunity to identify features of the pack-ice failure envelope. Fig. 4 shows the hourly averaged stress resultant invariants (from [6]) measured in the middle of a large multi-year floe about 1.6 m thick for the months of October and November, 1988, in the eastern Arctic Ocean. Stress resultant, the integral of the horizontal stress through the thickness, is taken to be the measured ice stress times the thickness. With the pressure invariant on the horizontal axis and the shear invariant on the vertical axis, the line at 45° is the boundary between compression in all directions (below the line) and tension in some direction (above). Since the line at 45° also represents a uni-axial compression stress state, these pack ice data indicate that pack ice is near a state of uni-axial compression most of the time.

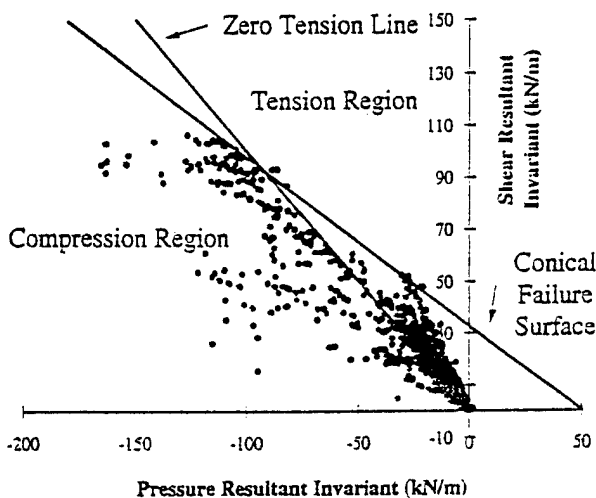


Fig. 4. Hourly averaged stress resultant invariants.

For the anisotropic pack ice constitutive law, the x-axis of Fig. 4 corresponds to the axis of the cone and the y-axis corresponds to the radial distance (in stress resultant space) out from the axis of the cone (refer to Fig. 3b). The cone in Fig. 3b is thus represented by the conical failure surface in Fig. 4 which intersects the x-axis at about 50 kN/m with a slope of about -0.65. This failure envelope is insensitive to the data averaging period over the range from 2 minutes to 12 hours. In this case, the points below this line (within the cone failure envelope) can be interpreted as a time of no ice failure or a time when a refrozen lead has offered a failure envelope interior to the cone. This failure envelope corresponds to a uni-axial (unconfined) compressive

strength of about 180 kN/m. In contrast, laboratory sea ice samples have a uni-axial compressive strength of between 1 and 6 Mpa, which corresponds to 1600 to 9600 kN/m in 1.6-m pack ice. Apparently the cracks and other inhomogeneities in the thick ice greatly reduce its strength.

The assertion that the CEAREX ice stress measurements represent geophysical stress was examined. In the installation of the stress gauges, a procedure was developed and followed to achieve a measurement of geophysical ice stress which is consistent with a procedure outlined in [8]. They suggest placing the stress sensors in the middle of a large floe, in a relatively flat area free from major cracks, at a depth from one-third to one-half the ice thickness from the surface, such that the whole floe acts as a pressure transducer. Stress sensors near the middle of a large floe avoid the higher stresses found along the edges of the floe [9]. A relatively flat area is needed to avoid stress variations associated with thickness variations. Placing the sensor at mid-depth to a great extent avoids tensile and compressive stresses resulting from bending stresses caused by temperature changes near the upper surface of the ice (the so-called thermal stresses) [10].

There are other potential error sources in the data: inclusion factor, transducer accuracy, zero drift, zero accuracy, tensile stress measurements, and direct thermal effects. The inclusion factor is the ratio of pressure in the stress sensor to the far-field ice stress. Based on the stress gauge calibration measurements, the inclusion factor for these gauges exceeds 0.95, which includes any errors in transducer accuracy. The zero drift was negligible, but the accuracy of the zero stress measurement is not as well known. For the data shown in Fig. 4, a zero stress state was assumed to occur at the end of a two-week period with no winds, no ice motion, and all the stress gauges reading near their minimum compressive value. The stress data look somewhat different if the zero stress state is assumed to occur at the beginning of the same time period when the floe was surrounded by open water since one of the stress gauges reads about 20 kPa more compression at the beginning than at the end of the time period. In addition, it is unclear from the data how well these gauges can measure tensile stress. These data show the ice experienced some tension but never far into positive pressure. Direct thermal effects on the components of the stress sensor above the ice surface are a concern, but there was no sunlight during the test period and the above-ice components were buried in snow. In all, we estimate that the sum of the errors is about 30 kN/m. From the discussion above, it seems clear this methodology can be used to measure the large scale failure stress of pack ice. In this way, a small scale measurement (ice stress) is used to determine a large scale parameter (the strength of thick pack ice).

The failure envelope may vary somewhat from season to season and from region to region. More will be known

when sufficient stress and deformation data are available to relate the failure stress to the ice motion at failure.

B. Ice Motion Measurements from SAR Imagery.

The Geophysical Processor System at the Alaska SAR Facility (ASF) automatically generates fields of sea ice motion using pairs of ERS-1 SAR images as input. These low resolution image pairs, typically separated in time by three days (43 satellite revolutions), have been radiometrically corrected and geolocated onto a polar stereographic projection. The image pixel size is 100 meters and the area coverage is approximately 100 square kilometers. The ice tracking algorithm automatically selects the image pairs from the ASF archive using a model of ice drift based on the geostrophic wind field. A regular array of grid points with five kilometer spacing is also defined on the same polar stereographic projection. The algorithm proceeds by attempting to track the ice at each grid point to its new location in the later image. In the central pack ice, a cross-correlation technique is used to identify corresponding points. Near the coast or in the marginal ice zone, a feature matching technique is used as well as cross-correlation, since ice floes can undergo large rotations in those areas. Finally, a set of consistency checks and filters is applied to remove bad matches. The result is a set of corresponding points, or equivalently, displacement vectors, on a regular five kilometer grid [11]. Each ice motion product contains, on average, over 200 matches or vectors. More than 4000 ice motion products have been archived at the ASF since the Geophysical Processor System became operational in February 1992. These products cover the period from September 1991 through September 1992 in the Beaufort and Chukchi Seas and the central Arctic Ocean. More ice motion products are generated every week.

During the Commissioning Phase and the first Ice Phase of ERS-1, from July 1991 through March 1992, the satellite was in a three-day repeat orbit, providing many thousands of image pairs for ice motion analysis. During the Multi-disciplinary Phase, from April 1992 through December 1993, the satellite is in a 35-day repeat orbit with a drifting three-day subcycle. This still provides good swath overlap at far northern latitudes, but the potential number of ice motion products is less than that provided during the exact three-day repeat orbit. Finally, ERS-1 will be in the second Ice Phase from January through March 1994, again providing large amounts of three-day repeat imagery.

Reference [12] surveys the uses of ice motion data from SAR and emphasizes their importance. SAR-derived ice motion is being combined with data from drifting buoys to improve our understanding of the circulation of the Arctic Ocean. Lead dynamics are being studied in connection with ice deformation. Ice motion also plays an important role in

the equation governing the ice thickness distribution, which describes the balance between ice production, advection, and melting.

The data from an ice motion product could be displayed by simply drawing all the displacement vectors on a map. But sea ice tends to move in large rigid pieces over long distances, so it is difficult to see the small differential motion between adjacent vectors. By subtracting the mean displacement vector and displaying the resulting deviations from the mean, the differential motion stands out more clearly. Fig. 5 shows a field of such deviations, magnified by a factor of five relative to the grid spacing of five kilometers. This scene is located just off the southwest tip of Prince Patrick Island in the Canadian Archipelago, and represents the ice motion between March 11 and March 14, 1992. The mean displacement vector is shown in the upper left corner, approximately 13.8 kilometers in length. A linear zone of convergence, where the arrows point toward one another, runs from the upper left to the lower right.

The ice deformation in this and 2000 other ice motion products have been analyzed [13]. They computed area-averaged values of the strain invariants e_I (divergence) and e_{II} (shear) as well as $|e| = (e_I^2 + e_{II}^2)^{1/2}$ and $q = \arctan(e_{II}/e_I)$. The magnitude of deformation is measured by $|e|$, and the type of deformation is characterized by q : pure divergence ($q = 0^\circ$); uniaxial extension ($q = 45^\circ$); pure shear ($q = 90^\circ$); uniaxial compression ($q = 135^\circ$); and pure convergence ($q = 180^\circ$). For the ice motion in Figure 5, which covers an area of 5475 km², $|e| = 2.6\%$ and $q = 129^\circ$ for the three-day period. The net convergence is 1.6%, representing an area loss of 89 km² which is presumably accounted for by the closing of leads and ridge building.

On a smaller scale, strain invariants can be computed from displacement (or velocity) derivatives that in turn are computed from simple finite difference expressions. If u_1 and u_2 are the x -components of displacement (or velocity) at two adjacent grid points, then $(u_2 - u_1)/Dx$ is approximately $\partial u/\partial x$ at the midpoint. It is not possible to compute derivatives at scales smaller than $Dx = 5$ km with the Geophysical Processor System data, but it is possible to acquire the SAR images and track ice features whose separation distance is very small. This has been done in [14] using a semi-automated tracking program based on area correlation. As a practical matter, the geolocation errors in the images and the uncertainty in tracking the ice features limit the separation distance to a minimum of several pixels (several hundred meters). The full resolution SAR images offer no advantage over the low resolution images since the geolocation errors are on the order of 100 meters in both, and the precise identification of features in the full resolution images is complicated by the presence of speckle. Thus, the smallest scale on which strain invariants can be computed is on the order of half a kilometer, using

the low resolution images.

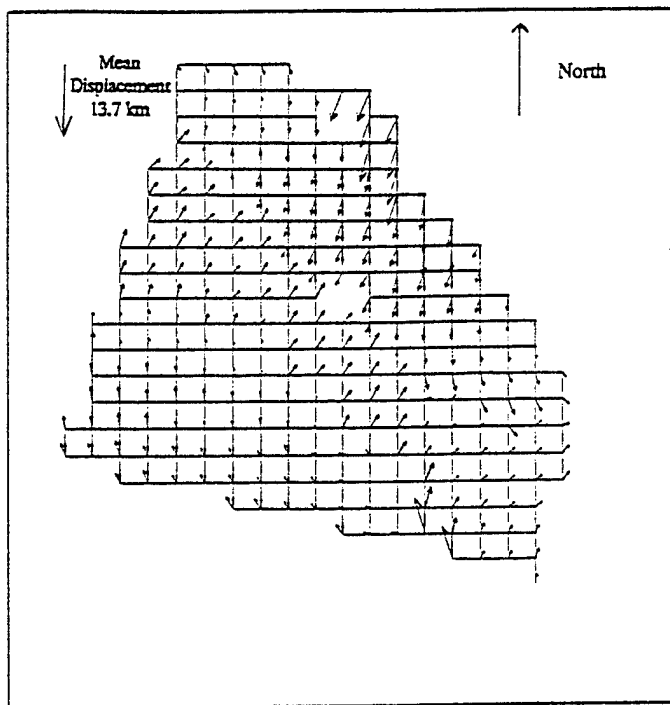


Fig. 5. Example of differential motion vectors derived from SAR imagery. The differential vectors are magnified five times relative to the 5 x 5 km grid.

IV. DATA COLLECTION DURING 1993-1994 ICE SEASON

During September 1993, three ice stress stations will be deployed by NWRA in the southern Beaufort Sea as part of ONR's Sea Ice Mechanics Initiative (SIMI). These stations will provide data through April 1994 and perhaps longer. During the same period, ice motion data will be gathered by fifteen GPS buoys placed on floes in the vicinity of the SIMI camp by the National Oceanic and Atmospheric Administration's Pacific Marine Environmental Laboratories. Ice strain will be used from these buoys and from ice motion vectors from the ASF which will be supplemented by more detailed motion analyses done by the Polar Science Center for selected ice motion/stress events. The combined SAR derived motions and buoy measurements will be used with the directional stress data to construct failure surfaces needed by the anisotropic constitutive model.

V. CONCLUSIONS

1. Ice motion and field stress measurements can be combined to define the failure surfaces for pack ice of various thicknesses.

2. In the absence of motion data, the failure envelope for thick pack ice can be obtained from stress measurements alone.
3. We measured the unconfined compressive strength of thick ice in the eastern Arctic Ocean during October and November 1988 to be 120 kN/m, much less than a strength based on laboratory tests of sea ice samples.
4. The differential ice motion data generated routinely from sequential ERS-1 SAR imagery can be used to help define failure surfaces of sea ice in refrozen leads.

ACKNOWLEDGMENTS

The authors thank Dr. Robert Thomas of NASA for his interest in, and support of, this work. We appreciate the cooperation of Dr. Tom Curtin of the Office of Naval Research, who is technical monitor of the SIMI program that is acquiring the stress data that will be used for the validation efforts.

REFERENCES

- [1] Coon, M.D., D. C. Echert, and G. S. Knoke, "Pack ice anisotropic constitutive model," *IAHR 92, Proceedings of the 11th International Symposium on Ice*, Banff, Alberta, p. 1188, 1992.
- [2] Coon, M. D., G. A. Maykut, R. S. Pritchard, D. A. Rothrock, and A. S. Thorndike, "Modeling the pack ice as an elastic-plastic material," *AIDJEX Bulletin No. 24*, University of Washington, Seattle, pp. 1-106, 1974.
- [3] Coon, M. D., "A review of AIDJEX modeling" in *Sea Ice Processes and Models*, edited by R. S. Pritchard, University of Washington Press, Seattle, 1980, pp. 12-27.
- [4] Hibler, W. D. III, "A dynamic/thermodynamic sea ice model," *Journal of Physical Oceanography*, Vol. 9, No. 4, pp. 815-846, 1979.
- [5] Pritchard, R. S. "Mechanical behavior of pack ice," in *Mechanics of Structured Media*, Part A, edited by A. P. S. Selvadurai, Elsevier, New York, 1981, pp. 371-405.
- [6] Lau, P.A. and G.S. Knoke, "Arctic ice stress measurements," *Proceedings of OCEANS'91*, Honolulu, HA, October, 1991.
- [7] Tucker, W. B. III and D. K. Perovich, "Stress measurements in drifting pack ice," *Cold Regions Science and Technology*, in press.
- [8] Croasdale, K. R., G. Comfort, R. Frederking, B. W. Graham, and E. L. Lewis "A pilot experiment to measure Arctic pack-ice driving forces," *POAC 87*, Proceedings of the Ninth International Conference on Port and Ocean Engineering under Arctic Conditions, Fairbanks, Alaska, 1987.
- [9] Perovich, D. K., K. Jones, and W. B. Tucker III "Observations of sea ice stress in the eastern Arctic," *IAHR 92, Proceedings of the 11th International Symposium on Ice*, Banff, Alberta, pp. 979-990, 1992.
- [10] Lewis, J. K., "A model for thermally-induced stresses in multi-year sea ice," *Cold Regions Science and Technology*, in press.
- [11] Kwok, R., J.C. Curlander, R. McConnell, and S.S. Pang, "An ice-motion tracking system at the Alaska SAR Facility," *IEEE J. Oceanic Eng.*, 15, 44-54, 1990.
- [12] Rothrock, D.A., "Using SAR to study sea ice and climate," presented at the ASF SAR Users Meeting, Seattle, Washington, 27-29 July, 1993.
- [13] Rothrock, D.A., H.L. Stern, and R. Kwok, "Sea ice lead dynamics from ERS-1 SAR," Presented at the Second ERS-1 Symposium, Hamburg, Germany, 11-14 October, 1993.
- [14] Rothrock, D.A., and A.J. Schweiger, "Monitoring sea ice flux through Fram Strait," Presented at the Second ERS-1 Symposium, Hamburg, Germany, 11-14 October, 1993.

The Sea Ice Mechanics Initiative (SIMI)

M.D. Coon,
G.S. Knoke,
and
D.C. Echert

Proceedings of
The 26th Annual Offshore Technology Conference (OTC), 1994
Houston, TX



OTC 7612

The Sea Ice Mechanics Initiative (SIMI)

M.D. Coon, G.S. Knoke, and D.C. Echert, Northwest Research Assocs. Inc.

Copyright 1994, Offshore Technology Conference

This paper was presented at the 26th Annual OTC in Houston, Texas, U.S.A., 2-5 May 1994.

This paper was selected for presentation by the OTC Program Committee following review of information contained in an abstract submitted by the author(s). Contents of the paper, as presented, have not been reviewed by the Offshore Technology Conference and are subject to correction by the author(s). The material, as presented, does not necessarily reflect any position of the Offshore Technology Conference or its officers. Permission to copy is restricted to an abstract of not more than 300 words. Illustrations may not be copied. The abstract should contain conspicuous acknowledgment of where and by whom the paper is presented.

ABSTRACT

The Sea Ice Mechanics Initiative (SIMI) is a five-year U. S. Navy Office of Naval Research (ONR) program. The main SIMI field experiment was in the Beaufort Sea from September 1993 through April 1994, with numerous other small field experiments, laboratory experiments, and modeling efforts. The goals of this program are to understand sea ice constitutive laws and fracture mechanics over the full range of geophysical scales, to determine the scaled responses to applied external forces, and to develop physically-based constitutive and fracture models. About twenty principal investigators are working to achieve these goals along with their associates. The SIMI experiments include ice stress, strain, strength, tilt, motion, temperature, and response to controlled load experiments. This work will provide new ice information for loads on structures and for Arctic operations, both private and government.

INTRODUCTION

The goals of the Sea Ice Mechanics Initiative (SIMI) Arctic research program are stated in the SIMI Summary Plan (Curtin, 1993). These are:

- Understand sea ice constitutive laws and fracture mechanics over the full range of geophysical scales and determine the scaled responses to applied external forces.

- Develop physically-based constitutive and fracture models.

These goals were developed at the Sea Ice Mechanics Workshop (Curtin, 1991), along with an assessment of the limits of current understanding, a list of priority research issues, and state-of-the-art methods for the many aspects of sea ice mechanics. Individual projects within the program were defined around the scale size used in the ice mechanics work.

This paper describes SIMI, focusing on the field program initiated in September 1993.

BACKGROUND

The Office of Naval Research held a Sea Ice Mechanics Workshop at Airlie, Virginia on November 12-14, 1990, where sea ice mechanics was examined from different perspectives, both methodological (theoretical modeling, laboratory experiments, and field observations) and behavioral (material, structural, and acoustical aspects). The Workshop Proceedings (Curtin, 1991) outline limits of current understanding, prioritizes research issues, and documents innovative methods of approach. The workshop participants included representatives from government agencies and laboratories as well as from universities, the oil industry, and other private sector engineers and scientists. The Workshop Proceedings were used to shape the five-year (1992-96) SIMI program.

ONR sponsored another workshop at Dunsmuir Lodge, Sidney, British Columbia, Canada on October 12-14, 1992 (Curtin, 1993). During this workshop, the detailed plan for SIMI was worked out. The main field experiment included a

Nomenclature and references at end of paper.

drifting camp in the Beaufort Sea collecting data from Fall 1993 through Spring 1994. The SIMI plan and the field program are described below in a quote from Curtin (1991).

"A major question in understanding and predicting the mechanical behavior of Arctic sea ice involves the effect of size on the dynamics. The notion that the scales of a specimen alone influences the operative physics has fundamental implications. The prime example is the pressure versus contact area relationship, suggesting a decrease in strength with an increase in size. There was consensus that obtaining a comprehensive quantitative relationship spanning from microscale to structural scale behavior is too ambitious on a five-year horizon; however, establishing the linkage between a few scales (e.g., centimeters to meters, meters to tens of meters) is achievable and should be pursued.

"Theoretical modeling is essential in relating behavior across scales and developing parameterizations. Improved models are required for both continuum and fracture behavior. Continuum and fracture models should be linked where possible. Small-scale laboratory experiments are required to link micromechanical properties with physical behavior and to identify mechanisms that may be important across scale. Intermediate scale laboratory tests under carefully controlled conditions can provide a crucial link between small and large scales. There was consensus on the need to establish the critical scales at which microscale processes become measurably important to larger scale behavior.

"Brittle or ductile sea ice behavior depends to a large extent on loading rates, which in nature typically range from 10^{-7} to 10^{-4} s $^{-1}$. Continuum behavior at different rates, particularly at larger scales, needs further investigation. Rate effects on fracture need to be quantified.

"While it is well known that temperature can determine elastic or viscous plastic behavior under isothermal conditions, the behavior of sea ice with realistic temperature gradients, as in the Arctic, remains to be characterized. The effects of temperature on fracture need to be resolved. Porosity, salinity, and microcrack distribution are important at small and medium scales. Gradients in these properties, in addition to those in thickness, degree of ridge consolidation, and macroflaw distribution at larger scales, need to be ordered and quantified in the effects on the governing mechanics.

"Coherent and economical field tests designed to definitively relate forcing and response under the range and limits of conditions in nature are essential. Controlled loading tests in the field are necessary to understand large-scale behavior. In-situ ice properties and stresses can be monitored to some extent with current technology. Methods for more complete spatial mapping of these fields are needed. Techniques to measure three-dimensional flaw generation and distribution within full scale floes need development.

"The roles of mixed mode and non-simultaneous failure in reducing large-scale loads needs to be understood, as well as the important mechanisms in the initiation of long fractures (leads) in pack ice. The relative importance of bending, buckling, crushing, and crack nucleation/propagation in overall failure needs to be determined. Factors causing ice of the same thickness to ridge in some cases and raft (including finger rafting) in others need to be determined. Thermal stresses may be as important as mechanical stresses in preconditioning the ice for the propagation of cracks. The role of existing flaws and the residual stress state in the generation and propagation of long fractures requires study.

"The transition from laboratory to floe scales is best addressed within a hypothesis-testing framework. One hypothesis is that the behavior of samples under tensile stress and the distribution of this stress is most important in floe-scale cracking processes. Therefore, these stress conditions should be examined experimentally and parameterized in larger scale relationships that can be tested in floe experiments.

"Bridging the gap in understanding of ice processes from floe to regional scales may come from relating floe measurements to a viable statistical measure of the structure of regional scale distributions of ice. The measurements of environmental forcing and regional strain, for instance, can be related to average pack ice forces measured on the floe. Careful study of the relationships, particularly during deformation, should lead to improved regional constitutive laws. Also, fracture models developed for a single floe may be applicable to a collection of floes. Thus, selected geophysical parameters obtained from aerial or satellite imagery of a region combined with environmental forcing, will produce time-dependent theoretical and numerical models that can predict with improving degrees of skill the spatial distribution of new leads and ridges."

MODELING SUMMARY

The modeling studies included in the SIMI program are summarized below, grouped by scale size.

100 KM SCALE (PACK ICE)

- Coupled air-ice-ocean
- Fracture characteristics
- Deformation characteristics

10 KM SCALE (FLOE CLUSTER)

- Granular media rheology
- Anisotropic constitutive law

1 KM SCALE (FLOE, RIDGE, LEAD)

- Ridge building energetics
- Fracture mechanics, size effect

1-100 M SCALE (MACROCRACK)

- Thermal fracture
- Physically-based constitutive laws

- Fracture mechanics, size effects

1 CM - 1 M SCALE (MICROCRACK-CRYSTAL)

- Ductile-brittle transition, failure surfaces
- Crack nucleation

MEASUREMENT SUMMARY

The experimental studies in the SIMI program are summarized below, grouped by scale size.

100 KM SCALE (PACK ICE)

FORCING

Mechanical

- Regional surface winds (NOGAPS, NMC)
- Regional surface currents (GPS buoy array)

Thermodynamic

- Surface temperature (Argos buoy array)

DEFORMATION/FRACTURE

- Point strain field (Argos buoy array)
- Image strain field (satellite AVHRR, SSMI, SAR)

PROPERTIES

- Thickness distribution (low frequency acoustics)

10 KM SCALE (FLOE CLUSTER)

FORCING

Mechanical

- Stress on floes (GPS buoy array)

Thermodynamic

- Surface temperature (15 element GPS buoy array)

DEFORMATION/FRACTURE

- Image strain field (satellite SAR/ASF)
- Image strain field (satellite AVHRR, SSMI)
- Point strain field (15 element GPS buoy array)

PROPERTIES

- Thickness distribution (AUV)
- Ridge event distribution (SAR/ASF, AVHRR)
- Ice type distribution (SAR/ASF)

1 KM SCALE (FLOE, RIDGE, LEAD)

FORCING

Mechanical

- Wind, ocean stress (main floe station)
- Ice stress array (24-30 stress sensors)

Thermodynamic

- Surface temperature, radiation (main floe station)

DEFORMATION/FRACTURE

- Strain, tilt, acceleration (sensor clusters)
- Ridging event detection, localization (hydrophone array)

PROPERTIES

- Morphology, ridge-lead distribution (main floe survey)
- Thickness distribution (AUV, submarine)
- Ridge event distribution (SAR/ASF, AVHRR, buoys)

1-100 M SCALE (MACROCRACK)

FORCING

Mechanical

- Controlled loads (stress gauge array)

Thermodynamic

- Ice temperature profiles (thermistor arrays)

DEFORMATION/FRACTURE

- Event localization and magnitude (hydrophone, geophone arrays)
- Ridging event seismo-acoustic inversion (geophone, hydrophone arrays)
- Ridging deformation (high resolution GPS, stress sensors, tilt-strain meters, and inflatable air jack)
- Fracture energy, failure modes (first-year ice controlled load)
- Fracture energy distribution (first-year ice controlled load-acoustic, seismic response: borehole jack, hydrophone, geophone arrays)

PROPERTIES

- Seasonal evolution of elastic and shear wave properties and fissures on flat ice (controlled impulse source)
- Seasonal evolution of elastic and shear wave properties and fissures in ridged ice, crack event localization, failure mode detection (acoustic tomography)
- Seasonal evolution of ridge elastic, structural properties (coring, thermistor arrays)
- Seismo-acoustic scattering from ridges (pencil beam and explosive sources, hydrophone and geophone arrays)
- Block friction (in-situ tests)

1 CM - 1 M SCALE (CRYSTAL-MICROCRACK)

FORCING

Mechanical

- Experiments under controlled loads

Thermodynamic

- Surface temperature (NWS)

DEFORMATION/FRACTURE

- Flexure, fracture related to microstructure (in-situ samples)
- Flexure, fracture related to microstructure (pit-pond tests)
- Fracture related to microstructure (testing machine)
- Low strain rate creep (testing machine)
- Internal friction, anelasticity (cyclic loading)
- Multiaxial compressive strength (pit-pond, testing machine)
- 3-D failure surfaces (testing machine)

PROPERTIES

- Microstructure linked with growth conditions (in-situ samples)

Figure 1 shows the SIMI experiment schedule, including tests near Resolute, Northwest Territories, Canada, near Barrow, Alaska, and in the Beaufort Sea. A workshop to present and discuss preliminary SIMI results will be scheduled in the first half of 1995.

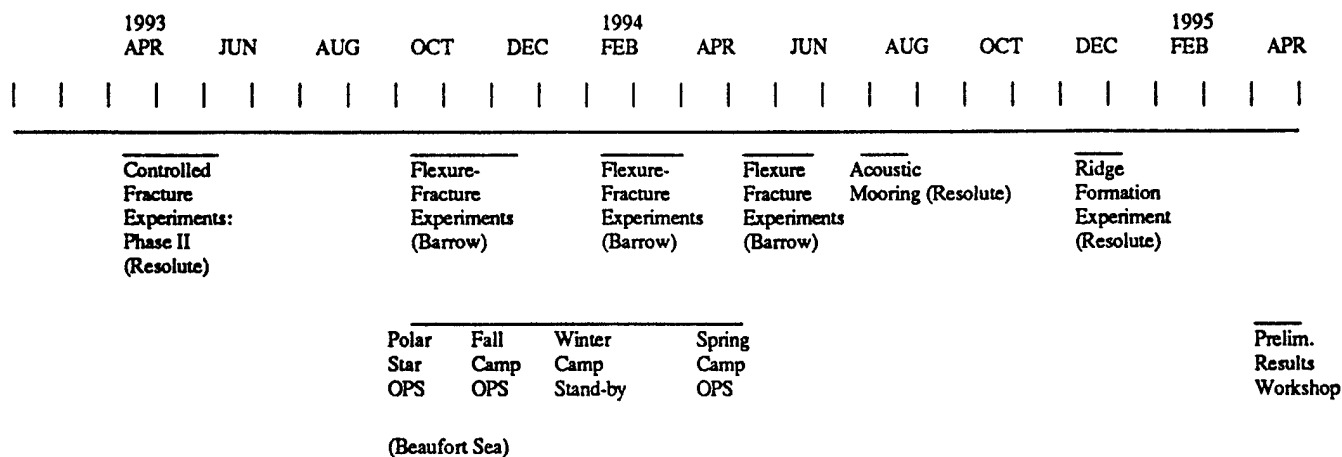


Figure 1. SIMI Experiment Schedule

BEAUFORT SEA FIELD PROGRAM

The field program in the Beaufort Sea was deployed from an icebreaker, the U.S. Coast Guard Cutter Polar Star. A temporary camp was established on the pack ice north of Alaska during the latter half of September 1993. The approximately 25-30 tons of camp cargo moved to the site by Polar Star allowed the construction and subsequent support of a 20-person temporary ice camp. The facilities included heated insulated quarters, electric power, communications, navigation, surface transportation, and food, fuel and lumber supplies to last beyond the scheduled December 1 closure of camp. While the camp was being set up, investigators riding the ship started setting up their experiments on the ice. The Polar Star helicopters supported operations to select the floe for the main camp, deploy the position/stress buoy array, perform rafting studies, and obtain a photo mosaic of the buoy area.

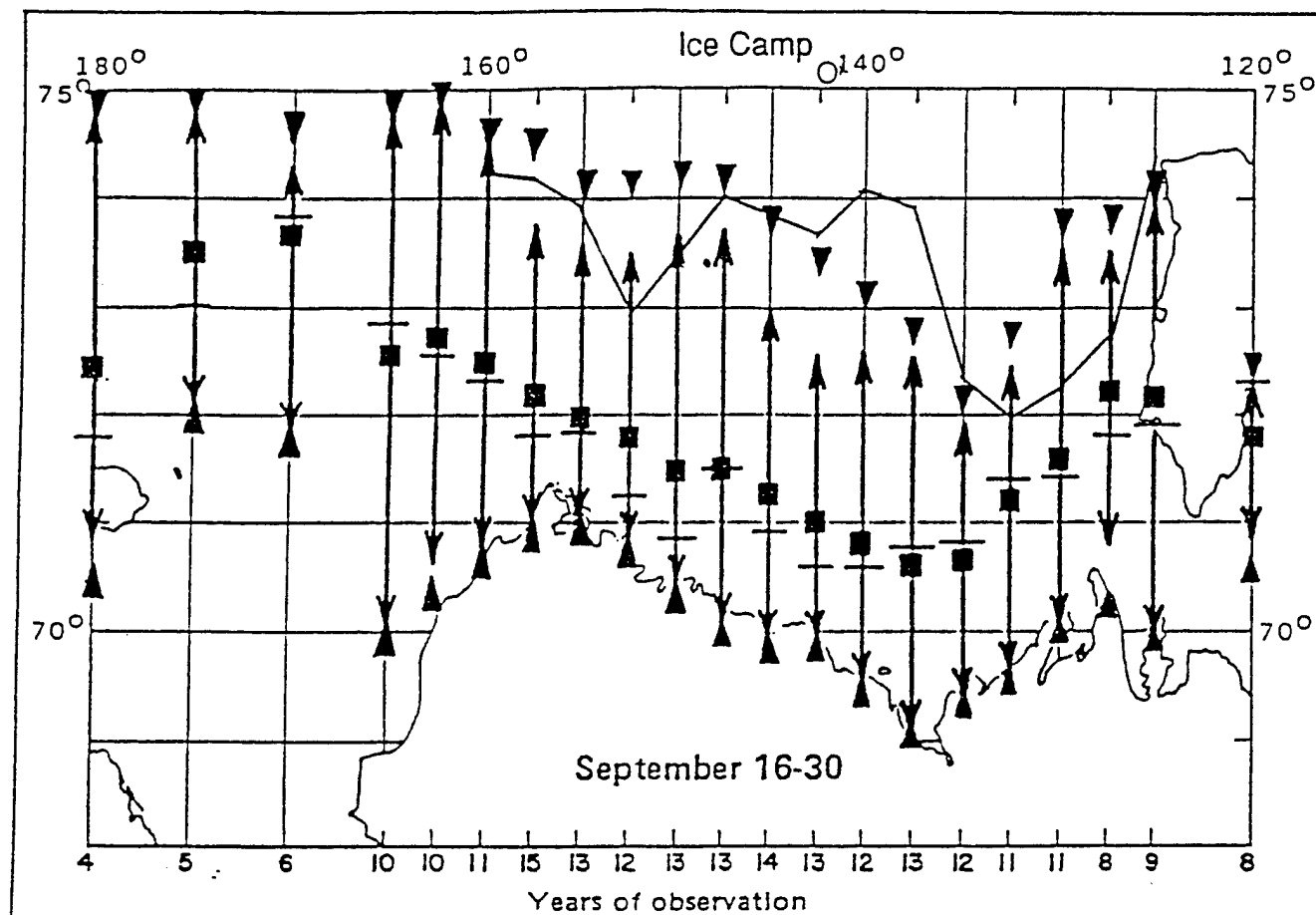
Even before boarding the Polar Star, it was recognized that the camp would have to further north and west than originally planned due to an unusually light ice year in the Beaufort. Figure 2 illustrates the degree to which 1993 was an unusual ice year (adapted from Brower et al., 1977). The jagged solid line is the ice edge taken from an AVHRR image for September 28, 1993; the circle is the initial location of the SIMI ice camp. The ice edge at 140°W was 100 km further north than the limit shown on the chart, making it impossible to deploy the ice camp at the desired location of 73°N, 138°W. For an average year, the desired camp location would have been over 200 km north of the ice edge, presumably in heavy multi-year ice. The new location to look for a Main Camp floe was set as 75°N, 141°W.

The science crew boarded the Polar Star by helicopter, and the cargo by barge, on September 16, 1993, from Deadhorse, Alaska. Some scientific work was performed on the

Polar Star in the wet lab and science room. The ice edge was crossed near 74°00'N, 143°30'W. An ice floe was drilled at 74°50'N, 141°10'W; it was found to be rotten ice with a thin layer on melt ponds. SLAR airplane and helicopter overflights (with landings to drill the ice) were used to search for an adequate floe in the vicinity of 75°N, 141°W. It was recognized that, without sufficient ice for a runway, the science team could not be left at the ice camp as planned. After another day of helicopter flights, a floe was selected at 75°10'N, 142°10'W with a promising future runway with ice 30-90 cm thick. The camp construction was begun on September 20, in balmy -5°C weather. Interested members of the science team were provided site selection helicopter overflights. The Polar Star helicopters were also used to deploy twelve GPS and four stress buoys at distances up to 10 km around the main floe. Alternative runways were identified and marked on nearby floes and radio communications were established between the ice camp, ship, and shore. The 10-km square buoy array area was mapped and photographed from the helicopters. A few science experiments were started in the vicinity of the camp. Based on ice conditions, the decision was made to close the camp when the Polar Star departed and reopen it on October 25 when colder temperatures should prevail. On September 29, a crew of four was left to complete camp construction and prepare the runway. On the southward trip, the ice edge was crossed at 73°7'N, 143°W.

During the interim period, the crew at the ice camp reported temperatures as high as 0°C with rain! The same storm removed the 20 cm of snow on the floe. By the time the camp was reactivated on October 19, there was, however, 20 cm of new snow on the floe. Twin Otter service from Deadhorse to the ice camp was established on October 25. At that time there was still at least 150 km of open water north of Alaska.

The camp averaged about fourteen persons from October 25 through December 4, with many groups in camp for only



Legend

- ▼— Extreme northern latitude
- ↑— Most northern latitude of 15-day means
- +— Median
- Mean
- ▼— Most southern latitude of 15-day means
- ▲— Extreme southern latitude

Source: G.J. Potocsky, 1975. *Alaskan Area 15- and 30-Day Ice Forecasting Guide*.

Figure 2. 1993 was an unusual ice year.

a week or two. This allowed the relatively small camp staff (five) to support over thirty science personnel. Most of the planned scientific experiments were accomplished or set up for winter-over data collection. The camp staff personnel left the camp on December 9, with the intent to return in the spring.

ICE FLOE CONDITION

The ice floe for the SIMI main camp was like an uneven grillage in the sense that it had multi-year ice perforated with many holes formed by melt ponds. It was similar to six other floes that were drilled except for the runway, in which much of the ice was 90 cm thick. The runway had thick multi-year ice on three sides of it; however, there were places where the runway ice was only 30 cm thick. The 90-cm ice was apparently formed by a triple raft. On further examination, it was determined that this "floe" was formed from two pieces of multi-year ice which came together and formed the runway by rafting. The west end of the floe (about 1/3) was not truly part of the "floe" but was separated pieces of multi-year ice embedded in thin (30 cm) ice which also connected them to the floe. The floe boundary was defined by a "line" of pressured ice (blocks pushed up) but not ridged ice.

One of the reasons for a fall SIMI program was to see how a multi-year floe changed through the fall, winter, and spring. To this end, this year was good for the experiment.

Some observations of note. There were many 'ridged' areas that were not winter ridges of first-year ice with typical sail and keel. These ridges were formed from single (maybe a few) blocks of old ice pushed up to form a ridge with a sail but no keel. This floe was considered to be 'near the ice edge' even though it was at 75°N because it was in such an extreme condition of melt.

ICE DRIFT

The ice drift of the main camp is shown in Figure 3 through January 1994. With some data gaps, the '+' marks represent the main camp GPS buoy position every six hours. Each part of the figure shows the whole trajectory through the end of the month indicated. The cluster of points encircling both ends of each trajectory indicate the positions of fourteen GPS buoys deployed by PMEL around the main camp. Although there are some data gaps, the relative motion of the surrounding buoys are small, less than 3 km. These data will be combined with ice stress data as described in Coon et al. (1993) to analyze the energy dissipation in the pack ice surrounding the main camp for the development of a pack ice anisotropic constitutive law (Coon et al, 1992).

DISCUSSION AND FUTURE PLANS

Since the plan was to reoccupy the fall experiment site in the spring, we had to take into account the expected drift of the ice when choosing the location in the fall. Since the fall effort was supported and recovered by airplane, the site needed

to be within Twin Otter range from shore. For this reason, the fall experiment site was chosen to be 500 km northeast of Deadhorse. Because of the light ice year, however, the camp was established further north and west than planned to remain 500 km from Deadhorse.

The floe for the camp had a location for an ice runway; it was not possible, however, to land a Twin Otter on September 29 when the Polar Star was to leave. Therefore, a crew of four was left at the ice camp with plans to resume full operations in late October 1993 when the runway ice was colder and stronger. SIMI has demonstrated that it is possible to establish an ice camp (which can be later supported by aircraft) in the fall from an icebreaker, even in a light ice year.

As of this writing, the ice camp has drifted to 74°40'N, 155°W, roughly north of Barrow, Alaska. Should the camp remain within 500 km of a useful airfield, the spring field operations will continue as planned. If, however, the camp drifts too far out or the main floe is unusable, the scientific and ice camp equipment will be recovered in a prudent manner and a new ice camp will be established north of Deadhorse, Alaska, for the spring field operations.

ACKNOWLEDGMENTS

We wish to acknowledge Dr. Tom Curtin of ONR for sponsoring the SIMI program. We wish to thank Capt. R. J. Parsons ("Never say 'no' to the Science Team") and the eager and highly professional crew of the U.S.C.G.C. Polar Star, as well as Mr. Andreas Heiberg and the dedicated logistics team from the University of Washington's Polar Science Center. Finally, we wish to thank Dr. Jim Overland and Ms. Sigrid Salo of PMEL for Figure 3. The author's work was funded by ONR contract number N00014-92-C-0027.

NOMENCLATURE

ASF	Alaska SAR Facility
AUV	Autonomous Underwater Vehicle
AVHRR	Advanced Very High Resolution Radiometer
GPS	Global Positioning System
NMC	National Meteorological Center
NOGAPS	Navy surface wind analysis code
NWS	National Weather Service
ONR	Office of Naval Research
SAR	Synthetic Aperture Radar
SIMI	Sea Ice Mechanics Initiative
SLAR	Side Looking Airborne Radar
SSMI	Special Sensor Microwave Imager
PMEL	National Oceanic and Atmospheric Administration's Pacific Marine Environmental Laboratory
USCG	United States Coast Guard

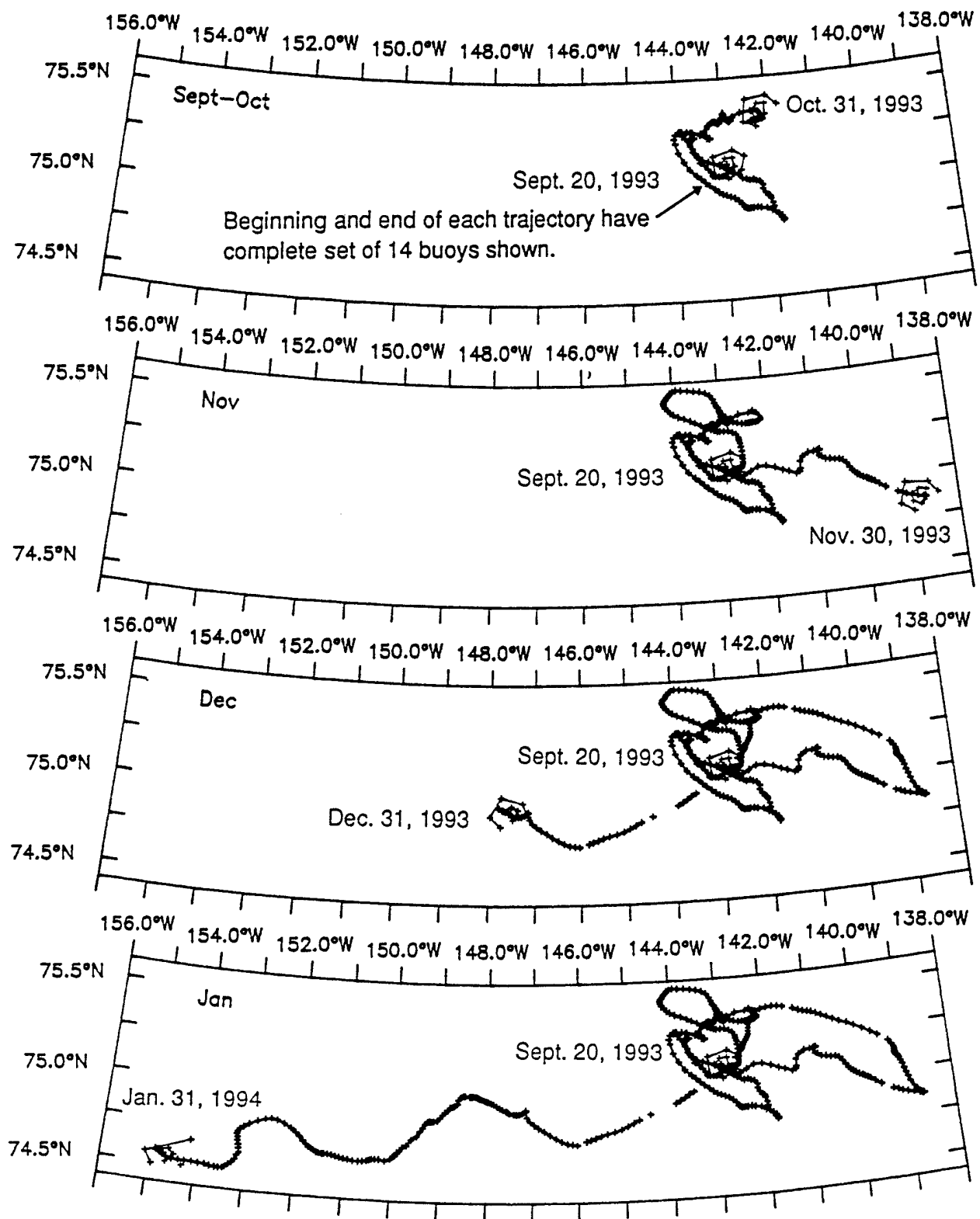


Figure 3. SIMI Ice Camp Drift (with six-hour data intervals)

REFERENCES

- Brower, W. A., Jr., H. F. Diaz, A. S. Prechtel, H. W. Searby, and J. L. Wise (1977) *Climate Atlas of the Outer Continental Shelf Waters and Coastal Regions of Alaska*, Vol. III, Chukchi-Beaufort Sea, U. S. Department of Commerce, National Oceanic and Atmospheric Administration, Alaska Outer Continental Shelf Environmental Assessment Program (OCSEAP) Final Report -- Research Unit 347.
- Coon, M. D., G. S. Knoke, and D. C. Echert (1992) "Pack Ice Anisotropic Constitutive Model," LAHR 92, Proceedings of the 11th International Symposium on Ice, Banff, Alberta, June.
- Coon, M. D., G. S. Knoke, D. C. Echert, and H. L. Stern (1993) "Analysis of Contemporaneous Measurements of Pack Ice Stress and Ice Strain Measurements from SAR Imagery," OCEANS'93, Victoria, B.C., Canada, October.
- Curtin, T. B. (Editor) (1991) "Air-Ice-Ocean Interaction: Lead Dynamics, Ice Mechanics, Ice Acoustics; Proceedings of the Sea Ice Mechanics Workshop, 12-14 November 1990, Airlie, Virginia," Office of Naval Research, Arlington, VA, April.
- Curtin, T. B. (Editor) (1993) "Sea Ice Mechanics Initiative (SIMI), Summary Plan, FY94-95," Office of Naval Research, Arlington, VA, August 27.

Sea Ice Mechanics Research

D.M. Coon,
D.C. Echert,
and
G.S. Knoke

Proceedings of
The Sea Ice Mechanics and Arctic Modeling Workshop, 1995
Anchorage, AK

Sea Ice Mechanics Research

Dr. Max Coon (P.I.), Mr. Skip Echert, and Dr. Stu Knoke of Northwest Research Associates (NWRA).

Scope of Model and/or Data Set

The NWRA team performed a variety of experiments during the SIMI field program: ice-stress measurements, controlled-load and noise-generation tests, ice-on-ice friction tests, ridge-strength tests, and a multiyear floe evolution study.

Ice-Stress Measurements -- NWRA successfully deployed flatjack, fluid-filled stress sensors with an automatic pressurization-check feature in an autonomous station configuration. We installed these sea-ice-stress "buoys" at four sites; each buoy measured ice stress in four directions, from which we will derive the ice-stress state in the horizontal plane. A ridging event buried the first buoy, installed near Mt. Curtin at the West SIMI Ice Camp (Map 2, E7), after one month. The second buoy, installed about two miles north of West Camp on Floe 4 (Map 1, E4), operated continuously for over nine months. The crack that flooded portions of the West Camp disabled the third buoy after three months (Map 2, F5), but we repaired it and operated it for an additional three weeks at the East Camp (Map 4, C6). Table 1 lists the operational lifetime of the four buoy installations and the number of thermistors used to measure ice temperatures. The buoys wrote ice stress to an internal storage module at five-minute intervals and transmitted ten-minute data through the Argos satellite relay system. The buoys also stored and transmitted temperature readings from the higher (colder) two thermistors on the same schedule but stored and transmitted the lower (warmer) thermistor readings and a battery voltage every six hours.

Table 1. Ice-stress buoys

Buoy number	Test site	Start date	End date	Number of thermistors
1	Mt. Curtin	29 Oct. 93	4 Dec. 93	4
2	Floe 4	31 Oct. 93	3 Aug. 94	4
3	Lake Andy	22 Nov. 93	25 Feb. 94	8
4	East camp runway	1 Apr. 94	23 Apr. 94	8

In support of the sea-ice-stress buoys, NWRA performed various other ice-stress sensor experiments at 22 locations near the two ice camps:

- Individual stress sensor measurements,
- "High-data-rate" stress tests with data collection rates to 4 Hz,
- "Sensor/ice contact" tests to check contact between the sensor and the ice,

- "Inclusion" tests to calibrate the response of the stress gauge to the ice stress produced by an air jack a few decimeters away, and
- Comparison tests with other types of ice-stress and strain sensors.

We installed and tested individual stress gauges at the 22 locations listed in Table 2. Dataloggers generally collected this stress and temperature data at five-minute intervals. The two winter-over sites also collected temperature data hourly. The first site (Map 2, F4) tested the installation of a stress gauge in the low, flat, multiyear hummocks in the early autumn. The second site (Map 2, F5) tested the freeze-in of gauges installed at various depths in autumn first-year ice; the lowest was half in the water at installation. The sensors at the third site (Map 2, F5) were installed identically to the stress sensors on the buoys to obtain inclusion test data to support the interpretation of the buoy data. The fourth site (Map 2, F4) again tested the installation of stress gauges in the low flat hummocks of multiyear ice in the autumn. The fifth site (Map 2, E3) was used for the comparison tests in the West camp runway ice. The sixth site (Map 2, E5 and F5) studied the horizontal and vertical variation of ice stress in a large area of flat first-year ice, Lake Andy. (We hypothesize that Lake Andy had been a large, bottomless melt pond during the previous summer.) The seventh site (Map 2, F4) studied the local variations of ice stress near a hummock. The final site (Map 4, C6) was installed for inclusion test data to support the nearby stress buoy.

Table 2. Individual ice-stress gauge sites

Site number	Test site	Start date	End date	Number of stress gauges	Number of thermistors
1	Study area	23 Sept. 93	27 Sept. 93	1	0
2	Lake Andy	27 Sept. 93	16 Nov. 94	5	0
3	Lake Andy	15 Nov. 93	28 Nov. 94	3	2
4	Study area	17 Nov. 93	21 Nov. 93	2	2
5	West camp runway	18 Nov. 93	26 Nov. 93	2	2
6	Lake Andy	29 Nov. 93	27 Feb. 94	4	2
7	Study area	30 Nov. 93	17 Mar. 94	3	2
8	East camp runway	5 Apr. 94	23 Apr. 94	2	0

"High-data-rate" is a relative term; we use it to mean data rates of one to four readings per second as compared to our standard interval of five minutes. We performed high-data-rate tests with one to four stress sensors at a time, looking for stress signals we otherwise would have missed due to sampling rate. We also obtained ice-stress data at one-second intervals for six 15-hour periods and at 1/4-second intervals for one three-hour period.

Two methods were used to evaluate stress sensor installations: sensor/ice contact tests and inclusion tests. Turning a screw-plunger assembly added additional fluid to each ice-stress sensor to assure good contact with the surrounding ice. The additional fluid caused

either an abrupt increase in fluid pressure in the sensor or no response at all. The stress buoys performed these tests automatically on a schedule, which proved useful for timing the melt-out in the spring. Each stress sensor received one or more sensor/ice contact tests; the response varied with season, ice temperature, and ice type. If the sensor showed an increase of at least 50 kPa during the test, we considered the sensor to be in good contact with the ice. Sensors that failed the test also failed to respond to air jack stress and natural ice stress.

Air jacks were used to perform inclusion tests, which were stress sensor response tests at geophysical stress levels (0 to 300 kPa) and geophysical loading rates (1 to 100 kPa/min.). We used a square, flat, air jack about 0.6 meter on a side to apply pressure to ice containing one or two sensors. We performed "square-wave" tests, for which we adjusted the air jack pressure in an on-off cycle, and "ramp" tests, for which we adjusted the pressure in a slow-increase, slow-decrease pattern. The square-wave test was a quick gauge calibration, but the ramp test simulated realistic loading rates based on our prior field data. We measured the stress-sensor inclusion factor on 20 sensor installations. Both 15-cm and 20-cm diameter sensors were tested using square-wave and ramp tests. On the square-wave tests, the air jack pressure was varied from 20 kPa to 200 kPa above ambient; on the ramp tests, the air jack pressure was 100 to 200 kPa above ambient. The square-wave tests typically had a cycle period of a minute, while each up and down ramp test took from one to three hours.

In cooperation with Jackie Richter-Menge from the Cold Regions Research and Engineering Laboratory (CRREL) and Dr. Peter Wadhams from the Scott Polar Institute (SPI), we performed a test series to provide a head-to-head comparison of the CRREL three-wire stress sensor with the NWRA flatjack sensor and of the SPI strain gauge with the NWRA flatjack sensor. We ran a set of square-wave tests and a ramp test. In each, the air jack pressure was varied from ambient to about 60 kPa above ambient, and the resulting stress and strain sensor readings were recorded.

Controlled-Load and Noise-Generation Tests -- NWRA, working with Dr. Robert Pritchard of IceCasting, Inc. (ICI), performed over 30 controlled-load tow tests and 40 other tests to generate various types of the noise representing potential Arctic acoustic sources. These tests were performed at the Football Field (Map 4, D6), East Pond (Map 4, C6), South Camp (about 18 km south of East Camp), and the IOS site (Map 4, B6). Dr. Henrik Schmidt's group from MIT/WHOI and/or Dr. David Farmer's group from the Institute for Ocean Sciences recorded the acoustic signals generated by many of these tests with hydrophones and/or geophones. The tow tests consisted of towing a block of ice on partially submerged ice to simulate rafting, on snow-covered or bare ice to simulate over-ride, and under young ice to simulate under-ride. On each of the tow tests, the tow load was usually recorded at 16 Hz and showed irregular slip-stick oscillations. We also measured the tow speed, the block dimensions and weight, and the snow thickness so that we could calculate the minimum and maximum sliding friction coefficient.

The other tests included dropping blocks onto ice, flopping blocks onto snow-covered or bare ice, tipping blocks into water, tipping blocks underwater to float up, releasing blocks underwater to bounce on the bottom of the ice, and breaking cantilever beams. Table 3 lists these acoustic experiments.

Table 3. Acoustic Source Tests

Block Motion	Number of Tests	Number of Unique Blocks Used for Test Series
Flop onto bare ice	5	5
Flop onto snow	7	5
Drop	10	9
Splash	2	2
Underwater flop	2	2
Underwater bounce	7	2
Cantilever beam	3	3

Ice-on-Ice Friction Tests -- During April 1993, NWRA ran a series of tests to measure the ice-on-ice friction coefficients on "natural" cracks generated in the sea ice near Resolute, NWT. These tests were conducted in conjunction with Dr. John Dempsey of Clarkson University, who conducted sea-ice fracture and ice characterization tests. All of these tests were performed in the 1.8-meter thick, first-year sea ice in Allen Bay. The test parameters are listed in Table 4.

Table 4. Test Parameters for Ice-on-Ice Friction Tests

Normal air pressure (kPa)	Number of tests	Total face displacement (mm)
40	7	13-65
200	8	41-54
400	4	38-93
Varied 15-170	2	77-89

Ridge-Strength Tests -- NWRA ran strength tests on first-year ridged ice using the air jack to simultaneously load the ice and measure the displacement. In November, we obtained underwater video and one inflation sequence of the air jack in the keel at the bog site (Map 2, H5). In April, we characterized the sail and keel geometry of a ridge formed from first-year ice, inflated the air jack in four slots, and recorded the acoustic emissions during the air-jack tests at our ridge site (Map 4, A4). The ridge configuration in the vicinity of the four air-jack slots was characterized by drilling 12 holes and through observations with an underwater camera (but no video tape). Dr. Robert Pritchard recorded the noise using Dr. David Farmer's hydrophone equipment.

Multiyear Floe Evolution Study -- We studied the evolution of a 60-by-60-meter area of multiyear ice near the SIMI West Camp by measuring ice thickness, snow cover, ice temperature, ice salinity, and ice stress (Map 2, F4). Our dataloggers recorded ice temperatures at three depths at four sites every hour from September 1993 to March 1994. We measured ice salinities from core samples taken in September. We also made aligned ice-stress measurements at three sites from November 1993 to March 1994. Ice thickness and snow cover were measured in September and March at nine locations in the study area. We obtained underwater video of the bottom of the ice in September through four holes in the ice using an underwater camera mounted on a pole. Also, U.S. Coast Guard divers from the USCGC Polar Star took underwater videos of the underside of the ice in September with a hand-held camera.

Findings to Date

Ice-stress Measurements -- NWRA buoys measured comparable ice-stress events lasting three to nine days in December (days 350-358), February (days 33-35), and April (days 91-95), as can be seen in Figure 1. Figure 1 shows six-hour samples of the stress-sensor oil-pressure data transmitted via Argos satellite for the full life of the buoy, including spikes resulting from the auto-pressurization cycles. There were no major stress events after mid-May, and the ice apparently melted away from the sensors in early July, totally relieving all residual ice stress around the sensors.

We found comparable stress in the first-year ice on opposite sides of a hummock but much lower stresses in the hummock itself. Some hummocks were strong ice (the stress gauges responded as though they were in lake ice), but others were very soft or porous ice since the stress gauges did not respond to sensor/ice contact tests or inclusion tests. We also found significant stress variations across the length of Lake Andy, a large area of first-year ice surrounded by multiyear ice. We hypothesize that a slip-stick ice motion event caused the most interesting signal which we recorded during the high-data-rate tests (Figure 2). From the inclusion tests, we found that, at these load values and load rates, the sensor response is significantly lower than prior laboratory measurements indicate, implying that ice-stress levels may be two to five times more than the measured sensor fluid pressure.

Controlled-load and Noise-generation Tests -- Blocks of ice sliding over or under flat ice generally exhibited slip-stick behavior with large fluctuations in the sliding friction, as illustrated for the tow load history in Figure 3. Figure 3 shows the first 12 seconds of Test 8-13, a dry over-ride test; the signal almost immediately settles into a repetitive slip-stick pattern. The load fluctuations on the ramp-ups are caused by cable oscillations since the ice block was stationary during those times. The ice-deformation mechanisms that generated more acoustic noise were blocks dropping or flopping onto bare ice, blocks sliding over snow-covered ice, and blocks falling into the water. Quiet ice-deformation mechanisms included blocks sliding or bumping underwater, rafting (lubricated by water), and blocks dropping or flopping onto snow-covered ice.

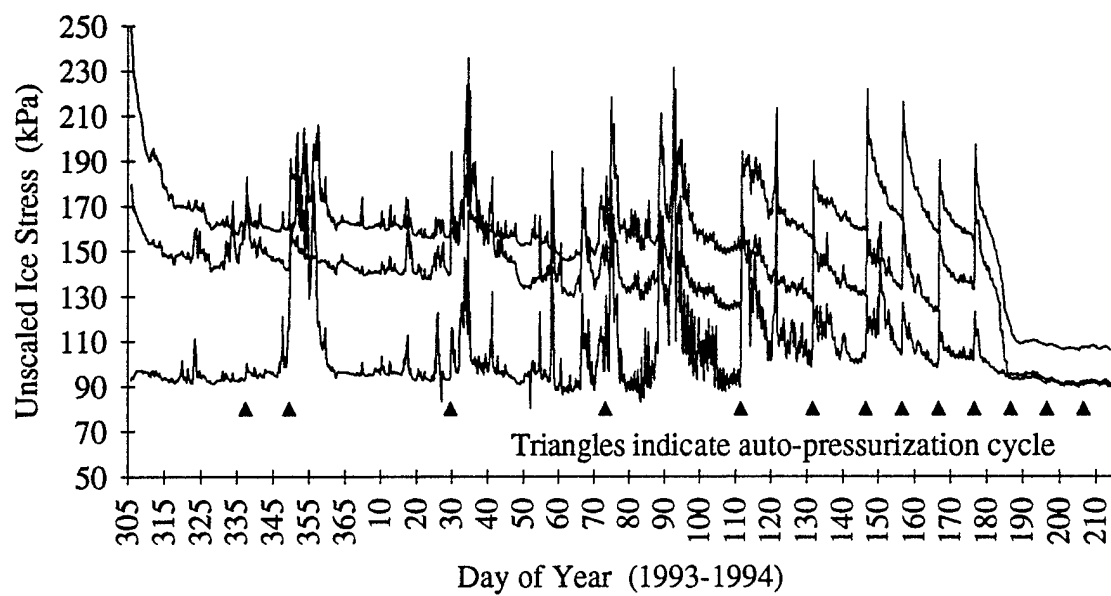


Figure 1. Ice-stress Buoy 2 (Floe 4) data via Argos, Nov. 1, 93 - Aug. 3, 94

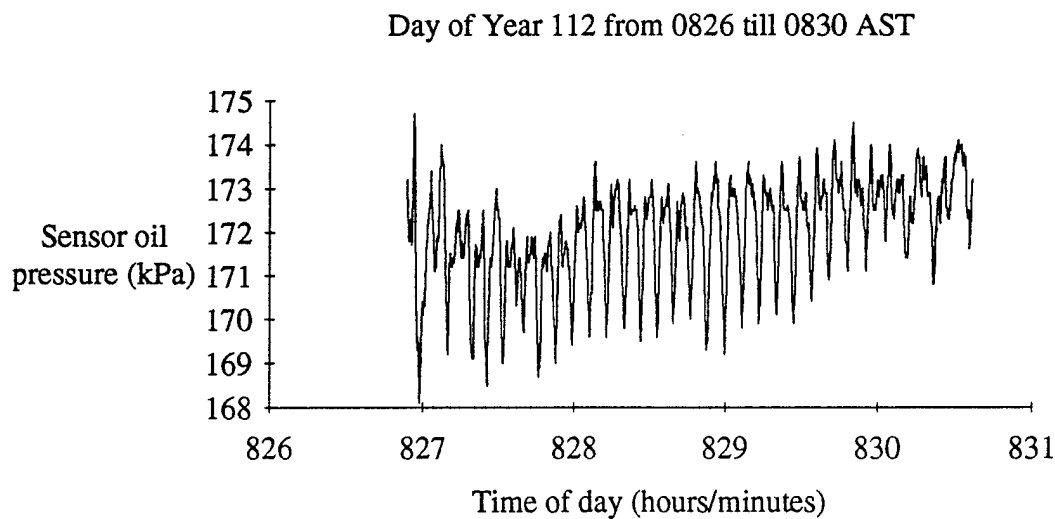


Figure 2. Ice-stress signal recorded near East Camp

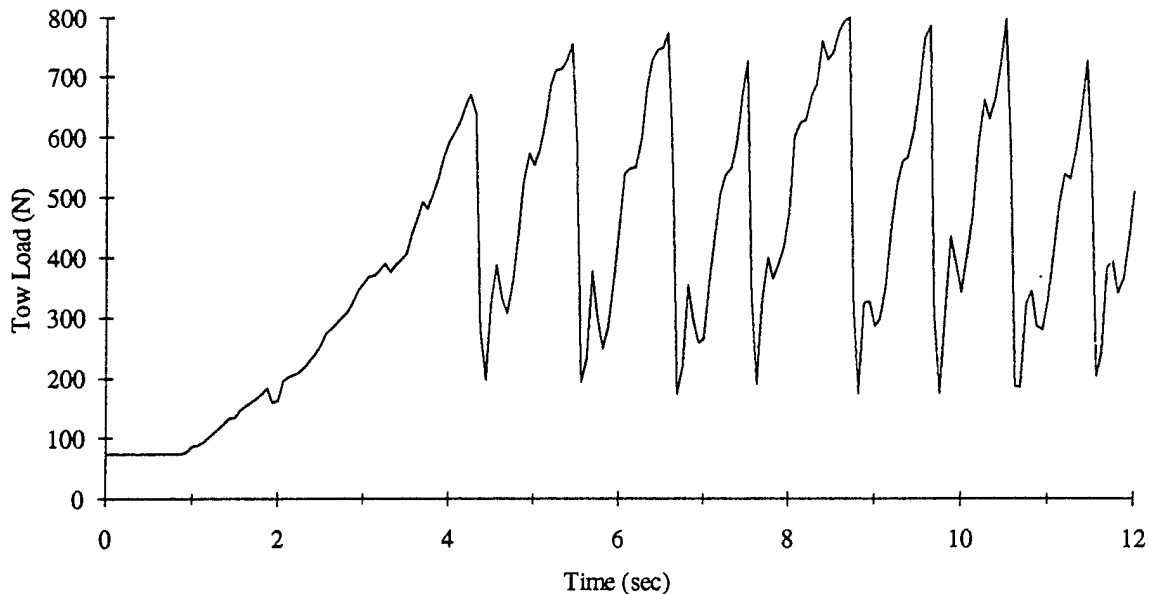


Figure 3. Tow load time series from an over-ride test (Test 8-13)

Ice-on-Ice Friction Tests -- In the configuration tested at Resolute, the shear force to cause shear motion along a fresh crack was surprisingly steady and smooth, except for the initial start-up motion. This may have resulted from having an air jack provide the normal force and a hydraulic jack provide the shear force. These dynamics are very different from an ice block being pulled with a winch. The measured coefficients of friction of natural cracks in first-year sea ice are consistent with the friction angle of pack ice calculated from ice-stress measurements made during the CEAREX program.

Ridge-strength Tests -- The strength of the fused ice in the ridge was highly variable, ranging from essentially solid ice near the surface to loose pieces floating underwater at or near their melting point temperature. Figure 4 shows an intermediate case of air jack pressure versus time. We interpret the down steps during the long rise as ice-to-ice contacts breaking and slipping. We stopped the displacement of the air jack when it had reached maximum stroke. We caused the large down step at the end by releasing the pressure in the air jack. These tests suggested that a better test of ridge keel strength would require a larger volume displacement, on the order of 8 cubic meters or more.

Panel Report on 100 km Scale (Pack Ice)

M.D. Coon,
R. Preller,
and
A. Proshutinsky

Proceedings of
The Sea Ice Mechanics and Arctic Modeling Workshop, 1995
Anchorage, AK, 1995

PANEL REPORT ON 100 KM SCALE (PACK ICE)

Chairman: Max D. Coon
NorthWest Research Associates, Inc.

Ruth Preller, Recorder
Naval Research Laboratory

Andre Proshutinsky, Recorder
Institute Marine Science, U of AK, Fairbanks

This panel met Wednesday, April 26, 1995, in the morning. The discussion of the 100 km scale (pack ice) centered around the anisotropic behavior of the pack ice as indicated and driven by the formation, deformation, and closure of leads.

GOALS

The SIMI goals are reported in Appendix B, Vol. 1, of these Proceedings.

- Understand sea ice constitutive laws and fracture mechanics over the full range of geophysical scales and determine the scaled responses to applied external forces
- Develop physically based constitutive and fracture models

One of the aims of the Sea Ice Mechanics Initiative (SIMI) was to bridge scales in sea ice mechanics. This can and has been done by considering pack ice on a scale from 3-100 km as made up of two types of ice as shown in Figure 1. The two types of ice are not necessarily represented by presently used nomenclature. The scene in Figure 1 is intended to represent a sea ice element system with an active lead in it. A lead system is made of parallel leads that are shown as one lead in the element of Figure 1.

So, what is the Type-1 material in Figure 1? The ice in material Type-1 includes multiyear ice, first-year ice, ridged-ice, rafted-ice, and inactive refrozen leads. The material has a wide distribution of sea ice thickness and is made up of closely-fitting, angular particles, grains, or cells, often diamond shaped in the winter. Type-1 material is deformable, controlled by a 2-D Coulomb behavior with no significant thickness redistribution due to deformation. The particles, grains, or cells that make up Type-1 material are of order 100 meters, and they have been formed by out-of-plane loadings such as thermal loading or isostatic imbalance. These loadings have led to cracks which have produced the grains or cells, and the cracks have only partially healed. This cracking and rehealing are the small-scale mechanisms which cause the Type-1 material to have its properties. When this material deforms, it produces new areas for Type-2 material (leads).

<p>Ice Forecasting for Ship Routing and Operations</p> <p>Ice Gouging of the Sea Floor</p>	<p><i>Flue Splitting</i> - The fracture research in the SIMI program will determine the scale dependence on the tensile failure strength as well as provide a fracture model that is applicable to sea ice in the range of 0.1 to 1 km.</p> <p>The SIMI anisotropic plasticity ice dynamics model can describe and forecast ice behavior on smaller scales (~ 3 km) than previous models.</p> <p>What we now know:</p> <p>The form of the gouge depth distribution at a given instant of time is a negative exponential.</p> <p>The coefficients of the gouge depth distribution function vary systematically with water depth.</p> <p>To obtain meaningful statistics concerning the number of gouges per km or per km² per year, a sampling period of several years duration is required.</p> <p>Gouges generally run parallel to the isobaths.</p> <p>The deepest, as well as the most frequent, gouges occur at water depths of between 25 and 40 m.</p>	<p>Complete the interpretation of the SIMI experimental work to develop a size effect law for fracture and splitting. Develop a new theory for flow splitting from the above (with and without surrounding pack ice).</p> <p>Develop failure laws for a complete suite of full-scale processes (e.g., opening, rafting, and ridging), develop a numerical scheme, and test model performance.</p> <p>There is a critical need to develop procedures for determining gouge depth distributions for regions where sediment transport is so large that gouges are so quickly destroyed as to leave no record on the sea floor.</p> <p>Small-scale (2 to 10 km) ice-ocean model development and validation, including the anisotropic parameterizations of ice mechanics, to properly characterize the nearshore ice motion since oil transport is primarily by ice motion.</p>
<p>Oil Spills and Oil Transport by the Ice</p>	<p>What we now know:</p> <p>Improved coupled ice-ocean models for central Arctic have been constructed.</p> <p>Nested ocean and ice model techniques have been applied to Arctic problems.</p> <p>Improvements in the convection parameterization in ocean models has been shown to accelerate the melting rate of ice.</p> <p>Improved wind fields from atmospheric models has been applied for input to ice-ocean models.</p>	

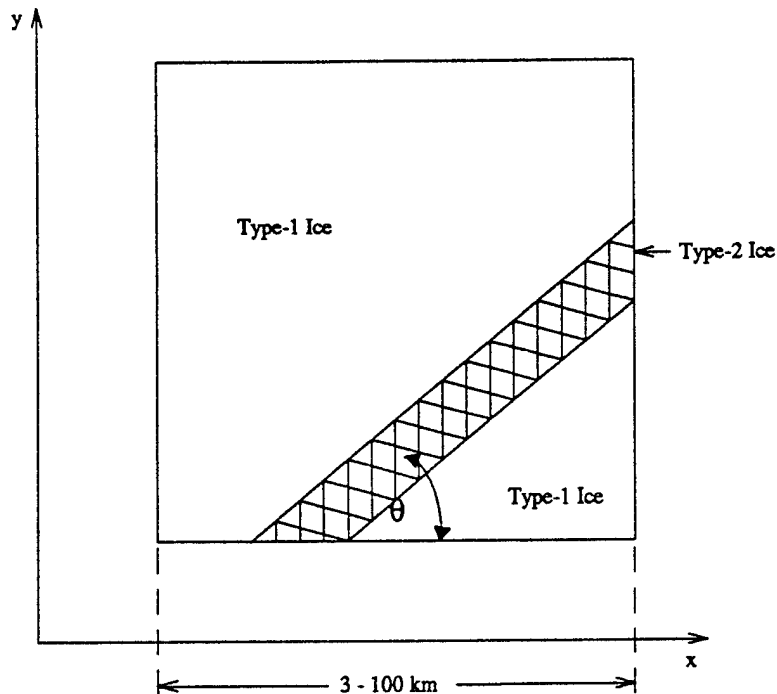


Fig. 1. Element of pack ice with a refrozen lead.

Type-2 material is what we typically think of as lead ice or rafted-lead ice or ridged ice. It is the ice that was formed in the openings made in Type-1 material and then deformed. Therefore, the constituents of Type-2 ice are open water, thin new ice, thick new ice, rafted ice, ridged ice, and floating broken pieces of the lead ice. This material has a thickness distribution which is associated with a direction, θ in Figure 1, and the redistribution is caused by deformation. This material has two discrete kinds of behavior, both of which are the small-scale mechanisms. One is the failure or initialization of dynamics of the Type-2 ice. This initialization is controlled by small-scale mechanisms such as the strength of an intact new ice sheet in tension, compression, or shear. This type of behavior is affected by ice thickness, temperatures, salinity, grain size, and strain rates. Another type of failure of this material is controlled by buckling instabilities which might be elastic under short-term loadings or visco-elastic under longer duration loadings. A third intermediate type of initialization of failure for this material is the buckling of individual (ridged) blocks that might be floating in the lead. The second kind of behavior here is that of the mechanical redistribution of the ice, and this is then controlled by either the rafting process which depends on ice thickness and friction or the ridging process which is controlled by thickness, friction, and change in energy state.

Type-1 ice is isotropic and has a failure surface which can be expressed in terms of stress resultant invariants which change very slowly and may be approximated as constant in time.

The Type-2 ice is oriented, and its failure surface cannot be expressed in terms of invariants and its failure surface varies over shorter time scales (hours) driven by the ridging and

rafting pressures. Pack ice is a combination of Type 1 and Type 2 and has an anisotropic behavior whose properties can change over time periods of hours.

Coon et al. [1992] introduced a method for incorporating the behavior of individual leading, rafting, and ridging events into the large-scale constitutive behavior of pack ice. This was not expressed in terms of Type 1 and Type 2 materials, but that is what it represents. The concept is that the large-scale stress state must lie within all of the yield surfaces that describe failure of individually resolved ice features. Ice conditions are described in terms of an oriented thickness distribution including the thickness of ice in leads. In resolving behavior on scales from one to hundreds of kilometers, processes of leading, rafting, and ridging that describe and control the behavior of sea ice are explicitly considered. Previous models [e.g., Coon et al., 1974] are applicable only over scales large enough that the multiplicity of ice features give rise to an isotropic response.

SIMI included nested arrays of drifting buoys to measure deformation on different scales. The large, pack scale Arctic buoy array, with resolution of order tens of kilometers, is not useful for locating individual events. The floe cluster array of GPS and the stress buoys was deployed at roughly 3 km intervals over a uniform grid 15 to 20 km on a side, allowing the deformation of individual events to be tracked. Vol. 1 of these Proceedings discusses the data taken.

The SIMI data collection plan for this scale is given in Appendix B of Vol. 1 which said: "An anisotropic model enables measurements of stress, deformation, and ice conditions associated with individual leading, rafting, and ridging events to be used as components of a large-scale model. During SIMI, these variables will be measured during specific events. At times, isolated events with length scales of order 100 m will likely occur within the floe cluster array while the remainder of the array will be nearly rigid. Such events will be described by observations on the scale of 3 to 15 km by the deformation of the array and by direct ground observations. Airborne imagery of the region near the end of October will help identify earlier events and provide a baseline for comparison in spring. Ice motion vectors will be derived from SAR and AVHRR imagery." A test of this model and data is given by Coon et al. [1995] in this Volume. For the first time, simultaneous measurements of sea ice stress on both sides of a lead, ice motion from sequential SAR imagery, and ice motion from drifting GPS/Argos buoys are compared. The lead, which appeared early in Day 35 (Feb. 4), 1994, was observed, relative motions were calculated across and along the lead direction, and stresses were transformed to this same coordinate system. The lead orientation and approximate location were determined from SAR images of the pack ice surrounding the SIMI camp, as well as net ice motion at 3-day intervals. The ice motion around the lead was provided in greater detail by an array of drifting GPS/Argos buoys producing hourly positions. Sea ice stress was measured on each side of the lead using flapjack sensors. The ice motion normal to the lead and the ice stress normal to the lead are compared as well as the ice shear motion and the ice shear stress.

Shortly before the lead opening motion is apparent in the ice motion data, the ice stress state abruptly changed from biaxial compression to uniaxial compression with traction on the lead near zero. We thus measured the stress conditions at lead creation as sheared compression; there was no tension at the time. The Type-1 ice, made up of closely fitting angular particles, begins to

fail and create a lead under shear and compressive stress just as sand can expand under shear and compressive stress by going from a closely packed configuration to a loosely packed configuration. As the lead continues to open the stress normal to the lead is zero, the stress parallel to the lead is compression, and there are no tensile stresses. Excellent correlation was observed between ice motions measured with SAR products and drifting buoys. The SAR products provide a more precise definition of the orientation of the lead. It was also concluded that a properly installed 20-cm stress gauge in a single floe can provide a reasonable measurement of the large-scale (50-km) pack ice stress resultant.

The needs of two user groups were expressed during the meeting. Ruth Preller expressed needs from the National Ice Center for methods of predicting leads (interpreted to mean direction and area) and a need for smaller scale, i.e., a few kilometer resolution. Ruth went on to describe the plans for the Navy in its Polar Ice Prediction System (PIPS) to have a model which would cover all areas in the northern hemisphere covered by sea ice with a resolution down to 20 kilometers. There was discussion and concern about one model being acceptable for the multi-year pack ice in the central Beaufort Sea and the marginal sea ice zones. One model can be made to work if the ice properties in the model vary sufficiently such that the multi-year and marginal regions can be described.

The needs of the oil industry were articulated by Albert Wang. Albert explained that for the oil industry real-time information was important. Forecasting of the pressure in the ice was a key as well as the ice conditions including leads and thickness distribution. There is a desire to use large-scale ice models to get large-scale forces that would be valuable for loads on structures. There is a need for ground truthing of the models such that confidence can be developed. For the oil industry and offshore operations, a three-to-four-day forecast of extreme events would be desirable but a one-day forecast could lead to a form of orderly shutdown.

Kate Hedstrom discussed ice modeling work at Rutgers University where they are coupling an ocean model to an ice-atmosphere climate model (ARCSyM, from U. of AK, Fairbanks). They also have done ice-ocean modeling for use in oil spill risk assessment studies for MMS. A third project involves the development of a spectral finite element ocean model to be used on a global, variable-resolution grid. Several of these projects require an ice model with better small-scale ice physics. For additional information, see Hedstrom (1995) in this Volume.

Igor Appel of Fairweather Forecasting discussed a model they use. The approach used is described in Appel (1990) and results of the model are presented in Appel and Samuels (1995). In this model the anisotropic behavior (interpreted as leads) is described by a viscous model. The viscosity depends on the value of principal strain rate. In this model the leads would open across the direction of the principal extension strain rate direction. This is a difference between this model and that of Coon et al. (1992) when there would be an angle between the direction of the lead and principal strain rate direction. In the work of Cunningham et al (1994), there is evidence of such an angle.

There is also a model by Moritz (1995) that accounts for leads in a statistical manner. In this model and the viscous model discussed by Appel there is no direct way to bring in the small scale ice mechanics as there is with the Coon et al. model.

The need to be able to account for leads and their behavior is a theme that comes up in many of the other panel discussions on ice behavior and applications in this Volume. Accounting for this behavior and using small scale mechanics to do so will meet the goals of SIMI as stated above.

The discussion of the panel is summarized by the two lists below. The first item in each list is that of most importance.

LIST OF THINGS WE HAVE LEARNED:

- 1) From GPS buoys, stress buoys, and SAR, the importance of lead formation and direction, on the large scale behavior of pack ice, has been verified. New leads have been shown to be created from states of compression and shear stress as measured on the scale of a floe but representing stress on tens of km. Also when leads are open the measured stress state is compression parallel to the lead and zero perpendicular to the lead. These findings are new and very important to the large (100 km) behavior of the ice.
- 2) We have developed a formulation for an anisotropic behavior (constitutive law) for pack ice which can account for creation and direction of leads
- 3) Examples of improved ice-ocean models are northern hemisphere PIPS, ARCSyM (U. of AK, Fairbanks and Rutgers University), etc. Desirable features are:
 - Higher resolution coverage,
 - Ability to assimilate satellite data, and
 - Coupling to the atmosphere.

WHAT NEEDS TO BE DONE NEXT:

- 1) Need formulation and verification of model against deformation (strain rates), leads (direction and deformation), and ice concentration using buoy and satellite data.
- 2) Need to put new rheology into improved models.
- 3) Need to use SIMI data to quantify the terms in the new constitutive law.
- 4) Need to incorporate results of smaller-scale models in large-scale model.
- 5) More aware of user needs.

LIST OF ATTENDEES

- Ruth Preller, Naval Research Laboratory
- Kate Hedstrom, Rutgers University
- Mike Vanwort, Office of Naval Research
- Igor Appel, Fairweather Forecasting
- Andre Proshutinsky, Institute Marine Science
- Max Coon, NorthWest Research Associates, Inc.
- Ed Fremouw, NorthWest Research Associates, Inc.
- Albert Wang, Exxon Production Research Company

REFERENCES

- Appel, I.L. "Mathematical Modeling of the Ice Cover Evolution in the Arctic Seas during the Melt Period" in proceedings of IAHR 10th International Ice Symposium, Espoo, Finland, 1990.
- Appel, I.L., and B.S. Samuels "Simulated Sea Ice Data" in proceedings of Fourth Conference on Polar Meteorology and Oceanography, Dallas, Texas, 1995
- Coon, M. D., Knoke, G. S., and Echert, D. C. "Anisotropic Pack Ice Constitutive Law" in *Proceedings of IAHR 11th International Ice Symposium*, Banff, Alberta, June 15-19, 1992.
- Cunningham, Glen F., Ronald Kwok and Jeff Banfield (1994) "Ice Lead Orientation Characteristics in the Winter Beaufort Sea," IGARSS '94.
- Hedstrom, Kate (1995) "A Coupled Ice-Ocean-Atmosphere Model of the Bering Sea," this volume, Part II.
- Ukita, Jinro and Richard E. Moritz (1995) "Yield Curves and Flow Rules of Pack Ice," *Journal of Geophysical Research*, 100 (C3), 4545-4557.

PANEL REPORT ON THE 10 KM SCALE - FLOE CLUSTER

Jim Overland, Chairman
NOAA- PMEL

Bryan Kerman, Co-Chairman
AES Canada

Jackie Richter-Menge, Recorder
CRREL

Gordon Cox, Recorder
Amoco Eurasia

The 10 km scale is critical to understanding and modeling spatial and temporal variability of sea-ice dynamics (Figure 1). Applications are ice forecasting, ice loads on structures, and pollution transport. At this scale there are two important transitions as the scale increases: from understanding ice as discrete floes to a continuum medium and from a stochastic view of ice processes to deterministic parameterizations. In the early 1970s, during AIDJEX, researchers developed the concept of sea ice on the regional scale as a strain-hardening plastic material. This remains the prevailing approach. In a plastic response, as the external forcing increases, the stress in the ice pack will increase up to a certain failure limit, at which point the ice will deform. As the pack ice converges, its strength/compactness/thickness increases and thus its failure limit increases and the pack "hardens". This process results in the development of regional stresses in the ice cover, which probably relates to sea-ice features such as the long, linear leads seen on AVHRR images. The question exists as to whether these sea-ice dynamics assumptions are valid based on measurements at the 10 km scale, where we consider a cluster of floes.

The essential processes that control ice-dynamics behavior are leading, rafting, and ridging. The present generation of isotropic sea-ice models were originally developed to describe ice dynamics on scales averaged over 100 km and larger. Researchers hypothesized that this scale was large enough to include the effects of many leads and/or ridges at random orientation within the sampling scale. There are times, however, when an individual large feature can dominate behavior even on these scales; for example, if one huge lead opens or narrow, linear discontinuities propagate in from boundaries. The isotropic model may adequately represent behavior averaged over 10 km, such as during conditions just after freeze-up when the floes are small (<1 km) with randomly oriented thin ice between them. As the scale is reduced from 100 km, however, the likelihood of encountering strongly oriented features increases, particularly for winter pack ice conditions. Thus, to resolve regional sea-ice dynamics behavior it appears necessary to account for anisotropy. Deriving more accurate solutions by reducing grid size in existing models is beneficial, but these solutions must still be interpreted as averages over the larger scale. A major conclusion of SIMI research is that it is important to understand and model

anisotropic sea-ice processes on the 10 km scale to correctly interpret processes on the 100 km scale. The final summary discussion of the meeting noted a need to merge the 10 and 100 km scales in terms of understanding ice mechanics.

The findings of LEADDEX and SIMI Experiments indicate a mismatch in scales between the forcing on the ice field, primarily wind and coastal orientation, and pack ice itself. Atmospheric storms have large spatial scales (order of 800 km), and small temporal scales (order of days). Regional sea-ice motion has a temporal scale of a week or longer and a spatial scale of kilometers. Therefore, the cluster scale response of the sea ice is not directly forced by a similar cluster scale variability in the wind. The cluster scale response of the ice is determined by the aggregate mechanical properties of the ice field in response to nearly uniform wind fields, acting over 3-5 days, before or after passages of a storm front. Figure 2 shows a SAR motion vector plot for a shear/opening event near day 35 in early February 1994. The vectors are 5 km apart. There are large regions (plates?) which behave with apparent solid body motion separated by long (100 km), narrow (<5 km) shear lines. The sea-ice problem on the 10 km scale is the aggregate problem: describe a material which under uniform winds, subject to boundary forcing, will respond by the formation of plates, which are large compared to the floe size and separated by discontinuities. Also, what pack-ice mechanical processes result in this material description when aggregated? A goal of SIMI and post SIMI research is to describe and model this internal sea-ice mechanics.

During the SIMI field program, researchers examined sea ice dynamics concepts at a variety of spatial and temporal scales. The 10 km studies concentrated on identifying and studying cluster-scale events during an extended period with both Synthetic Aperture Radar (SAR) data and Global Positioning System (GPS) buoy data (Days 23 to 75). Three technical advances facilitated this work at the 10 km scale. The first was the availability of ice motion vectors derived from SAR data processed at the Alaska SAR Facility. This product uses sequential SAR images to track ice motion at a 5 km resolution over an area of 80 X 80 km per product. Taken together, these products can define regional (80 x 400 km) deformation fields at a three day sampling interval. The second technical advance was that the accuracy of the GPS allowed researchers to resolve relative motions between adjacent floes in the vicinity of the SIMI ice camps. These GPS measurements provided a comparison between the differential GPS ice motion with the SAR-derived ice motion fields. The third advance was the deployment of arrays of stress sensors that had been developed and tested on earlier experiments. Two major events were studied during the SIMI period. One significant event occurred in early February 1994 (days 38 to 41) with uniform northerly winds in which a convergence/shear event propagated northward away from the coast, reaching the location of the SIMI ice camp 400 km north of Alaska in 3 days. A major opening/shear event occurred between days 63 to 74.

Preliminary results from a 20 km stress and deformation array, centered about the west camp floe, suggest a correspondence between stress and deformation at the 10 km scale, but not at the 5 km scale. Further, a comparison of in situ stresses on the central ice floe show a strong linear correlation in time, indicating that the floe responds to regional (10 km), rather than local (1 km) deformation events. Together these results imply that there is a lower bound, between 10 and 5 km, for considering the ice floes in a region as a continuum. There is a higher frequency of

major stress and regional deformation events as compared to large-scale (50 to 100 km) deformation events, defined by the formation of shear line patterns observed in SAR images. This may indicate several levels of continuum behavior, with the basic unit being a cluster of floes on the scale of 10 km. Once the floes within these clusters have moved into a close-packing, the clusters themselves can lock together in response to a forcing system. This structure can then form regional plates separated by discontinuities.

There are several promising approaches to describe the ice interaction and the spatial evolution of stress at the 10 km scale. One approach is to model the pack ice as a classical granular material with an effective stiffness and strength. Results of such models suggest that variation in size, shape, and orientation of the granular elements, or ice floes, are important to producing fracture-like features. Application of this technique could lead to the development of an effective (i.e., large-scale parameterization) constitutive response (i.e., stress/strain rate relationship). A very promising approach is to directly observe the aggregation properties of pack ice through the analyses of SAR imagery. Two state parameters, texture and structure, can be derived from measures of nearest neighbor pixel intensity differences on the SAR data. Sharp changes in the slopes of observational points on a texture/structure axis plot have an analog to phase transitions and may correspond to boundaries between different ice types. There is a relationship of "information content" between these analyses and similar 1-D analysis of ice thickness estimates from sonar. There are subsets of SAR pixels which possess a similarity property which are multi-fractal. These sets display a critical connectivity tentatively associated with ice fracture nucleation, i.e., similar to avalanche phenomena. A value exists of the nearest neighbor probability measure where pixels are mobilized into a space-spanning path called the percolation cluster. For large-scale compression of a mixture of stiff, brittle inclusions (i.e., multi-year ice floes?), and the percolation cluster (i.e., the rubble field?), the least unconsolidated part absorbs the strain. In materials other than ice, observations show that stress is transmitted along such poorly bonded paths. If the analog of sea ice to other stochastically described materials is consistent, then the percolation cluster hypothesis associated with FY rubble/ridges, may relate to the load-bearing capacity of the ice field.

A third approach to model pack ice at the 10 km scale is the oriented pack ice constitutive law. This law includes the creation of new leads in thick ice and the effects of leads and their orientations on the strength of the ice cover. The behavior requires an oriented ice thickness distribution to account for the growth and deformation of ice in refrozen leads. The shear and compressive strength of each lead are functions of the lead's ice thickness distribution. This approach predicts the orientation of lead systems and accounts for the highly anisotropic strength of the pack ice resulting from lead systems.

In summary, wind and coastal boundaries have large spatial scales (order of 500 km) while ice response is at all scales, with a tendency to form long, linear discontinuities at the 10-100 km scale. There are distinct patterns apparent in currently active leads and ridges which depend on boundary conditions and the type of forcing. Historical ridges and leads may appear more random. There appears to be a scale discontinuity in understanding between the regional and smaller scales. At the 0.1-100 m modelers can provide scaling laws for strength. However, at the 1 km scale much of the work on ridging is focused on linear compression, where evidence from

SAR analyses suggests that shear is a major yield mechanism and that failures follow lightening bolt, fault-like structures. Studies of strengths and failures of 1 km structures need to be coordinated with the horizontal 2-D percolation ideas discussed above. It is important to understand how stress propagates through the pack based on coastal orientation, wind forcing and ice property distribution on a 10 km scale.

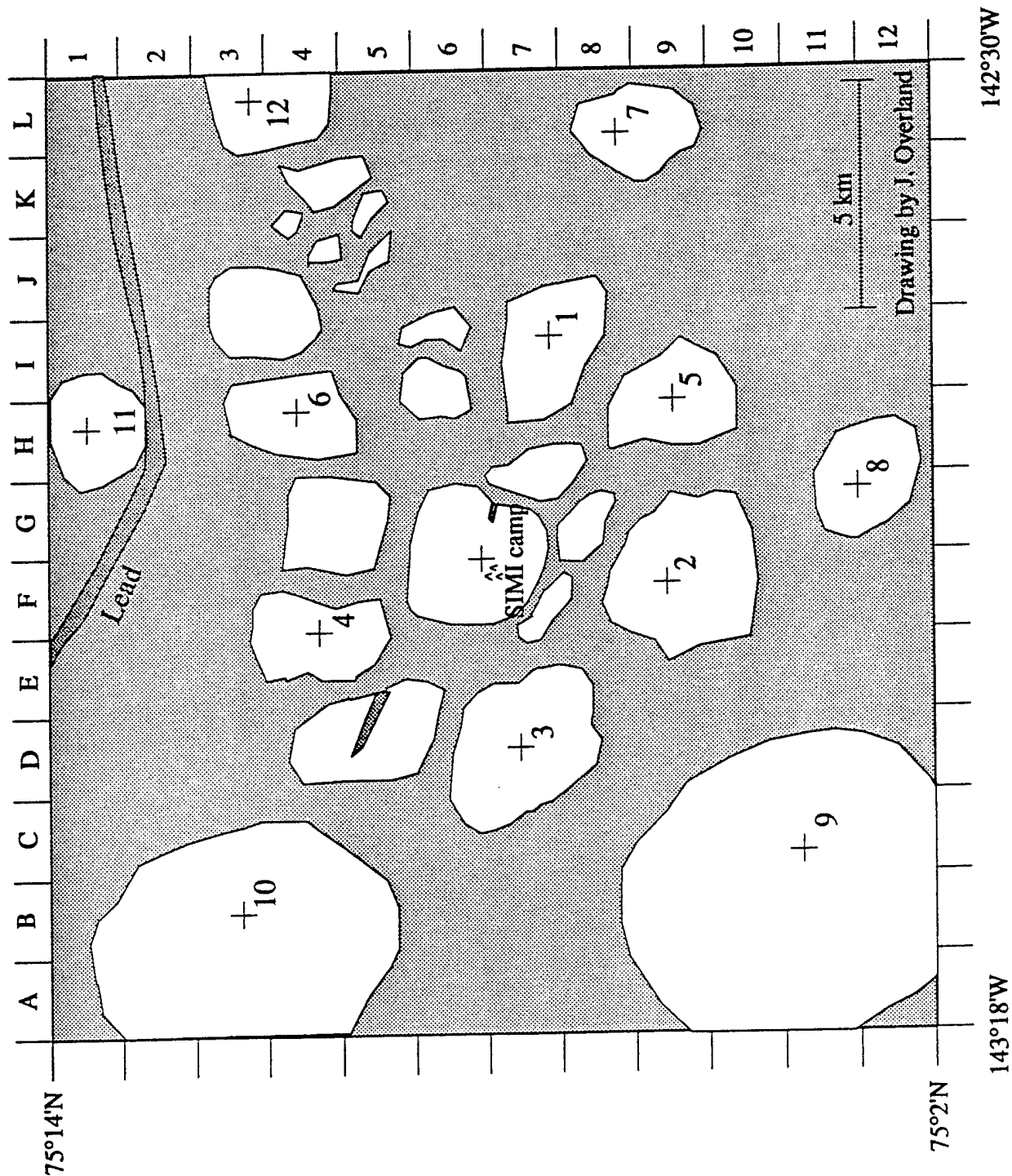
The group stated that the most important SIMI accomplishment was to acquire the first major data set of stress and strain rate of a pack ice cover on the 10 km scale, and to correlate this with results from both smaller and larger scale observations. There was good correlation between stress and strain rate at the 10 km scale, but not at small scales, even though the stress and strain measurements existed down to a 1 km scale. We believe that ice can be treated as a continuum at 10 km as long as the medium allows plate/discontinuity type structures.

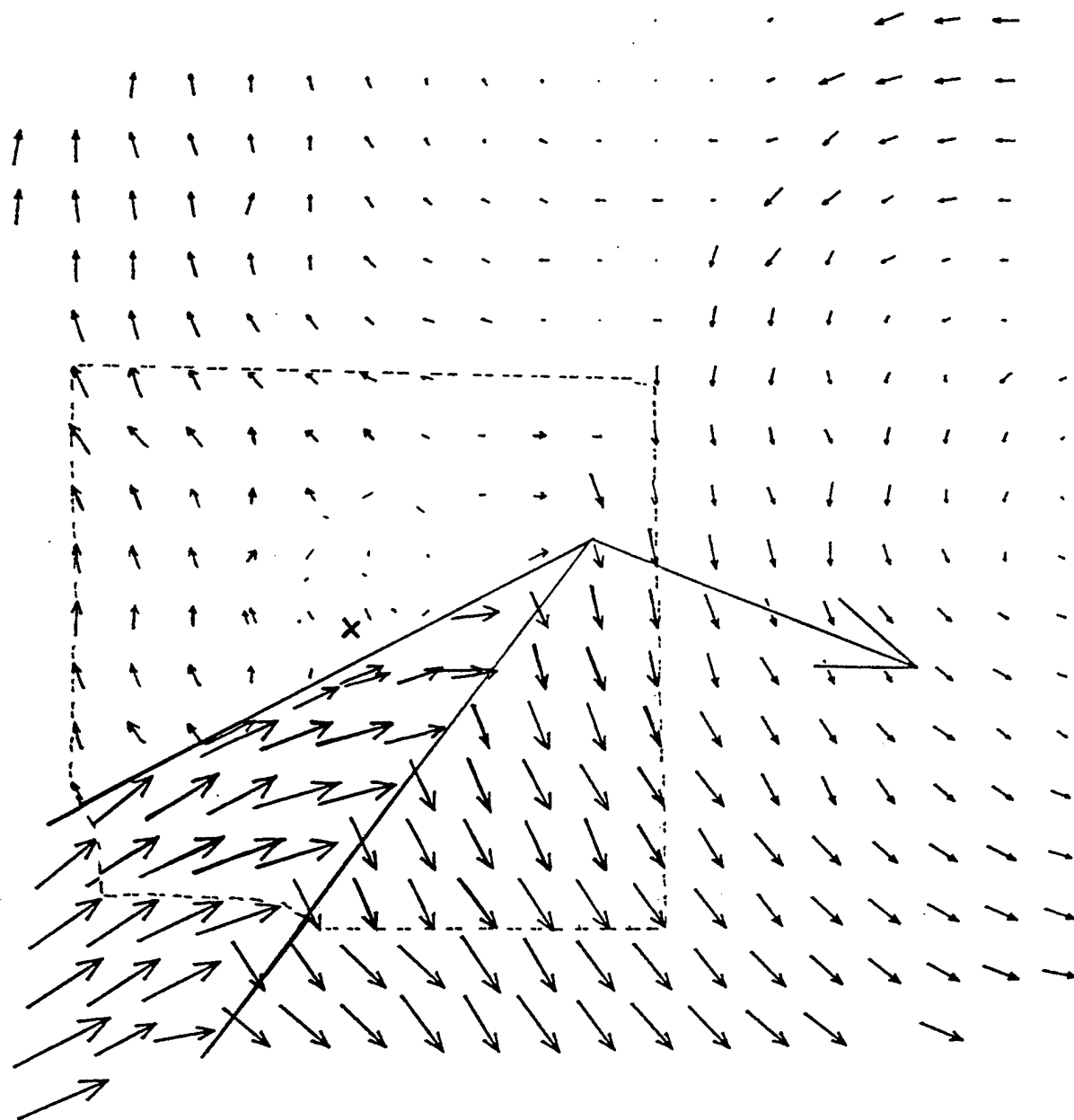
The group recommended that the main goal for future research is to understand what mechanical processes control the spacing of discontinuities (slip lines, leads, etc.). On AVHRR imagery there seems to be a preference for a 15 km and a 35-40 km separation scale. There is a need for more case studies of the stress-strain relationship for ice deformation events and modeling of buckling, rafting, and ridging in a 3-D context to characterize the anisotropic strength parameters of pack ice in terms of an oriented thickness distribution.

Figure 1. Distribution of large floes in the vicinity of the SIMI camp. Space between the larger floes was filled with rubble and small floes.

Figure 2. Relative motion of an ice field in the vicinity of the Ice Camp on day 35-38, 1994 from 5 km spacing SAR motion data. The large arrow is north. (Figure courtesy of H. Stern).

Map 1. Vicinity of SIMI West Camp, September 1993.





REPORT OF THE 1-KM-SCALE PANEL

By

Mark Hopkins

US Army Cold Regions Research and Engineering Laboratory

and

Henrik Schmidt

Massachusetts Institute of Technology

The large-scale composition of the ice pack is the aggregate of the basic 1-km-scale building blocks, discrete parcels of multiyear and first-year ice, and leads. Similarly, large-scale deformation is the aggregate of the basic 1-km-scale processes of pressure ridging, rafting, in-plane sliding, and opening, which redistribute energy from larger scales to smaller scales. By determining stress levels in the surrounding pack, 1-km-scale processes help define design loads on offshore structures. The 1-km-scale work in the SIMI program should be assessed on the basis of the following criteria:

- Contribution to understanding of the processes of ridging, rafting, floe splitting, and in-plane sliding between ice parcels;
- Contribution to determination of realistic estimates of forces on offshore structures;
- Contribution to large-scale modeling efforts.

1-KM-SCALE PROCESSES

Pressure Ridging

A realistic computer model of the pressure ridging process [Hopkins] was developed in SIMI. This two-dimensional ridging model is based on a concept of ridge growth in which an intact sheet of thin ice is driven against a thick ice floe. The key assumption is that the ice sheet breaks in flexure. The important features of the ridging model are: a dynamic linear viscous-elastic model of a floating ice sheet, flexural failure (including buckling) of the ice sheets, blocks broken from the parent sheet at points where tensile stress exceeds strength, secondary flexural breakage of rubble blocks, inelastic contacts between rubble blocks, frictional sliding contacts between blocks, separate friction coefficients for submerged and above water contacts, buoyancy of the ice sheets and rubble, and water drag. Simulations were performed with the model to determine the energetics and dynamics of the ridging process. Major unknowns in modeling the ridging process are the various friction coefficients.

In-situ friction measurements between blocks of sea ice were made during SIMI by Coon et al. and Pritchard. Preliminary analysis [Pritchard] of data from dry override tests points to a coefficient of sliding friction of approximately 0.8 ± 0.2 and a static friction coefficient of approximately 1.2 ± 0.2 . Corresponding values in wet rafting tests were approximately 0.2 and 0.4. In pressure ridge simulations [Hopkins], the various friction coefficients were found to control the relative volumes of the ridge sail and keel. The coefficients which gave the most realistic balance between sail and keel volume were in the range 0.8 to 1.0 – very similar to the values found by Coon and Pritchard. The ridge simulations were less sensitive to the underwater (wet) friction coefficient, but again values of 0.3 to 0.6 used in the simulations were similar to the values reported by Coon and Pritchard. Because sliding friction is the dominant energy sink in the processes of ridging, rafting, and the compression of floating rubble, this data set should be studied carefully.

Based on the results of long-term ridging simulations [Hopkins], the pressure ridging process can be divided into three phases. The first phase begins with an intact sheet of relatively thin ice impacting a floe and ends when the maximum sail volume is reached. In the second phase, the ridge keel maintains a triangular shape, deepening and growing in the leadward direction, eventually creating a rubble field of more or less uniform thickness. The second phase continues as long as there is a sufficient driving force and a supply of thin ice. The third phase is the compression of the rubble field between floes. In this scenario, the formation of rubble fields naturally follows the formation of ridges.

The effect of consolidation on the strength of first-year pressure ridges and rubble fields was the subject of numerous discussions during the workshop. In coastal areas, consolidated rubble fields and pressure ridges are an important consideration in the design of offshore structures. Consolidated pressure ridges are a major impediment to ship passage and may increase the severity and depth of scour events in near-shore areas. Future pressure ridge modeling efforts should focus on the effects of consolidation on the strength of ridges and rubble fields. The study of the consolidation of a first-year ridge by Shapiro et al. will be useful in such an effort.

Opening

Macro-cracks in first-year and multiyear ice precede lead formation. Deformation and fracture processes at the scale of 1 km are characterized by formation of ordered systems of cracks as well as coupled systems of cracks and ridges. Tensile crack formation perpendicular to a ridge was detected acoustically during the SIMI field program [MIT]. Systems of cracks perpendicular to ridge lines have been theoretically predicted by Goldstein and Osipenko (1995).

Acoustics provide the only viable remote sensing capability for detecting, characterizing, and identifying failure mechanisms in natural sea ice on the 1-m to 10-km scale. A major SIMI accomplishment is the development of a layered approach to seismo-acoustic mapping of sea ice fracture processes. The concept uses a 32-element horizontal hydrophone surveillance array with a 500 aperture. Focus beamforming is performed using parallel processing, producing a real-time

map of ice seismicity over a floe cluster, permitting early detection of active floe boundaries. When an active region is identified, a mobile array of five 3-component geophones and a single hydrophone is rapidly deployed to provide near-field measurements of the acoustic emission from the ice fractures. An important component of this concept is the development of a novel digital telemetry system, providing a wireless extension to a local-area network in the camp. This permits wireless data transfer from geophone clusters.

During the Fall and Spring SIMI experiment the layered concept successfully detected, located, and monitored several ice-mechanical events [MIT]. A particularly interesting event was a large, 1-km-scale fracture, mentioned above, which propagated transversely from a new ridge located N of East Camp. Another event was the formation of a major lead 2 km NE of East Camp in the latter part of the experiment. The dynamics and refreezing of this lead was monitored by two geophone clusters for several days, providing near-field measurements of acoustic emissions from rafting and early ridge building processes. At the same time, strong signals corresponding to what are believed to be "edge waves" were recorded. A preliminary analysis of this data suggests that the signals were associated with a 20 s stick/slip behavior along a lead which was part of a large, 30 – 40-km long, lead structure. Similar waves were recorded by tilt-meters and accelerometers at a ridge on the perimeter of the West Camp floe [Wadhams].

Another accomplishment on the floe scale was the execution and monitoring of plate wave experiments performed at Resolute as part of SIMI using automated hammer blows and geophone arrays. The analysis of the data collected [MIT] suggests strongly frequency dependent, transverse anisotropy of the sea ice. The precise nature of the frequency dependence is unresolved.

The analysis of SIMI seismographic data will address the following issues:

- Spatial and temporal statistics of ice events in the vicinity of the West Camp. The spatial distribution of fractures in relation to old and new ridges is of particular interest;
- Analysis of data from geophone arrays for fracture type, size, and speed. The analysis is expected to reveal the dominant fracture mechanisms associated with rafting and ridging. The results should be compared with recent theoretical predictions of compression induced ice fractures [Goldstein];
- High-resolution analysis of plate wave data has revealed frequency dependent anisotropy of sea ice. This behavior may be associated with unknown phenomena having a length-scale of 20 – 40 m;
- Edge waves were observed in SIMI along leads [MIT/WHOI] and along ridges on the floe perimeter [Wadhams]. The floe recordings of Wadhams indicate narrow-line spectrum, whereas the lead recordings by MIT/WHOI are of a more wide band nature which suggest a 20 s period, stick/slip dynamic behavior of motion parallel to leads. This observation may shed light on the dynamics of in-plane sliding between ice sheets.

**Sea Ice Deformation and Stress
A Comparison across Space Scales**

M.D. Coon,
D.C. Echert,
G.S. Knoke,
J.E. Overland,
S. Salo, R.S. Pritchard,
D.A. Rothrock,
and H.L. Stern

Sea Ice Mechanics and Modeling Workshop, 1995
Anchorage, AK

SEA ICE DEFORMATION AND STRESS, A COMPARISON ACROSS SPACE SCALES

M. D. Coon, D. C. Echert, and G. S. Knoke
Northwest Research Associates, Inc.

J. E. Overland and S. Salo
Pacific Marine Environmental Laboratory

R. S. Pritchard
IceCasting, Inc.

D. A. Rothrock and H. L. Stern
Polar Science Center, University of Washington

ABSTRACT

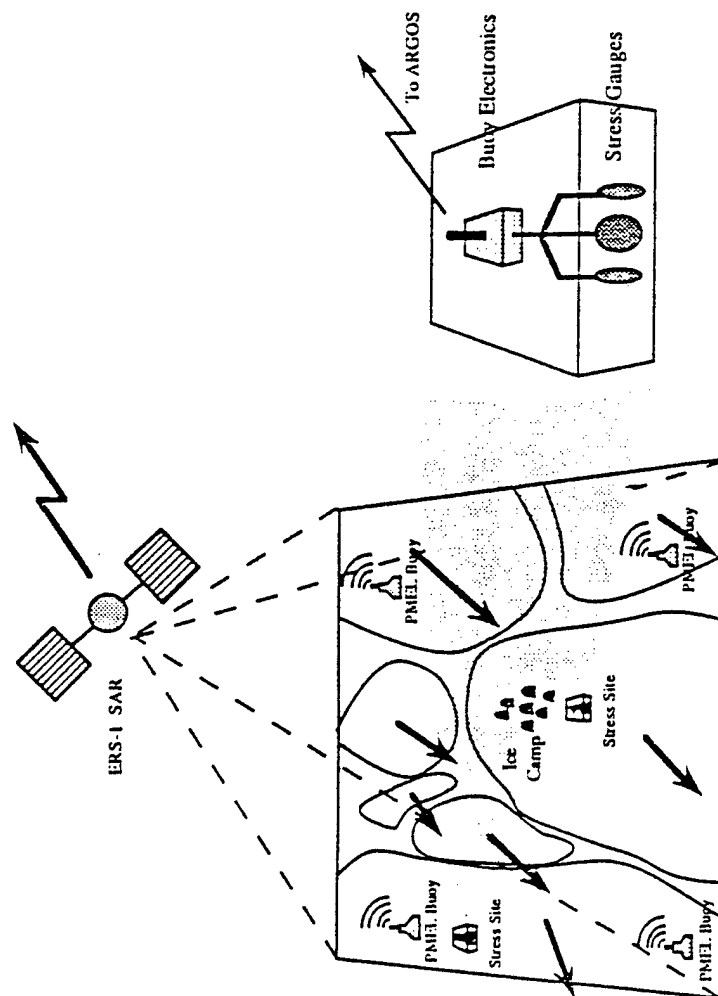
For the first time, simultaneous measurements of sea ice stress on both sides of a lead, ice motion from sequential SAR imagery, and ice motion from drifting GPS/Argos buoys are compared. The lead, which appeared early in Day 35 (Feb. 4), 1994, was observed, relative motions were calculated across and along the lead direction, and stresses were transformed to this same coordinate system. The lead orientation and approximate location were determined from SAR images of the pack ice surrounding the SIMI camp, as well as net ice motion at 3-day intervals. The ice motion around the lead was provided in greater temporal detail by an array of drifting GPS/Argos buoys producing hourly positions. Sea ice stress was measured on each side of the lead using flatjack sensors. The ice motion normal to the lead and the ice stress normal to the lead are compared as well as the shear ice motion and the ice shear stress.

Shortly before the lead opening motion is apparent in the ice motion data, the ice stress state abruptly changed from biaxial compression to uniaxial compression with traction on the lead near zero. We thus measured the stress conditions at lead creation as sheared compression; there was no tension at the time. We observe excellent correlation between ice motions measured with SAR products and drifting buoys. The SAR products provide greater spatial detail and a more precise definition of the orientation of the lead while the drifting buoys provide greater temporal detail. We also conclude that a properly installed 20-cm stress gauge in a single floe can provide a reasonable measurement of the large-scale (50-km) pack ice stress resultant.

We thank R. Colony, R. E. Moritz, and L. McNutt for their helpful technical discussions concerning these data.

Overview of Experiment

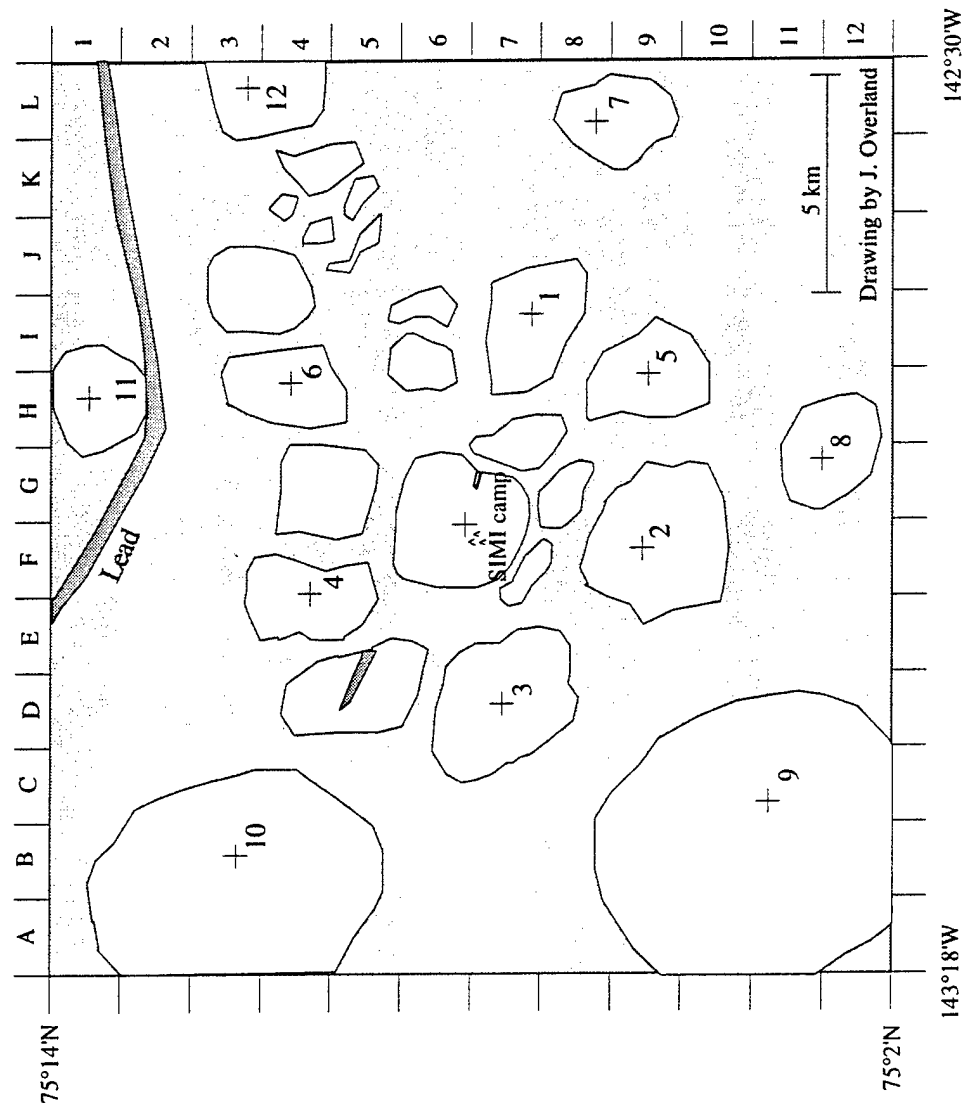
These results closely follow the experiment plan described in Section IV of "Contemporaneous Field Measurements of Pack Ice Stress and Ice Strain Measurements from SAR Imagery," by Coon, Knoke, Echert, and Stern (in Proceedings of OCEANS'93, Victoria, B.C., October, 1993). The schematic below, first published in 1991, accurately describes the overview of this 1994 experiment. Note that three satellite systems (ERS-1, GPS, and Argos) were utilized in this experiment.



Vicinity of SIMI West Camp

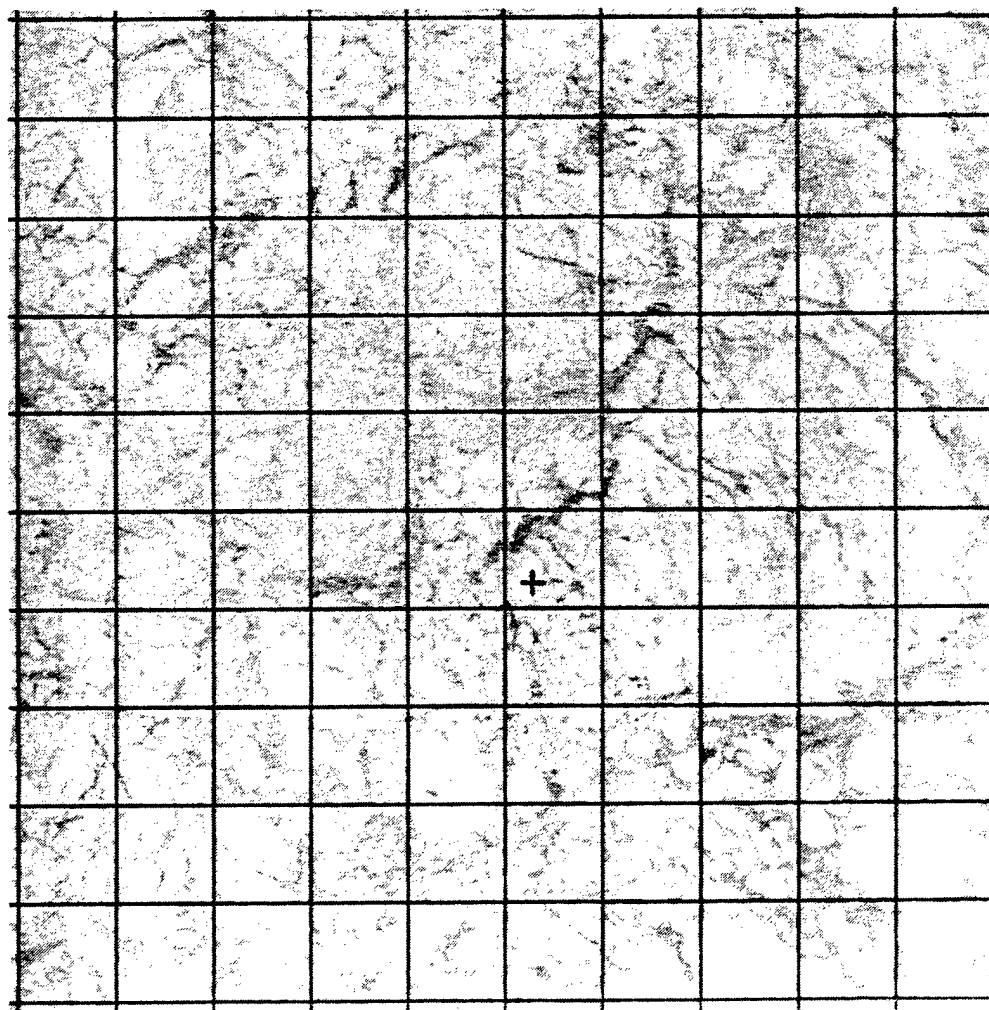
The map shows the locations and numbers of the main floes around the SIMI Camp (later called West Camp) in September 1993. The gray areas indicate small floes, rubble ice, and new ice between the large, multiyear floes. Each plus-sign (+) indicates the site of a PMEL GPS/Argos buoy deployed in September. NWRA stress buoys were deployed on Floe 4 (E4) and at the SIMI camp (F5) in November 1993.

Map 1. Vicinity of SIMI West Camp, September 1993.



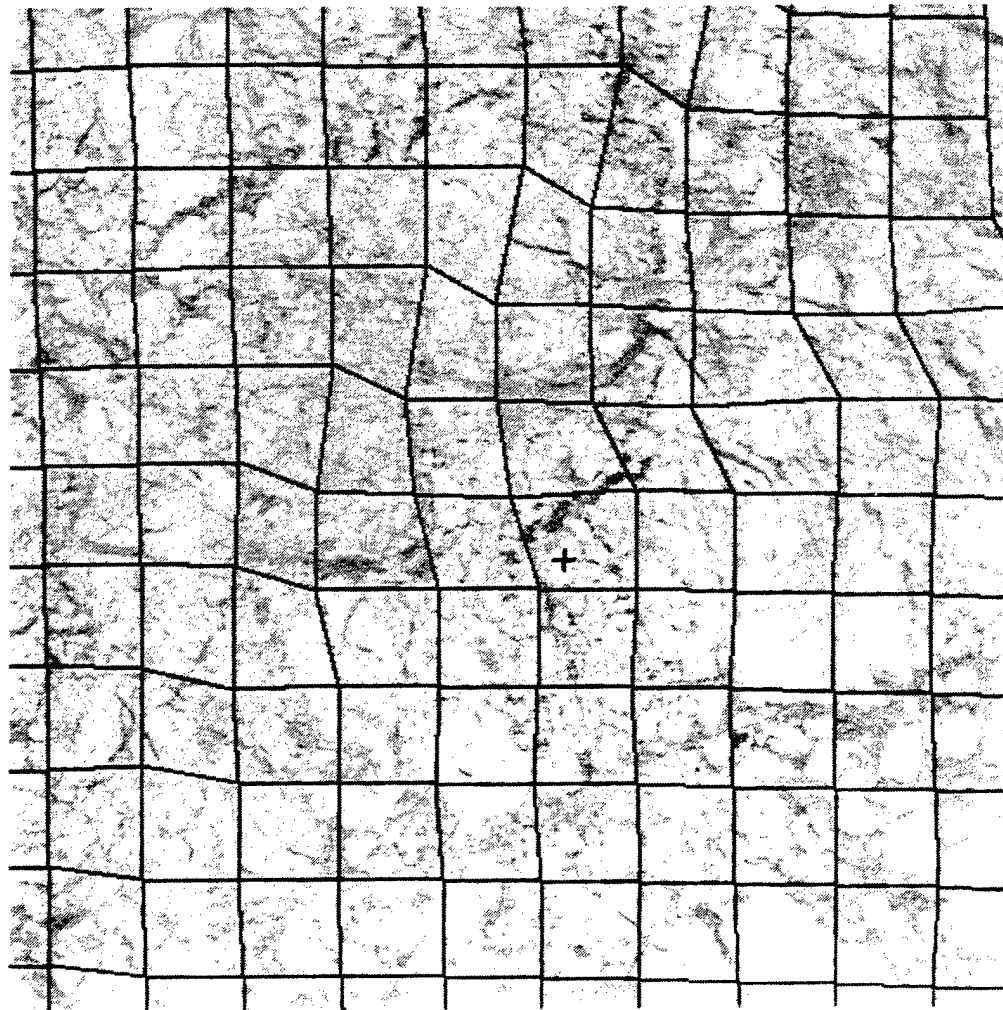
Synthetic Aperture Radar (SAR) Image with SIMI Camp

This is a synthetic aperture radar (SAR) image acquired by the ERS-1 satellite on February 4, 1994 (Day 35). The SIMI Camp is marked with a plus-sign (near the middle of the image). The grid lines have a spacing of five kilometers, so the whole scene is about 50 x 50 kilometers. The image is Copyright ESA 1994.



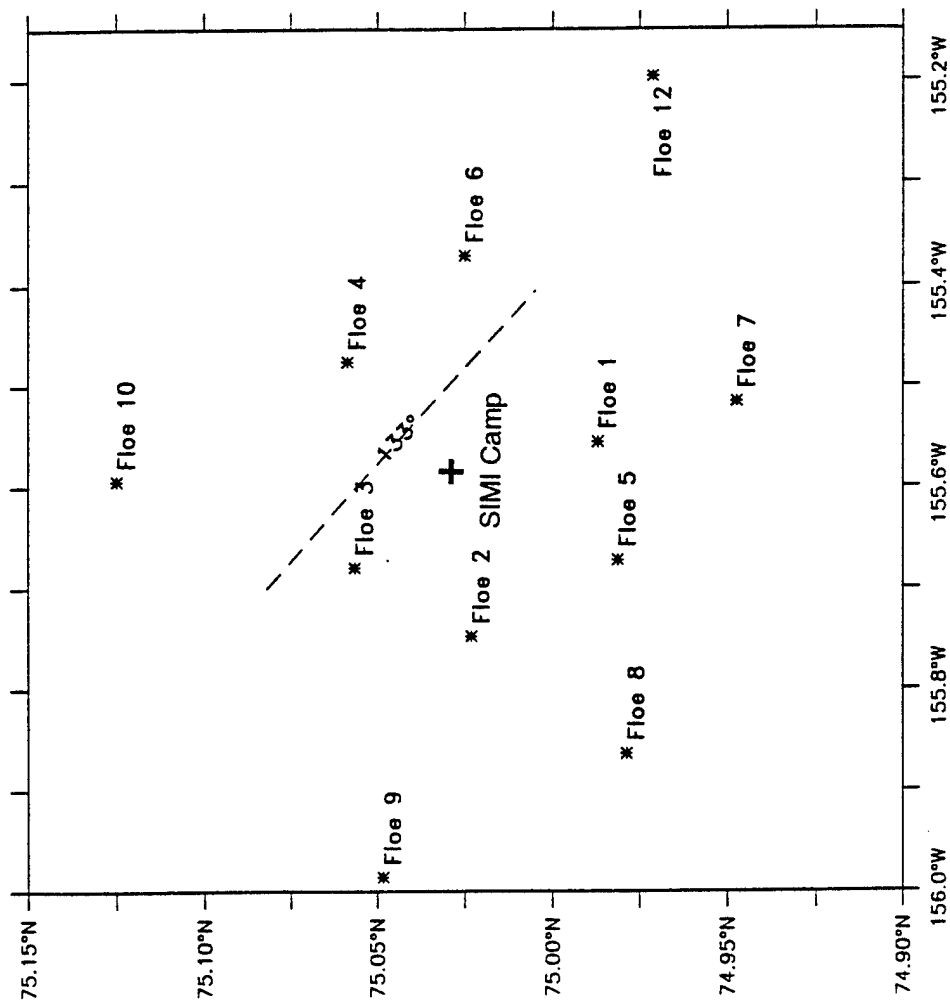
SAR Image with Deformed Grid

This is a SAR image acquired on February 7, 1994 (Day 38). The SIMI camp is again marked with a plus sign (near the middle of the image). The slightly deformed grid shows how the configuration of the sea ice has changed over the three day period. This deformed grid was obtained by an automatic ice-tracking procedure that uses area correlation to find corresponding features in two SAR images. The image is Copyright ESA 1994.



Positions on Day 35, 1994

This figure shows the positions of the PMEL GPS/Argos buoys at the SIMI camp and on the floes around it at 0000Z on Day 35 (February 4), 1994. We also include the orientation (though not necessarily the accurate position) of a lead which separated Floes 4, 6, 10, and 12 from the camp.

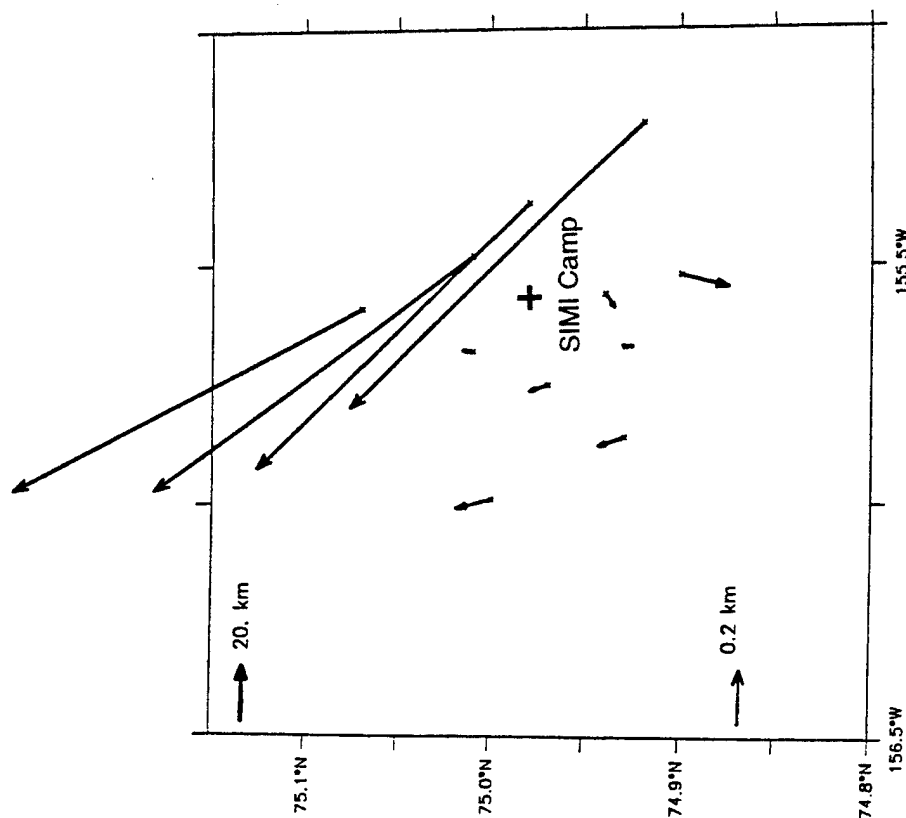


Positions on Day 35, 1994

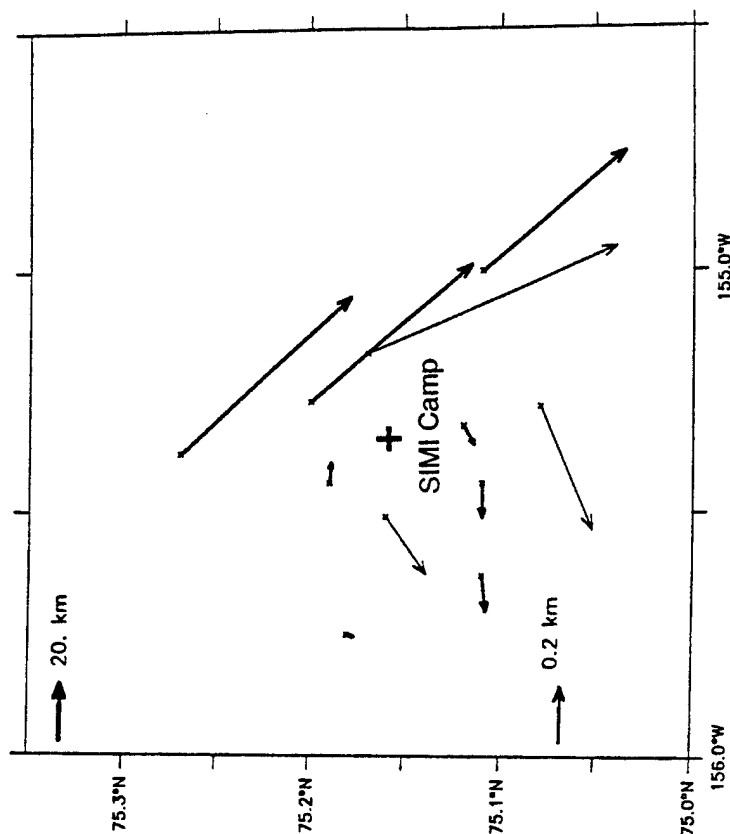
Relative Displacements

These figures depict 3-day displacements of the GPS/Argos buoy array relative to the displacement of the SIMI camp (plus sign). The left figure is Day 35 to Day 38; the right figure is Day 41; the figure axes and the buoy positions are latitude and longitude. The velocity vectors, scaled by the 0.2 km arrow in the lower left corner, indicate buoy displacements relative to the SIMI camp. These arrows are bold if the displacements were obtained from GPS data only and thin if the displacements use any Argos or splined data.

Note the relative displacement of Floes 4, 6, 10, and 12 to the northwest between Days 35 and 38, followed by relative displacements in the opposite directions during the next three days.



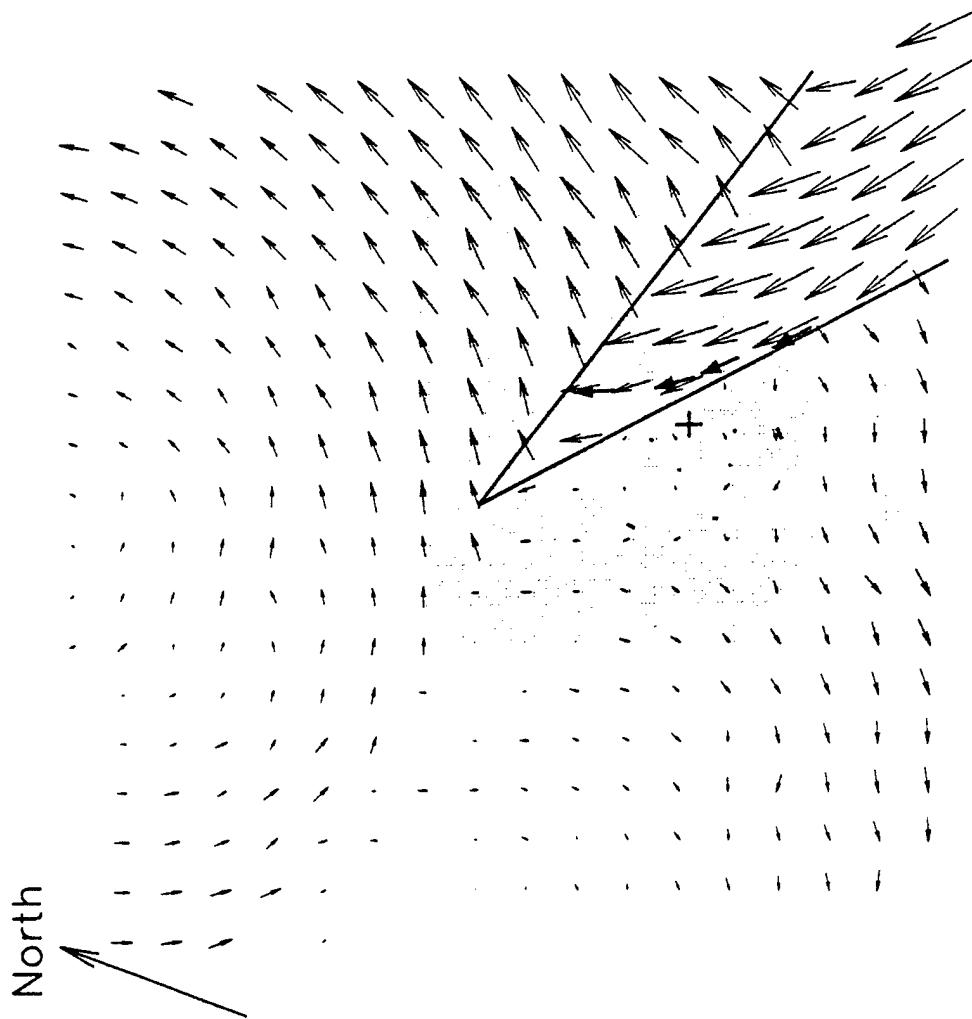
9403500-9403800 Relative Displacement



9403800-9404100 Relative Displacement

Vector Ice Motion Comparison

This figure shows SAR displacement vectors for Days 35 to 38 relative to the SIMI camp (plus sign) on the same 5-km grid as before but for an area of about 85 x 85 kilometers. The gray area corresponds roughly to the portion of the SAR image shown before. The majority of the arrows are displacements derived from the sequential SAR images (exaggerated by a factor of three). The darker arrows show the motion of the PMEL buoys relative to the main camp over the same three-day period (also exaggerated by a factor of three). The two intersecting lines denote the velocity discontinuity lines, implying active leads or ridges. The angle from North to the active lead near the main camp is approximately 133 degrees. These data show excellent correlation between ice motions measured with SAR products and drifting buoys.



Jump in Normal and Shear Velocity Across the Lead

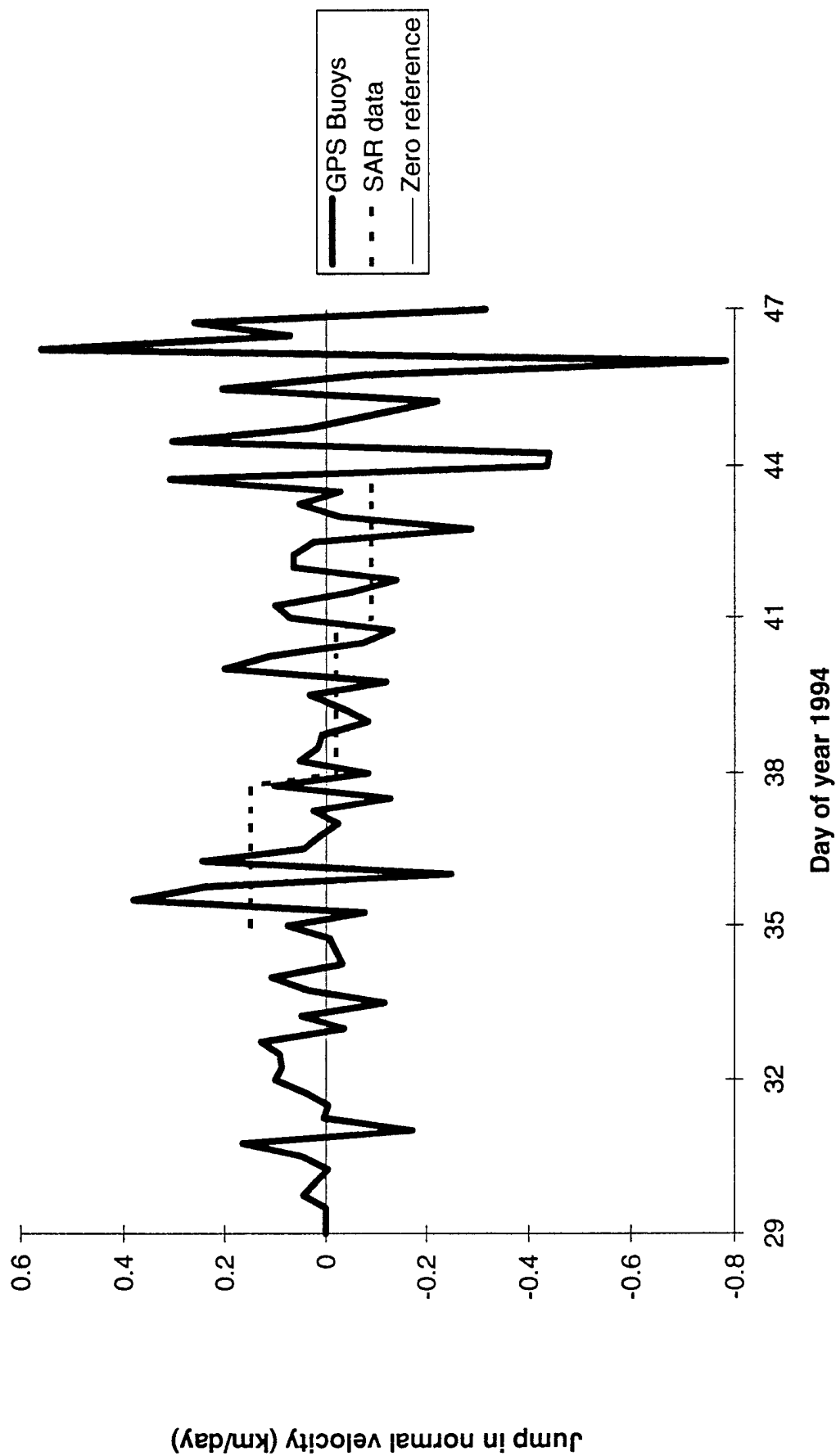
Here we combine data from PMEL's GPS/Argos position buoys with data derived from SAR images. The following two figures compare the jumps in ice velocity normal to the lead and the jumps in shear velocity.

In calculating the ice motions from GPS buoy data, we sub-sampled the relative displacements (buoy displacement - main camp displacement) every six hours and rotated the components to the lead coordinate system. We then averaged the normal and shear components for the far-side buoys on Floes 4, 6, 10, and 12 and subtract the average components for near-side buoys at the main camp and on Floes 1, 2, 3, 5, 7, 8, and 9. A positive shear motion is southeast (Heading 133°T); a positive normal motion is northeast (Heading 043°T).

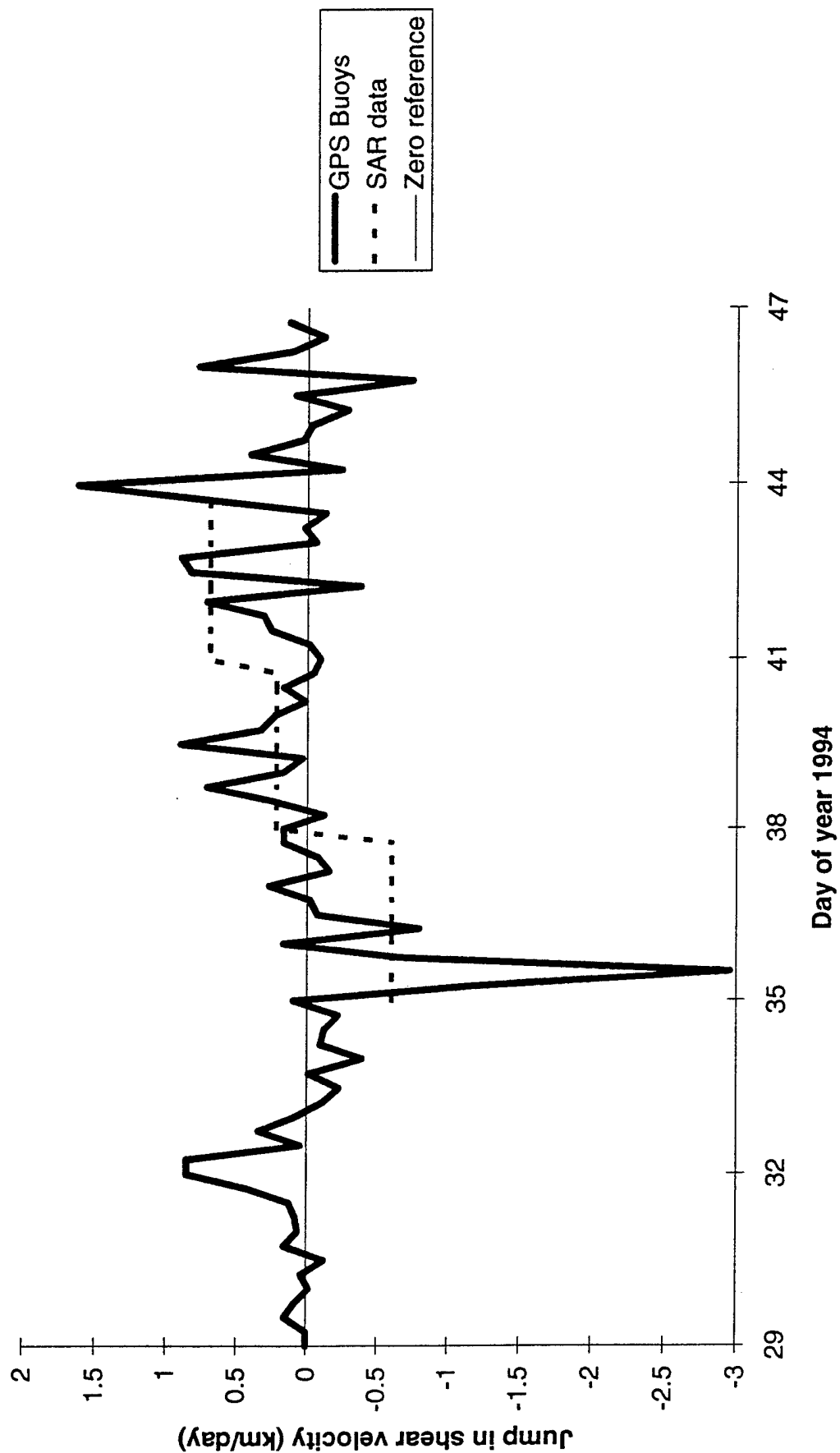
In calculating the ice motions from SAR products, the velocity jump across the lead was resolved into components parallel (shear) and perpendicular (normal) to the lead. The velocity jump is the difference of the average velocities of ten locations on the far side of the lead from camp and of ten locations on the same side of the lead as the camp.

Most of the relative motion toward the northwest occurred in roughly 12 hours of Day 35, while the southeastward motion occurred more gradually. The jump is shear velocity was larger that the jump in normal velocity for both events.

Jump in normal velocity across the lead derived from 6-hour GPS positions and jump in normal velocity across the lead derived from 3-day SAR images



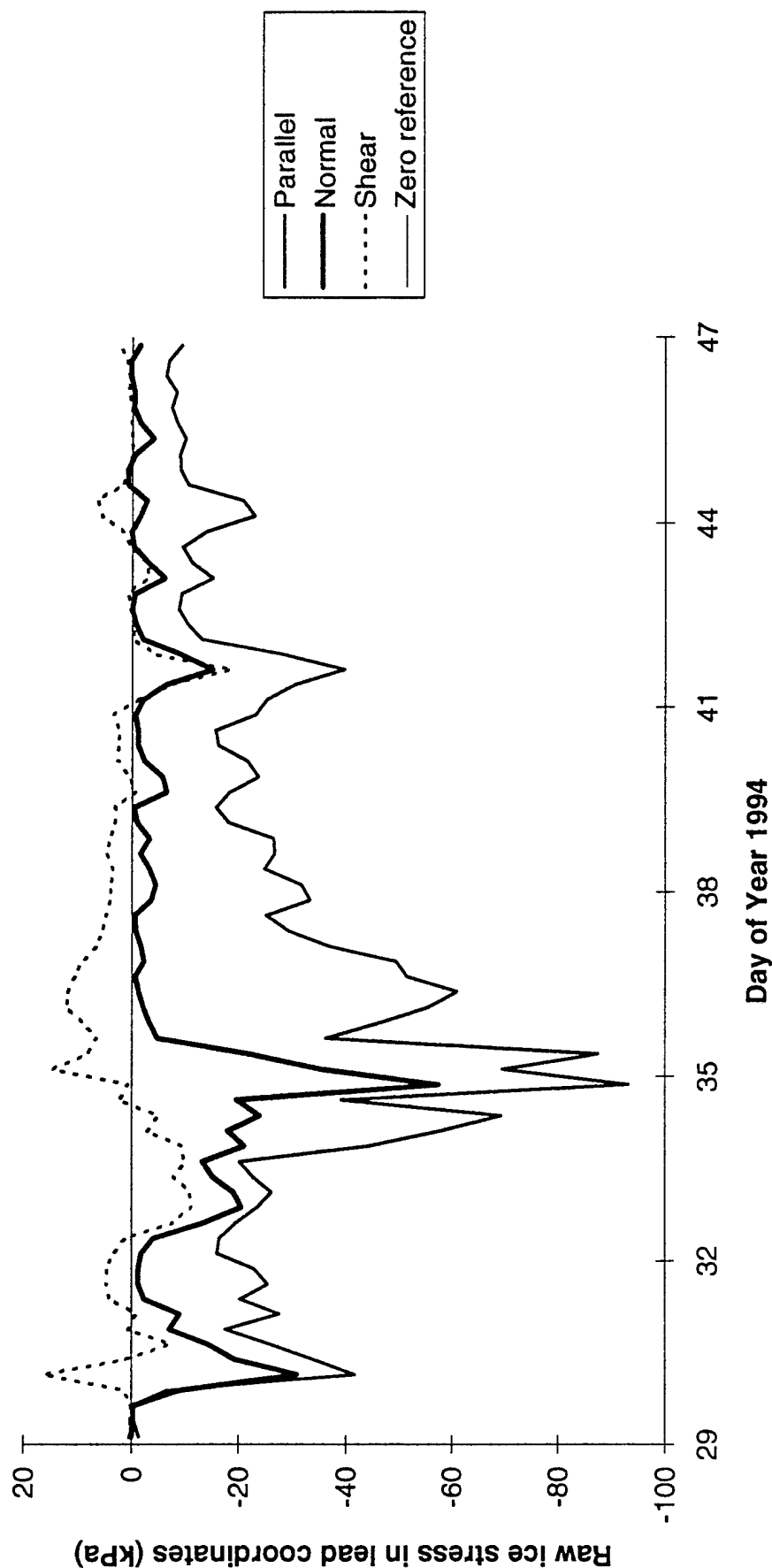
Jump in shear velocity across the lead derived from 6-hour GPS positions and jump in shear velocity across the lead derived from 3-day SAR images



Sea Ice Stress Measured at Floe 4 Expressed in Lead Coordinates

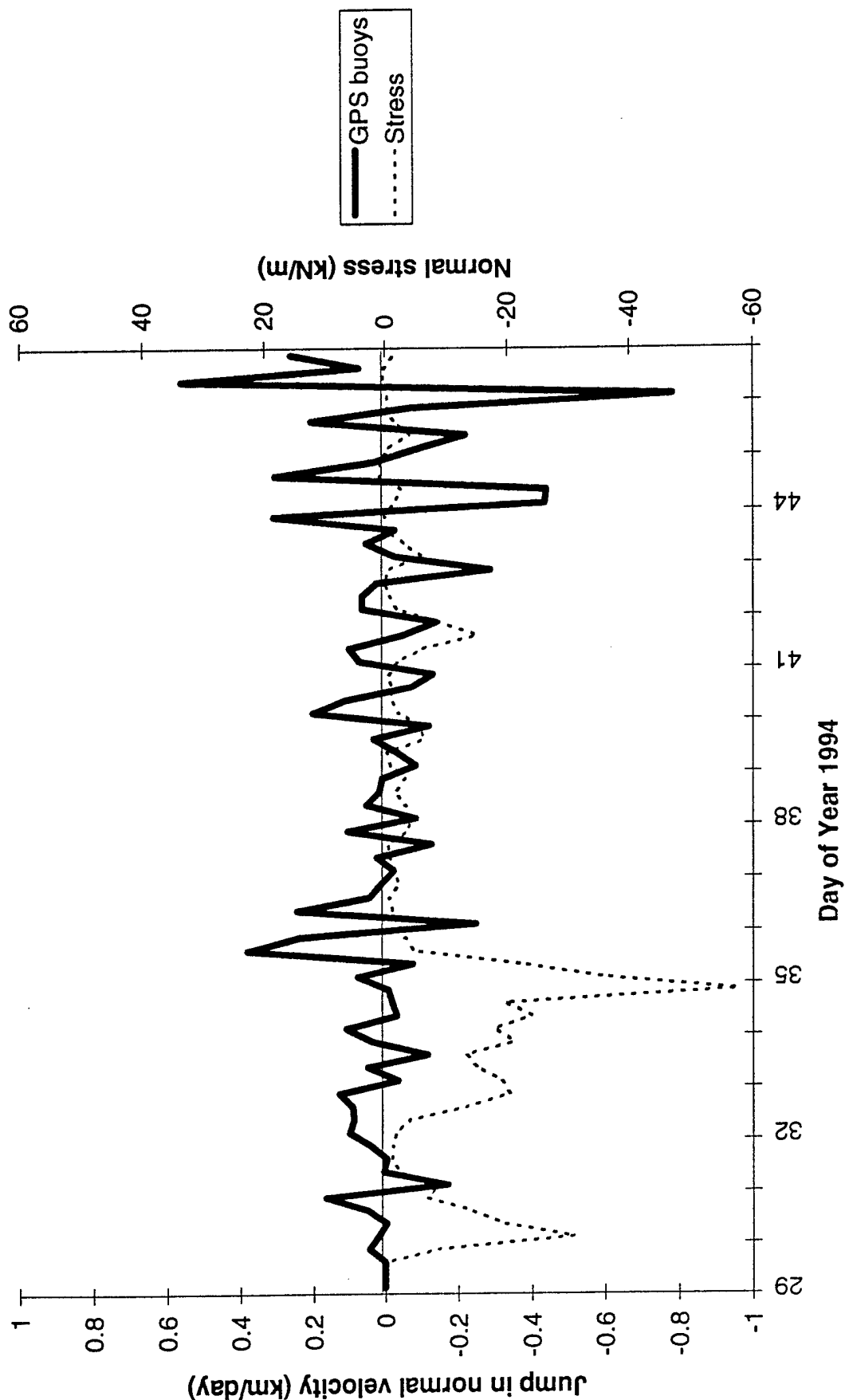
Sea ice stress was measured in Floe 4 in three directions in the horizontal plane using flatjack ice stress sensors. Coordinate transformations of 6-hour averaged data yield the parallel, normal, and shear stresses in lead coordinates shown below. The term 'raw ice stress' indicates that we have not included the effects of the inclusion factor of the stress sensor in the ice.

Shortly before the beginning of Day 35 (when the lead activity was apparent in the ice motion data), the ice stress state abruptly changed from biaxial compression to uniaxial compression. The traction on the active lead near zero for at least 11 days following lead creation. Note that there was compression in both directions when the lead was created at the beginning of Day 35, indicating shear failure of the pack ice, not tensile failure.



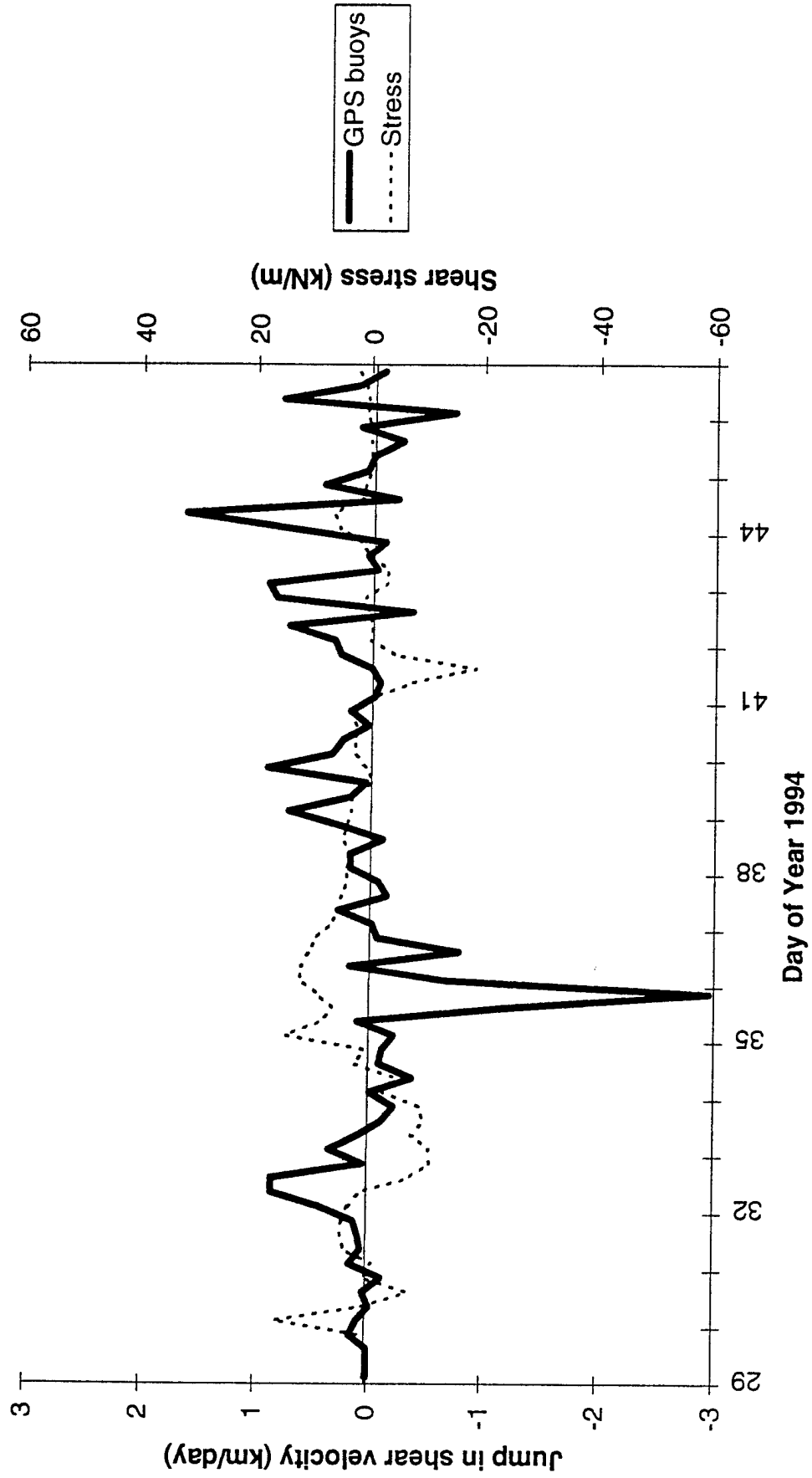
Normal Stress and Jump in Normal Velocity

The ice stress normal to the lead and the jump in ice velocity normal to the lead are plotted versus time. Positive motion is opening, and positive stress is tension. Ice stress normal to the lead plummets shortly before the lead opening is apparent in the ice motion data. The stress normal to the lead remained small (less than 20 kN/m) for the next 11 days.



Shear Stress and Jump in Shear Velocity

The ice shear stress and the jump in ice shear velocity are plotted versus time. During positive shear motion, the opposite side of the lead moves to the right. Positive shear stress has the same sense. The shear stress is generally small (less than 20 kN/m) for entire time period.



Acoustic Signatures of Falling Ice Blocks

R.S. Pritchard,
Y.Xie,
M.D. Farmer,
M.D. Coon,
G.S. Knoke,
and
D.C. Echert

AMD-Ice Mechanics, Vol. 207, ASME, 1995

ACOUSTIC SIGNATURES OF FALLING ICE BLOCKS

R. S. Pritchard
IceCasting, Inc.
Seattle, WA

Y. Xie and D. M. Farmer
Institute of Ocean
Sciences
Sidney, BC
CANADA

M. D. Coon, G. S. Knoke, and
D. C. Echert
Northwest Research Associates, Inc.
Bellevue, WA

ABSTRACT

During the April 1994 Sea Ice Mechanics Main Field Experiment, we conducted a set of *controlled-load* tests to mimic the small-scale processes that are active during the formation of rafts and ridges. Each test approximated the behavior of *in situ* sea ice, except that each process was isolated and the loading was artificially applied. In this paper we report results of the tests in which blocks of ice were dropped onto the ice sheet.

The acoustic signals emitted were separated into the forced acoustic wave generated by the first impact and the flexural oscillation of the floating ice sheet. For the forced impact, the total radiated acoustic energy is proportional to the kinetic energy at impact. When the ice sheet is bare (no snow cover), the ratio is about 11×10^{-6} . With a 1.3-1.5 cm snow cover, the ratio is about 2×10^{-6} . Variations in block size and ice sheet thickness are less important than the impact energy. The spectra were also determined for all tests. The snow cover reduced sound amplitude above 200 Hz by about 10 dB.

INTRODUCTION

As a ridge builds, there are numerous small-scale processes that occur: the ice sheet is bent, buckled, crushed, and cracked, blocks pile up and down, these same blocks tumble down and up along the sail and keel, blocks splash into the water, blocks are pushed over and under the ice, and the ice rafts. This last process is separated from over and under-ride because the ice blocks (and ice sheet) are pushed up and downhill, and the amount of wetness differs between over-ride and under-ride. It is difficult to quantify the physical processes that contribute to the noise generated during formation of a ridge because these processes occur simultaneously and in unknown amounts.

Of these processes, cracking has received extensive study (*e.g.* Stein, 1993). Our focus is on the other processes. Furthermore, when we listen to under ice noise, it is not cracking that dominates, but instead it is blocks falling against the ice sheet, and blocks sliding over and/or under the ice sheet, and rafting of ice sheets.

As one component of the April 1994 Sea Ice Mechanics Main Field Experiment (e.g., Coon et al., 1995, Xie and Farmer, and Pritchard, 1995), we conducted a set of *controlled-load* experiments. Each experiment approximated the behavior of *in situ* sea ice, except that one process was isolated and the loading was artificially applied. The *controlled-load* experiments included over-ride, under-ride, rafting, flopping, dropping, underwater bumping, and splashing. Each of these processes occurs during the formation of a ridge or raft. Each type of test is now described more completely: *over-ride* - towed a cold ice block over the surface of the intact ice sheet; *under-ride* - towed a warm ice block under the intact ice sheet; *raft* - towed a warm ice block (freshly excavated from refrozen lead ice) up and over a cantilevered beam section of the ice sheet; *drop* - dropped a block of ice (both flat and at a 45 degree angle) onto the intact ice sheet; *flop* - tipped a standing block of ice over onto the intact ice sheet; *splash* - tipped a standing block of ice over into the water; *bump* - allowed a submerged block of ice to float up and bump against the underside of the ice sheet; *cantilever* - lifted the free end of a floating cantilever beam until the beam failed in flexure; and *fracture* - split a floating ice sheet with air jacks.

Some of these processes affect the mechanical response of the ice, whereas all processes generate acoustic energy. The emission of waves from the impact is a valuable signal for probing the interaction process even though the emitted energy accounts for an extremely small amount of the input mechanical energy. The signal is useful from two points of view: it is readily measurable, and its signatures reflect the interaction process. The analyses of radiated signals allow possible reconstruction of such processes. Hydrophones, geophones, ice strain sensors, and ice tilt sensors were installed in arrays around the *controlled-load* tests.

The goal of this work is to understand the large-scale behavior of sea ice, and the noise emitted as it moves and deforms. The large-scale process that dominates ice behavior on this scale are rafting and ridging. Therefore we focus on these processes. Rafting is also a precursor to ridging. With better understanding of the small-scale mechanical processes that contribute to ridging and of the acoustic signals that are emitted by these processes, we hope to develop better models of ambient noise under the ice and inversely to use sound measurements as a gage to measure ice behavior. We envision a library of probability distribution signatures in phase space corresponding to the noise generation mechanisms. A general Arctic noise time series of an ice deformation event could then be partitioned into the library of events. The converse may also be possible, that is, to generate artificial or predictive time series of ambient noise that include the appropriate proportions of library signatures.

Here we present the acoustic signatures of these drop and flop tests. We estimate the acoustic emissions from individual processes, the spectral densities, and the ratio of total radiated acoustic energy to the mechanical input energy. The falling blocks studied here result from rearrangement of blocks in the ridge sail during the ridge building process. This redistribution was first modeled by *Parmerter and Coon* (1972) to match the angle of repose. The potential energy of the ridge was then incorporated explicitly by *Rothrock* (1975) into the Aidjex model. This and other energy measures were then used by *Pritchard* (1984, 1990) as a proxy variable for describing ambient noise generated by ridging. Finally, *Hopkins* (1994) estimated the energy balance during ridge building using a discrete element model of the forces acting on individual ice blocks in the ridge.

ACOUSTIC DATA ACQUISITION AND ANALYSIS

To investigate radiated energy from small-scale ice processes, an array of geophones and hydrophones were deployed at both East and West test sites from the Main camp. Figure 1 is a sketch of aerial view of the array deployed at East Camp. This array consisted of five tri-axial geophones (frozen into the ice surface) and the five omni-directional hydrophones (deployed at 5-m depth in the water). The maximum spacing of the array was approximately 30 meters. We are reporting on twelve tests at this site. A similar array was deployed on the West site. However, the West site array had a much greater maximum spacing of up to 200 meters; the hydrophones were deployed at 20-meter water depth. We are reporting on four tests at this site. Detailed descriptions of these arrays can be found in *Xie and Farmer* (1994a, 1995), *Coon et al.* (1995), and *Pritchard* (1995). For each test, acoustic and seismic emissions were digitally recorded on VHS tape.

To interpret the mechanical waves recorded on a sensor some distance away from the impact point, one must understand how the seismic and acoustic waves propagate in the Arctic environment. There have been extensive studies on various wave propagation mechanisms in the Arctic ocean (see *Stein*, 1993, *Xie and Farmer*, 1994b). There are two propagation channels for mechanical waves generated by the ice process: the floating ice sheet and acoustically up-refractive water column. The ice sheet guides various elastic waves in the ice. The water column provides signal channels for acoustic waves coupled into the water from the impacted local ice; it also allows the leakage of elastic waves from the ice sheet into the ocean. It has been shown that the characteristics of the guided elastic waves are mainly determined by the mechanical properties of the ice and its geometry, especially the

thickness. The elastic waves relevant to the present study are flexural waves, P-waves and SH-waves. The acoustic wave that is coupled directly from the ice impact has a signature that is affected both by the local ice properties and, most importantly, by the interaction process between the falling block and the ice sheet. It is the acoustic wave that provides more valuable information on the interaction process.

Both the SH-wave and flexural waves are trapped in the ice and upper water column due to horizontal polarization and subsonic phase velocities, respectively. However, P-waves leak into the water column in an efficient manner governed by Snell's law. Acoustic waves can propagate for a long distance (of order 10 km in a 500 meter deep water column) before being reflected from the bottom of the ice sheet. A layer of sea ice enriches the physics of underwater sound field in the Arctic ocean by projecting various elastic waves into the ocean. The co-existence of elastic (leaked from the ice) and acoustic (coupled directly from local failure processes in the ice) waves complicates the underwater sound field especially in the upper water column. From a signal detection point of view (in the water), one observes different signal structures arriving at different times, corresponding to the above described wave-process. With these theoretical descriptions and understandings of seismic and acoustic processes, we can examine the observed signals.

The total radiated acoustic power assuming a dipole distribution is

$$RA(t) = \int \frac{|p|^2}{\rho c} ds \quad (1)$$

where $p(r, \theta) = p_o \cos \theta / r$, ρc is acoustic impedance, θ is the radiation angle, p_o is source pressure observed at range r , and s is the spherical radiation area at range r . The total radiated acoustic energy is

$$TRAE = \int RA(t) dt \quad (2)$$

which can be rewritten using Parseval's equality as

$$TRAE = \int \frac{\cos^2 \theta}{r^2 \rho c} ds \cdot \left| 2 \int_0^\infty |\hat{p}_o(f)|^2 df \right| \quad (3)$$

where $\hat{p}_o(f)$ is the Fourier transform of $p_o(t)$.

RESULTS

On 8 April 1994 twelve drop tests were conducted at the East Camp and on 22 April 1994 four tests were conducted at West Camp. In each test a block of ice was either set on its edge and tipped so that it flopped onto its side or it was dropped onto the ice sheet. On 8 April the ice sheet was 0.25 m thick, it was covered by 1.3 cm of snow (although this was scraped off for some of the tests), temperature of the upper surface (under the snow) was -16.4 C, and the air temperature was -20 C. On 22 April the ice sheet was 0.51 m thick, covered by 1.5 cm of snow, and air temperature was -12.3 C.

A falling ice block dissipates its initial potential energy by interacting with the surrounding ice fields before reaching the minimum energy level. One of the common interacting modes is the impact of these free-fall ice blocks onto the surface of the underlying ice sheet. *Xie and Farmer (1994b)* found that a weight (an 11-kg lead ball) dropped onto a 2-meter thick first-year ice sheet created a dipolar acoustic source beneath the ice. Very small fractions of the total potential energy were radiated out from the impact as acoustic waves in the water column and flexural waves in the ice sheet. This implies that most potential energy of a falling weight is dissipated by deforming the local ice at the impact.

Figure 2 shows a time series of the acoustic signals for Test 8-1: an ice block flopping onto a snow-covered ice sheet. These signals were recorded by the array of five hydrophones deployed at the East site (see Figure 1). Since the impact occurred very close to H_1 (about 6 meters in range), the signal saturated this channel precluding estimation of acoustic source levels from this phone. Figure 3 is the acoustic signal due to a similar flopping test (Test 8-2) except that snow was cleared off from the ice surface before the test. These signals are discussed in the following three paragraphs.

The nearest hydrophone (H_1) was saturated for most tests. Channel H_2 was used for most analyses because it was farthest from the impact site and its signal had the best separation of acoustic and flexural waves. However, to see the flexural wave, we must look at H_3 or another hydrophone because the large, heavy data acquisition boxes were located along the path to H_2 , which reduced its flexural wave signal. We are interested primarily in

the dipole acoustic wave generated by the first impact because it propagates farther than the other signals.

The acoustic emissions recorded near the source by H_1 and shown in Figures 2 and 3 reveal that the impact generated two different vibrational responses in the ice sheet. These are motions forced by the impact and, subsequently, by the flexural response of the ice sheet. The impulse due to the forced motion couples directly into the water column and propagates at a speed of 1438 m/s in the water (we call this impulse signal the acoustic wave). Motions due to the flexural response of the ice spreads out as flexural waves from the impact point to the surround ice field (we call this flexural signal the seismic wave). Being an evanescent wave, the flexural motion is restricted in the ice sheet and upper water column. The wave travels in the ice at anomalously dispersive group speeds significantly lower than the sound speed in the water. Due to the shallow depths of the hydrophones, flexural wave signals can still be detected on these hydrophone channels. The speed difference between the acoustic wave (due to the initial impact) and flexural waves separates the arrivals of the two signals as they propagate. This effect is clearly illustrated by the wave signals recorded on channel H_3 in Figure 2: the acoustic signal arrives 58.7 ms ahead of the flexural wave, which yields a flexural group speed of 217 m/s. The dominant flexural wave frequency is estimated to be 20 Hz. This value is close to 250 m/s, a numerical result based on the dispersion curve obtained by Stein (1993). The signal amplitude is estimated from the first peak of the signal observed at hydrophone H_2 . This peak value is used to help isolate the flexural wave. The TRAE levels are presented in the Table I. The ratio of total radiated acoustic energy to the input energy is also presented.

The flop tests on snow-covered surface generated very little high-frequency acoustic radiation in the water. This implies that the snow layer makes the impact a soft landing on the ice sheet, absorbing high-frequency energy. Figure 2 shows the spectrum for a block flopping onto a snow-covered ice sheet and Figure 3 shows the spectrum for a block flopping over onto a bare ice sheet. The primary difference is the 10 dB reduction in sound above about 200 Hz.

The unique feature for falling tests is that the acoustic signatures radiated from these tests are more variable from test to test. Figure 4 shows the acoustic signals from a flat-dropping block. The signal consists of processes due to both forced motion by the impact and the flexural response of the ice sheet. However, the initial signal is no longer a single pulse but has a multi-pulse structure because the block shattered when it impacted the ice sheet. When falling at an angle, the ice block generated an even more complicated signal structure. An example is shown in Figure 5 where the signal due to forced motion is characterized by multiple pulses because the falling block bounced and shattered when it impacted the ice sheet. It is interesting to note that no significant flexural waves were excited by this impact.

For each test, block properties are presented in the Table I. These properties include: block size and shape (length L , width B , thickness H , and weight $W=Mg$, where M is mass), presence of snow, initial and final height of the center of gravity. The block sizes were representative of blocks observed in ridges (Tucker and Govani, 1981). The total energy input during each test is defined by the potential energy change $PE = PE_i - PE_f$, where potential energy at the beginning of the test was PE_i , potential energy at the end of each test was $PE_f = WH/2$. The kinetic energy at the moment of first impact was KE . For the flop tests, initial potential energy was

$$PE_i = \frac{W}{2}(L^2 + H^2)^{1/2}. \quad (4)$$

For the drop tests, initial potential energy was $PE_i = WZ$, where Z was the initial height of the center of gravity of the block. Kinetic energy at impact for the flop tests equals the change in potential energy. Kinetic energy at initial impact of blocks dropped flat onto the ice equals the difference between initial and final potential energy

$$KE = PE_i - PE_f \quad (5)$$

For blocks dropped from an initial angle of 45 degrees, the kinetic energy was equal to the difference between initial potential energy and potential energy at impact

$$KE = W(Z - \sqrt{2}(L+H)/4). \quad (6)$$

Table I. Parameters for Drop and Flop Tests.

Test No.	Test Type	L (m)	B (m)	H (m)	M (kg)	Snow	Initial CG Z(m)	Final CG (m)
8-1	Flop	0.50	0.50	0.25	60	Yes	0.28	0.13
8-2	Flop	0.50	0.50	0.25	60	No	0.28	0.13
8-3	Flop	1.00	0.50	0.25	120	No	0.52	0.13
8-4	Flop	0.53	0.51	0.10	24	No	0.27	0.05
8-5	Drop Flat	0.53	0.51	0.24	58	Yes	0.43	0.12
8-6	Drop Flat	0.53	0.51	0.24	58	No	0.73	0.12
8-7	Drop 45	0.48	0.51	0.24	56	No	0.61	0.12
8-8	Drop Flat	0.53	0.51	0.25	62	No	0.43	0.13
8-9	Drop Flat	0.43	0.36	0.06	9	No	1.25	0.03
8-10	Drop 45	0.51	0.46	0.10	24	No	1.22	0.05
8-11	Drop 45	0.53	0.51	0.08	24	No	0.61	0.04
8-12	Drop 45	0.99	0.53	0.10	49	Yes	0.91	0.05
22-4	Flop	0.51	0.48	0.07	15	Yes	0.26	0.03
22-5	Flop	0.49	0.50	0.15	38	Yes	0.26	0.08
22-6	Flop	0.51	0.48	0.07	15	No	0.26	0.03
22-7	Flop	0.49	0.50	0.15	38	No	0.26	0.08

Table II. Total Radiated Acoustic Energy (TRAE), Potential Energy (PE), and Impact Energy (KE) for Drop and Flop Tests.

Test No.	Test Type	PE (J)	KE (J)	TRAE (J)	TRAE/PE $\times 10^6$	TRAE/KE $\times 10^6$	Comments
8-1	Flop	89	89	0.000444	5.00	5.00	AE+Flexure
8-2	Flop	89	89	0.001034	11.64	11.64	AE+Flexure
8-3	Flop	459	459	0.004053	8.83	8.83	AE+Flexure
8-4	Flop	52	52	0.001171	22.50	22.50	AE+Flexure+1 bump
8-5	Drop Flat	172	172	0.000419	2.43	2.43	Double Impact
8-6	Drop Flat	344	344	0.002572	7.47	7.47	AE+Flexure+1 bump
8-7	Drop 45	268	194	0.001907	7.13	9.83	3 Impacts
8-8	Drop Flat	186	186	0.002341	12.60	12.60	AE+Flexure
8-9	Drop Flat	114	114	0.000961	8.44	8.44	AE+Flexure
8-10	Drop 45	275	237	0.000786	2.85	3.32	AE + Multi-bump
8-11	Drop 45	135	93	0.000277	2.06	2.98	AE + Multi-bump
8-12	Drop 45	419	256	0.000264	0.63	1.03	Multiple Impact
22-4	Flop	34	34	0.000010	0.29	0.29	AE
22-5	Flop	67	67	0.000055	0.82	0.82	AE
22-6	Flop	34	34	0.000516	15.15	15.15	AE + small bump
22-7	Flop	67	67	0.000985	14.70	14.70	AE + small bump

Parameters listed in the Table I were varied in an attempt to understand the physical behavior of falling blocks of ice. It was our desire to understand which variables affected the sound emitted and to quantify these effects.

All blocks dropped onto bare ice broke (tests 8-2 through 8-4, and 8-6 through 8-11). This was true whether flopped or dropped flat or at an angle. One result of such breaking was to generate multiple impacts from all pieces of the block, rather than clean single or double impacts when dropped flat or at an angle. Although the block in test 8-5 was initially level, it was dropped at an (unknown) angle, which caused a double impact. Test 8-7 was dropped at an angle and produced two distinct impacts; first when the edge hit the ice sheet, and second when it flopped over flat.

We assume that a relationship exists between the total energy radiated by the acoustic waves and the energy input by dropping the block, and we test this hypothesis. The energy available from dropping the block is easily estimated by calculating the change in potential energy before dropping the block and the instant it impacts the ice sheet. This calculation is somewhat different for the various geometries.

The *TRAE* is compared directly with the impact kinetic energy (*KE*) in Figure 6. Open symbols indicate ice blocks falling onto snow-covered ice; black symbols onto bare ice. Different symbol shapes have been used to identify the different kinds of tests (flat drop - square, drop at 45 degrees - diamond, and flop - triangle). For all drops on a bare ice sheet, the average ratio of *TRAE* to potential energy was 11×10^{-6} . Two data points (tests 8-10 and 8-11) had lower ratios. Both of these ice blocks shattered, which likely cause the lower *TRAE* values. When snow is present, the average ratio of *TRAE* to potential energy is reduced to 2×10^{-6} . These results appear to be consistent over the full range of impact energy.

The data were also examined for correlations with block area, mass, test type, and angle of the drop. None were as strong as variations with snow cover. We recognize of course that this is a small test set, and definitive correlations are difficult. For the lead ball used by *Xie and Farmer* (1994a), the average ratio of *TRAE* to potential energy was about 20×10^{-6} , so that ice blocks are less than half as efficient at generating acoustic energy as the idealized spherical lead ball. We noted earlier that these block sizes are representative of ice blocks found in ridges. We note here that the range of distances from which they were dropped (0.15-1.22 m) is also representative of distances that blocks fall during ridging. We have also compared the total change in potential energy, but the ratio between *TRAE* and *PE* is not as consistent as is the ratio of *TRAE* to *KE*.

CONCLUSION

Sixteen tests were conducted in which ice blocks were either dropped or flopped onto the ice sheet. The acoustic signals emitted were separated into the forced acoustic wave generated by the first impact and the seismic wave generated as a flexural oscillation of the floating ice sheet. We focused analysis on the acoustic wave that has approximately a dipole pattern. It propagates to longer ranges than does the flexural wave.

When the ice blocks were dropped at an angle, several distinct impacts observed. When the blocks were dropped onto bare ice they broke, which also generated multiple impacts.

The total radiated acoustic energy was found to be proportional to the kinetic energy at impact. When the ice sheet was bare (no snow cover), the ratio was about 11×10^{-6} . With a 1.3-1.5 cm snow cover, the ratio was about 2×10^{-6} . Variations in block size and shape appeared to be less important than the impact energy. There was no apparent dependence on ice sheet thickness (over the range 0.25-0.51 m) for the first impact acoustic signal studies here. We would expect such a dependence to exist for the flexural wave. The spectra were also determined for all tests. The snow cover reduced sound amplitude above 200 Hz by about 10 dB.

These results suggest that a model could be developed to describe the acoustic emission from the blocks falling during formation of a ridge. The model would require that we estimate the kinetic energy available for blocks falling onto the ice sheet and the probability distribution of events, but these variables can be estimated from modern ice dynamics models.

ACKNOWLEDGMENTS

This study was funded by the Office of Naval Research (ONR) under contracts N00014-C-92-0052 to IceCasting, Inc., N00014-J-92-1256 to the Institute of Ocean Sciences, and N00014-C-92-0027 to NorthWest Research Associates, Inc. All authors greatly appreciate the encouragement and support given by Dr. T. B. Curtin, ONR High Latitude Team Leader. We also thank A. Heiberg, J. Ardai, D. Stewart, and S. Vorhees for their support in the field.

REFERENCES

- Coon, M. D., Knoke, G. S., and Echert, D. C., *Sea Ice Mechanics Research*, presented at Sea Ice Mechanics and Arctic Modeling Workshop, Anchorage, April 25-28, 1995.
- Farmer, D. M., and Xie, Y., *Acoustic and Seismic Studies of Ice Mechanics*, presented at Sea Ice Mechanics and Arctic Modeling Workshop, Anchorage, April 25-28, 1995.
- Hopkins, M. A., "On the Ridging of Intact Lead Ice," *J. Geophys. Res.*, vol. 99, pp. 16351-16360, 1994.
- Parmerter, R. R., and Coon, M. D., "Model of Pressure Ridge Formation in Sea Ice," *J. Geophys. Res.*, vol. 77, pp. 6565-6575, 1972.
- Pritchard, R. S., "Sea Ice Noise-Generating Processes," *J. Acoust. Soc. Am.*, vol. 88, no. 6, pp. 2830-2842, 1990.
- Pritchard, R. S., "Arctic Ocean Background Noise Caused by ridging of Sea Ice," *J. Acoust. Soc. Am.*, vol. 75, pp. 419-427, 1984.
- Pritchard, R. S., "Sea Ice Failure Mechanisms," presented at Sea Ice Mechanics and Arctic Modeling Workshop, Anchorage, April 25-28, 1995.
- Rothrock, D. A., "The Energetics of the Plastic Deformation of Pack Ice by ridging," *J. Geophys. Res.*, vol. 80, no. 33, pp. 4514-4519, 1975.
- Stein, P. J., "Prediction and Measurements of the Directivity of a Monopole Source in a Floating Ice Plate," in *Natural Physical Sources of Underwater Sound (2)*, ed. B. Kerman, Kluwer Academic Press, Norwell, MA, 1993.
- Tucker, W. B., III, and Govani, J. W., "Morphological Investigation of First-Year Sea Ice Pressure Ridge Sails," *Cold Regions Science and Technology*, No. 5, pp. 1-12, 1981.
- Xie, Y and D. Farmer, *Acoustic and seismic perspective of ice events observed in SIMI '94 Experiment A* report to the Office of Naval Research, published at Institute of Ocean Sciences, Sidney, BC, Canada, December, 1994a.
- Xie, Y. and D. M. Farmer, "Seismic-acoustic Sensing of sea ice wave-mechanical properties," *J. Geophys. Res.*, Vol 99, No. C4, pp 7771-7786, 1994b.

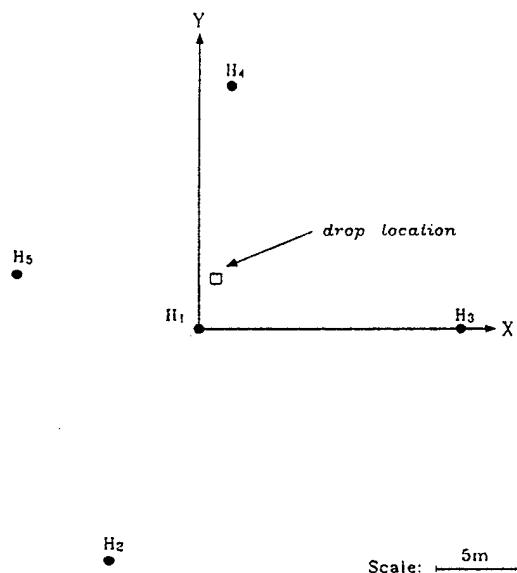


Figure 1. Hydrophone Array at SIMI East Camp.

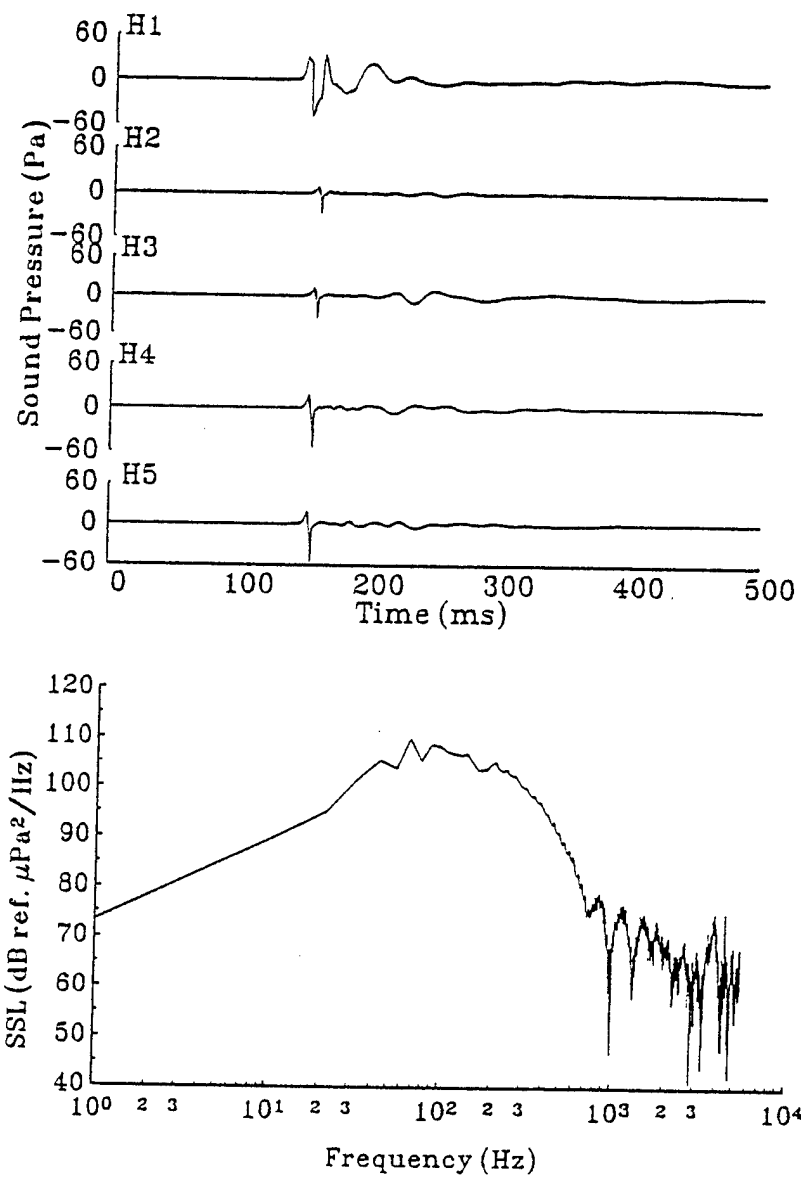


Figure 2. Sound Emitted by Ice Block Flopping Onto Snow-covered Ice Sheet (Test 8-1). Top: Pressure History at Five Hydrophones. Bottom: Sound Spectrum Level (SSL) at Hydrophone H₂.

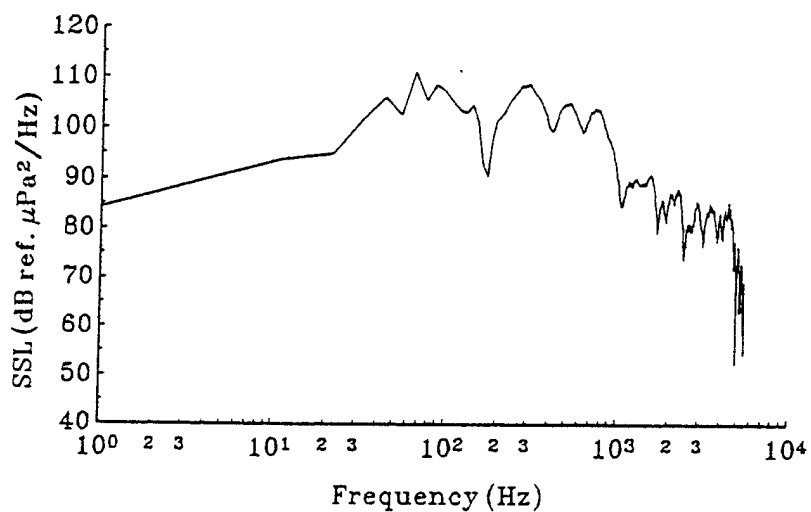
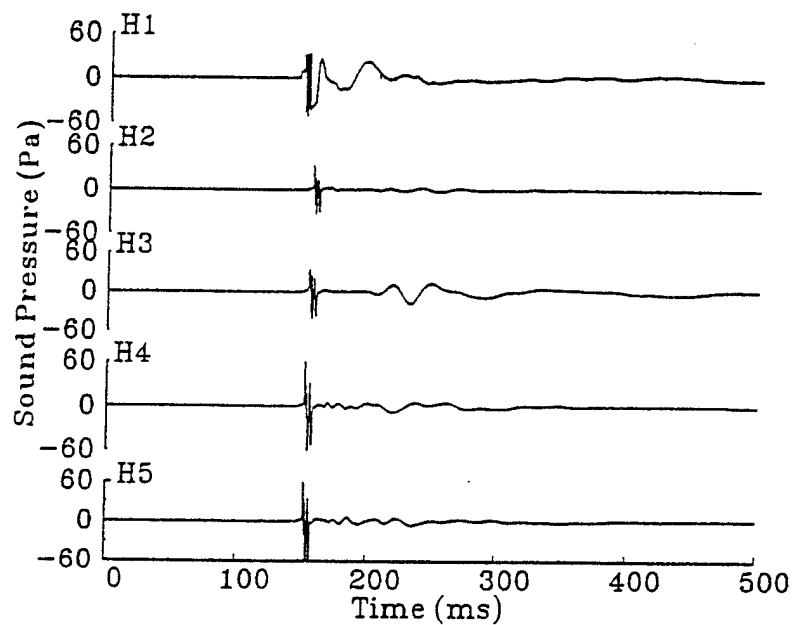


Figure 3. Sound Emitted by Ice Block Flopping Onto Bare Ice Sheet (Test 8-2). Top: Pressure History at Five Hydrophones. Bottom: Sound Spectrum Level (SSL) at Hydrophone H₂.

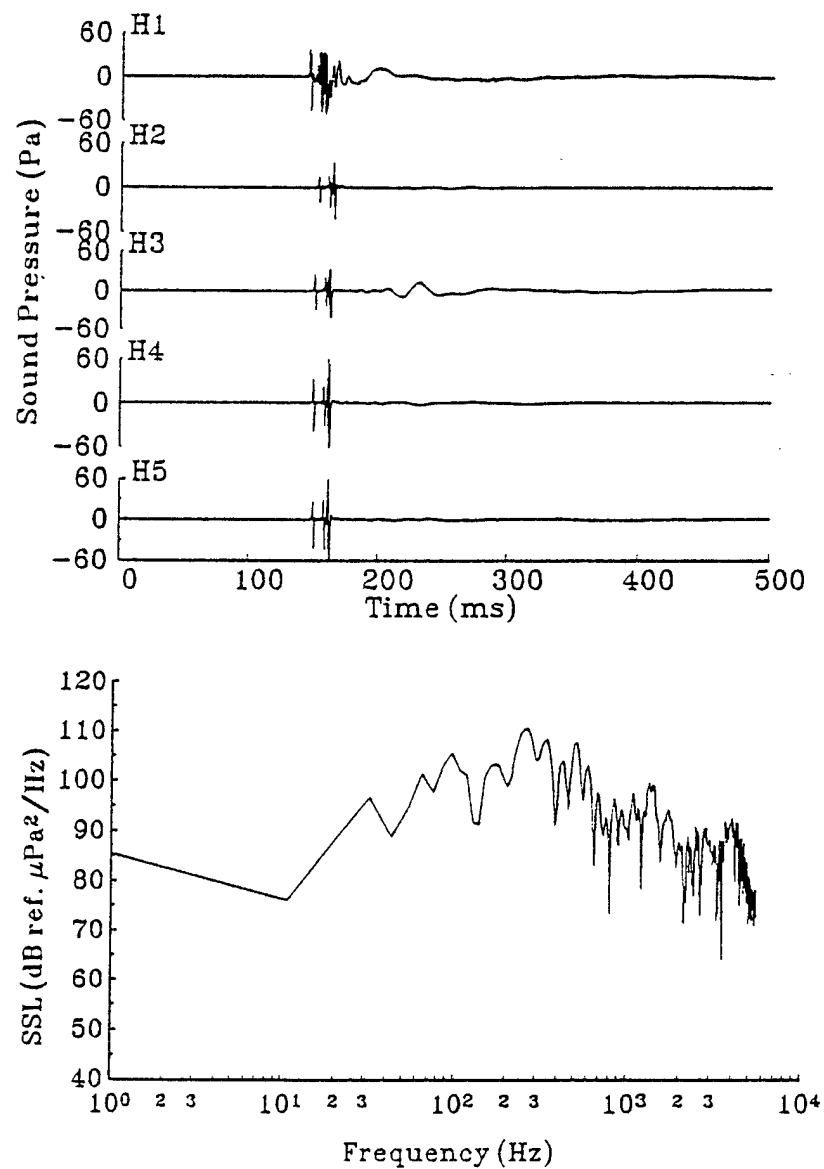


Figure 4. Sound Emitted by Ice Block Dropping Flat onto Bare Ice Sheet (Test 8-9). Multiple Impacts Result from Shattering of the Ice Block. Top: Pressure History at Five Hydrophones. Bottom: Sound Spectrum Level (SSL) at Hydrophone H₂.

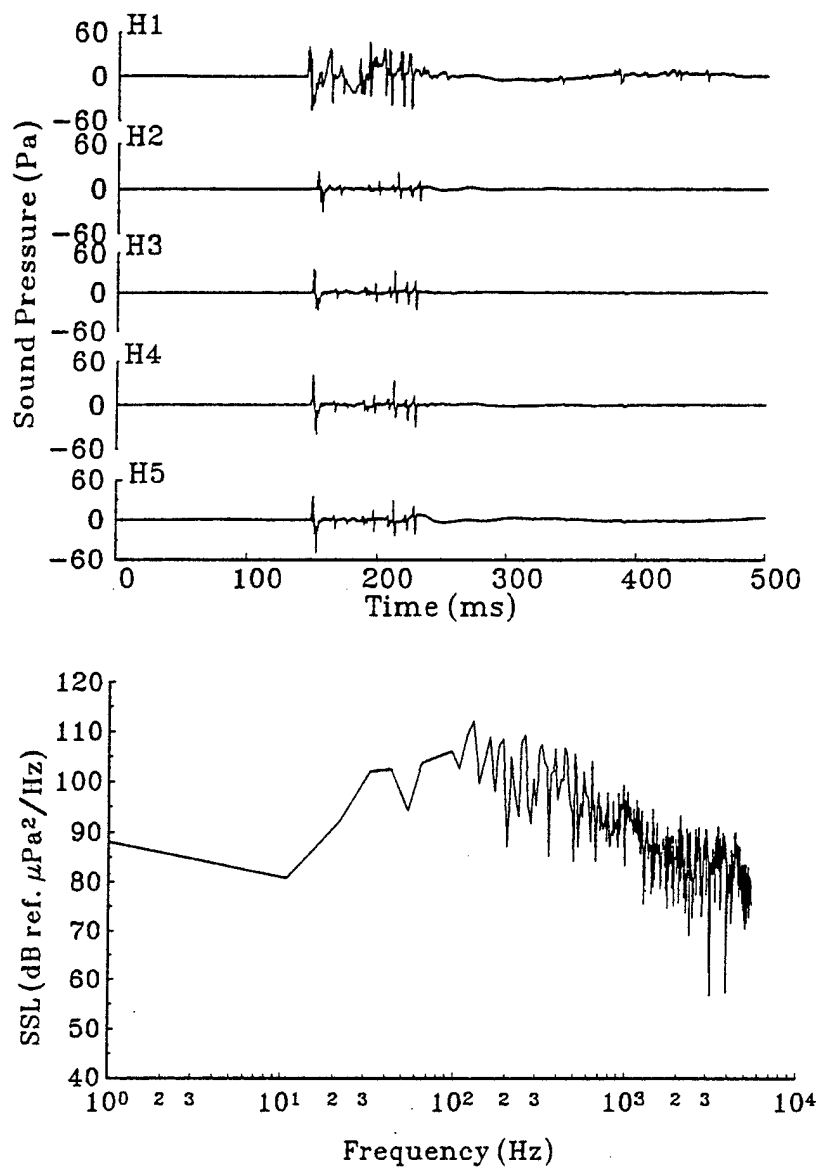


Figure 5. Sound Emitted by Ice Block Dropping at 45 Degree Angle onto Bare Ice Sheet (Test 8-10). Multiple Impacts Result from Initial Angle of Drop and Shattering of the Ice Block. Top: Pressure History at Five Hydrophones. Bottom: Sound Spectrum Level (SSL) at Hydrophone H₂.

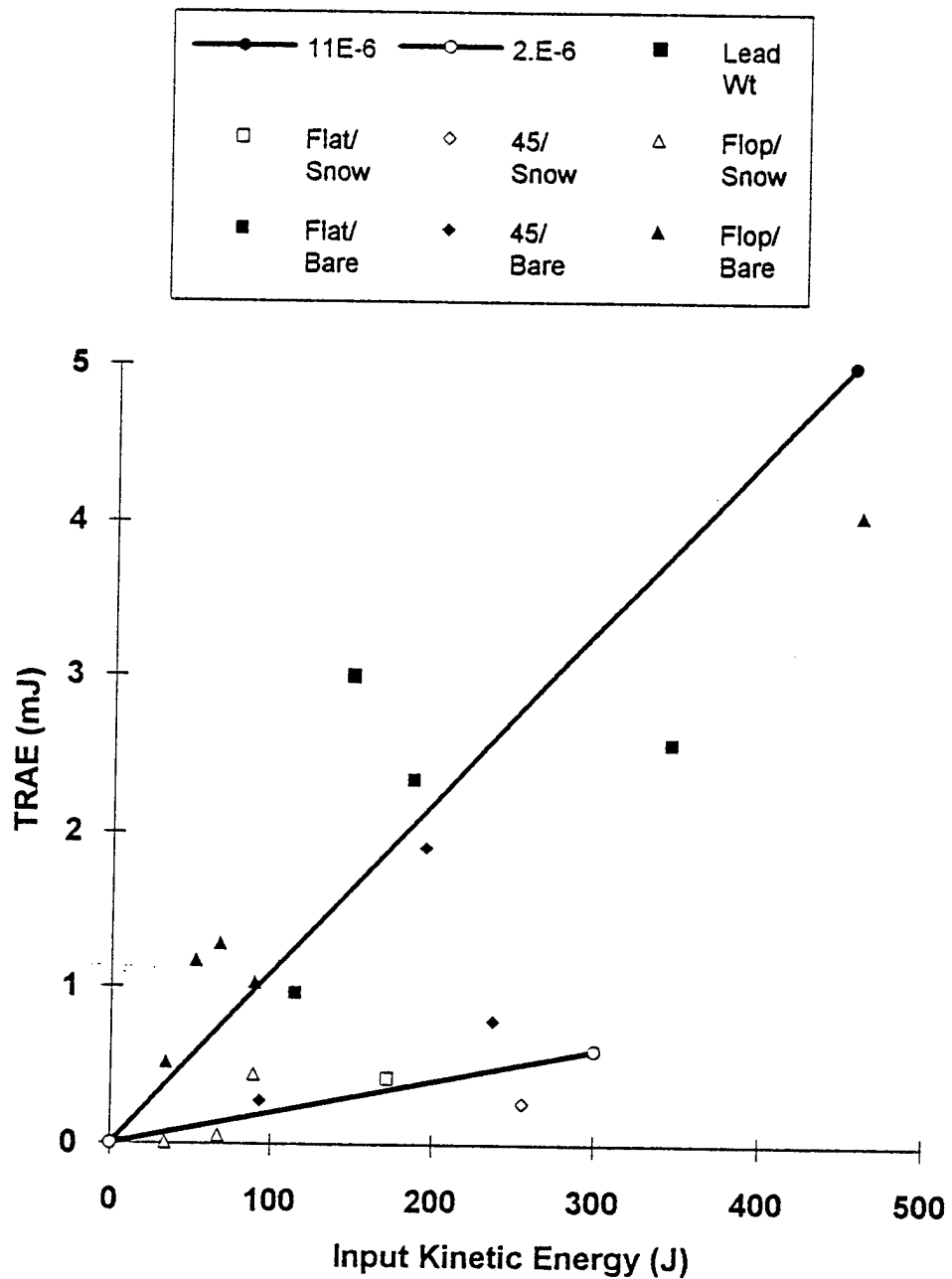


Figure 6. Relationship Between Total Radiated Acoustic Energy (TRAE) and Input Kinetic Energy (KE). Ice Blocks Dropped onto Bare Ice had a Ratio (TRAE/KE) of 11×10^{-6} . Ice Blocks Dropped onto Snow-covered Ice had a Ratio of 2×10^{-6} . A Lead Ball Weight had a Ratio of About 20×10^{-6} .

**Force-Displacement Measurements
of a First-Year Pressure Ridge Keel**

D.M. Coon,
D.C. Echert,
and
G.S. Knoke

AMD-Ice Mechanics, Vol. 207, ASME ,1995

FORCE-DISPLACEMENT MEASUREMENTS OF A FIRST-YEAR PRESSURE RIDGE KEEL

Max D. Coon
Douglas C. Echert
Gerald S. Knoke
Northwest Research Associates, Inc.
Bellevue, Washington

ABSTRACT

The strengths of the consolidated and partially consolidated parts of a first-year sea ice ridge keel may be the design parameters for structures to be placed in regions covered seasonally by first-year ice. These strengths are also important for large-scale ice dynamics models which can account for leads and discontinuous ice motion. The strength of a first-year, partially consolidated keel has not been measured with certainty because of the heterogeneous nature of the broken ice and the large size of the keel. The authors have developed and have performed an initial field test of a system to measure the strength of a first-year partially consolidated keel. The system consists of a wheeled chain saw, a 60x60x2-cm air jack (a stiffened rubber bladder), an air compressor, and an air pressure recorder. After removing a portion of the sail of the test ridge, the wheeled chain saw is used to cut a vertical slot into the keel for the air jack. Inflating the jack provides the pressure-displacement curve which in turn provides the limit load of plastic deformations of the keel, an index of keel strength. Four measurements were made on a small, first-year ridge in the Beaufort Sea during April of 1994. The maximum pressures were variable: 20, 40, 210 and greater than 700 kPa. Calculations of the load for a continuing motion solution based on laboratory test data on unconsolidated rubble resulted in a significantly smaller value than the measured limit load. We believe significant consolidation of the keel occurred in the two weeks between the ridging event and our tests. The fully consolidated layer between the sail and keel generally provides the majority of the ridge strength. Future work should include tests of a ridge in fall, winter, and spring to track strength with consolidation.

INTRODUCTION

Ice ridges can control the total load on structures in parts of the Arctic (Wang and Poplin, 1995). First-year ridges are also involved in the dynamics of pack ice through the ice thickness distribution (Thorndike et al., 1975) and, in models such as the oriented pack ice constitutive law, the large-

scale strength (Coon et al., 1992). The strength of ridges is as important as the ridge shape, frequency of occurrence, and keel depth because the strength is required to determine the load on a structure or ship as well as the amount of force that pack ice can transmit. Field measurements of ridge strength provide scale for laboratory measurements done on the friction and cohesion of broken ice in a shear box (Ettema and Schaefer, 1986; Ettema and Urroz, 1989; Keinonen and Nyman, 1978; Urroz and Ettema, 1987; Weiss et al., 1981; and Wong et al., 1987). For example, Prodanovic (1979) ran laboratory model tests to measure the shear strength and the simulated loads on cylindrical structures. Allyn and Wasilewski (1979) analyzed the strength of rubble fields in connection with artificial islands. The laboratory tests, however, are nearly always performed on unconsolidated ice blocks. As a ridge gradually changes from being unconsolidated through partially consolidated (as ours was) to a fully consolidated multi-year ridge, its strength increases.

This paper presents a description of the ridge tested (block size distribution, porosity, temperature, and salinity) followed by the test procedure, the test results, hindcast analysis, and discussion.

EXPERIMENT

The force-displacement measurements of a first-year pressure ridge keel were made about 500 km north of Prudhoe Bay, Alaska on April 14-16, 1994, with multi-year ice on both sides of the ridge and refrozen lead studied. The equipment for this experiment was tested in the fall of 1993, and data were collected in the spring of 1994 with modified equipment (see Coon et al., 1994). The strength of first-year ridged ice was measured using an air jack (a stiffened rubber bladder) to simultaneously load the ice and measure the displacement. In addition, we characterized the sail and keel geometry of a ridge formed from first-year ice, and inflated the air jack in four slots. The ridge configuration in the vicinity of the four air-jack slots was characterized by drilling 12 holes and with observations with an underwater camera.

The ridge was selected by searching the area around the SIMI East Camp from a helicopter, looking for a crisp, new, first-year ridge. The ridge was about 2 km from the SIMI camp, which was manned during the formation of the lead from which the ridge was built and during the ridge building.

Ridge data

Holes were drilled to establish the extent of the keel and refrozen lead ice. The lead ice had ridged against a multi-year floe, causing a large block of multi-year ice to fracture and tilt down. The refrozen lead ice had continued to grow thicker after the ridging event, which probably took place on March 30. After looking at the underside of the test area with an underwater video camera using poles inserted through other holes in the ice for visual reference, we cleared off some sail blocks and selected the locations for cutting slots for the air jack.

Block size distribution. Nearly all the blocks in a 100 block survey of the ridge sail had a thickness of 0.14 m. Their longest dimension averaged 0.49 m with a standard deviation of 0.29 m. Based on their average width, the block area averaged 0.20 m² with a standard deviation of 0.22 m². These results are typical for ridges built from first-year ice, falling between the two empirical fits provided in Tucker and Govoni (1981) on their Figure 10.

Porosity. To establish the location of voids in the keel near the air jack slots, three sets of holes were drilled and logged. Figure 1 shows the plan view of the slots and the holes; there are two rows of holes outside the test area and a set of holes drilled alongside the slots after the force-deformation tests. Figure 2 illustrates the locations of the voids in the two rows of holes. The sail is to the left in

these figures while the 0.46 m refrozen lead ice is to the right. Each hole drilled started with a hard, solid layer which averaged 0.56 m thick; at the bottom of that layer, we hit softer ice or a void. After the force-deformation tests, the holes shown in Figure 3 were drilled and logged. Hole numbers 12 and 13 were drilled alongside the slots for Tests 1 and 2; holes 14 and 15 alongside Test 3; and holes 16 and 17 alongside Test 4. The average porosity for all the holes was 25 to 35%, depending upon whether mushy soft ice is considered as solid ice or void. These results are similar to those of Frederking and Wright (1982).

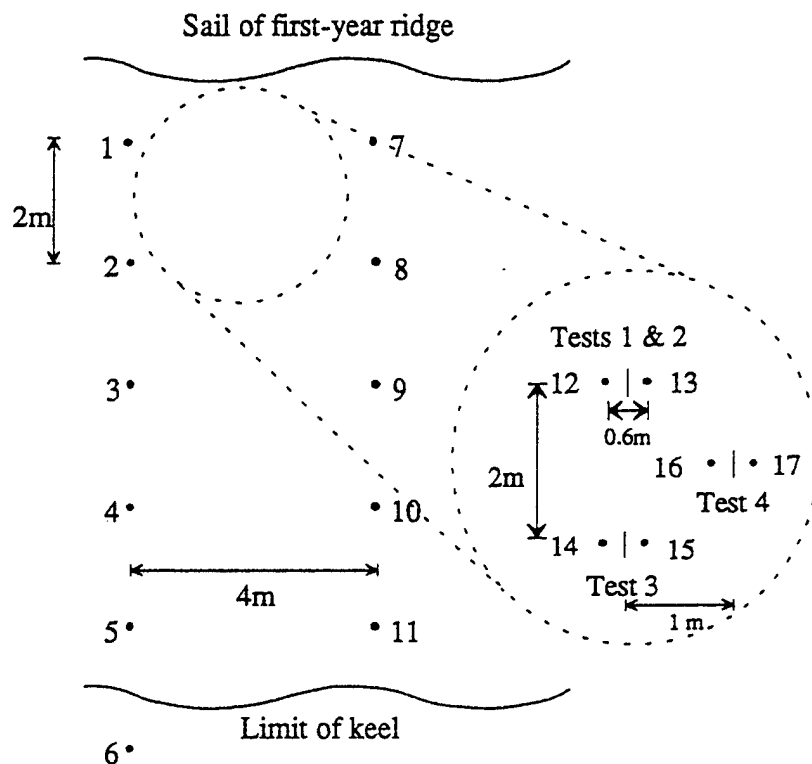


FIGURE 1. PLAN VIEW OF TEST SITE

The measured ice thicknesses in the refrozen lead and the ridge blocks were compared to values computed from ice camp temperatures using the formula for mean ice growth developed by Zubov (1944),

$$I^2 + 50I - 8R = 0 \quad (1)$$

in which I is the ice thickness in cm and R is the cumulative freezing degree days in °C-days using 0°C as a reference. As indicated in Figure 4, the lead was most likely formed during an ice motion event observed at the East Camp on March 26 and the ridge was probably formed during the storm and ice motion event observed at East Camp on March 30. The resulting ice thicknesses for the ridge blocks

are consistent with Zubov's formula. The formula under-predicted the lead ice thickness on April 14 by 17%.

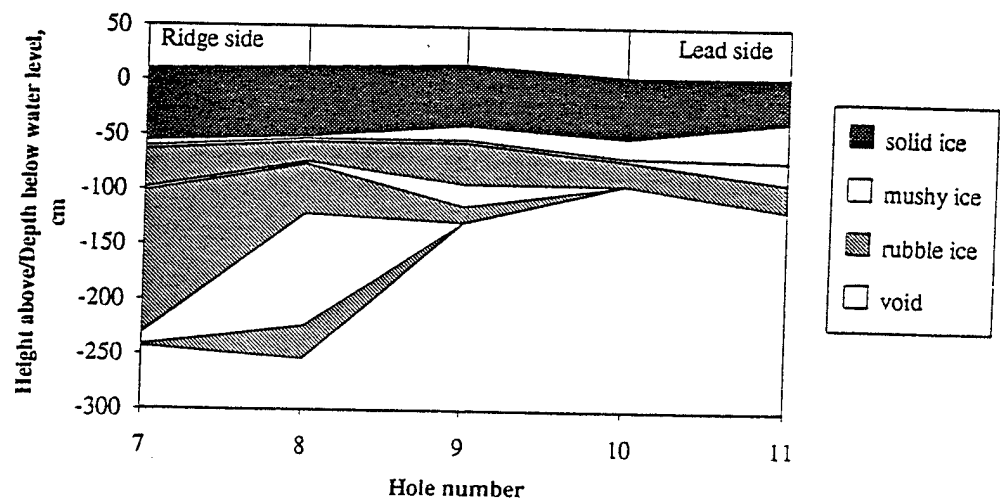
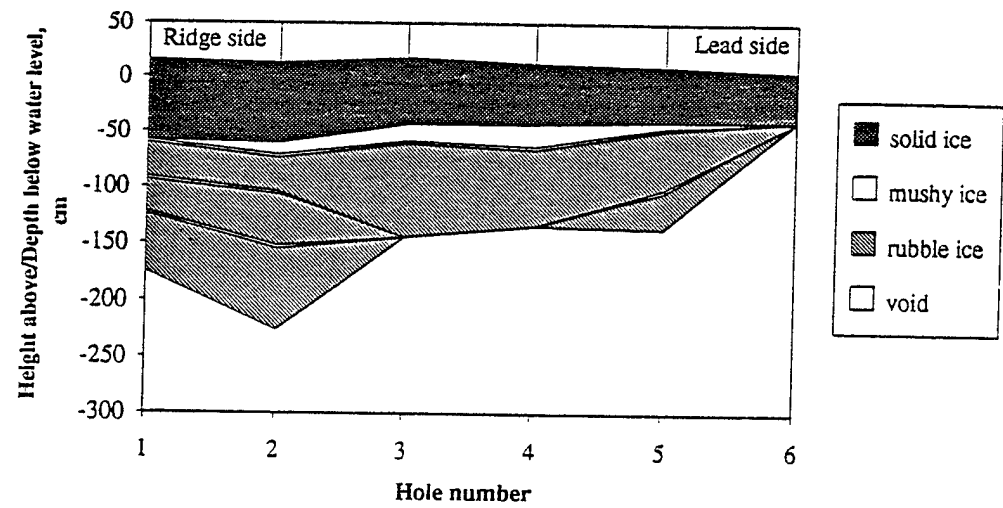


FIGURE 2. TWO KEEL CROSS-SECTIONS SHOWING VOIDS AS WHITE

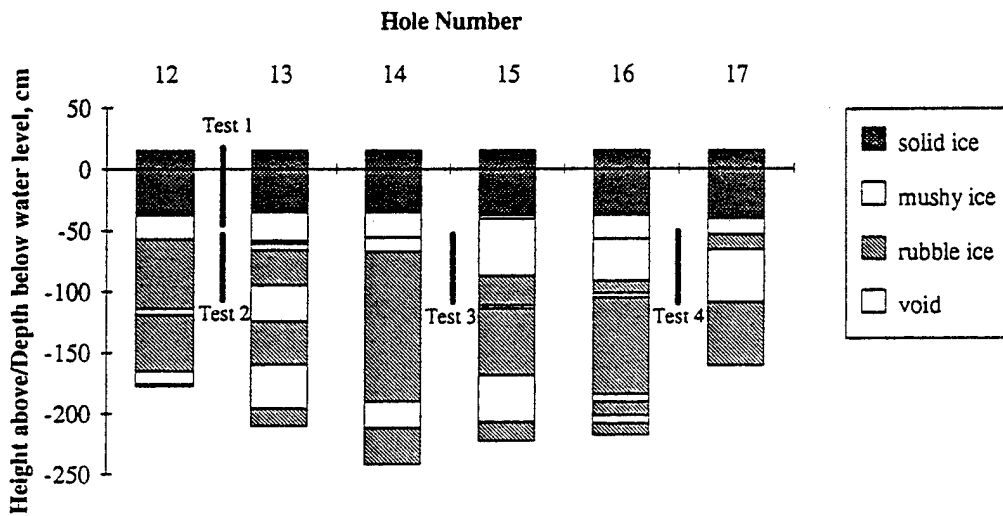


FIGURE 3. RELATIVE LOCATIONS OF THE AIR JACK TEST LOCATIONS AND THE SIX HOLES DRILLED ALONGSIDE THE AIR JACK SLOTS (VOIDS ARE SHOWN AS WHITE IN THE HOLES)

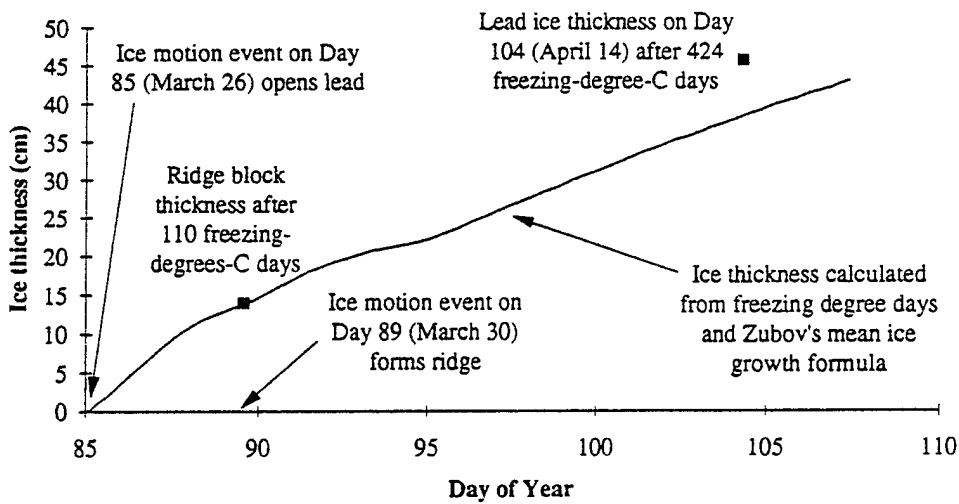


FIGURE 4. LEAD ICE THICKNESS IS CONSISTENT WITH OBSERVED ICE MOTION EVENTS

Temperature/salinity. Temperatures of blocks from the keel were measured with a thermistor; the results are provided in Table 1. The temperature measurements were obtained by drilling small holes into the ice blocks pulled from the first air jack slot, which extended down into the keel.

TABLE 1. TEMPERATURE AND SALINITY DATA

Location of reading	Temperature (°C)	Salinity (‰)
Sample from 15 cm below surface	-9.4	5.4
Sample from 40 cm below surface	-4.1	4.4
Sample from 75 cm below surface	-1.4	5.0

Salinity samples were taken from the same blocks; these results are also given in Table 1. A field study by Frederking and Wright (1982) indicate that 4-5 ‰ salinity is typical for submerged rubble.

Load tests

The load tests in the keel were performed with an air compressor inflating an air jack in a slot in the keel while recording the air pressure with a pressure transducer and a datalogger (see Figure 5). The air jack allowed a compact, light-weight system to deform the ice up to 30 cm (15 cm in each direction from the centerline) and measure the deformation. The test is analogous to the ice strength measurement test procedure described by Iyer and Masterson (1987) who froze thin-walled metal flat-jacks into multi-year ice to determine its strength.

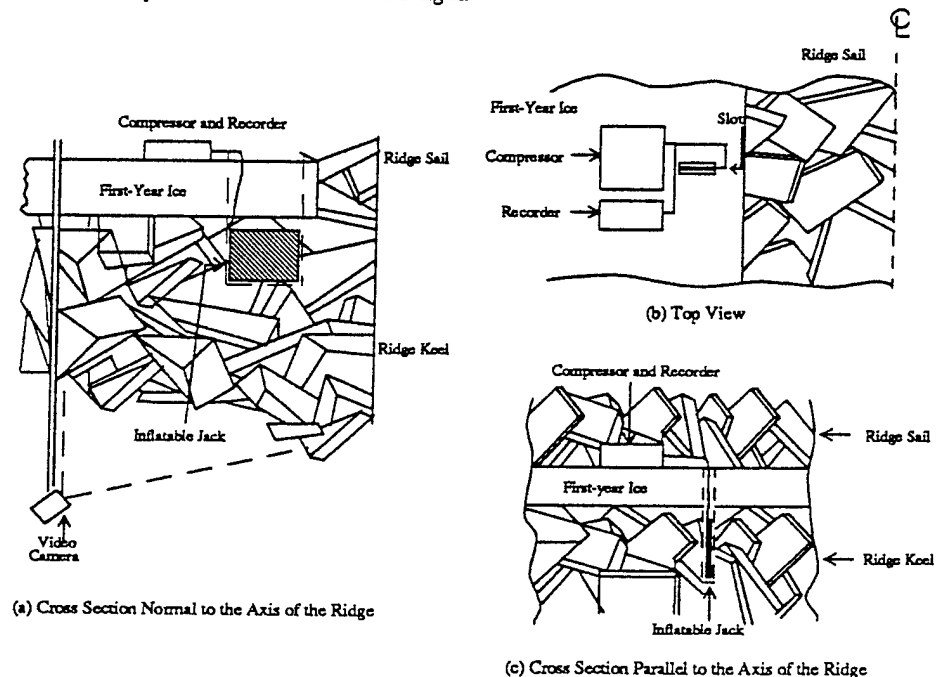


FIGURE 5. RIDGE STRENGTH EXPERIMENT

The jack displacement was derived from the compressor performance curve and the recorded pressure history by a series of laboratory calibration tests on the air compressor and the air jack. The slot for the air jack was cut with a modified wheel-mounted chain saw with a 1.5-m bar, as shown in Figure 6, made by the Ditcher Saw Company, Inc. Two cuts were made for each slot; the blocks of ice between were lifted from the slot for temperature and salinity measurements. From probing the slots, we know the slot cutting did not dislodge or free up the keel blocks.

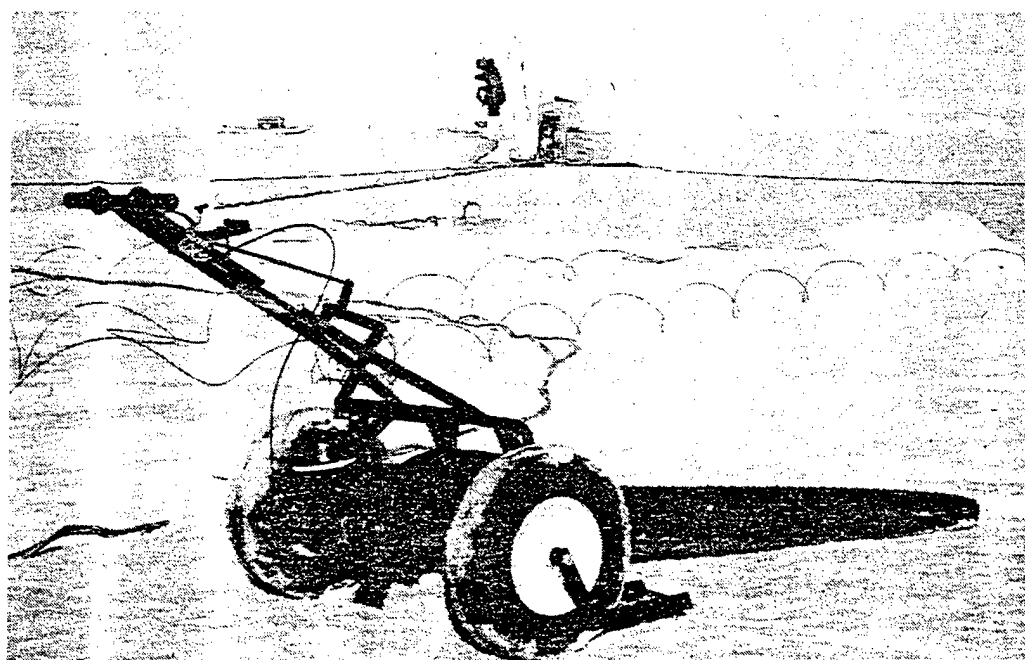


FIGURE 6. WHEEL-MOUNTED CHAIN SAW FOR CUTTING AIR JACK SLOTS

The Power Team air jacks used were 60x60x2 cm thick with a maximum rated pressure of 800 kPa and a displacement of 33 cm. We had no trouble dropping the air jack into these precut slots in the manner shown in Figure 7. Once in the slot, the air jack was inflated by a small Black and Decker air compressor (for automobile tires) which operated off a 12V lead-acid gel-cell battery. The air pressure was measured with a factory-calibrated PSI-tronix pressure transducer and recorded with a Campbell Scientific CR-10 data logger and SM-192 storage module, which operated off a second 12V gel-cell battery.

We performed four inflation tests. As illustrated in Figure 3, the first test was in the consolidated layer, the second test was in the partially consolidated ice directly below it in the same slot, and the third and fourth tests were in the partially consolidated ice in separate slots. The top of the jack was 60 cm below the ice surface for the last three tests.



FIGURE 7. AIR JACK INSERTION

RESULTS

Pressure-displacement curves for the Northwest Research Associates tests from the spring of 1994 are shown in Figure 8. Both graphs in the figure show the same four tests, with different pressure scales. As seen in the figure, the strength of the partially consolidated ice in the ridge was highly variable on the scale of the air jack. Test 1 (in the top layer of consolidated ice) saw the highest pressures. It was stopped because of pressure/volume limitations of the air jack. Given the precision of the calculated displacement, we interpret Test 1 as having negligible displacement. The other three tests showed varying degrees of resistance to the jack and were stopped because of displacement conditions. All three show numerous displacement events at erratic time intervals. Test 3 had a large, abrupt displacement event with a corresponding rapid pressure drop (due to the expansion of the air in the jack) just before the compressor was stopped.

The fluctuations in air jack pressure (ram force) seen here are similar to those found in laboratory tests (e.g., Urroz and Ettema, 1987) despite the fact that the ratio of the ram size to ice block size is much smaller in these air jack tests. These fluctuations result from a combination of slip-stick block motion, breaking of cohesion bonds, and the ram stiffness. It is, therefore, necessary to average the results of numerous tests in the same ridge to increase the precision of the test results.

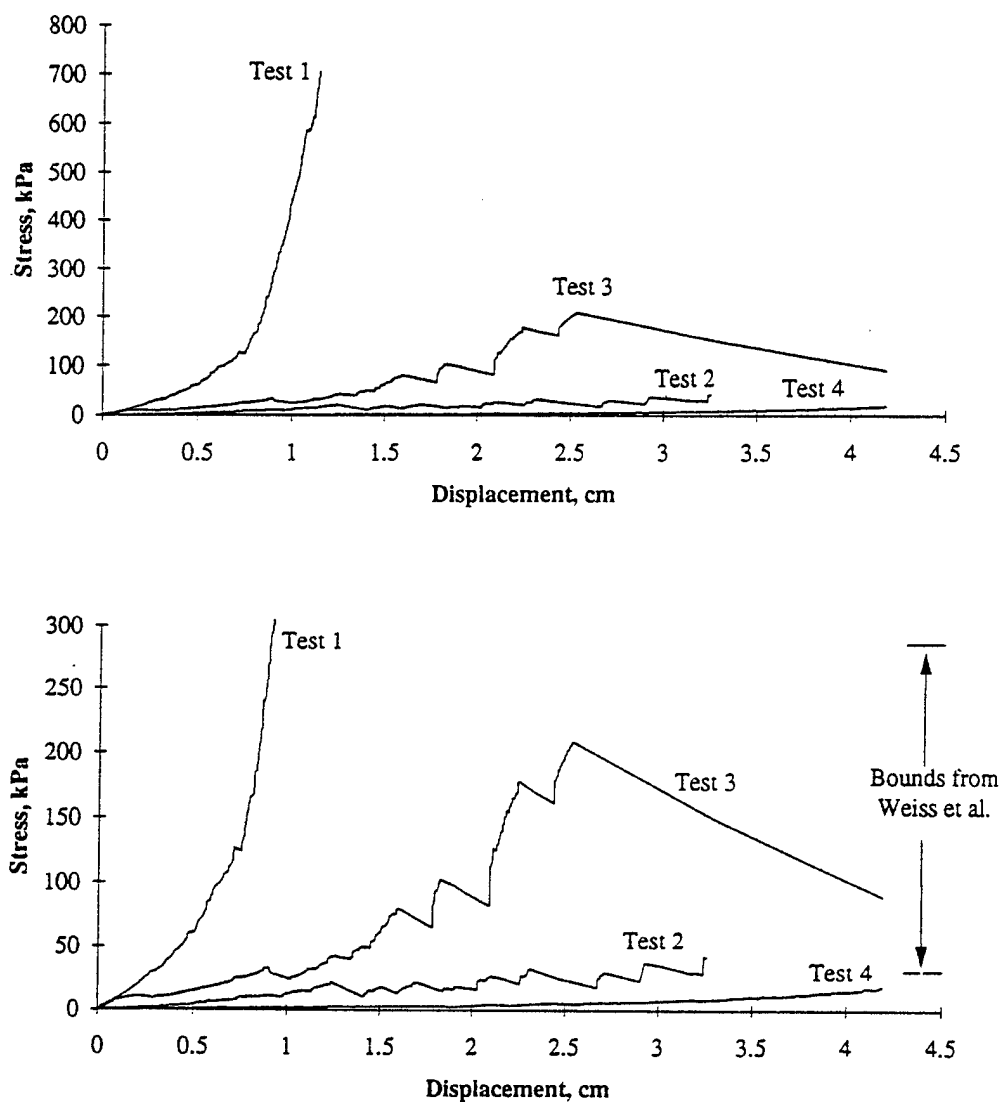


FIGURE 8. PRESSURE-DISPLACEMENT CURVES FOR RIDGE TESTS

RIDGE STRENGTH HINDCAST ANALYSIS

Laboratory test data from Weiss et al. (1981) were used with an analysis method from Coon et al. (1984) to hindcast the rigid-plastic limit load for Tests 2-4 in the partially consolidated portion of the keel. As shown in Table 2, the field test parameters matched quite well with the laboratory test parameters. The ridge ice blocks were slightly warmer with lower salinity, which is consistent with

being immersed in sea water for two weeks. Weiss reported their test results in terms of the Coulomb failure parameters: the effective angle of internal friction and the apparent cohesion.

TABLE 2. ANALYSIS PARAMETERS

Parameter	Laboratory data from Weiss et al. (1981)	SIMI ridge on April 14, 1995
Ice sheet thickness (cm)	15	14
Void ratio, η (porosity)	0.24 to 0.36	0.35
Ice block salinity (‰)	10 to 11	5
Ice block temperature (°C)	-2.5 to -5	-1.4
Displacement rate (mm/s)	3	0.4
Load area (m ²)	0.55	0.31
Consolidation state	Unconsolidated	Partially consolidated
Effective angle of internal friction, ϕ	26°	---
Apparent cohesion, C (kPa)	2.3	---

Figure 9a shows the plastic failure zone assumed for this analysis, and Figure 9b shows the corresponding Coulomb failure surface in Mohr space. The vertical dimensions in Figure 9a are based on the average values from the six drilled holes shown in Figure 3. The air jack or ram applies a uniform pressure, P_a , over a square area with the dimension, a , on a side just below the consolidated layer. The plastic failure zone extends down and away from the ram.

As an approximate solution to the problem shown in Figure 9, a closely related, plastic solution for Coulomb failure caused by a rectangular indenter will be used, after Coon et al. (1984). For this problem, the loaded area extends to the bottom of the keel as shown in Figure 10, in which the ice sheet is inverted to expose the bottom of the keel. A large volume of ice has been failed, and it is assumed that the load is on a half space. In Figure 10, there are three failing regions. ABCDEF moves in the direction of the load and up. The regions BHCF and ADGE move to the side and up. If it is assumed that the failure load of Figure 10 is the same as that of Figure 9a, then the indenter pressure, P_i , is smaller than the equivalent air jack pressure because of the load area difference

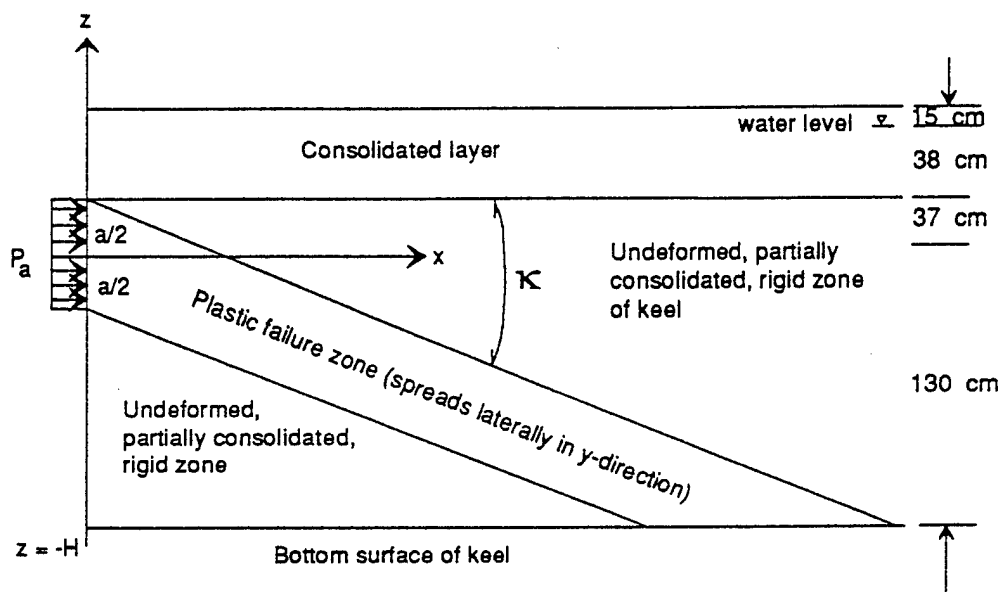
$$\text{Failure load} = P_i ah = P_a a^2 \quad (2)$$

The indenter failure pressure is given in Equation 17 of Coon et al. (1984) as

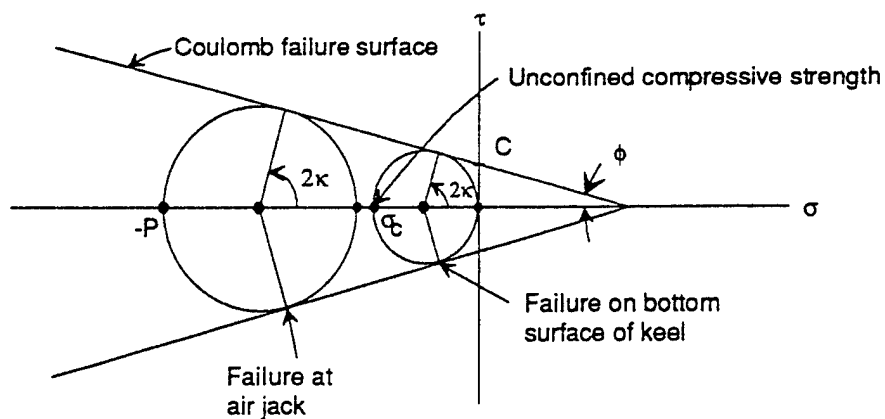
$$P_i = \sigma_c \left(1 + C_1(\phi) \frac{h}{a} \right) \quad (3)$$

where σ_c is the unconfined compressive strength of the Coulomb material and $C_1(\phi)$ is a correction coefficient derived in Coon et al. (1984) and presented graphically in Figure 11. From the geometry of the triangle in Figure 9b with ϕ at one apex and 2κ at the other, the unconfined compressive strength is related to the apparent cohesion and effective angle of internal friction given in Table 2:

$$\sigma_c = \frac{2C \cos \phi}{1 - \sin \phi} \quad (4)$$



a) Plastic failure zone in the keel



b) Mohr circles for stresses showing Coulomb failure surface

FIGURE 9. RIGID-PLASTIC COULOMB FAILURE ANALYSIS

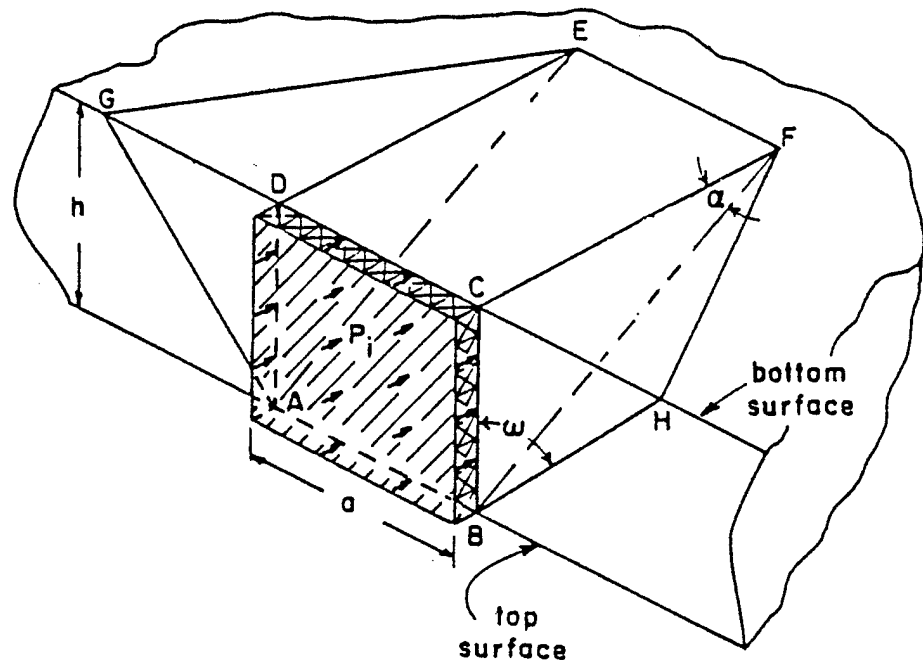


FIGURE 10. ASSUMED FAILURE MECHANISM FOR MOHR-COULOMB MATERIAL
(ADAPTED FROM FIGURE 11 IN COON, EVANS, AND GIBSON, 1984)

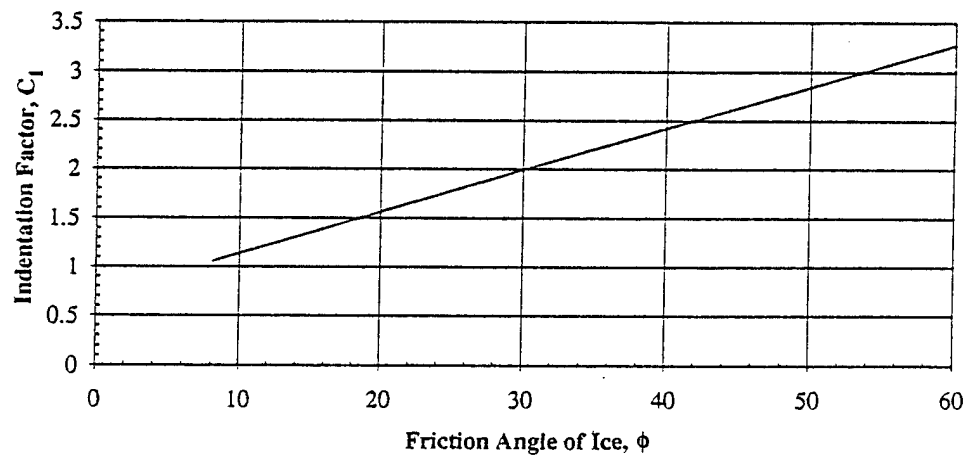


FIGURE 11. CORRECTION COEFFICIENT FROM COON ET AL. (1984)

FIGURE 11. CORRECTION COEFFICIENT FROM COON ET AL. (1984)

Combining Equations 2, 3, and 4 yields

$$P_a = \frac{h}{a} \frac{2C \cos \phi}{1 - \sin \phi} \left(1 + C_1(\phi) \frac{h}{a} \right) \quad (5)$$

Table 3 includes a selection of solutions to Equation 5 using the dimensions from Figure 9a (167 cm for h, and 56 cm for a). Table 3 is examined row by row in the following. In the first row, the value of 26° for ϕ from Weiss et al. (1981) and the curve in Figure 11 are used to find a value of 1.8 for $C_1(\phi)$ and to predict a value of 140 kPa for the air jack pressure. The average jack pressure achieved in the three tests in the partially consolidated keel was 90 kPa. In the second and third rows in Table 3, the values for friction angle and cohesion were adjusted one at a time to match the air jack pressure from the tests. These all represent reasonable agreement considering the scatter in the three tests and the approximations made in the prediction.

In addition, Figure 12 compares our data to those of Weiss et al. (1981) for tests on similar size blocks. Figure 12 is adapted from Figure 3 in Weiss et al. (1981); the solid circles are the data from their slow tests. The solid line marked "slow" is their best fit through the slow data, and corresponds to the top row in Table 3. We have added four more lines, corresponding to the bottom four rows in Table 3. The last two rows in Table 3 are a lower bound and an upper bound for the Weiss "slow" data. The predicted air jack pressures from these bounds are 30 and 290 kPa; these two pressures are shown as horizontal lines in Figure 8. Tests 2 and 3 clearly fall within this range, and Test 4 may have as well if the test had been run to larger displacements.

TABLE 3. ANALYSIS RESULTS

Identification	Line number	Effective angle of internal friction, ϕ	Apparent cohesion, C (kPa)	Correction coefficient, $C_1(\phi)$	Air jack pressure from Eqn. 5 (kPa)
Weiss et al.	1	26	2.3	1.8	140
Adjust cohesion	2	26	1.5	1.8	90
Adjust angle	3	15	2.3	1.4	90
Lower bound	4	10	1	1.1	30
Upper bound	5	27	4.5	1.9	290

CONCLUSIONS AND DISCUSSION

The strength of the ridge keel in this experiment was tested at only one time; it is possible, however, to develop a clear picture of the keel strength from its formation to the time of the strength tests, as listed in Table 4. On March 30, the keel was formed with an overall depth of 220 cm comprised of a 14-cm ice sheet and a 206-cm unconsolidated keel. On April 14, the sheet was 53 cm thick near the test slots, leaving 167 cm of partially consolidated keel. For a strength comparison, it is assumed that the unconfined compressive strength of the ice sheet is 700 kPa, which is the horizontal unconfined compressive strength of unoriented columnar sea ice at a low strain rate taken from American Petroleum Institute (API) Bulletin 2N (1988). Although we stopped our test in this ice at 700 kPa, the limit load pressure of an air jack confined in this ice is related to the out-of-plane failure strength of

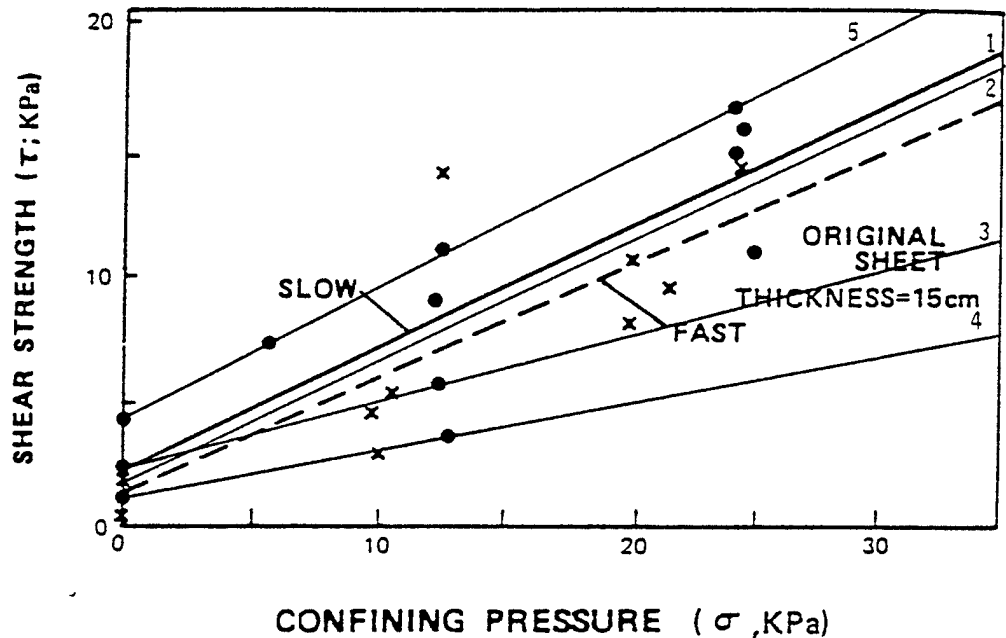


FIGURE 12. UNCONSOLIDATED ICE RUBBLE SHEAR STRENGTH (ADAPTED FROM WEISS ET AL., 1981)

TABLE 4. RIDGE STRENGTH EVOLUTION

Parameter	March 30	April 14
Ice sheet thickness (m)	0.14	0.53
Keel thickness (m)	2.06	1.67
Ice sheet unconfined compressive strength (kPa)	700	700
Keel unconfined compressive strength (kPa)	7.4	7.4
Ice sheet strength resultant (kN/m)	98 (87%)	371 (97%)
Keel strength resultant (kN/m)	15 (13%)	12 (3%)
Total strength resultant (kN/m)	113 (100%)	383 (100%)

The strength resultant is the product of the strength and the depth. The values for compressive strength resultant in Table 4 are calculated using the unconfined strengths and depths in Table 4. It shows that the total unconfined strength of a unit width of the keel has increased by more than a factor of three from March 30 to April 14 and that the percentage contribution from the keel has decreased from 13% to only 3%. Therefore, it appears that the unconsolidated part of the keel contributed a

minor portion of ridge strength. However, it is important to remember there are very little field data on which to base this conclusion.

The variation of the stress-displacement curves for the partially consolidated keel in Tests 2-4 in Figure 8 imply that the jack size of 0.31 m^2 is not large enough to measure the average strength in a single test. This is not surprising given that the blocks had a thickness of 0.14 m with an average area of 0.20 m^2 with a standard deviation of 0.22 m^2 . It is desirable to have the jack size be much larger than the block size; this, however, requires very large equipment to make the slots and to install and inflate the large jack. It is reasonable to increase the size of a rectangular jack to about 1 m^2 and use it with a system that can be transported by helicopter. For field tests such as these, the transportability is very desirable. The load rate can be increased with a larger compressor. The larger jack also allows for a larger displacement, which helps determine when steady state motion is achieved in the tests. If many tests are run, then the average should be same as the result from a larger jack.

Our original plan was to test a ridge in the fall, winter, and spring to track strength with consolidation. That was not possible in this experiment but still seems to be a worthy objective.

ACKNOWLEDGMENTS

This work was done as part of the Office of Naval Research (ONR) Sea Ice Mechanics Initiative (SIMI). We thank Dr. Thomas Curtin of ONR for sponsoring this work as well as the overall SIMI Program. The authors also thank Andreas Heiberg, Jay Ardai, Dean Stewart, Steve Voorhees, and Suzanne O'Hara for their logistical support during the field program. The author's work was funded by ONR contract number N00014-92-C-0027.

REFERENCES

- Allyn, N., and B. R. Wasilewski, 1979, "Some Influence of Ice Rubble Field Formations Around Artificial Islands in Deep Water," in *Proceedings of 1979 Conference on Port and Ocean Engineering under Arctic Conditions*, Trondheim, Norway, Vol. 1, pp. 39-55.
- American Petroleum Institute, 1988, "Recommended Practice for Planning, Designing, and Constructing Fixed Offshore Structures in Ice Environments," API Recommended Practice 2N, First Edition, June 1, American Petroleum Institute Production Department, Dallas, TX.
- Coon, M. D., D. C. Echert, and G. S. Knoke, 1992, "Pack Ice Anisotropic Constitutive Model," in *IAHR 92, Proceedings of the 11th International Symposium on Ice*, Banff, Alberta, p. 1188.
- Coon, M. D., R. J. Evans, and D. H. Gibson, 1984, "Failure Criteria for Sea Ice and Loads Resulting from Crushing," in *Proceedings of IAHR Ice Symposium 1984 Hamburg*, Vol. III, pp. 1-16.
- Coon, M. D., G. S. Knoke, and D. C. Echert, 1994, "The Sea Ice Mechanics Initiative (SIMI)," in *Proceedings of the 26th Annual OTC Conference*, Houston, TX, May.
- Ettema, R., and J. A. Schaefer, 1986, "Experiments on Freeze-Bonding Between Floating Ice Blocks," *Journal of Glaciology*, Volume 32, No. 112, pp. 397-403.
- Ettema, R., and G. Urroz, 1989, "On the Internal Friction and Cohesion in Unconsolidated Ice Rubble," *Cold Region Science and Technology* 16, pp. 237-247.
- Frederking, R. M. W. and B. Wright, 1982, "Characteristics and Stability of an Ice Rubble Field, Issungnak, February-March 1980," NRC Technical Memorandum, Jan. 1982, No. 134, pp. 230-247.
- Iyer, S. H., and D. M. Masterson, 1987, "Field Strength of Multi-Year Ice Using Thin-Walled Flat Jacks," *Ninth International Conference on Port and Ocean Engineering Under Arctic Conditions*, Fairbanks, Alaska, pp. 57-73.
- Keinonen, A., and T. Nyman, 1978, "An Experimental Model Scale Study on the Compressible, Frictional and Cohesive Behavior of Broken Ice Mass," in *Proceedings of IAHR Symposium on Ice*, Luleå, Sweden, Vol. 2, pp. 335-353.
- Prodanovic, A., 1979, "Model Tests of Ice Rubble Strength," in *Proceedings of 1979 Conference on Port and Ocean Engineering under Arctic Conditions*, Trondheim, Norway, Vol. 1, pp. 89-105.

- Thorndike, A. S., D. A. Rothrock, G. A. Maykut, and R. Colony, 1975, "The Thickness Distribution of Sea Ice," *Journal of Geophysical Research*, Vol. 80, No., 33, pp. 4501-4513.
- Tucker, W. B., and J. W. Govoni, 1981, "Morphological Investigation of First-Year Sea Ice Pressure Ridge Sails," *Cold Regions Science and Technology*, No. 5, pp. 1-12.
- Urroz, G., and R. Ettema, 1987, "Simple Shear Box Experiments with Floating Ice Rubble," *Cold Region Science and Technology* 14, No. 2, pp. 185-199.
- Wang, A. T., and J. P. Poplin, 1995, "Challenges in Arctic Technology for Offshore Sakhalin Development," in *Proceedings of the Tenth International Symposium on Okhotsk Sea and Sea Ice*, Mombetsu, Hokkaido, Japan, February.
- Weiss, R. T., A. Prodanovic, and K. N. Wood, 1981, "Determination of Ice Rubble Shear Properties," in *Proceedings of IAHR International Symposium on Ice, Quebec*, Volume II, pp. 860-870.
- Wong, T. T., A. D. Gale, D. C. Sego, and N. R. Morgenstern, 1987, "Shear Box Tests on Broken Ice," in *Proceedings of the Ninth International Conference on Port and Ocean Engineering Under Arctic Conditions*, POAC 87, Fairbanks, Alaska, pp. 97-107.
- Zubov, N. N., 1944, *The Arctic Ice, Main Northern Sea Route*, Publishing House, 360 pp.

An Oriented Thickness Distribution for Sea Ice

D.M. Coon,
D.C. Echert,
G.S. Knoke,
and
R.S. Pritchard

Submitted to *JGR*, 1997

An oriented thickness distribution for sea ice

Max D. Coon, Gerald S. Knoke, and Douglas C. Echert
NorthWest Research Associates, Inc.
Bellevue, WA, USA

Robert S. Pritchard
IceCasting, Inc.
Seattle, WA, USA

ABSTRACT

This paper describes the kinematics and ice-thickness redistribution of pack ice while accounting for lead and ridge orientation. The pack ice deformations are described in terms of velocity discontinuities rather than invariants, allowing direct interpretation of open-water production and ridging. This description of pack ice allows an oriented ice-thickness distribution to account for the growth and ridging of ice in refrozen leads. The shear, compressive, and tensile strengths of each refrozen lead are functions of the lead ice thickness. Results of simple model calculations for ice-thickness distribution appear reasonable. Results for kinematics indicate that most of the apparent scatter in isotropic calculations of open-water production can be explained by accounting for lead orientation. The theory presented in here is a small part of that which is required to implement a large-scale, anisotropic model; a companion paper addresses the architecture of such a model. We conclude that, to have high resolution with cell size of 5 to 100 km, an ice dynamics model must account for lead orientation.

INTRODUCTION

In polar regions, the sea-ice cover acts as a barrier between the atmosphere and the ocean, curtailing the transfer of thermal and mechanical energy as well as curtailing mass transport. The large-scale motion of the pack ice creates a small amount of open water, in the form of leads. In the Arctic winter and spring, leads are linear features often several hundred kilometers long. As these leads close and shear, rafted ice, pressure ridges, shear ridges, and rubble are created along these same linear features. SAR ice motion products show active leads as linear slip-lines in the pack ice (Stern et al., 1995). For convenience, we will refer to all these linear features as leads.

An ice dynamics model that assumes isotropy in the ice cover can adequately characterize an ice cover in the absence of leads, e.g., summer/autumn ice with multi-year floes surrounded on all sides by open water or thin ice. However, once a lead forms, the ice becomes anisotropic and is best described by a model that accounts for this property. Careful modeling of leads in sea ice is important not only because leads provide the opportunity for the heat exchange necessary for ice production but also because the refrozen lead ice controls the ice dynamics through its strength (Coon et al., 1992). The dependence of lead ice strength on lead ice thickness must be established from experimental data supported by theories such as Coon et al. (1989).

In order to account for lead and ridge orientation for pack ice on the scale of 5 to 100 km, we suggest two types of large-scale pack ice:

- *Isotropic* ice is consolidated multi-year and thick first-year ice. Much of it is the jointed ice described above; *isotropic* ice is assumed rigid in this paper.
- *Oriented* ice includes open water, new ice, nilas, young ice, first-year ice, rafted ice, and ridged ice that occur in long, narrow features. Based on Advanced Very High Resolution Radar (AVHRR) images, these features are assumed linear for (grid, element, or cell) scales of 5 to 100 km. All pack ice deformations are assumed to occur in the *oriented* ice. In addition, the linearity assumption implies that a shearing deformation of a lead does not cause rafting or ridging of the *oriented* ice and does not cause any failure of the *isotropic* ice.

In the next sections, we describe the pack-ice kinematics accounting for lead and ridge orientation, the redistribution of *oriented* ice-thickness categories, and the results of model calculations. The theory presented in this paper is only a small portion of that which is ultimately required for implementation in a large-scale ice dynamics model. A companion paper (Coon et al., 1997a) includes discussions of the following:

- The problems to be addressed before an oriented ice thickness distribution can be implemented in an ice forecasting or climate model.
- The mechanical response, including the formation, advection, and dissolution of the leads.
- Methods to verify model results, such as comparing them with satellite-SAR ice-motion products for lead orientation, ice motion, and ice thickness distribution.

KINEMATICS

To account for the anisotropy resulting from leads and ridges, we developed a new kinematic description of the pack ice motion which is consistent with the general kinematic relations for pack ice presented in Pritchard (1975). The orientation of the velocity-discontinuity lines where leads and ridges are formed is referred to as the lead direction. Each active lead direction contributes to the plastic deformation of the pack ice. The pack ice motion is therefore the sum of deformations along individual lead directions as well as drift and rotation. In this paper, we assume that there are negligible deformations of the *isotropic* ice between the leads (e.g., elastic deformations).

As illustrated in Figure 1, we align a coordinate system (ξ, η) to each lead direction such that the ξ -axis for the j -th lead direction lies at the angle θ_j to the x -axis of the reference (x, y) coordinate system. The velocities (u, v) correspond to the (x, y) directions, the velocities (U, V) correspond to the (ξ, η) directions, and $(\Delta x, \Delta y)$ and $(\Delta \xi, \Delta \eta)$ define the size of the cell in the reference and lead coordinate systems, respectively. In the lead coordinate system, the plastic stretching parallel to the lead is assumed zero, and the lead width is assumed locally constant along its length. We can express velocity derivatives normal to the lead direction (with respect to η) in terms of smooth gradients or in terms of any number of steps.

$$\begin{aligned}
 \frac{\partial U}{\partial \xi} &= 0 & \frac{\partial U}{\partial \eta} &= \frac{L \Delta U}{A} \\
 \frac{\partial V}{\partial \xi} &= 0 & \frac{\partial V}{\partial \eta} &= \frac{L \Delta V}{A}
 \end{aligned} \tag{1}$$

where $L (= \Delta\xi)$ is the average length of many parallel leads in the reference element or the length of a single lead in the reference element and $A (= \Delta x \Delta y = \Delta\xi \Delta\eta)$ is the area of the reference element. This model does not distinguish whether there is a single lead crossing the element or a continuum of parallel leads that cover the element.

For each lead direction, we form the plastic velocity gradient L_j , a second-order tensor with four components in the coordinate system parallel to the j -th lead direction:

$$L_j = \begin{bmatrix} \frac{\partial U}{\partial \xi} & \frac{\partial U}{\partial \eta} \\ \frac{\partial V}{\partial \xi} & \frac{\partial V}{\partial \eta} \end{bmatrix}_j = \begin{bmatrix} 0 & \left(\frac{\partial U}{\partial \eta} \right)_j \\ 0 & \left(\frac{\partial V}{\partial \eta} \right)_j \end{bmatrix} \quad (2)$$

The components of the corresponding plastic stretching tensor for the j -th lead direction are as follows:

$$D_j = \frac{1}{2}(L_j + L_j^T) = \begin{bmatrix} 0 & \frac{1}{2} \left(\frac{\partial U}{\partial \eta} \right)_j \\ \frac{1}{2} \left(\frac{\partial U}{\partial \eta} \right)_j & \left(\frac{\partial V}{\partial \eta} \right)_j \end{bmatrix} \quad (3)$$

where the superscript T indicates the transpose.

To find the contribution of each lead motion to the plastic stretching in the reference coordinate system, we introduce the rotation tensor \mathbf{Q}_j for the j -th lead direction. The rotation tensor is written in terms of θ_j , the angle from the reference x -axis to the ξ -axis parallel to the j -th lead direction:

$$\mathbf{Q}_j = \begin{bmatrix} \cos \theta_j & -\sin \theta_j \\ \sin \theta_j & \cos \theta_j \end{bmatrix} \quad (4)$$

To form \mathbf{D} , the plastic stretching in the reference coordinate system, we rotate each of the N lead tensors to the reference coordinate system to form \mathbf{D}_j and add the contributions of individual lead directions, so

$$\mathbf{D} = \sum_{j=1}^N \mathbf{D}_j = \sum_{j=1}^N \mathbf{Q}_j D_j \mathbf{Q}_j^T \quad (5)$$

The sum of the diagonal terms is D_I , the plastic divergence, which depends only on the $\left(\frac{\partial V}{\partial \eta} \right)_j$:

$$D_I = \text{trace } \mathbf{D} = \sum_{j=1}^N \left(\frac{\partial V}{\partial \eta} \right)_j \quad (6)$$

In words, the total divergence is equal to the sum of the normal velocity derivatives associated with each lead direction. For $\Delta x \Delta y$ equal to $\Delta \xi \Delta \eta$, the rate of area change in the cell is therefore equal to $\Delta x \Delta y D_t$.

In this anisotropic model, the motions of the leads are not uniquely determined in terms of the plastic stretching tensor; additional information is needed. As is discussed in a companion paper (Coon et al., 1997a), the solution to an anisotropic plasticity ice dynamics problem will accomplish the following:

1. Place the stress state on the anisotropic failure surface when plastic failure occurs.
2. Identify the specific failure mechanisms involved, e.g., closing lead 1 while shearing lead 2.
3. Allocate the stretching \mathbf{D} to the contribution of the j -th lead direction to the plastic stretching \mathbf{D}_j .

The inverse rotation of Equation (5) gives the plastic stretching components in lead coordinates:

$$\mathbf{D}_j = \mathbf{Q}_j^T \mathbf{D}_j \mathbf{Q}_j \quad (7)$$

Using Equation 3, the components of the matrix \mathbf{D}_j yield the velocity derivatives normal to the lead direction in terms of the components of the tensor \mathbf{D}_j :

$$\begin{aligned} \left(\frac{\partial U}{\partial \eta} \right)_j &= 2 D_{j,xy} \cos 2\theta_j - (D_{j,xx} - D_{j,yy}) \sin 2\theta_j \\ \left(\frac{\partial V}{\partial \eta} \right)_j &= D_{j,xx} + D_{j,yy} \end{aligned} \quad (8)$$

In this model, the velocity derivative normal to the lead directions \mathcal{V}_j is the only part of the kinematics that affects ice-thickness redistribution in the leads. This result depends on the assumption that the leads are locally straight (i.e., within a cell) so that shear motions across the lead do not redistribute the ice thickness, as opposed to the usual interpretation expressed in Thorndike (1975).

ICE-THICKNESS REDISTRIBUTION

The failure of *isotropic* ice results in open water in leads or at least slip lines with little open water. In our experience, rafting 2-m ice sheets is rare and ridges built from a 2-m ice sheet are unheard of. Although an occasional 2-m ice block is kicked up, we have never seen ridges with 10-m sails and 40-m keels made of 2-m blocks. Hence, we do anticipate the need for ridging isotropic ice in this model.

Subfreezing temperatures will cause *oriented* ice to form in leads, and ice deformations will cause a distribution of ice thickness within these leads. The distribution of ice thickness at each lead orientation can be described much as others have described the distribution of ice thickness (e.g., Thorndike et al., 1975). Figure 2 illustrates how we might characterize these ice-thickness distributions assuming *isotropic* ice has one ice-thickness category and *oriented* ice has four ice-thickness categories in two lead systems. The thickest *oriented* ice category may be

thicker than the *isotropic* ice, since the majority of the isotropic ice is multi-year ice. Certain properties define the i -th ice-thickness category in the j -th lead:

- Lead or lead orientation θ_j
- Ice thickness separating adjacent ice-thickness categories h_{ij}
- Area fractions of each ice-thickness category ΔG_{ij}
- Mean ice thickness in each ice-thickness category \bar{h}_{ij}

We assume the refrozen lead ice to be homogeneous (within each ice-thickness category). In addition, we assume the leads are straight so that a shearing deformation of the lead deforms neither *isotropic* ice nor *oriented* ice. We associate four ice-thickness categories with each lead direction, applying the term 'oriented thickness distribution' to distinguish it from the usual (isotropic) ice-thickness distributions (e.g., Thorndike et al., 1975).

When the air temperature is below freezing, new ice grows in the leads; its growth rate is often modeled simply as a function of air temperature (Anderson, 1961; Zubov, 1944; Lebedev, 1940), e.g., from Lebedev,

$$h = 0.0133(\text{FDD})^{0.58} \quad (9)$$

where h is the ice thickness in meters and FDD is the number of freezing-degree (C) days since the open water was formed. Alternatively, Thorndike et al. (1975) give the ice growth rate as a function of time of year for the central Arctic, and Maykut and Untersteiner (1971) compute it from the surface energy balance and ice thermal conductivity.

Based on Pritchard and Coon (1981), we have developed the mathematical equations and calculation procedures for the ice-thickness distribution with four ice-thickness categories in each lead. The pertinent parameters for each ice-thickness category are in Table 1. We define h_0 as the (fixed) ice thickness separating the open-water and thin-ice categories, h_{1j} as separating thin ice and medium ice in the j -th lead, and h_{2j} as separating medium ice and thick ice in the j -th lead. We let f_0 be the growth rate of ice of thickness h_0 calculated from the time-derivative of Equation (9). Except for the open-water category, the definition of the ice-thickness category itself accounts for thermal growth; i.e., the category limits h_{1j} and h_{2j} increase at the growth rate of ice of the same thickness. By assuming a linear ice-thickness distribution within the open-water and thin-ice categories, Pritchard and Coon derived the rate of area change due to thermal growth, Φ_{0j} . For the j -th lead,

$$\Phi_{0j} = \begin{cases} \frac{f_0 \Delta G_{0j}}{h_0} & \text{if } f_0 > 0 \text{ (freezing condition)} \\ \frac{f_0 \Delta G_{1j}}{h_{1j} - h_0} & \text{if } f_0 < 0 \text{ (melting condition)} \end{cases} \quad (10)$$

where ΔG_{0j} is the area fraction of open water in the j -th lead and ΔG_{1j} is the area fraction of thin ice in the j -th lead.

When the j -th lead is opening, i.e., when the lead's velocity gradient $\left(\frac{\partial V}{\partial \eta}\right)_j$ is positive, the following equations describe the total time rate of change of area fraction in the four ice categories:

$$\begin{aligned}\frac{D\Delta G_{0j}}{Dt} &= \left(\frac{\partial V}{\partial \eta}\right)_j - \Phi_{0j} & \frac{D\Delta G_{1j}}{Dt} &= \Phi_{0j} \\ \frac{D\Delta G_{2j}}{Dt} &= 0 & \frac{D\Delta G_{3j}}{Dt} &= 0\end{aligned}\quad (11)$$

where ΔG_{2j} is the area fraction of medium ice in the j -th lead and ΔG_{3j} is the area fraction of thick ice in the j -th lead. Equation (11) provides that the source for open water is opening the lead and that area is transferred between the first two categories by freezing or melting. These Lagrangian time rate of change equations can be easily converted to the usual Eulerian form by using the Eulerian derivative (see, e.g., Liepmann and Roshko, 1957):

$$\frac{Df}{Dt} = \frac{\partial f}{\partial t} + \mathbf{v} \cdot \nabla f \quad (12)$$

The ice category area fractions and the components of the lead direction ($\cos\theta$, $\sin\theta$) are advected along with the ice.

When the j -th lead is closing, i.e., when $\left(\frac{\partial V}{\partial \eta}\right)_j$ is negative, the following equations describe the rate of change of area fraction in the four ice categories:

$$\begin{aligned}\frac{D\Delta G_{0j}}{dt} &= \left(\frac{\partial V}{\partial \eta}\right)_j \left(\frac{\bar{h}_{1j}}{\bar{h}_{1j} - \bar{h}_0} u_0 (\Delta G_{0j}) \right) - \Phi_{0j} \\ \frac{D\Delta G_{1j}}{dt} &= \left(\frac{\partial V}{\partial \eta}\right)_j \left(\begin{aligned} & -\frac{\bar{h}_0}{\bar{h}_{1j} - \bar{h}_0} u_0 (\Delta G_{0j}) \\ & + \frac{\bar{h}_{2j}}{\bar{h}_{2j} - \bar{h}_{1j}} u_0 (\Delta G_{1j}) [1 - u_0 (\Delta G_{0j})] \end{aligned} \right) + \Phi_{0j} \\ \frac{D\Delta G_{2j}}{dt} &= \left(\frac{\partial V}{\partial \eta}\right)_j \left(\begin{aligned} & -\frac{\bar{h}_{1j}}{\bar{h}_{2j} - \bar{h}_{1j}} u_0 (\Delta G_{1j}) [1 - u_0 (\Delta G_{0j})] \\ & + \frac{\bar{h}_{3j}}{\bar{h}_{3j} - \bar{h}_{2j}} u_0 (\Delta G_{2j}) [1 - u_0 (\Delta G_{1j})] [1 - u_0 (\Delta G_{0j})] \end{aligned} \right) \\ \frac{D\Delta G_{3j}}{dt} &= \left(\frac{\partial V}{\partial \eta}\right)_j \left(-\frac{\bar{h}_{2j}}{\bar{h}_{3j} - \bar{h}_{2j}} u_0 (\Delta G_{2j}) [1 - u_0 (\Delta G_{1j})] [1 - u_0 (\Delta G_{0j})] \right)\end{aligned}\quad (13)$$

where \bar{h} indicates the average ice thickness within the ice-thickness category. Equation (13) provides the following:

1. Freezing and melting transfer the area between the first two categories.
2. Rafting transfers the area from the open-water category to the thin ice category.
3. Rafting transfers the area from the thin-ice category to the medium-ice category when the open water is gone.
4. Ridging transfers the area from the medium-ice category to the thick-ice category when the open water and thin ice are gone.

For convenience, we have introduced the unit step function $u_a(x)$ such that

$$u_a(x) = \begin{cases} 0 & \text{when } x < a \\ 1 & \text{when } x > a \end{cases} \quad (14)$$

The average ice thickness in each category increases at the growth rate of ice of the same thickness, except when opening occurs. In that instance, the average thickness of the ice in the open-water category is reduced by the contribution of true open water to the average.

RESULTS OF MODEL CALCULATIONS

The behavior of these ice-thickness redistribution equations is illustrated by a simple example for one lead; the results are shown in Figure 3. In this example, a cell of pack ice initially has only ice in the thickest category (white). At an air temperature of -40°C , the lead area fraction increases steadily at the rate of 10^{-5} s^{-1} for two days, then closes steadily at the same rate for two days. Initially, the open-water area fraction (black) increases rapidly at the expense of the thickest category. Gradually, freezing moves ice from the open-water category to the thin-ice category (dark gray). During closing, the open-water ice-thickness category is rafted into the thin-ice category. When the open-water category is fully consumed, the thin-ice category is ridged into the medium-ice category (light gray). When the thin-ice category is consumed, the medium-ice category is ridged into the thick-ice category (white). If the cell size is fixed (Eulerian), then there is mass flux into and out of the cell.

We also compared open-water production using the anisotropic model to open-water production using the usual isotropic models. Isotropic models approximate the open-water production as a single function of the ratio of the stretching invariants (Thorndike et al., 1975; Stern et al., 1995). For example, Thorndike et al. approximated open-water production normalized by the stretching magnitude as a function of the angle from pure divergence to the invariant stretching vector:

$$\frac{\text{Opening}}{|\mathbf{D}|} = \alpha_0 = \frac{1}{2}(1 + \cos \Theta) \quad (15)$$

where

$$\begin{aligned} D_I &= D_{xx} + D_{yy} & D_{II} &= \sqrt{(D_{xx} - D_{yy})^2 + 4D_{xy}^2} \\ \Theta &= \tan^{-1} \left(\frac{D_{II}}{D_I} \right) & |\mathbf{D}| &= \sqrt{D_I^2 + D_{II}^2} \end{aligned} \quad (16)$$

Figure 6 in Stern et al. shows considerable scatter in the opening found from 342 strips of SAR data for which the time interval was three days when compared with three isotropic functions, including Equation (15). They explained the scatter in the data as "measurement error" because restricting the data to the more active scenes, defined as those having $|D| > 0.07$, reduced the scatter. We suggest that accounting for lead orientation may explain much of the apparent scatter.

Based on the actions of one or two lead systems, we generated families of curves for opening as a function of Θ with a fixed angle between two lead systems of 34° (angle from Cunningham et al., 1994). These results are applicable over all scales for which the leads are linear, e.g., from 5 to 100 km; these results are therefore comparable to a SAR pixel or an entire SAR strip. From Equations (3), (4), (5), the total stretching is the sum of N lead stretching contributions rotated to the reference coordinate system:

$$\begin{aligned} D_{xx} &= \sum_{j=1}^N \left[\left(\frac{\partial V}{\partial \eta} \right)_j \left(\frac{1}{2} - \frac{1}{2} \cos 2\theta_j \right) + \left(\frac{\partial U}{\partial \eta} \right)_j \left(-\frac{1}{2} \sin 2\theta_j \right) \right] \\ D_{yy} &= \sum_{j=1}^N \left[\left(\frac{\partial V}{\partial \eta} \right)_j \left(\frac{1}{2} + \frac{1}{2} \cos 2\theta_j \right) + \left(\frac{\partial U}{\partial \eta} \right)_j \left(\frac{1}{2} \sin 2\theta_j \right) \right] \\ D_{xy} &= \sum_{j=1}^N \left[\left(\frac{\partial V}{\partial \eta} \right)_j \left(-\frac{1}{2} \sin 2\theta_j \right) + \left(\frac{\partial U}{\partial \eta} \right)_j \left(\frac{1}{2} \cos 2\theta_j \right) \right] \end{aligned} \quad (17)$$

Applying Equation (17) to the case of two leads at an angle to each other can be used to demonstrate that any stretching can be accomplished from opening, closing, and shearing the two leads. This result implies that a third lead cannot be formed until one of the first two leads is totally closed.

The open-water production is calculated directly from the positive values of $\left(\frac{\partial V}{\partial \eta} \right)_j$:

$$\text{Lead 1 opening with Lead 2 closing:} \quad \frac{\text{Opening}}{|D|} = \frac{\left(\frac{\partial V}{\partial \eta} \right)_1}{|D|} \quad (18)$$

$$\text{Both leads opening:} \quad \frac{\text{Opening}}{|D|} = \frac{\left(\frac{\partial V}{\partial \eta} \right)_1 + \left(\frac{\partial V}{\partial \eta} \right)_2}{|D|} \quad (19)$$

Figures 4, 5, and 6 show that open-water production depends strongly on the presence of lead systems. Figure 4 shows curves on which the ratio of lead-2 opening velocity to lead-1 opening velocity is varied over a wide range. The curve corresponding to the opening function in Equation (15) is shown for reference as Thorndike. The case in which only lead 1 is active and opening is shown. Only a limited range of values for Θ are possible because the stretching parallel to the lead is zero, forcing D_{II}/D_I to be greater or equal to one and therefore $45^\circ < \Theta < 135^\circ$. The case in which lead 1 is opening and shearing to the right along with lead-2 closing with no shear

passes close to Equation (14). The case in which lead 1 is opening with no shear and lead 2 is closing with no shear produces small values of opening. The case in which lead 1 is opening and shearing to the left along with lead-2 closing with no shear produces large values of opening. Such large values of opening can occur only until lead 2 is closed, which, depending upon the rates involved, may take hours or days. This limitation suggests that the reduced scatter seen by Stern et al. when they considered only the more active scenes, results from closing the second lead during the 3-day period.

Figure 5 shows curves on which the ratio of lead-1 shearing to opening is varied over a wide range. Lead-2 shearing is zero. The opening function from Thorndike et al. is again shown for reference. The cases have the ratio of lead-2 opening to lead-1 opening fixed at the indicated value. This family of curves shows opening even at very high values of Θ . Figure 6 shows curves on which the ratio of lead-2 shearing to opening is varied over a wide range. Lead-1 shearing is zero. Equation (14) from Thorndike et al. is again shown for reference. The cases have the ratio of lead-2 opening/closing to lead-1 opening fixed at the indicated value; lead 2 is opening when the ratio is positive and closing when the ratio is negative. This family of curves shows extremely large opening at low values of Θ . The three figures together show that reasonable values for the various velocity ratios (less than $\pm 10:1$) produce a broad range of opening normalized by the stretching magnitude for most values of Θ .

The results of these calculations indicate that the apparent scatter in open-water production can be explained by accounting for lead orientation. There is no longer the one-to-one mapping of stretching to open-water production as there is with an isotropic model. Additional constraints imposed by the relations between stress, stretching, and the corresponding plastic failure surface, however, may provide bounds on the opening not seen in these figures.

CONCLUSIONS

We have developed a formulation for pack ice kinematics and an *oriented* ice-thickness distribution that accounts for the orientation of existing leads and ridges. It is concluded that:

1. The plastic deformations of pack ice can be expressed as the sum of contributions from the active leads and ridges.
2. Two active lead/ridge systems can produce all possible deformations, so a third cannot form until one of the first two is closed.
3. The opening/closing of individual lead/ridge systems can be determined from solving the plastic equations for pack ice but cannot be determined solely from the stretching tensor.
4. The opening/closing of individual lead/ridge systems can be used to directly redistribute the ice thickness.

This oriented thickness distribution will be appropriate for use in ice dynamics models, in climate dynamics, in pollution-transport studies, and in ice-motion and noise forecasting. In addition, we have concluded that it is inappropriate to scale down an isotropic large-scale ice dynamics model to a cell size of a few kilometers without separately modeling the *isotropic* ice and the *oriented* ice.

NOTATION

\mathbf{D}	plastic stretching tensor (2nd-order) (1/s)
\mathbf{D}_j	contribution to plastic stretching tensor due to j-th lead direction (1/s)
D_j	components of \mathbf{D}_j in j-th lead coordinates (2nd-order matrix) (1/s)
D_I, D_{II}	first invariant (divergence) and second invariant (shear) of plastic stretching (1/s)
D_{xx}, D_{xy}, D_{yy}	components of plastic stretching tensor (1/s)
f_0	growth rate of ice of thickness h_0 (m/s)
h	ice thickness (m)
h_0	ice thickness separating open water from thin-ice category (fixed) (m)
h_{ij}	greatest ice thickness in i-th category in j-th lead system (m)
\bar{h}_{ij}	average ice thickness in i-th category of j-th lead system (m)
L_j	contribution of velocity gradient tensor due to j-th lead (1/s)
N	number of lead directions
\mathbf{Q}_j	orthonormal rotation tensor (2nd-order) for j-th lead direction
u, v	velocity components in reference coordinate system (m/s)
U, V	velocity components in lead coordinate system (m/s)
u_a	unit step function
x, y	reference coordinate system (m)
α_0	opening coefficient from Thorndike (1975)
ΔG_{ij}	area fraction of i-th ice-thickness category in the j-th lead system (m)
$\Delta U, \Delta V$	velocity jumps across $\Delta \eta$ in lead coordinate system (m/s)
$\Delta x, \Delta y$	cell dimensions in reference coordinate system (m)
$\Delta \xi, \Delta \eta$	cell dimensions in lead coordinate system (m)
Θ	in stretching invariant space, the angle from pure divergence to the invariant stretching vector, equal to the inverse tangent of the shear divided by the divergence (radians)
θ_j	angle from x-axis to j-th lead direction (radians)
ξ, η	lead coordinate system (m)
Φ_{0j}	rate of area change due to thermal growth (1/s)

Acknowledgments

The NWRA authors gratefully acknowledge the National Aeronautics and Space Administration (under Contract Number NASW-4701) and the Office of Naval Research (under Contract Numbers N00014-92-C-0027 and N00014-96-C-0096) for funding this work. Our thanks to Dr. Robert Thomas of NASA and Drs. Thomas Curtin and Michael Van Woert and Cdr. Robert Edson of ONR for their guidance and support during this effort. RSP gratefully acknowledges the Office of Naval Research (under Contract Numbers N00014-94-C-0215 and N00014-96-C-0174) for funding this work. NWRA funded the preparation of this paper through an independent research and development project.

REFERENCES

- Anderson, D. L., Growth rate of sea ice, *Journal of Glaciology*, Vol. 3, pp. 1170-1172, 1961.
- Coon, M. D., D. C. Echert, and G. S. Knoke, Pack ice anisotropic constitutive model, in *IAHR 92, Proceedings of the 11th International Symposium on Ice*, p. 1188, Banff, Alberta, 1992.
- Coon, M. D., G. S. Knoke, and P. A. Lau, Time dependent effects on ridge initiation in sea ice leads, in *Proceedings of the OCEANS'89 Conference*, Seattle, WA, September, 1989.
- Coon, M. D., G. S. Knoke, D. C. Echert, and R. S. Pritchard, The architecture of an anisotropic elastic-plastic sea ice mechanics model, to be submitted to JGR in April, 1997a.
- Coon, M. D., G. S. Knoke, and D. C. Echert, Geophysical pack-ice stress measurements, to be submitted to JGR in April, 1997b.
- Cunningham, G. F., R. Kwok, and J. Banfield, Ice lead orientation characteristics in the winter Beaufort Sea, in *Proceedings of the International Geoscience and Remote Sensing Symposium*, Pasadena, August, pp. 1747-1749, 1994.
- Lebedev, V. V., New formulas on the growth of ice in arctic rivers and seas, in Russian. *Meteorologiya i Gidrologiya*, 6, No. 8, p. 40-51, 1940.
- Liepmann, H. W. and A. Roshko, *Elements of Gasdynamics*, John Wiley and Sons, New York, 1957.
- Maykut, G. A. and N. Untersteiner, Some results from a time-dependent, thermodynamic model of sea ice, *Journal of Geophysical Research*, Vol. 76, pp. 1550-1575, 1971.
- Pritchard, R. S., An elastic-plastic constitutive law for sea ice, *Journal of Applied Mechanics*, Vol. 42, No. 2, pp. 379-384, 1975.
- Pritchard, R. S., and M. D. Coon, Canadian Beaufort Sea ice characterization, in *POAC'81, Proceedings of the Sixth International Conference on Port and Ocean Engineering under Arctic Conditions*, pp. 609-618, Université Laval, Quebec, Canada, 1981.
- Stern, H. L., D. A. Rothrock, and R. Kwok, Open-water production in Arctic sea ice: satellite measurements and model parameterizations, *Journal of Geophysical Research*, Vol. 100, No. C10, pp. 20,601-612, 1995.
- Thorndike, A. S., D. A. Rothrock, G. A. Maykut, and R. Colony, The thickness distribution of sea ice, *Journal of Geophysical Research*, Vol. 80, No. 33, November 20, pp. 4501-4513, 1975.
- Zubov, N. N., *The Arctic Ice, Main Northern Sea Route*, Publishing House, 360 pp., 1944.

LIST OF FIGURES

- Figure 1. Coordinate system and velocity components of a rotated cell aligned with the lead.
- Figure 2. Ice-thickness distribution includes the *oriented* ice in each lead direction separately along with the *isotropic* ice.
- Figure 3. Example of redistribution of ice thickness expressed as area fractions for four ice-thickness categories resulting for opening and closing a lead.
- Figure 4. Accounting for lead orientation results in families of curves for opening as a function of Θ . Failure of the *isotropic* ice falls on the curve for one active lead. The three higher loops result from varying the opening of the second lead for three values of shear to opening for the first lead.

Figure 5. Family of curves for opening formed by holding shear in the second lead at zero and selecting specific values of the ratio of opening in lead 2 to lead 1.

Figure 6. Family of curves for opening formed by holding shear in the first lead at zero and selecting specific values of the ratio of opening in lead 2 to lead 1.

Table 1. Ice-Thickness Categories

Ice-thickness Categories	Ice Types	Area Fraction in j-th Lead	Thickness Range	Average Thickness
Open water	Open water, new ice, and nilas	ΔG_{0j}	$0 < h < h_0$	\bar{h}_0
Thin ice	Young ice and rafted ice	ΔG_{1j}	$h_0 < h < h_{1j}$	\bar{h}_{1j}
Medium ice	First-year ice and low ridges	ΔG_{2j}	$h_{1j} < h < h_{2j}$	\bar{h}_{2j}
Thick ice	Ridged ice and multi-year ice	ΔG_{3j}	$h_{2j} < h$	\bar{h}_{3j}

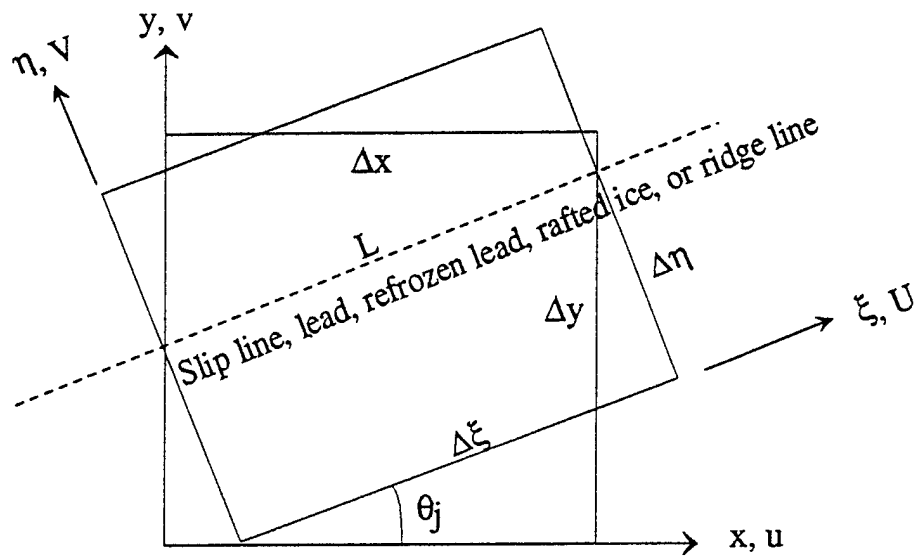


Figure 1. Coordinate system and velocity components of a rotated cell aligned with the slip line.

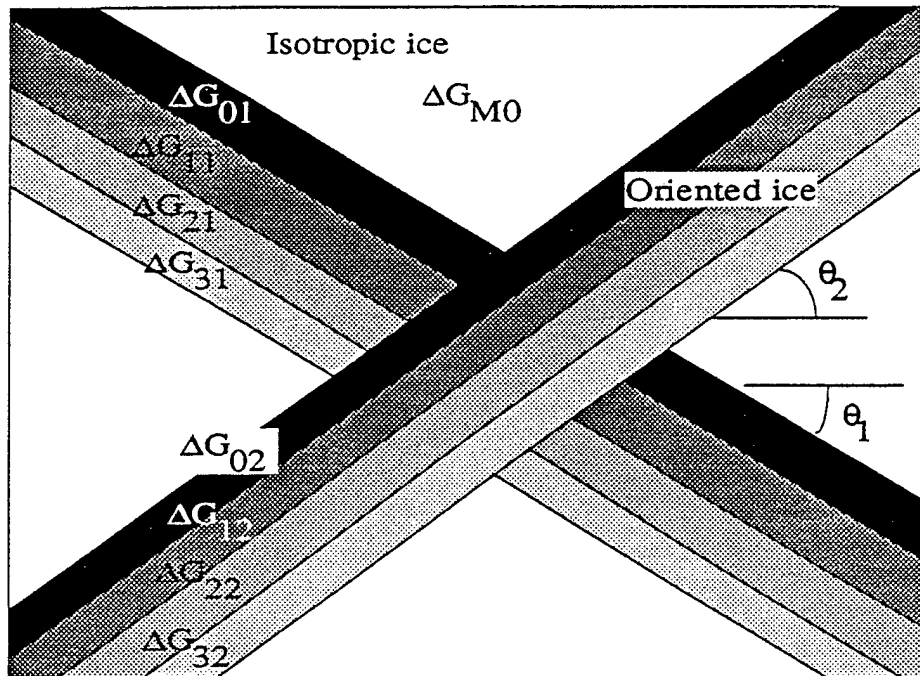


Figure 2. Ice thickness distribution includes the oriented ice in each slip-line directions separately along with the isotropic ice.

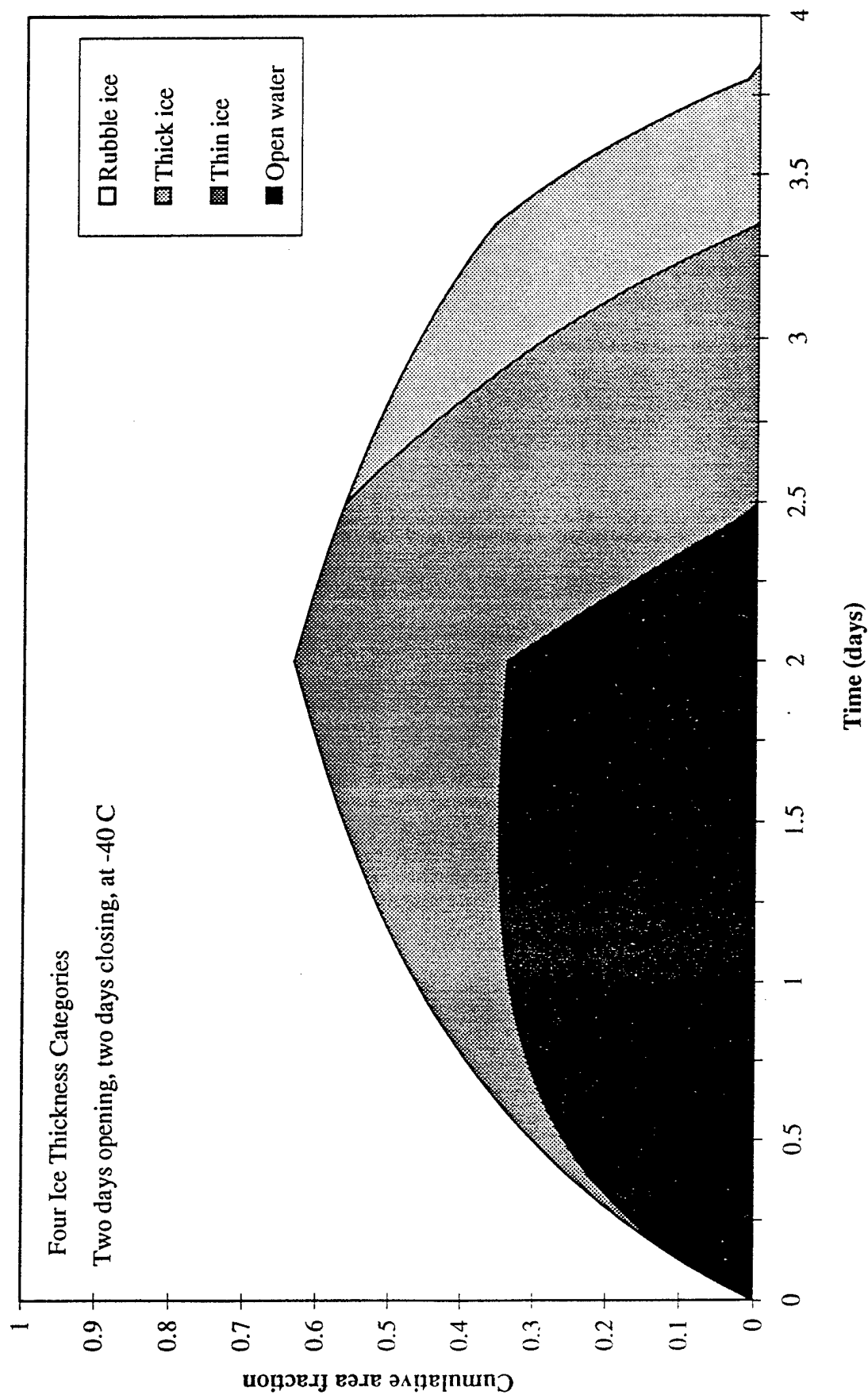


Figure 3. Example of redistribution of ice thickness expressed as area fractions for four ice-thickness categories resulting for opening and closing a lead.

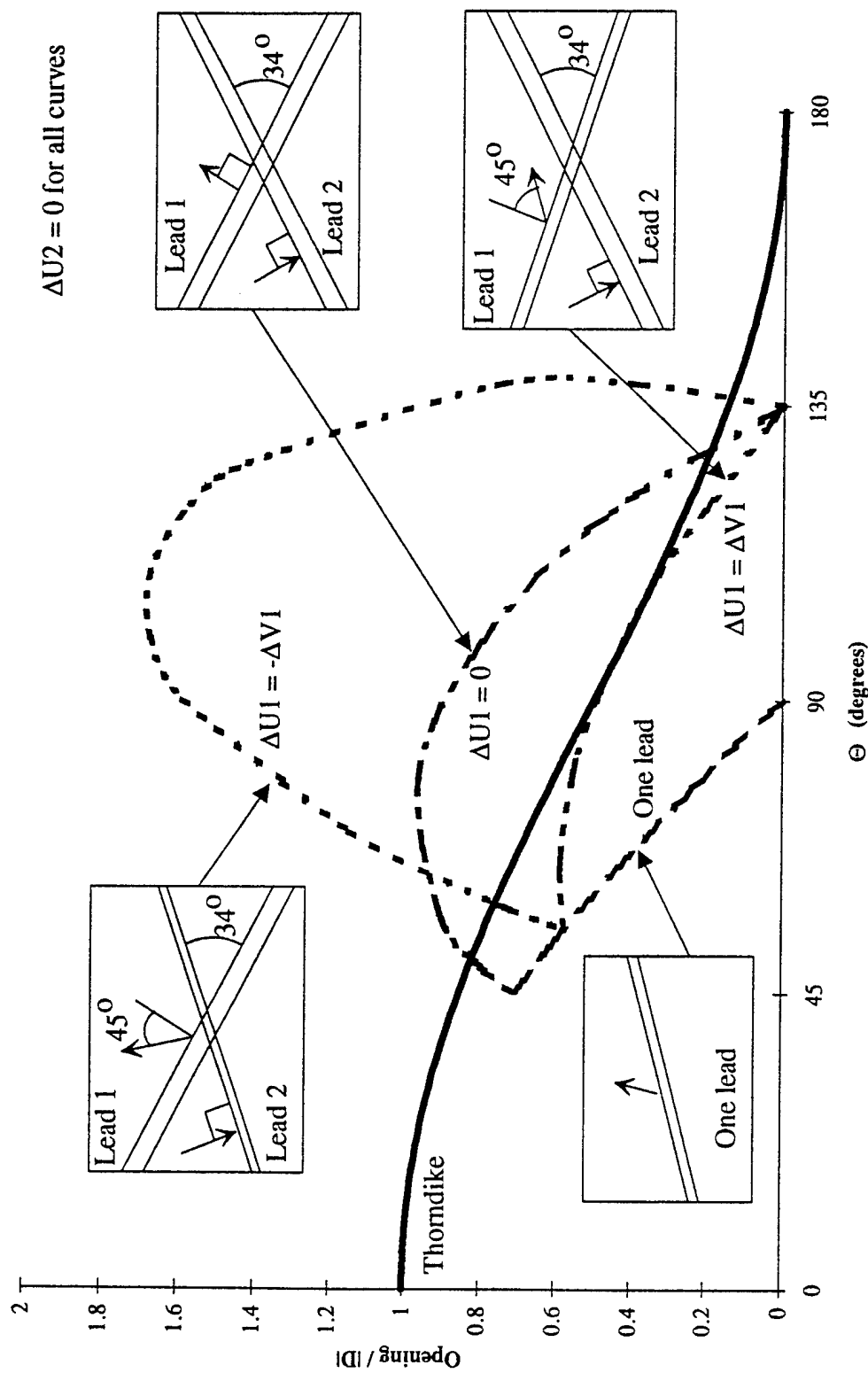


Figure 4. Accounting for lead orientation results in families of curves for opening as a function of Θ . Failure of isotropic ice falls on the curve for one active lead. The three higher loops result from varying the closing of the second lead for three values of the shear to opening ratio for the first lead.

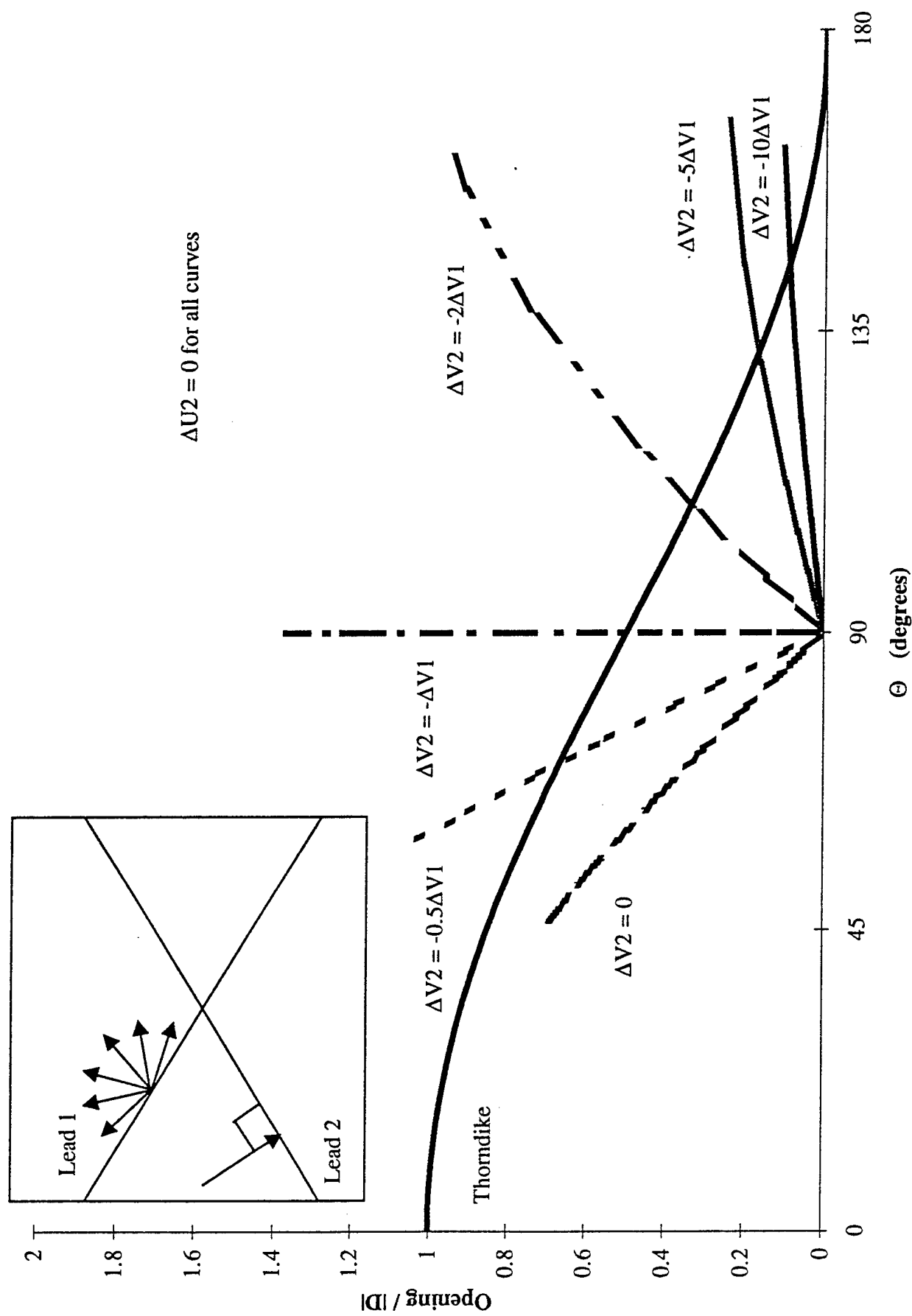


Figure 5. Family of curves for opening formed by holding shear in the second lead at zero and selecting specific values of the ratio of opening in lead 2 to lead 1.

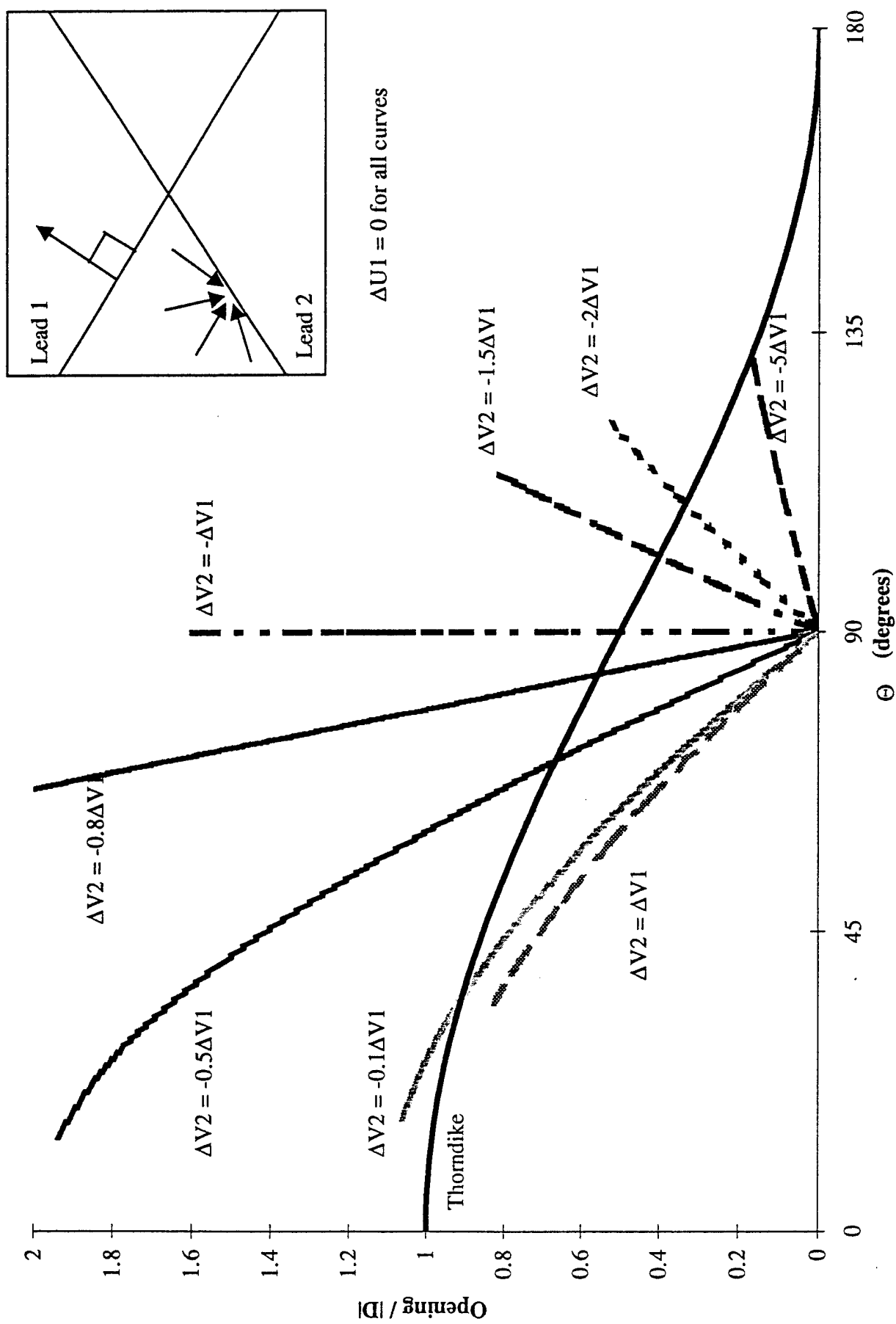


Figure 6. Family of curves for opening formed by holding shear in the first lead at zero and selecting specific values of the ratio of opening in lead 2 to lead 1.